

Sous le sceau de l'Université européenne de Bretagne

Télécom Bretagne

En habilitation conjointe avec l'Université de Bretagne-Sud

Ecole Doctorale - sicma

---

# Evaluation of optical technologies for home networking at very high speed

*Évaluation des technologies optiques pour les réseaux domestiques à très haut débit*

---

## Thèse de Doctorat

Mention : STIC

Présentée par **Hani Al Hajjar**

Département : OPTIQUE

Directeur de thèse : Jean-Louis de Bougrenet de La Tocnaye

Soutenue le 14 mars 2013

### Jury :

M. Zabih Ghassemlooy, Professeur, University of Northumbria, Newcastle, UK (Rapporteur)  
M. Jean-Pierre Vilcot, Professeur, IEMN, Lille (Rapporteur)  
M. Jean-Louis de Bougrenet de La Tocnaye, Professeur, Télécom bretagne, Brest (Directeur de thèse)  
Mme Nathalie Julien, Professeur, Université Bretagne-Sud, Lorient (Examineur)  
M. Olivier Bouchet, Ingénieur R&D, Orange Labs, Rennes (Examineur)  
M. Bruno Fracasso, Professeur, Télécom Bretagne, Brest (Encadrant)  
Mme Dominique Leroux, Maitre de conférences, Télécom Bretagne, Brest (Encadrant)



# Acknowledgments

If this PhD was well accomplished, it is partly due to the efforts and support of many people who have contributed directly or indirectly. I would like to thank them along these few lines.

First of all, I would like to thank Jean-Louis de Bougrenet de la Tocnaye, head of the Optics Department to welcome me and to give me the opportunity to do the thesis in the Optics Department.

I would like to thank my supervisor, Bruno Fracasso, for the patient guidance, encouragement, advice, support and friendship which were invaluable on both academic and personal level, and for which I am extremely grateful. I would like to express my deep gratitude and respect also for my co-supervisor, Dominique Leroux for all I have learned from her in the field of signal processing and for her continuous help and support in all stages of this thesis. I have been extremely lucky to have supervisors who cared so much about my work, and who responded to my questions and queries so promptly. Their attention, moral support and timely suggestions were useful in the preparation of my thesis. I am very much thankful to my supervisors for putting me in the track of this research.

I also thank the jury members Zabih Ghassemlooy, Jean-Pierre Vilcot, Nathalie Julien, Olivier Bouchet for agreeing to evaluate this work.

I would like to thank all members of Optics Department and especially, Marie-Laure Moulinard and Tatiana Loukina for their technical help and lending of optical equipment, Frédéric Lucarz for fruitful discussions and scientific and linguistic redaction advices, Michel Gadonna who allowed me to use his imaging device in my experimental work, Kevin Heggarty who provided me with some diffractive optical elements and gave me the opportunity to visit the labs of Cambridge University, Bernard Della for his technical help, Jean-Pierre Clere for the fabrication of many mechanical pieces, Anne Catherine Cariou for her administrative help in the starting of my work and Jennifer Romer who helps me in the large administrative load at the end of this work. I also thank Serge Pinel from the Microwave Department for his help in the fabrication of the optical concentrator prototypes.

I also wish to express my sincere thanks to Carmen Vasquez to welcome me in the Electronics and Technology Department of Universidad Carlos III of Madrid

---

during three months and to allow me to perform complex and determining experiments on polymer optical fiber transmission to speed up my PhD work, and for all members of her department especially, Carlos, David, Pedro, Juan Carlos and Jesus.

I also express big thanks to my departmental colleagues who gave me a lot of advice and simplified my life during this PhD especially Damien, Bogdan, Charbel, Aurélie, Lida, Samir, Bo, Kedar, Mervin, Yulia, Rabiaa, Khalil, Vinicius (and his wife Suellen), Corinne, Hai, Ion, Nam, Suman, Pascaline, Maina, Yves and Jennifer again for the very happy moments spent with them doing parties, sports, diners, discussions and others activities.

I wish to express my sincere thanks to all my projects students especially Èlodie and Daniel for their contributions in simulations and experimental works.

I would like to thank Institut Mines-Telecom for partly funding this project, the Collège Doctoral International/Univeristé Européenne de Bretagne (CDI/UEB) and Conseil régional de Bretagne for their financial help.

I take this opportunity to record my sincere thanks to all my friends Walid, Ammar, Jad, Khodor, Amina, Georges for their help and encouragement.

I would like to conclude by many thanks to my parents and my two brothers who encouraged me every day during these 3 years and found always the time to listen to me and to help me in different manners.

---



# Abstract

Over the last ten years, the number of laptop computers, personal digital assistants and other mobile terminals has massively increased. This evolution has led to a huge demand of wireless communications to supply mobility in various places such as offices, homes, rail stations or airports. To date, this indoor mobility is mainly offered by radio frequency (RF) communications using Wi-Fi channels, with a maximum bit rate of 300 Mbps. However, new indoor applications such as non-compressed high-definition (HD) video transfer or remote hard-disk backup require bandwidths (much) greater than the Gbps, which can be theoretically reached using an optical wireless communications (OWC) system. In this thesis, a new indoor OWC architecture is proposed and studied in the purpose of meeting the above requirement. It is based on distributed free-space optical femto-cells in each room of a building using fiber optics interconnections to provide bit rates exceeding 1 Gbps. The work is divided into three parts: (i) definition and dimensioning of the system including the selection of suitable opto-electronics technologies, (ii) characterization of the all-optical hybrid channel combining the optical fiber link and the narrow line-of-sight (NLOS) free-space cell, both analytically and by simulation using the standard VPI transmission maker software, and (iii) experimental measurements to assess the system performance. The validation of the optical architecture and its implementation is first performed using a link power budget approach. For the fibered part, a perfluorinated gradient-index polymer optical fiber (PF-GI-POF) is selected owing to its good trade-off between bandwidth, flexibility and endurance in indoor environments. This fiber has been experimentally studied and characterized during a mobility stay at University Carlos III of Madrid (Spain) in terms of transmission loss, frequency response and far-field profile, according to the input launching conditions. This step is crucial to validate the ease of installation and connection maintenance that can be carried out by the end users. A virtual system prototype is then designed using the VPI and Matlab softwares in cosimulation showing that downlink transmissions at 2 Gbps bit rate can be expected, provided that the real components characteristics match the simulation models. The energy efficiency (in J/Mbit) of the proposed system is also estimated, showing a large advantage as compared to existing radio frequency wireless systems. The optical free-space femto-cell is theoretically dimensioned in reach and size, depending on the optical receiver characteristics, the maximal permissible power in free-space (eye safety), and the influence of different noise sources. It is shown that using standard optoelectronic devices, the ceiling-table distance (2-3 m) can be covered with 20 cm femto-cells. A physical system prototype of the optical downlink is presented, combining the fiber

---

span and the free-space transmission at 1550 nm, at bit rates up to 2 Gbps. The quality of this link is assessed by measuring the received eye diagrams and bit error rate.

---

# Résumé

Durant la dernière décennie, le nombre d'ordinateurs portables, assistants numériques personnels et terminaux mobiles a considérablement augmenté. Cette évolution a conduit à une énorme demande de communications sans-fil dans le but de fournir la mobilité dans divers endroits tels que les bureaux, les maisons, les gares ou les aéroports. À ce jour, cette mobilité dans les réseaux domestiques est principalement offerte par les communications radiofréquence (RF), et principalement le Wi-Fi, ayant un débit maximum théorique de 300 Mbit/s. Cependant, de nouvelles applications "indoor" telles que le transfert vidéo non-compressé en haute définition (HD) ou la sauvegarde de disque dur à distance nécessitent des débits dépassant largement le Gbit/s. Un système de communication optique sans-fil semble être une solution prometteuse à ce déficit.

Dans cette thèse, une architecture de réseau optique sans-fil pour les réseaux domestiques à très haut-débit ( $> 1$  Gbit/s) est proposée et étudiée dans le but de répondre aux exigences décrites ci-dessus. Ce système est basé sur la distribution de femto-cellules optiques dans chaque pièce d'une maison par l'intermédiaire d'un réseau d'interconnexions en fibre optique. Le travail de cette thèse a été divisé en trois parties : (i) la définition et le dimensionnement de l'architecture, incluant la sélection des composants opto-électroniques du système, (ii) la caractérisation du canal tout-optique hybride combinant le lien fibré et la distribution des cellules optiques à faible divergence sans-fil, à travers un dimensionnement théorique et par simulation, utilisant le logiciel de transmission optique VPI Transmission Maker et enfin (iii) la mesure expérimentale du prototype incluant l'ensemble des composants caractérisés, dans le but de valider la performance du système.

L'architecture optique et sa mise en œuvre ont été conçues par validation du bilan de liaison optique. Une fibre polymère perfluorée à gradient d'indice (PF-GI-POF) est sélectionnée en raison de son bon compromis entre la bande passante, la souplesse et l'endurance mécanique en environnement intérieur. Cette fibre a été expérimentalement étudiée et caractérisée en pertes de transmission, de réponse en fréquence et de profil de champ lointain, en fonction des conditions d'injection par rapport à l'axe de la fibre. Cette étape est cruciale pour justifier la facilité d'installation et de maintenance de la connexion par les utilisateurs eux-mêmes.

Un prototype virtuel du système a ensuite été conçu en utilisant le logiciel VPI transmission maker en cosimulation avec Matlab, montrant la validité de la liaison descendante à un débit de 2 Gbit/s, à condition que les caractéristiques réelles des composants correspondent aux modèles de simulation. L'efficacité énergétique (en J/Mbit) du système proposé est également estimée, montrant un grand avantage par

---

rapport aux systèmes sans-fil RF existants. La femto-cellule optique en espace libre a été dimensionnée théoriquement en portée et en couverture en fonction des caractéristiques optiques du récepteur, de la puissance maximale admissible dans l'espace libre (sécurité oculaire) et de l'influence des différentes sources de bruit. Cela nous a permis de montrer qu'en utilisant des dispositifs opto-électroniques standard, le plan de communication situé à une distance de 2 à 3 m du plafond peut être recouvert de femto-cellules de 20 cm de diamètre. Finalement, un prototype physique de la liaison optique descendante est présenté, en combinant un tronçon de fibre et la transmission en espace libre à 1550 nm, à des débits allant jusqu'à 2 Gbit/s. La qualité du lien est évaluée en observant les diagrammes de l'œil reçus et en mesurant le taux d'erreur binaire.

---

# List of Acronyms

<b>AGC</b>	Asahi Glass Company
<b>AM</b>	Amplitude Modulation
<b>AOLT</b>	Allowable Offset Launch Tolerance
<b>APD</b>	Avalanche Photodiode
<b>AWG</b>	Arbitrary Wave Generator
<b>AWGN</b>	Additive White Gaussian Noise
<b>BER</b>	Bit Error Rate
<b>BPS</b>	Bit Per Second
<b>BSS</b>	Basic Service Set
<b>CCD</b>	Charge Coupled Device
<b>CPC</b>	Compound Parabolic Concentrator
<b>DAS</b>	Distributed Antenna System
<b>DFB</b>	Distributed Feedback
<b>DOE</b>	Diffraction Optical Element
<b>DTIRC</b>	Dielectric Totally Internally Reflecting Concentrator
<b>DWDM</b>	Dense Wavelength Division Multiplexing
<b>ECC</b>	Error-Correcting Code
<b>EDFA</b>	Erbium-Doped Fiber Amplifier
<b>EMI</b>	Electromagnetic Interference
<b>E/O</b>	Electro-Optic
<b>FCC</b>	Federal Communications Commission
<b>FFP</b>	Far-Field Pattern
<b>FFT</b>	Fast Fourier Transform
<b>FM</b>	Frequency Modulation
<b>FOV</b>	Field of View
<b>FP</b>	Fabry Perot
<b>FSK</b>	Frequency Shift Keying
<b>FSO</b>	Free-space Optic
<b>FVP</b>	Free View-point
<b>FTTH</b>	Fiber To The Home
<b>FWHM</b>	Full Wave at Half Maximum
<b>GDAF</b>	Displays and photonics Applications Group
<b>GFSK</b>	Gaussian shaped Frequency Shift Keying
<b>GI</b>	Graded-Index
<b>GI-POF</b>	Graded-Index Polymer Optical Fiber

---

<b>GOF</b>	Glass Optical Fiber
<b>HD</b>	High Definition
<b>HOE</b>	Holographic Optical Element
<b>HV</b>	High Voltage
<b>ILC</b>	Input Launching Conditions
<b>IM-DD</b>	Intensity Modulation with Direct Detection
<b>IOW</b>	Indoor Optical Wireless
<b>IPTV</b>	Internet Protocol-Based Television
<b>IrDA</b>	Infrared Data Association
<b>IrFM</b>	Infrared Financial Messaging
<b>ISI</b>	Inter Symbol Interference
<b>LAN</b>	Local Area Network
<b>LC</b>	Launching Conditions
<b>LCA</b>	Lightwave Component Analyser
<b>LD</b>	Laser Diode
<b>LED</b>	Light Emitting Diode
<b>LOS</b>	Line Of Sight
<b>LTE</b>	Long Term Evolution
<b>LV</b>	Low Voltage
<b>M-ASK</b>	M- Amplitude Shift Keying
<b>M-FSK</b>	M- Frequency Shift Keying
<b>M-PAM</b>	M- Pulse Amplitude Modulation
<b>M-PDM</b>	M- Pulse Duration Modulation
<b>M-PPM</b>	M- Pulse Position Modulation
<b>M-PSK</b>	M- Phase Shift Keying
<b>M-QAM</b>	M- Quadrature Amplitude Modulation
<b>MAS</b>	Mono Antenna System
<b>MC</b>	Multi Carrier
<b>MEMS</b>	MicroElectroMechanical System
<b>MIMO</b>	Multiple Input Multiple Output
<b>MLOS</b>	Medium Line Of Sight
<b>MMF</b>	Multimode Fiber
<b>MU</b>	Mobile Unit
<b>MV</b>	Medium Voltage
<b>NA</b>	Numerical Aperture
<b>NHK</b>	Nippon Hoso Kyokai
<b>NLOS</b>	Narrow Line Of Sight
<b>NRZ</b>	Non-Return-To-Zero
<b>OAP</b>	Optical Access Point
<b>OCS</b>	Optical Control Station
<b>OFDM</b>	Orthogonal Frequency Division Multiplexing
<b>OFL</b>	Overfilled Launching
<b>OOK</b>	On-Off keying
<b>PDA</b>	Personal Digital Assistant
<b>PF-GI-POF</b>	Perfluorinated Graded Index Polymer Optical Fiber

---

<b>PIN</b>	P-Intrinsic-N Photodiode
<b>PLC</b>	Power Line Communications
<b>PMMA</b>	Poly(methyl methacrylate)
<b>PmP</b>	Point to Multipoint
<b>POF</b>	Polymer Optical Fiber
<b>PRBS</b>	Pseudo Random Binary Sequence
<b>PSD</b>	Power Spectral Density
<b>QoS</b>	Quality of Services
<b>RAU</b>	Remote Antenna Unit
<b>RF</b>	Radio Frequency
<b>RGB LED</b>	Red Green Blue LED
<b>RML</b>	Restricted Mode Launching
<b>RMS</b>	Root Mean Square
<b>RoF</b>	Radio over Fiber
<b>RPM</b>	Rotation Per Minute
<b>RTSP</b>	Real Time Streaming Protocol
<b>RZ</b>	Return-to-Zero
<b>SC</b>	Single Carrier
<b>SER</b>	Symbol Error Rate
<b>SI PIN</b>	Silicon PIN
<b>SI-POF</b>	Step-Index Polymer Optical Fiber
<b>SMF</b>	Single-mode Fiber
<b>SNR</b>	Signal-to-Noise Ration
<b>SPS</b>	Symbol Per Second
<b>TIA</b>	Transimpedance Amplifier
<b>UC3M</b>	University Carlos III of Madrid
<b>UWB</b>	Ultra Wide Band
<b>VCSEL</b>	Vertical-Cavity Surface Emitting Laser
<b>VLC</b>	Visible Light Communications
<b>VLCC</b>	Visible Light Communications Consortium
<b>VOD</b>	Video On Demand
<b>WDM</b>	Wavelength Division Multiplexing
<b>WiFi</b>	Wireless Fidelity
<b>WLOS</b>	Wide Line Of Sight
<b>WPAN</b>	Wireless Personal Area Network

---

## List of Symbols

$a$	Fiber core radius
$a_k$	OOK-NRZ Symbols
$A$	Photodetector detection area
$A_d$	Detector area
$A_i$	Coefficients of the resonant material
$A_{eff}$	Photodetector effective detection area
$\alpha$	Divergence semi-angle
$\alpha_c$	Source chirp parameter
$\alpha_\nu$	Modal attenuation
$Att_{FS}$	Free-space attenuation
$B_e$	Photodiode electrical bandwidth
$\beta_0''$	First order chromatic dispersion parameter
$C_1$	Communication plane
$C_2$	Ground plane
$C_{CB}$	BJT collector-base capacitance
$C_D$	Photodiode capacitance
$C_{EB}$	BJT emitter-base capacitance
$C_{tot}$	Total receiver capacitance
$d$	Distance between the transmitter and the receiver
$D$	Effective bitrate
$D_0$	Modal velocity dispersion averaged over all guided modes
$d_1$	Distance between the OAP and the communication plane
$d_c$	Distance between the OAP and the cornea
$d_r$	Thickness of the i-region
$\Delta$	Relative refractive index
$\Delta C$	Reconstructed cell dimensions
$\delta h$	DOE resolution
$\Delta H$	DOE size
$\delta I$	Spatial resolution of the reconstructed image
$\Delta I$	Size of the reconstructed image
$\delta O$	spacing between two adjacent diffraction orders
$\delta s$	Smallest speckle size
$\Delta_\lambda$	Optical bandwidth of the filter
$\epsilon_0$	Permittivity of free-space
$\epsilon_r$	Relative permittivity of semiconductor material

---



---

$\eta$	Quantum efficiency
$E_b$	Energy required to transmit one bit
$E_{bk}$	Irradiance of the background ambient light
$E_c$	Upper irradiance level that the cornea can support
$E_s$	Irradiance of the optical signal impinging at the concentrator input
$f$	Focal length
$f_{sharp}$	Lens $f$ -number
$F$	Preamplifier noise figure
$f_s$	Symbol rate
$f_s^{OFDM}$	Symbol rate per subcarrier
$\gamma$	Duty cycle
$G$	Concentrator gain
$G_{bk}$	Optical gain of the concentrator for the ambient light
$g_m$	Conductance
$I_{av}$	Averaged Photocurrent
$I_c$	Collector current
$I_{amb}$	Average photocurrent created by the ambient light
$I_D$	Dark current
$I_p$	Photodiode photocurrent
$I_{pp}$	Peak-to-peak Photocurrent
$I_{tot}$	total input referred noise current
$K$	Boltzman constant
$L$	Radiance
$\lambda_0$	Center wavelength at the normal incidence
$\lambda_{normal}$	Wavelength of peak transmission for normal incidence
$\lambda_{pk}$	Wavelength of peak transmission for light incident at angle $\theta$
$l_i$	Wavelengths of the resonant material
$m$	Principle mode group number
$m_f$	Butterworth order of the optical filter
$M$	Avalanche multiplication factor
$M_m$	Symbol
$M_t$	Total number of mode groups that can be excited
$n$	Refractive index of the environment that surrounds the concentrator
$n'$	Concentrator refractive index
$N^*$	Effective refractive index of the filter
$n_1$	Refractive index at the axis of the fiber
$NA$	Numerical aperture
$n_2$	Refractive index at the core/cladding interface
$N_{amb}$	Ambient noise current power spectral density
$N_D$	Dark noise current power spectral density
$N_{ord}$	Number of orders in the reconstructed cell
$N_{pop}$	Number of pixels per period in the DOE
$N_{preamp}$	Preamplifier noise current power spectral density
$N_{preamp\ f^2}$	Preamplifier $f^2$ noise current power spectral density
$N_{pts}$	Number of sampling points in the DOE per dimension

---

---

$N_q$	Quantum noise current power spectral density
$N_{sn}$	Shot noise current power spectral density
$N_{tn}$	Thermal noise current power spectral density
$NA$	Numerical aperture
$n(\lambda)$	Sellmeier development
$n(r)$	Radial profile of truncated parabolic index
$\nu$	Different mode group carried by the fiber
$\omega$	Baseband angular frequency
$\Omega$	Frequency of the RF modulating signal
$P$	Spatial period of the DOE
$P_0$	Maximum allowed emitted power in free-space
$P_{amb}$	Received optical background power
$P_e$	Symbol error probability
$P_{pp}$	Peak-to-peak optical power detected by the photodiode
$P_{preamp}^i$	Equivalent input spectral power density of the preamplifier
$P_s$	Average detected optical power by the photodiode
$P_{tot}$	Overall consumed electric power by all system components for a given technology
$q$	Charge of electron
$r_\lambda$	Responsivity photodiode parameter
$R_1$	Half-width of the diffracted pattern
$R_b$	Bitrate
$R_L$	Load resistance
$R_{sh}$	Photoreceiver shunt resistance
$R(x, z, w)$	Modal power in the Fourier domain
$S$	Threshold of the decision circuit
$S_0$	Averaged dispersion slope
$SNR$	Signal-to-noise ratio
$\sigma^2$	Variance of the received symbol
$\sigma_c$	Related directly to the optical source linewidth
$\sigma_\lambda$	Root mean square line width of the driving source
$T$	The ambient temperature
$\bar{T}$	Average optical filter transmission
$t_0$	Initial sampling time
$\tau_\nu$	Time delayed of each sample
$T_0$	Transmittance of the optical bandpass filter at $\lambda_0$
$T_f$	$m$ th order Bandpass optical filter Butterworth response
$T_{f0}$	Peak optical filter transmission
$\theta_i$	Angle of incidence
$\theta'$	Maximum angle of rays outgoing from the concentrator
$\theta_c$	Maximum angle of rays impinging onto the concentrator
$w$	Beam half-width at the lens plane
$W$	Optical source linewidth
$z$	Fiber length

---

# Contents

<b>1</b>	<b>Indoor network communications</b>	<b>21</b>
	Introduction . . . . .	23
I	Communications in the access network . . . . .	23
	I.1 Evolution of communications in the access network . . . . .	23
	I.2 End-user new and future services in in-building networks . . . . .	24
II	Wired communications for indoor networks . . . . .	26
	II.1 Coaxial cable . . . . .	26
	II.2 Optical fiber communications . . . . .	27
	II.3 Power line communications . . . . .	28
	II.4 Conclusion . . . . .	29
III	Wireless communications using radio and microwave frequencies . . . . .	29
	III.1 Bluetooth . . . . .	29
	III.2 WiFi . . . . .	30
	III.3 Ultra wide band . . . . .	31
	III.4 60 GHz wireless communications . . . . .	32
	III.5 Radio-over-fiber . . . . .	33
	III.6 Conclusion . . . . .	34
IV	Optical wireless communications . . . . .	35
	IV.1 Outdoor optical wireless communications . . . . .	37
	IV.2 Indoor optical wireless communications . . . . .	39
	IV.2.1 Visible light communications . . . . .	39
	IV.2.2 Infrared optical wireless communications . . . . .	40
V	Advantages of optical wireless communications . . . . .	42
VI	Conclusion . . . . .	43
VII	Objectives and outlines of the PhD thesis . . . . .	44
	Bibliography . . . . .	50
	Figures and tables . . . . .	51
<b>2</b>	<b>Design of the wireless optical cells</b>	<b>53</b>
I	Proposed architecture . . . . .	54
	I.1 Downlink description . . . . .	54
	I.2 First downlink geometry approach . . . . .	55
	I.3 Optical access point . . . . .	57
	I.4 Different Uplink options . . . . .	58
	I.4.1 Radio frequency uplink . . . . .	58

---

I.4.2	Optical uplink . . . . .	59
II	Optical sources . . . . .	60
III	Operational constraints . . . . .	62
III.1	Eye and skin safety constraints . . . . .	62
III.2	Ambient noise . . . . .	63
III.3	Reflected beams . . . . .	63
IV	Wavelength choice . . . . .	64
V	Power link budget: first approach . . . . .	65
VI	Optical control station . . . . .	67
VII	Green aspects of proposal system . . . . .	68
VIII	Conclusion . . . . .	70
	Bibliography . . . . .	71
	Figures and tables . . . . .	72
<b>3</b>	<b>Fiber-distributed optical cells</b>	<b>73</b>
	Introduction . . . . .	74
I	Optical fiber for home networks . . . . .	74
II	Perfluorinated graded index polymer optical fiber . . . . .	75
II.1	Fabrication and physical properties . . . . .	75
II.2	Theoretical transmission model of the PF-GI-POF . . . . .	78
II.3	PF-GI-POF characterization . . . . .	80
II.4	Temporal transmission characterization of the PF-GI-POF . . . . .	81
II.4.1	Modeling and simulation of the PF-GI-POF . . . . .	81
II.4.2	PF-GI-POF loss measurement . . . . .	85
II.4.3	Frequency response measurement . . . . .	90
II.5	Far-Field transmission characterization of the PF-GI-POF . . . . .	91
II.5.1	One-dimensional Far-Field profile . . . . .	92
II.5.2	Two-dimensional Far-Field measurement . . . . .	92
II.5.3	Far-field speckle modelling . . . . .	96
III	Single-mode fiber for home networks . . . . .	97
III.1	Physical characteristics . . . . .	97
III.2	Spatial characterization of the G657 far-field profile . . . . .	97
IV	Conclusion . . . . .	99
	Bibliography . . . . .	102
	Figures and tables . . . . .	103
<b>4</b>	<b>Optical free-space cell dimensioning</b>	<b>105</b>
	Introduction . . . . .	107
I	Optical access point . . . . .	107
I.1	Diffraction optical element . . . . .	107
I.2	Optical beam free-space profile . . . . .	110
II	Wireless receiver . . . . .	112
II.1	Optical filter . . . . .	112
II.2	Optical concentrator . . . . .	113
II.2.1	CPC design, fabrication and gain simulation . . . . .	116

---

---

II.2.2	CPC gain measurement . . . . .	116
II.3	Pre-amplified photodiode . . . . .	118
II.3.1	Photodiode characteristics . . . . .	118
II.3.2	Preamplifier characteristics . . . . .	120
II.4	Receiver noises . . . . .	121
II.4.1	Different receiver noise types . . . . .	122
II.4.2	Ambient noise . . . . .	123
II.4.3	Conclusion . . . . .	124
III	NLOS free-space link performance . . . . .	124
III.1	Modulation scheme . . . . .	124
III.1.1	Transmission techniques . . . . .	125
III.1.2	On-Off Keying modulation . . . . .	127
III.2	Signal-to-noise ratio and receiver sensitivity . . . . .	130
III.3	Dimensioning of the NLOS link . . . . .	133
IV	Software modelling and simulation of the free-space link . . . . .	137
V	Conclusion . . . . .	139
	Bibliography . . . . .	141
	Figures and tables . . . . .	142
<b>5</b>	<b>Optical downlink performance: simulation and experimental re-</b>	
	<b>sults</b> . . . . .	<b>145</b>
	Introduction . . . . .	146
I	Downlink transmission software simulation . . . . .	146
II	Experimental test of the downlink . . . . .	148
III	Conclusion . . . . .	156
	Bibliography . . . . .	157
	Figures and tables . . . . .	158
	<b>Conclusions</b> . . . . .	<b>161</b>
<b>6</b>	<b>Résumé détaillé</b> . . . . .	<b>167</b>
I	Sujet, problématique et état de l'art . . . . .	168
II	Méthodologie . . . . .	169
III	Architecture proposée . . . . .	169
IV	Validation du budget optique . . . . .	170
V	Caractérisation de la fibre pour la distribution des cellules optiques en espace libre . . . . .	171
VI	Caractérisation de la cellule optique en espace libre . . . . .	174
VI.1	Point d'accès optique . . . . .	174
VI.2	Dimensionnement de la cellule optique en espace libre . . . . .	174
VII	Simulation et test expérimental du système global . . . . .	175
VII.1	Simulation du lien descendant . . . . .	175
VII.2	Test expérimental du lien descendant . . . . .	177
VIII	Conclusion . . . . .	178
	<b>List of Publications</b> . . . . .	<b>181</b>

---

A	Definitions of some radiometry elements	185
B	Beam shaping at the Optical Access Point	187

---

# General Introduction

Wireless communications has shown its prodigy in the telecommunications domain. The fast development of wireless personal communications technologies in terms of devices, provided bit rate, services and applications has created a new society where most people want to be connected anywhere and anytime, accustomed to the comfortability of wireless access. Nowadays, mobile communications are offered by a large variety of radio frequency technologies, a generic term gathering several complementary access technologies.

In the last few years, the required bit rates for new services and applications began to exceed the bandwidth limits of radio frequency channels. Until recently, users were satisfied with the wireless services in outdoor environment which, despite a limited bit rate, have brought enough capacity to develop new applications such as video call, internet browsing, or TV watching at moderate bit rate.

In an indoor environment, see figure 1, the bit rate provided by wireless technologies (WiFi) is limited, and users suffer from waiting during the downloading of large files, sometimes exceeding the Gbit in size.

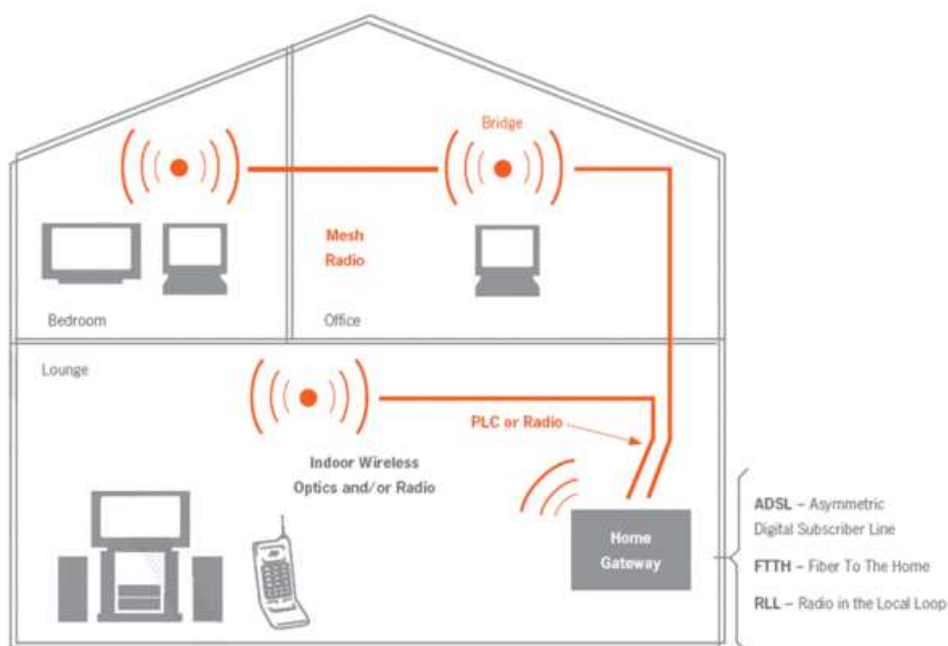


Figure 1: Omega project generic scheme [1] of a Gbps home network

In this framework, most network operators and service providers are investigating alternative techniques to provide wireless high bit rate channels in an indoor environment. Optical technologies are used on a large scale with optical fiber infrastructure now spread out from core to access network, as shown in figure 2. The present fiber-to-the-home massive deployment in most developed countries is a major step towards a high-speed internet access network. The next phase will be the extension of the high-speed optical technologies within home and buildings to provide end-to-end broadband networks. National or international research projects such as Alpha [2], Techim@ges [3] or Omega [1] have investigated the topic in order to provide Gbps bit rate demonstrators in indoor environment.

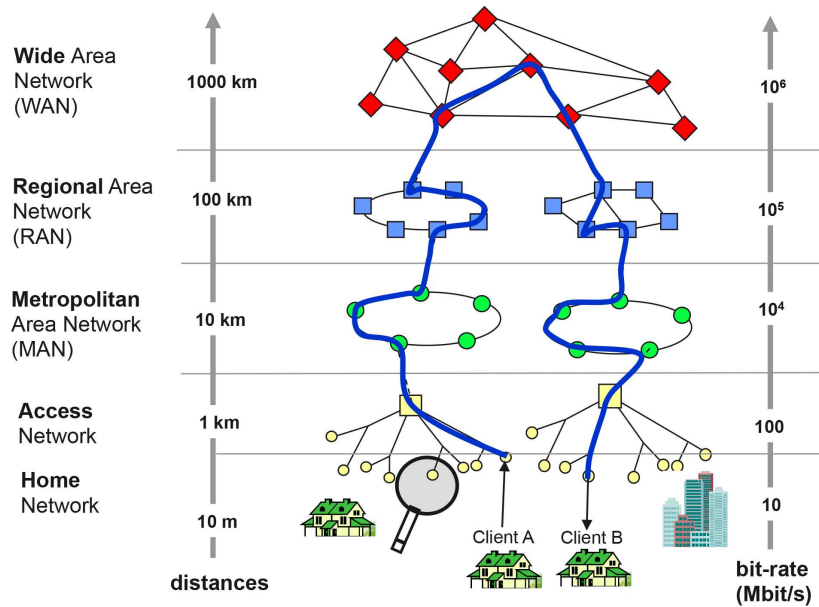


Figure 2: Network architecture from core to access network. Optical fiber links now extend over 98 % of the coverage, from the access to the WAN networks.

Another topic of interest is the ever increasing energy consumption in telecommunications networks. From a study performed by Deutsche Telekom in 2008, it was shown that the average daily energy consumption dedicated to communication technologies per household is about 2.5 KWh. The extrapolation to the whole population of Germany leads to a national estimated daily energy consumption of 100 GWh, only dedicated to the multimedia use. Surprisingly, this represents half of the production of a large nuclear plant. Concerning public health issues, many studies have investigated the effects of electromagnetic radiation, taking the radio frequency networks dimensions into account [4]. Despite many warnings from both biologists and customer associations, no precise harmful effect have been stressed, but wireless network deployments now tend to minimize the radio frequency "electrosmog" within densely populated areas.



As an alternative to radio frequency, wireless links can also be performed with light-waves propagating in free-space. For outdoor applications, the solution is referred to as "free-space optics" or FSO, while the "optical wireless" term or OW, is customary for indoor communications. Optical wireless communications offer attractive features, like the potential for very high data rates (more than 10 Gbps) owing to a huge bandwidth which is still available and unregulated, unlike the radio frequency spectrum, which is getting increasingly crowded. Moreover, Optical wireless does not produce any electromagnetic interference with systems operating in the radio frequency spectrum. Optical wireless can be classified as a function of the transmission wavelength. Two options are usually considered as the most attractive due to the availability of low-cost components (850 nm window) and robustness with respect to eye-safety (1550 nm window). Lately, there has been an increasing interest in developing visible light communications, where light emitting diodes primarily dedicated to lighting or signalling purposes have also been used to transmit high-speed digital information. Finally, most integrated optical components are characterized by a lower energy consumption as compared to radio frequency devices in addition to the reduction in the number of electro/optic conversions.

These points motivated us to study all-optical indoor high-speed wireless communications networks with potential reduced environmental and health impact. The proposed system aims at distributing optical wireless cells in different rooms of a home interconnect by optical fiber to a base station inside the home.

This thesis consists of five chapters, whose contents are briefly explained below.

Chapter 1 is dedicated to the state of the art of indoor communication systems. Access network and new end-users applications and services are introduced. Moreover, wired communications and the different radio frequency and microwave wireless technologies are presented. Finally, optical wireless communications and their advantages are tackled.

The design and the description of the proposed optical free-space cell system is the subject of chapter 2. System constraints, wavelength choice and different components used are introduced in this chapter.

Chapter 3 is dedicated to the fibered part of the proposed system, showing the study of the fiber that can be used in this application. A theoretical study, some simulation and experimental work are performed to characterize the fiber link and to assess the suitable fiber type for the studied architecture.

In chapter 4, the optical free-space cell is characterized. Using a theoretical modelling and a software simulation, the optical access point and the mobile receiver are thoroughly studied and their building modules are characterized. Furthermore, different noise sources at the receiver stage are evaluated in order to demonstrate the dominant noise, which enables us to study the performance of the narrow line-of-sight (NLOS) link in order to estimate the signal-to-noise ratio, and then to define

---

the limits of the free-space cell.

In the last chapter, we characterize the performance of the global downlink. Firstly, a simulation of the global system is performed based on the combination of the simulation presented in chapter 3 and 4. Furthermore, an experimental bench of the downlink is built. The eye diagram is displayed and the signal-to-noise ratio is measured to validate the feasibility of the proposed system.

The document is concluded by a summary of the main results and some perspectives of the future work.

This work was supported by a grant from *Institut Mines-Telecom*, in the framework of the *Futur et Ruptures* program.

## Bibliography

- [1] projet FP7-ICT (2008-10) OMEGA: Home Gigabit Access. [www.ict-omega.eu](http://www.ict-omega.eu).
  - [2] ALPHA: Architectures for fLexible Photonic Home and projet FP7-ICT (2008-10) Access networks. [www.ict-alpha.eu](http://www.ict-alpha.eu).
  - [3] Techim@ges project. <http://www.images-et-reseaux.com/fr/les-projets/>.
  - [4] C. Grangeat, C. Person, D. Picard, and J. Wiart. Measurement of the Specific Absorption Rate (SAR) on mobile phone - COMOBIO Project contribution to international standards. *Annals of telecommunications*, 58(5-6):1509–1511, May-Jun. 2003.
-

# Chapter 1

## Indoor network communications

### Contents

---

Introduction . . . . .	<b>23</b>
I Communications in the access network . . . . .	<b>23</b>
I.1 Evolution of communications in the access network . . .	23
I.2 End-user new and future services in in-building networks	24
II Wired communications for indoor networks . . . . .	<b>26</b>
II.1 Coaxial cable . . . . .	26
II.2 Optical fiber communications . . . . .	27
II.3 Power line communications . . . . .	28
II.4 Conclusion . . . . .	29
III Wireless communications using radio and microwave frequencies	<b>29</b>
III.1 Bluetooth . . . . .	29
III.2 WiFi . . . . .	30
III.3 Ultra wide band . . . . .	31
III.4 60 GHz wireless communications . . . . .	32
III.5 Radio-over-fiber . . . . .	33
III.6 Conclusion . . . . .	34
IV Optical wireless communications . . . . .	<b>35</b>
IV.1 Outdoor optical wireless communications . . . . .	37
IV.2 Indoor optical wireless communications . . . . .	39
IV.2.1 Visible light communications . . . . .	39
IV.2.2 Infrared optical wireless communications . . .	40
V Advantages of optical wireless communications . . . . .	<b>42</b>
VI Conclusion . . . . .	<b>43</b>
VII Objectives and outlines of the PhD thesis . . . . .	<b>44</b>
Bibliography . . . . .	<b>50</b>

---

Figures and tables . . . . .	<b>51</b>
------------------------------	-----------

---

## Introduction

In the past few years, an unprecedented raising of number of laptop computers, personal digital assistants (PDAs) and other mobile terminals has been observed. This evolution was accompanied by a huge demand for wireless data transmission, in the purpose of avoiding wires and connectors to supply some kind of mobility, especially, in cases where the distance between the transmitter and receiver is relatively small e.g. at airports, rail stations, offices or homes.

To date, wireless communications are mainly provided by radio frequency (RF) communications using WiFi channels, a widespread technology offering a maximum bit rate of 300 Mbps according to the 802.11n standard. But, new bandwidth-hungry services are used today, such as high definition (HD) video and 3D video, and such future applications as ultra high definition video, Web 3D and robotic assistant will require a higher bit rate, that will exceed the Gbps in the indoor network framework. These applications start to be realistic, mainly after providing this high bit rate in the access network, with the installation of the fiber to the home (FTTH).

These services and applications, that will be described later, give us a view of the future indoor network with the required high data rates (few hundred of Mbps to several Gbps). This network will support multiple services with widely varying characteristics and requirements having a better Quality-of-service (QoS) and less energy consumption.

In this chapter, a short history of the communications evolution will be presented. The most common technologies for wired and wireless communications having radio frequency and optical carriers in indoor environment will be shortly explained. Then, we will present the advantages of optical wireless communications, the new services in in-buildings networks and the required bit rate before concluding the chapter with the objectives and outline of this thesis.

## I Communications in the access network

### I.1 Evolution of communications in the access network

The communications evolution started in the 1790s with the french engineer Claude Chappe, who invented the optical telegraph. The system was based on a set of semaphores mounted on towers exchanging messages from one tower to the next one, in direct view. After 1845, the electrical telegraph appeared progressively replaced the optical telegraph. The next step was the telephone introduced in 1848. The first transfer of data called "computer networking" appeared in 1969, and a global system of interconnected computer networks was presented in 1983 under the name of "internet". Regarding mobile communications, the first generation (1G) of wireless telephone technology was introduced in 1980s. This first analog generation was replaced by the second generation (2G) of digital networks which was followed by the 3rd generation (3G) in the late 1990s, finding applications in wireless voice telephony, mobile internet access, fixed wireless internet access, video calls and mobile TV. A progression of this generation leads to 3.5G and 4G.

---

providing mobile broadband access of several Mbps to smartphones and mobile modems in laptop and computers. Nowadays, the new generation is being installed around the world through the long term evolution (LTE) marketed as 4G, which can provide a maximum downlink bit rate of 300 Mbps and a peak uplink of 75 Mbps. The different generations of this standard are mainly designed for smartphones and full mobility communications. Another area of wireless communications that has progressed in the late decade is the local area network (LAN) and the most spread technology used for that is the WiFi, where the mobility is full in a limited area around the access point. This technology is presented in a section below. On the other hand, wired communications in the access network were largely developed with the introduction of optical fiber yielding the development of FTTH networks to achieve potential Gbps bit rates, as benefits of the huge bandwidth of the optical fiber.

## I.2 End-user new and future services in in-building networks

High speed indoor wireless systems are nowadays subject of a large number of national and international research projects such as Omega [1], Alpha [2] which are parts of the seventh framework programme FP7 or Techim@ges [3] of "Pôle Images et Réseaux". These projects had the goal to provide a higher bit rate in comparison to the existing systems for the future applications and services, depending on different parameters such as bit rate, maximum latency tolerance, delay variations, mobility traffic priority and security. In this paragraph and based on these two studies, we shortly present some new and future services, their specific characteristics and their required bit rates.

- *Video on Demand (VoD) and Multimedia content production and delivery:* VoD uses Real Time Streaming Protocol (RTSP) to stream video to the end-user based on Internet Protocol-based television (IPTV). High quality video files having a size as large as 10 Gbit should be downloaded to the local server in the shortest possible time ( $< 1$  min) to permit the user to play it locally. A speed of 1 Gbps will be required to download quickly the video file and to satisfy users.
- *Video streaming:* It is referred to direct streaming of uncompressed video from media server or player (DVD, blu-ray disk) to one or several media renderers (TV set for instance) without downloading video before. The data rate of this transmission goes from several Mbps (VGA format or  $640 \times 480$  p @ 59.94/60 Hz) to 10.2 Gbps (in the case of Full HD TV or  $1920 \times 1080$  @ 59.94/60 Hz with 48 bit "Deep color").
- *Immersive TV:* The size limits of TV screens prevent an immersive experience with conventional TV or HDTV systems. A solution to overcome this size limit is to use a projector, but in this case, the number of pixels per inch is reduced limiting the image resolution. An immersive home TV can be provided using the technique proposed by Nippon Hoso Kyokai (NHK - Japan

---

Broadcasting Corporation) based on the use of classical flat screen instead of the dome for the projection introducing the Ultra HDTV [4] with a screen resolution of  $7680 \times 4320$  pixels, 16 times bigger than standard HDTV with bit rate of the uncompressed images of 24 Gbps. In 2006, NHK developed a codec to compress audio part of video signal in order to squeeze 24 Gbps into 600 Mbps [5].

- *Free view-point TV*: Free view point (FVP) is a TV service which allows the final user to freely chose the point of view of the show. A similar service is provided today by some broadcasters but limited to views, of different using cameras for broadcasting, while, the free view-point should permit the user any possible viewpoint not necessarily corresponding to a physical camera. An example of this service is presented on [6] where 15 cameras, each one, broadcasting an 1080p stream are used and the maximum required bit rate is  $15 \times 62.5 = 937.5$  Mbps.
- *Stereoscopic TV*: It represents different manners to recreate 3D images representation in the goal of transmitting to the end-user the correspondent feeling of depth with images not only on screen plane, but also behind and ahead the screen. This application requires a bit rate of 320 Mbps.
- *Web 3D*: The next expected major application in the internet will be the web 3D, especially with the recent development of 3D films and Video, the spread of 3D screens, 3D cameras and applications on 3D. Web 3D can offer an immersive experience which will attract a large user number as compared to the static graphical interface in today's Web. In the last years, a web 3D consortium was founded to create and deploy open standards that enable the communication of the real-time 3D across applications, networks and XML web services [7]. The required bit rate for this application is up to 1 Gbps.
- *Remote Residential Backup*: Today, end-users produce large amount of data, due to extensive use high resolution digital cameras and video equipments on mobile terminals. This data are shared between families and friends, but they need to be stored on local computer or media server, with storage spaces of more than 1 Terabyte [8]. The remote file backup is a service of increasing popularity, which requires an average capacity of 1 Gbps on about 2 hours to transfer the Terabyte. This duration gives the possibility to perform the backup during the time when the network is not congested (between 12 am and 4 am in business areas and between 10 am and 4 pm in residential areas).
- *Grid computing*: It is a grid of computer resources from multiple administrative domains (computing, storage,..) working together to solve a common problem, as, for example the online visualization of a virtual environment [9]. This application requires a bit rate exceeding the Gbps.

The services presented above and their required bit rates are summarized in table 1.1. Some of these services are ready for deployment and the others are expected

---

Table 1.1: New and future services and the required bit rates

Services	bit rate (Mbps)	Remarks
Stereoscopic TV	320	Future (1080p)
Remote Residential Backup	500	No packet loss
Immersive TV (UHDTV)	600	Compressed for broadcast 4230p
Free view point TV	937	Future (1080p)
Video on Demand	up to 1000	Compressed using MPEG-2 or MPEG-4
Web 3D	1000	Future
Grid computing	1000	Minimize energy consumption
Video streaming	1000 to 10000	Uncompressed
Immersive TV (UHDTV)	24000	Uncompressed 4320p

to be deployed for a large number of end-users. In addition to the high bit rate required, these applications should be provided for laptop and other mobile terminals which, induce operators and broadcasters to offer the high bit rate with some mobility degree.

In this context, users in indoor environment should have access to high-speed networks through a wired and wireless networks. Today, most end-users use two transmission channels to be connected all the time and change between these two channels, depending on their position and the required bit rate. Wired communications are used generally on a fixed place while wireless is used for mobile users but offering a smaller bit rate. In the next sections, different wired and wireless indoor communication technologies are described, showing their respective advantages and limits.

## II Wired communications for indoor networks

In this section, we present a brief description of wired communications used in indoor environment, explaining the differences between them, and the limits of each channel in terms of bit rate and distance link.

### II.1 Coaxial cable

The coaxial cable is a transmission line for radio frequency signals invented by the British engineer Oliver Heaviside in 1880 [10]. Today, it is the most commonly used cable in indoor networks to connect radio transmitters and receivers, computer networks, and distributing cable television signals. This cable was also used to transmit Ethernet standards, a family of computer networking technologies introduced in the 1980s as IEEE 802.3 [11] for local area networks. This cable is able to transmit a bit rate from 3 Mbps to more than 10 Gbps, over a distance up to 100 m [11].



## II.2 Optical fiber communications

The first serious proposal to employ optical fibers as a medium for telecommunications transmission dates back to 1966 by the Chinese engineer K. C. Kao and the British engineer G. A. Hockham. At that time, the problem was the high attenuation of the existing fiber which was about 1000 dB/km. The low bandwidth and the fragility were also an important issue. The progress of the fiber properties started to be rapid after 1970, when the United States company Corning Glass Works achieved a fiber with a loss less than 20 dB/km. Nowadays, the standard single-mode fiber (SMF) has a very low attenuation of 0.2 dB/km at  $1.55\ \mu\text{m}$ . The fiber progress was not limited to the attenuation, but to all other fiber parameters, making it able to be the support of high bit rate links over some hundred of kilometers. The fiber evolution was accompanied by the advancement of optoelectronic devices such as transmitters (light emitting diodes (LEDs), laser diodes (LDs)) and receivers (p-intrinsic-n (PIN) photodiodes and avalanche photodiodes (APDs)). In 1990, optical fiber communications system operating at a bit rate up to 2.5 Gbps were commercialized with a repeater spacing of about 60-70 km [12]. Earlier, the erbium-doped fiber amplifiers (EDFA), which can produce an optical gain higher than 20 dB over a large bandwidth (1525 - 1565 nm), contributed to a high progress in digital photonics transmission [13]. Shortly after, lightwave systems moved to wavelength division multiplexing (WDM), benefiting from the EDFA and then, dense WDM (DWDM) optical amplified transmission system were able to transmit multiple 10 Gbps channels. Nowadays, optical transmission systems provide a capacity of several Tbps [12]. This evolution led to a huge deployment of the fiber optic in the core, metropolitan and access network. FTTH is the last emerging technology of the optical fiber, which is currently being installed. Fibers for home networks demand some special characteristics mainly in terms of bending and fragility, which has motivated researchers to develop fibers with the required characteristics. In this frame, the perfluorinated graded index polymer optical fiber (PF-GI-POF) is a new model of polymer fiber with a large bandwidth, allowing the transmission of 40 Gbps over 100 m [14].



Figure 1.1: (a) Plastic optical fiber samples for home networks and (b) connector for plastic optical fiber (sc standard)

With this progression on optical fiber materials, high speed indoor communication



installation. At the beginning, indoor PLCs were focused on services related to control of electrical equipments, which require a relatively low bit rate with no real-time performance. These services can be operated easily in narrow-band PLC within the frequency range of 9-140 KHz, offering a data rate of some thousands bits per second [16]. The increasing use of internet and applications at high bit rates has encouraged the development of a broadband PLC requiring bandwidths up to 100 MHz [17].

In laboratory trials, PLC systems can offer transmission bit rates up to 500 Mbps in local area networks applications [18], and some commercial products reach 200 Mbps at the physical layer.

## **II.4 Conclusion**

Indoor wired communications were developed over the last decades to provide the high bit rate to the customers through different technologies. This evolution was accompanied by the diffusion of wireless communications systems giving the possibility to remain connected using a mobile terminal, anywhere inside a home. In the next section, the different wireless indoor communications technologies are presented and their advantages and limits are explained.

## **III Wireless communications using radio and microwave frequencies**

Wireless communication links were implemented over the years by different radio frequency technologies ranging from 535 KHz to LAN network channels at 2.4 GHz. Considering microwave signals, this range extends to 300 GHz, where the wavelength of the wave is 1 mm. The wireless communications based on RF technologies for indoor area are listed in the sections below.

### **III.1 Bluetooth**

Bluetooth is a wireless technology using a RF wavelength range designed for short distance communications to replace cables for printers, joysticks, keyboards or mice. It can be used also to interconnect portable computers or mobile phones. Bluetooth is an idea proposed by Ericsson Mobile communications, which started in 1994 to present a low power system to replace the cables used on its mobile phones and corresponding accessories. Ericsson formed with Nokia, IBM, Toshiba, and Intel the Bluetooth Special Interest Group which released in the next year the first Bluetooth protocol. 3COM, Agere (Lucent Technologies), Microsoft and Motorola joined this group in 2000 showing the high interest for this technology.

Bluetooth is an omnidirectional technology which does not require a direct view between the transmitter and the receiver. In most countries, Bluetooth devices use the band between 2.402 GHz and 2.4835 GHz, representing 79 1-MHz-wide channels. The channels are accessed using the Frequency-Hopping Spread Spectrum multiplexing technique offering a theoretical bit rate of 1 Mbps ( $\approx$  700 Kbps in

---

reality), using Gaussian shaped frequency shift Keying (GFSK) modulation. This modulation is a type of frequency shift keying modulation (FSK) which uses a Gaussian filter to shape the pulses before they are modulated in the goal of reducing the spectral bandwidth and out-of-band spectrum, to meet adjacent-channel power rejection requirements [19]. The new version of the Bluetooth standard is based on ultra-wide band and provides a maximum bit rate of 24 Mbps. The link distance can reach 100 m, depending on the emitted power [20].

As a conclusion, Bluetooth offers a relatively large covered area (100 m) with low consumption, but with a limited bit rate. The parameters of a typical Bluetooth link are summarized in table 1.2.

Table 1.2: Main characteristics of the Bluetooth technology [20]

Parameters	Min	Max	Units
bit rate	-	24	Mbps
Link distance	10	100	m
Carrier frequency	2.402	2.483	GHz
Number of users	2	8	
Power consumption	20	100	mW

### III.2 WiFi

The WiFi (or "Wireless Fidelity") is a RF technology respecting the IEEE 802.11 standard, basically providing a bit rate of 1 or 2 Mbps over some tens of meter. This standard used the spectrum ranging from 2.4 GHz to 5 GHz. This technology attracted a high number of customers encouraging the companies and researchers to increase this technology performance, resulting in the IEEE 802.11b standard (11 Mbps), and the 802.11a offering a bit rate of 54 Mbps [21]. The evolution of this standard was not limited to increasing the bit rate but also included the evolution of security and quality of service. There are no fixed link distance for WiFi, depending on the environment where the signal propagates, such as buildings, and other elements that can attenuate the signal. Figure 1.3 presents the general components of a WiFi network showing different access point on a basic service set (BSS) and the connexion between two BSS through a distribution system. It presents also an Ethernet connexion to servers or disks. The covered area of WiFi is limited on a zone of a diameter of several tens of meters around an access point and the bit rate is divided between the number of terminals connected to the same access point. The advantages of this technology are the ease and rapidity of installation, the full mobility in covered area, the unecessity of direct view. This technology suffers from some problems such as the need of high securing, the sharing of bandwidth between users and the limited bit rate. The last evolution of this technology is given by the 802.11n standard offering the possibility of more than 300 Mbps over a distance from 20 to 50 m in indoor environment around the access point, and 300 m in outdoor environment with the decrease in bit rate when the distance from the access point

increases [21].

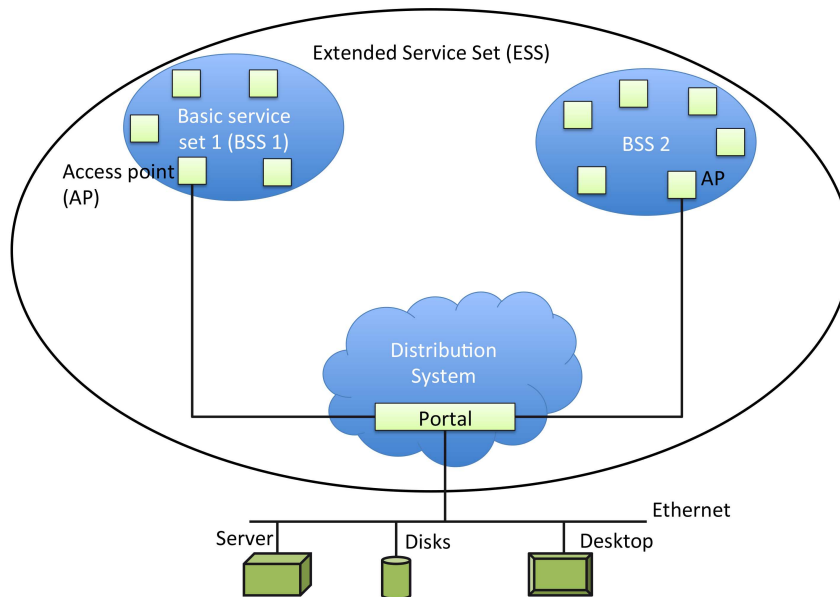


Figure 1.3: General components of a WiFi network (network view)

### III.3 Ultra wide band

The Ultra Wide Band (UWB) is a recent type of RF communications technology based on the transmission of short pulses with relatively low power spectral density (PSD). UWB technology gives the possibility to provide a high bit rate exceeding a Gbps wireless personal area networks (WPAN) over a relatively short distance (10 m) [22]. UWB uses an unlicensed wide band of RF spectrum defined by the Federal Communications Commission (FCC) in the range from 3.1 GHz to 10.6 GHz for indoor communications and from 22 to 29 GHz for vehicular radar applications [23], where each radio channel can have a bandwidth exceeding 500 MHz, depending on its center frequency. The FCC fixed the maximum radiated PSD to  $-41.3$  dBm/MHz in both cases to minimise interference between wireless services (licensed or unlicensed) [24]. The low power consumption motivated the use of UWB for radar systems, but it is used on many others applications such as:

- *Wireless personal area networks*: The UWB technology can be used to provide a high bit rate of several hundred Mbps within a short-range of 10-20 m with low cost and high power efficiency.
- *Sensor networks*: In this context, a large number of nodes is distributed in a defined geographical area. This network can be used for monitoring, pollution tracking, equipped on soldiers or military robots and emergency response situations. For that, UWB can be used in additional services e.g. underground,

through-wall, ocean imaging, medical diagnostics and border surveillance devices [25].

- *Vehicular radar systems:* UWB can be used for target differentiation, intelligent collision-avoidance. Airbag deployment, and adaption of suspension/breaking, depending on road conditions can be improved by using this technology. It is sometimes integrated into vehicular entertainment and navigation systems.

This technology is poorly developed for indoor environment and the commercialised devices are very limited.

### III.4 60 GHz wireless communications

The 60 GHz technology provides an attractive bandwidth for high bit rate communications offering the possibility of Gbps, standardized by the IEEE 802.15.3c.

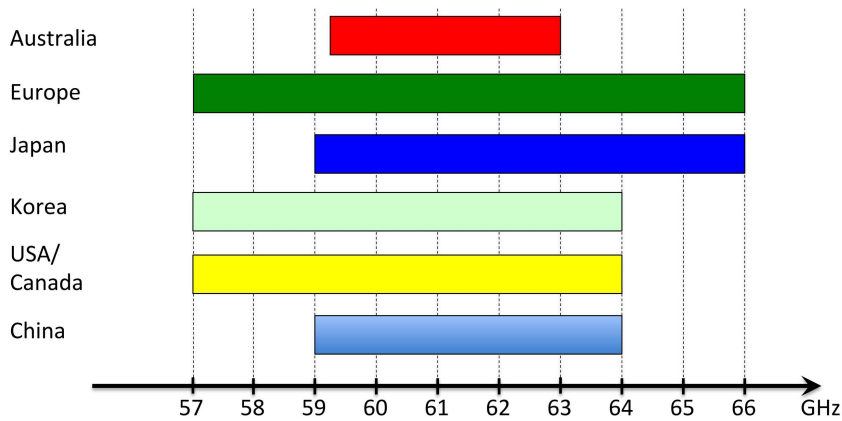


Figure 1.4: Worldwide band allocation for 60 GHz technology

As free-space attenuation of radio signals increases when the carrier frequency increases, 60 GHz technology is suitable for high bit rate communications over short distance line-of-sight (LOS) links.

In 2004, Applied Millimeter Wave Laboratory of Motorola Labs demonstrated a 3.5 Gbps link over 3 m [26], and in 2006, IBM T. J. Watson Research center shown a 630 Mbps link over 10 m [27]. Tomkins et al. from University of Toronto achieved in 2009 the demonstration of a transmission of data rates exceeding 6 Gbps of up to 2 m [28].

Figure 1.5 presents the architecture of a transmitter and a receiver designed Chalmers University and fabricated on 0.15  $\mu\text{m}$  AsGa pHEMT [29]. The transmitter contains a 3-stages power amplifier, a mixer and a local oscillator. The receiver is composed of low noise 3-stages amplifiers and an image rejecting mixer and a local oscillator ( $\times 8$ ). This technology is not yet commercialized and suffers from a very high attenuation due to the oxygen absorption band in the air.

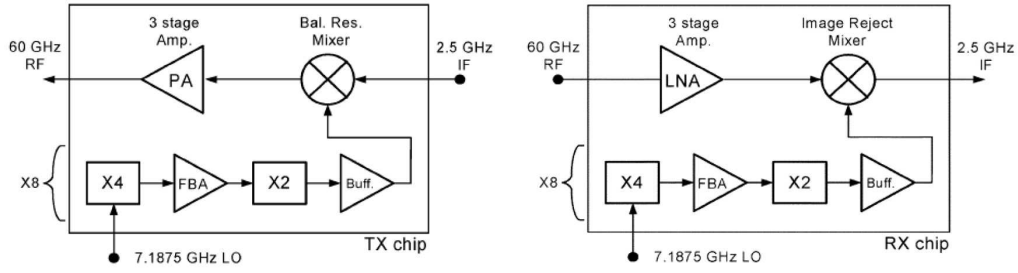


Figure 1.5: 60 GHz transmitter and receiver architectures [29]

### III.5 Radio-over-fiber

Radio-over-Fiber (RoF), as its name suggests, is a technology that uses the optical fiber to transmit RF signals. In free-space, the loss of an RF signal due to reflection and absorption increases with frequency, as for transmission lines. Therefore, the transmission of high frequency RF signals electrically or in free-space over a long distances is problematic and costly due to the necessity of regenerating equipments. The idea of RoF is to transmit the RF signals over an optical fiber as long as possible to benefit from the very low attenuation of optical fiber (0.2 dB/km at 1550 nm), and then to diffuse the RF signal over small distances, offering a high bit rate wireless solution. The RoF is also used to transmit existing RF technologies in order to increase the signal range of WiFi, UWB [30] and 60 GHz over fiber [31].

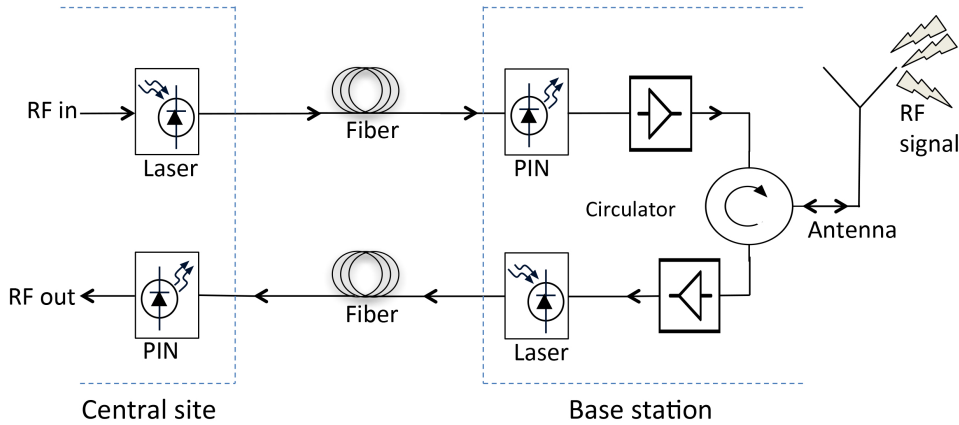


Figure 1.6: IM-DD Radio-over-Fiber scheme

Figure 1.6 presents the block diagram of a RoF channel using a circulator and one antenna to diffuse the RF signal for the downlink and to detect the RF signal for the uplink. This method uses Intensity Modulation with Direct Detection (IM-DD) which is the simplest form of the RoF link. For the downlink, at the central station, the RF signal directly modulates the laser diode and the resulting signal is



transmitted to the remote antenna unit (RAU) over the optical fiber. At the RAU, the transmitted RF signal is detected by the photodetector (PIN in general) and recovered by direct detection to be amplified and radiated by the antenna, and transmitted to the mobile unit (MU). The up-link RF signal generated by the MU is detected by the RAU. This signal is used to directly modulate the laser present at the RAU, then, transmitted over the optical fiber, and detected by the photodiode (also PIN in general) at the central site. The RoF based on IM-DD modulation is perfectly linear when the transmission is performed without chromatic and modal dispersion and in this case, the optical signal is transparent relatively to the RF signal. This modulation method can be used for indoor RoF where the fiber link is about some tens of meter (no chromatic and modal dispersion).

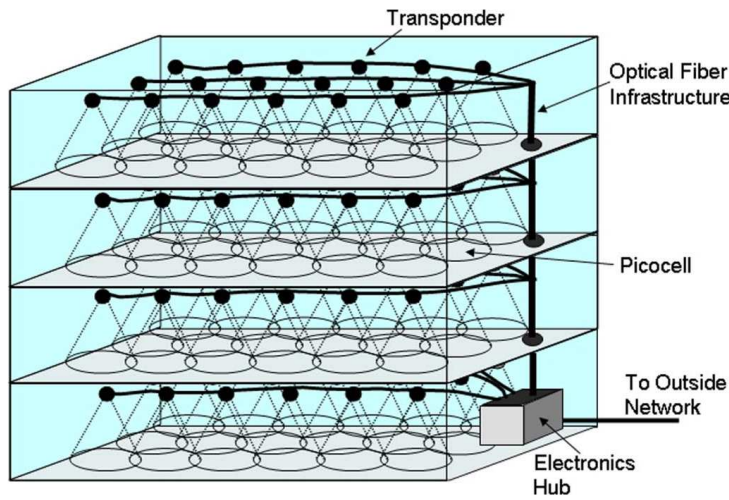


Figure 1.7: Radio-over-Fiber pico cellular architecture [32]

Figure 1.7 shows an example of RoF distributed picocells in in-building network, where a high number of user devices needs to be supported. The system presented on this figure is conceived to provide a high bit rate of 1 Gbps by using 60 GHz radio links.

The RoF technology is a way to increase the bit rate and to reduce power consumption due to the fiber transparency compared to the wireless transmitted signal over wall and other obstacle causing a high attenuation of the signal and then, the necessity to emit high power at the access point. The need to use of laser and antenna at the two extremities of the RoF link makes this type of link not very easy to use and increases the system price.

### III.6 Conclusion

Today, such RF technologies as WiFi and Bluetooth are hugely deployed around the world. These technologies are however limited in terms of bit rate (some tens of Mbps). Otherwise, another RF technologies were developed to provide the higher bit



rates required by new services and applications. These technologies presents also bit rate limitations to some hundred of Mbps and reveals sometimes very complex and expensive. Different RF technologies, their maximum bit rate and covered distance are summarized in table 1.3. An all-optical solution could be an alternative to increase the bit rate by eliminating the distribution of antennas at the fiber output. Different optical wireless communications technologies will now be presented in the next section.

Table 1.3: Summary of different RF technologies and their characteristics

Technology	bit rate (Mbps)	Link distance (m)
Bluetooth	24	100
WiFi	54	100
UWB	300	20
60 GHz	630	10

## IV Optical wireless communications

In parallel to the massive deployment of fiber optical communications in core, metropolitan and access networks connecting continents and providing bit rates that may exceed the Tbps, an alternative optical communication technology started about 30 years ago. It proposed to supply high bit rates in a part of the network where the installation of optical fiber is very difficult and expensive [33]. The concept is simple and similar to fiber communications with the difference that the transmission medium is free-space. The direction of the optical beam and its directivity can be defined relatively to the application and it can be determined by such simple optical components as lenses or prisms. Optical free-space links are strictly limited by the eye safety standards (and skin safety) defining the maximum permissible emitted power that does not have any harmful effects to the users. Optical wireless communication is a multidisciplinary domain of study including a wide range of areas: optical design, optoelectronics, electronics design, channel modelling, communication and information theory, modulation, wireless optical network architectures and many others. The type of optical free-space transmission is defined as a function of the beam divergence, classifying the link in three different topologies, as detailed in the next paragraphs.

**Line-of-Sight links** The line-of-sight (LOS) or point-to-point is the link with the quasi-alignment between the transmitter and the receiver. The low divergence beam and narrow field-of-view (FOV) detectors permit the rejection of high percentage of noise from ambient light. This type of link with narrow divergence does not provide a large coverage. However, a smaller attenuation is achieved compared to other topologies with higher divergence, and, the link distance can be longer. Whereas the total alignment to the optical signal is not possible but also in order to offer

some flexibility to the link, this free-space geometry includes very small divergence topologies ( $< 3^\circ$ ), referred to as narrow LOS (NLOS), as depicted in figure 1.8.

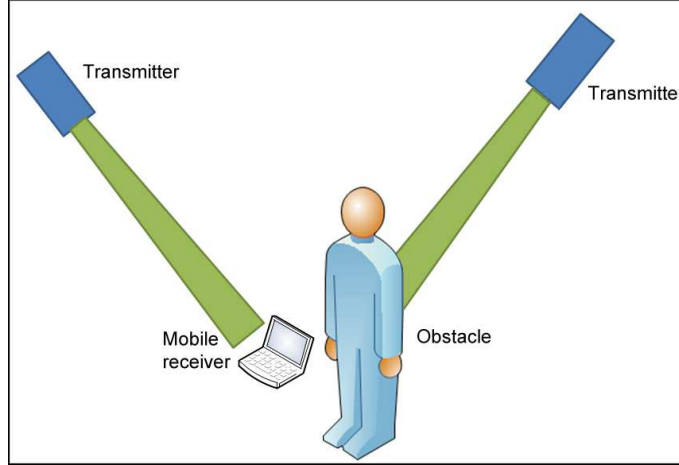


Figure 1.8: NLOS topology

This topology requires a direct view between the transmitter and receiver which reduces the flexibility of the link and makes it very sensitive to any obstacle. In this configuration, the signal does not suffer from multi-path distortion, hence no inter symbol interference (ISI), which makes the link bit rate only dependent from the power budget.

In a LOS link, the bit rate can be increased by spatial division multiplexing techniques. The mobility degree can be also increased by multiplying the number of LOS links or by tracking systems that achieve 155 Mbps over a distance of nearly 2 m in an indoor environment [34]. Although most LOS links use a single transmitter and receiver, a higher gain can be achieved by using multiple transmitters and receivers. The implementation of a Multiple-Input-Multiple-Output (MIMO) system requires the use of laser and photodiode arrays [35], or a spatial light modulator as a transmitter and an imager as a receiver. The MIMO LOS link is used in many applications such as 2D barcodes [36], page-oriented recording [37], holographic storage [38] and MIMO optical communications link [39].

**Wide Line-of-Sight links** The wide line-of-sight (WLOS) is characterized by a transmitter with a larger divergence angle as compared to the LOS. The receiver used also has a larger FOV. Figure 1.9 shows a WLOS topology scheme. The link geometry does not require the alignment between the transmitter and the receiver contrary to the direct view between them which is essential. The WLOS is characterized by a higher attenuation as compared to LOS or NLOS making the link distance smaller. The wide beam transmitter in this topology may cause multi-path due to reflexions from the wall and objects in the room, thus generating ISI and affecting the bit rate and the quality of the signal.

This topology is adapted for point to multipoint (PmP) applications where the sys-

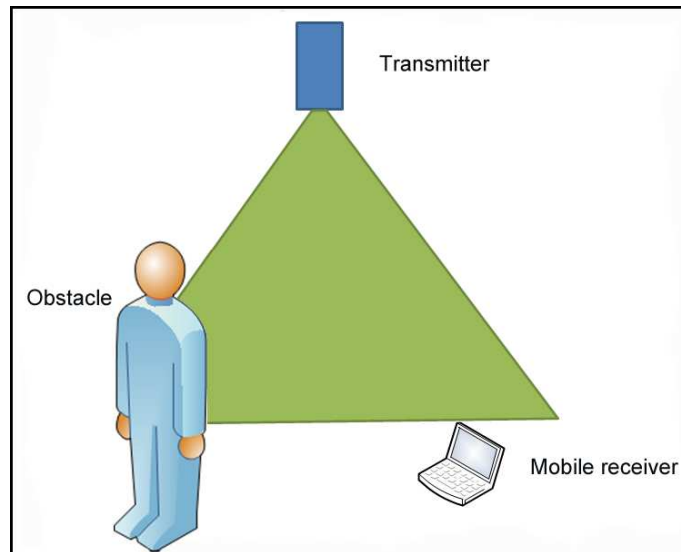


Figure 1.9: WLOS topology

tem contains an access point with a transmitter and multiple mobile receiver in covered zone [40].

**Diffuse indoor optical links** A diffuse indoor optical link is depicted in figure 1.10. In this configuration, an optical transmitter diffuses the optical signal in all possible directions. The signal at the receiver is the optical power collected by the photodiode coming from the transmitter directly or after many reflexions. This type of link does not need a direct view between the transmitter and the receiver. This link type is generally studied for indoor environment. A wide beam transmitter and a large FOV receiver is used to detect reflections of the diffused signal inside the room and to establish the communication link [39]. The received signal suffers from a multi-path dispersion caused by the large number of reflected rays at the receiver entrance area. As a result, a high ISI which reduces the maximum bit rate.

The first diffuse infrared system was proposed by Gfeller and Bapst, providing a bit rate of 1 Mbps at 950 nm wavelength [41]. The fastest totally diffuse system is reported by Marsh and Kahn [42] offering a bit rate of 50 Mbps, using a 805 nm wavelength optical carrier.

After presenting different free-space link geometries, we now propose an overview of optical wireless communications studied in outdoor and indoor environments.

## IV.1 Outdoor optical wireless communications

A large part of optical wireless communications consists of the outdoor systems known under free-space optic (FSO) links. This represents a complementary solution to the optical fiber local area network and broadband access network providing a "last-mile" high bit rate at low cost where the optical fiber installation is con-

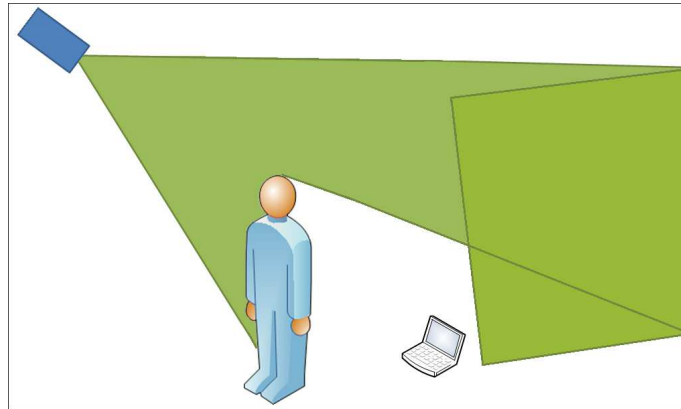


Figure 1.10: Diffuse link topology

sidered to be complicated [33]. Currently, a commercial FSO system working at 10 Gbps offers the possibility to connect some buildings in a city at distance of some km or some sites of university or company [43]. Figure 1.11 presents an example of FSO link and some impairments that may occur during the transmission.

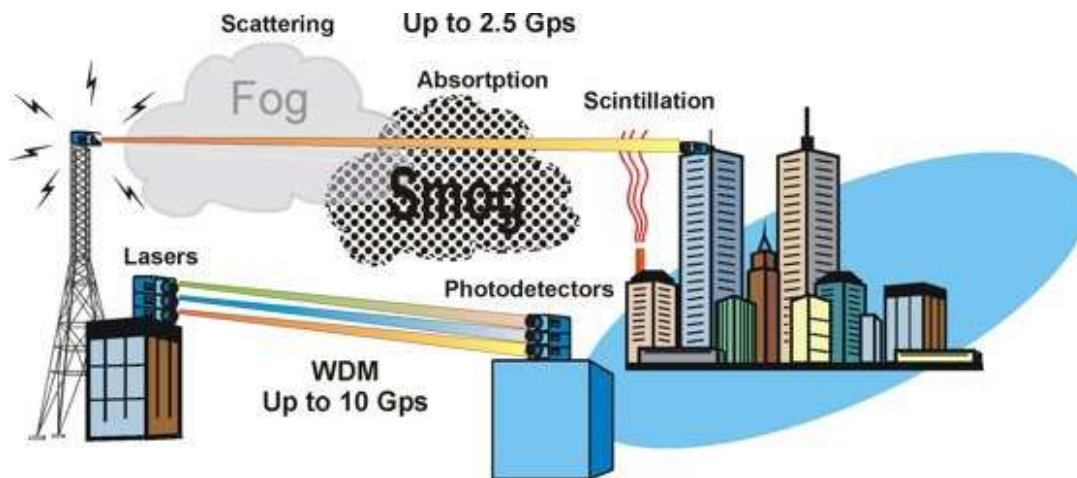


Figure 1.11: FSO transmission systems [44]

The FSO is a fixed point-to-point optical infrared transmission system which minimizes the probability to establish link, to localize it, to intercept it and detect the signal, contrary to the RF transmission. This characteristics make the FSO communication very suitable for high security military communications.

Obscuration (fog, clouds, snow, ...) along the link causes a multiplicative intensity noise which is known as scintillation, which reduces the received power and, then, the link distance. The attenuation of this type of link is not considered a major problem, especially for the used distance link (1-10 km). This consideration is reinforced by the fact that the system does not require to respect the standard for eye safety due to the absence of people on the link trajectory, given the possibility to

---

use a high power laser such as the product of CableFree solutions [45]. The Cable-Free Gigabit system offers from 622 Mbps to 1.5 Gbps transmission links using a semiconductor laser emitting approximately 100 mW (+20 dBm) [46].

The atmospheric turbulences in free-space also causes some performance degradation on FSO links such as the fluctuation of the intensity and progressive deterioration of circularly symmetric Gaussian beams when the distance increases. A decrease in the bit rate can result from this effect. The decrease in the coherence length of the laser beam and the fluctuations in the angle of arrival of the phase wavefronts at the receiver can also be noticed in FSO links.

All these atmospheric turbulences and their effects on a FSO link were and still are subjects of studies for a large number of researcher groups [47].

## IV.2 Indoor optical wireless communications

The study of indoor optical wireless (IOW) communications started before the FSO in the late seventies by Gfeller and Bapst [41]. Here, we summarize the progress of IWO along the years by presenting the different contributions in this field including, the various link design, different used wavelength, and referred applications.

### IV.2.1 Visible light communications

Visible light communications (VLC) is an optical communications channel dedicated to indoor environment in which the light is used simultaneously for general lighting and to transmit data over a wireless channel. VLC uses the spectral wavelength range between 380 and 750 nm, which provides a large bandwidth to transmit a high bit rate of several hundreds of Mbps. A high power white light emitting diode (LED) is the most commonly used optical source in this system. White LEDs are preferred in illumination due to their high energy efficiency, also characterized by their significant modulation bandwidth which permits the transmission of data rates ranging from several Mbps with a large FOV of 30 degrees to several Gbps with a FOV lower than 5 degrees [48]. As illustrated in figure 1.12, most visible light communication systems are based on light modulation provided by a matrix of LEDs fixed at the ceiling with a number of LEDs depending on the covered zone. This signal is demodulated at the mobile receiver to recover the transmitted data.

The interest in VLC technologies is largely seen through the foundation of the VLC consortium (VLCC) in 2003 [49], and recently, the work of VLC standardization through the IEEE 802.15.7 Task Group [50].

VLC transmission rates are limited by multipath dispersion and ambient light noise of sun and other artificial lighting source. These noise sources have been extensively studied to reduce their effects and increase the data rates. We can note the proposal of multiple carrier modulation technique (OFDM [51]), the MIMO systems [52], the coding schemes which are studied for dimmable VLC, and the study of adaptive equalization system. VLC transmission also suffers from the bandwidth limitation of phosphor-based visible LEDs where the LED is surrounded by phosphorus to

---

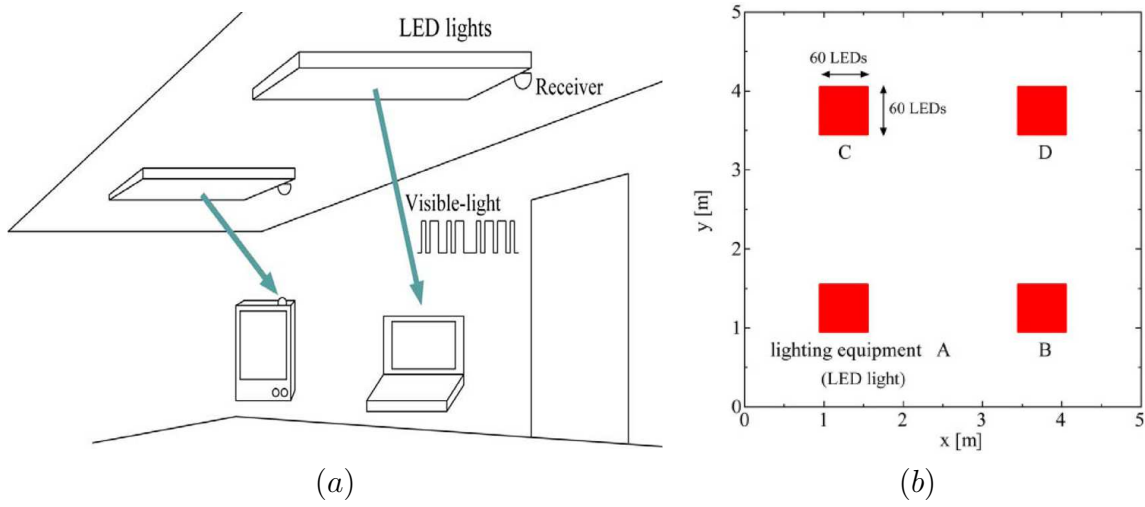


Figure 1.12: (a) Visible light wireless communication design, (b) Distribution and dimensions of LED matrices [48]

provide white light. Filtering and equalization at the transmitter or the receiver can increase this bandwidth by a factor of approximately 10. It is also increased by the use of discrete multi-tone OFDM that achieves bit rates exceeding 100 Mbps. White light can also be generated using also a combination of three distinct LEDs (a red, a blue and a green LEDs (RGB LEDs) while lighting at the same time and without suffering from bandwidth limitation. WDM can be used here to transmit data simultaneously over the same channel providing a higher bit rate. VLC is a technology proposed to complement wireless communication technologies with a large area of applications such as intelligent transport system, image sensor communications, networking, audio or position detection.

#### IV.2.2 Infrared optical wireless communications

Infrared optical wireless communications have been widely studied over the years for link topologies ranging from a diffuse configuration to a point-to-point link, and some systems were presented using different infrared wavelength bands, depending on the application and the environment. The studied systems had different characteristics regarding the components used and the bit rate provided. The most spread infrared link is the infrared data association (IrDa) link, offering a standard for low-speed infrared data communications. IrDa links and other infrared proposed systems are presented in the next paragraphs.

**IrDA links** The infrared data association was founded in 1993 by the collaboration between more than 50 companies in order to define an open standard for infrared data communications [53]. It gathers manufacturers of software and hardware components, telephone, cable and service providers. A link with the IrDA standard uses a near infrared wavelength between 850 and 950 nm with a maxi-

imum output intensity of 500 mW/sr, which is consistent with eye safety limitations. The first version of the resulting IrDA provided a low bit rate of about 115 kbps which was increased to 1.152 Mbps, 4 Mbps and 16 Mbps. A bit rate of 100 Mbps was expected in the near future with ultra fast IrDA systems. In this technology, the transmitter is generally a LED and the detector is a silicon PIN photodiode minimizing the system cost at lower speed, while a laser can be used to provide a higher bit rate. Some infrared link parameters are also recommended by the IrDA in a system using this protocol, such as the link distance which should be less than 1 m (200 mm for low power transceivers), the 3 dB half-width angle should range between 15 and 30° at the transmitter and 0 - 15° at the receiver, and the bit error rate (BER) which should be less than  $10^{-8}$  for a bit rate less than 16 Mbps and less than  $10^{-10}$  for a higher bit rate. Some examples of IrDA links are depicted in figure 1.13.

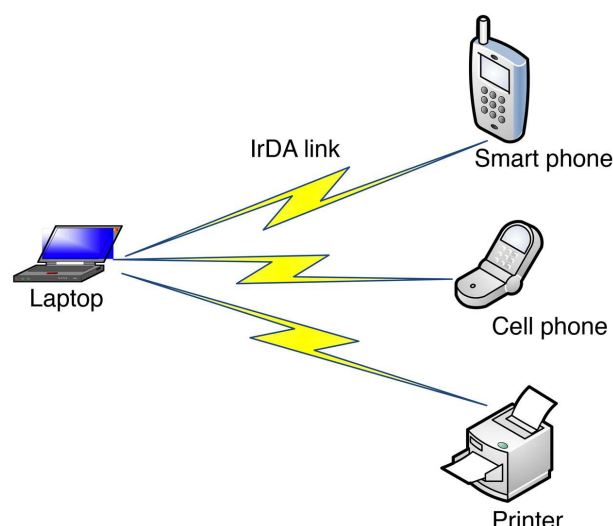


Figure 1.13: Normalized IrDA links for multimedia communications

The IrDA provides standards for many applications such as the Infrared Financial Messaging (IrFM) used to run digital payment applications using personal infrared communication devices [54].

**Infrared systems and prototypes** Over the years, a large number of infrared commercialized optical wireless systems and prototypes were proposed. In this paragraph, we present an overview of the system evolution:

- Gfeller channel [41]: In 1979, Gfeller and Bapst presented a diffuse infrared radiation at 950 nm wavelength offering a bit rate of 125 Kbps for indoor environment.
- JVC Luciole [55]: It is a point-to-point link presented by JVC as an optical HD transmission system to transfer HD video from a source to a large TV screen

offering a data rate of 1.5 Gbps over a range of 5 m at a 855 nm wavelength.

- Techim@ge prototype [3] : The French project Techim@ge designed a prototype to transmit a 1 Gbps bit rate over a range of up to 7 m. For the base station, the reception wavelength was 1550 nm, and 1560 nm was used for the emission. The emitted power was 30 dBm (1 W) with an emission angle of  $45^\circ$  and a FOV of  $45^\circ$ . For the modules, the emission power was about 25 dBm with an emission angle of  $15^\circ$  and a FOV of  $15^\circ$ .
- Omega prototype [56] [57]: The Omega project proposed two infrared prototypes. The first demonstrator operated at 820 nm and provided a bidirectional bit rate of 1.25 Gbps between two terminals "cells" having a FOV of  $25^\circ \times 8^\circ$  over a range of approximately 3 m. The second version of the demonstrator was working at the 850 nm wavelength, providing a bit rate of 224 Mbps. The prototype transceiver used 7 transmitters, receivers channels in order to cover a zone having a field of view of  $45^\circ$  with a distance of up to 4.5 m between the transceivers.

## V Advantages of optical wireless communications

The most widely used optical and RF technologies that were described in the previous sections are summarized with their bit rate and their coverage area in the figure 1.14. The two communication carriers present some advantages and disadvantages. The advantages are discussed in the perspectives of this work.

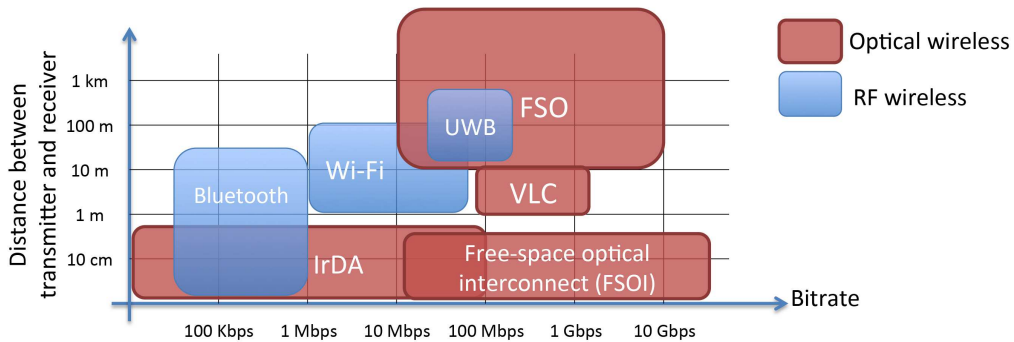


Figure 1.14: Optical and RF wireless technologies

- *High bit rate*: The optical signal is characterized by a very large bandwidth offering the possibility for ultra high-speed communications. In current optical fiber communications, the bit rate exceeds the Tbps, which is not an expected bit rate on free-space optical communications domain. The bit rate also depends on the transmitter and receiver bandwidths but a high bit rate of some Gbps is already performed with outdoor free-space optical communications.



- 
- *Low cost*: The low complexity and the wide deployment optoelectronic devices (laser diode, photodiode) in telecommunications keep the optical components as a low cost as compared to other communications systems.
  - *Electromagnetic Interference (EMI)*: The EMI is any electromagnetic disruption due to the radiation of any devices around the transmission link or the devices of the transmission link. Optical communications operate at a frequency of a few hundreds of THz, which is very far from the operating wavelength of radio frequency communications and electrical devices. This characteristic makes the optical link a dielectric guide without any EMI.
  - *Health immunity*: Optical communications are considered to be a healthy system with the absence of all types of radiation that can be harmful for health. The single point that should be verified is eye safety which is the most sensitive body part to the optical signal. All optical systems should respect the international standard of eye safety.
  - *Free license fees*: Unlike radio and microwave links, optical transmission is not licensed and the suitable wavelength for a system can be freely chosen, without any fees.
  - *Security of transmitted data*: The optical signal cannot cross wall and opaque surfaces, which makes impossible to any person outside the room where the wireless optical transmission is done to detect the signal and to access the data.

These advantages orientate us to search an optical wireless solution for indoor networks offering the required high bit rate for new services and applications through a wireless channel.

## VI Conclusion

The number of indoor multimedia equipments has hugely increased during the last few years, as well as, new applications and services. This evolution requires higher bit rates while maintaining the advantages of existing systems.

Considering the interest of users in wireless communications systems, the optical channel can be used to define new wireless technologies offering high bit rates responding to the users demand and based on low-cost components, reduced impact on human health and low energy consumption.

Different optical indoor architectures were previously studied using different wavelength bands. These are characterized by a high bit rate of several Gbps point-to-point links or very low bit rate of few Mbps diffuse links.

All these ideas motivated us to determine a new indoor all-optical communication system offering bit rates exceeding the Gbps with some degree of mobility.

---

## VII Objectives and outlines of the PhD thesis

Until a few years ago, optical communications were associated to the fiber communications and the radio frequency for the wireless communications and electromagnetic wires. However, researchers in the last years have started to combine the two transmission channels through new communication technologies having the advantages of both. The convergence between RF and optical communications is presented in figure 1.15 showing the radio-over fiber and optical wireless communications.

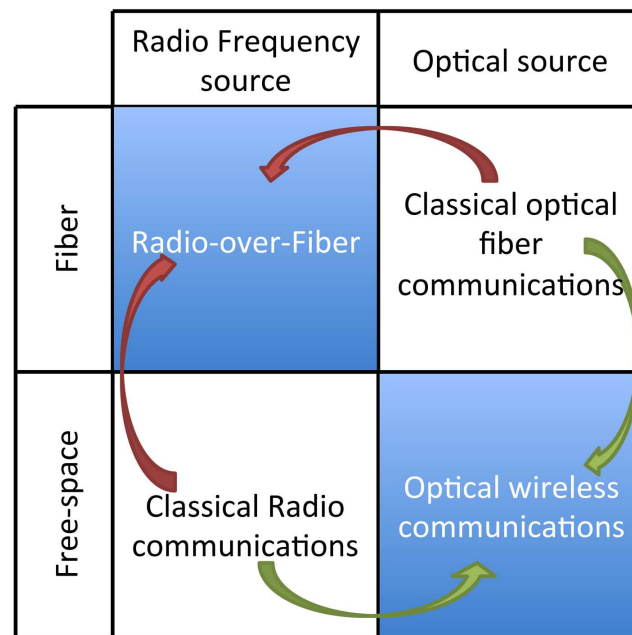


Figure 1.15: Convergence between optical and radio frequency communications

In this frame, and in order to provide Gbps bit rates, this work is focused on optical wireless communications in indoor environment with potential reduced health and environmental impact. This work has the goal to define and evaluate the physical layer of a high bit rate indoor optical wireless system, based on all-optical transmission links that can provide Gbps free-space optical cells using optical fiber interconnections. The proposed architecture should take energy consumption and low cost of installation and maintenance of the global system into account, to give the possibility of a large deployment of this system for all type of customers, and to satisfy green environmental requirements. This architecture is designated by the acronym GROWTH corresponding to "GReen Optical InTo Home network".

The scope of this thesis can be divided into three parts:

1. *Definition and dimensioning* of the GROWTH architecture, respecting the required characteristics, as well as, different system components to be used.
2. *Characterization of an all-optical hybrid channel* combining the optical fiber link and the free-space link. This part is divided in several parts such as

theoretical validation, simulation, and intermediate experiments to validate the function of some components of the system.

3. *Experimental validation of the architecture.* The last step of this work is to build a first prototype of the architecture including all components and then, to validate the system feasibility and its performance by successfully transmitting the expected bit rate.

## Bibliography

- [1] projet FP7-ICT (2008-10) OMEGA: Home Gigabit Access. [www.ict-omega.eu](http://www.ict-omega.eu).
  - [2] ALPHA: Architectures for fLexible Photonic Home and projet FP7-ICT (2008-10) Access networks. [www.ict-alpha.eu](http://www.ict-alpha.eu).
  - [3] Techim@ges project. <http://www.images-et-reseaux.com/fr/les-projets/>.
  - [4] M. Kanazawa, K. Mitani, K. Hamasaki, M. Sugawara, K. Okano, F. Doi, and M. Seino. Ultrahigh-Definition Video System with 4000 Scanning Lines. In *Acts of the International Broadcasting Convention (IBC)*, pages 321–329, Sep. 2003.
  - [5] E. Nakasu, Y. Nishida, M. Maeda, M. Kanazawa, S. Yano, M. Sugawara, K. Mitani, K. Hamasaki, and Y. Nojiri. Technical Development Towards Implementation of Extremely High Resolution Imagery System with More Than 4000 Scanning Lines. In *Acts of the International Broadcasting Convention (IBC)*, pages 345–352, Sep. 2006.
  - [6] O. Grau, A. Hilton, J. Kilner, G. Miller, T. Sargeant, and J. Starck. A Free-Viewpoint Video System for Visualisation of Sport Scenes. *Motion Imaging*, 116(5–6):213–219, May 2007.
  - [7] Web 3D Consortium. <http://www.web3d.org/realtime-3d/>.
  - [8] HP MediaSmart Server EX470/EX475. [http://www.hp.com/united-states/campaigns/mediasmart-server/hp\\_mediasmartserver\\_ex47x\\_datasheet.pdf](http://www.hp.com/united-states/campaigns/mediasmart-server/hp_mediasmartserver_ex47x_datasheet.pdf).
  - [9] J. Baert, M. De Leenheer, B. Volckaert, T. Wauters, P. Thysebaert, F. De Turck, B. Dhoedt, and P. Demeester. Hybrid Optical Switching for Data-Intensive Media Grid Applications, 2006.
  - [10] P. J. Nahin. *Oliver Heaviside: The Life, Work, and Times of an Electrical Genius of the Victorian Age*. The Johns Hopkins University Press, 2002.
  - [11] IEEE. IEEE P802.3ba 40Gb/s and 100Gb/s Ethernet Task Force. <http://www.ieee802.org/3/ba/>.
  - [12] G. P. Agrawal. *Fiber-optic communication systems*. 3rd ed. New York: Wiley, 2002.
  - [13] P. C. Becker, N. A. Olsson, and J. R. Simpson. *Erbium-doped fiber amplifiers, fundamentals and technology*. San Diego, CA: Academic Press, 1999.
  - [14] A. Polley and S. E. Ralph. 100 m, 40 Gb/s Plastic Optical Fiber Link. In *Conference on Optical Fiber communication/National Fiber Optic Engineers Conference (OFC/NFOEC'2008)*, pages 1–3, Feb. 2008.
-

- 
- [15] PLC utilities alliance 2004. Power Line communication. [http://www.ieee802.org/802\\_tutorials/04-March/plc-040308\\_IEEE\\_V4.pdf](http://www.ieee802.org/802_tutorials/04-March/plc-040308_IEEE_V4.pdf).
- [16] K. Dostert. *Powerline communications*. Prentice Hall, 2001.
- [17] M. Tlich, A. Zeddami, F. Moulin, and F. Gauthier. Indoor Power-Line Communications Channel Characterization Up to 100 MHz –2014; Part I: One-Parameter Deterministic Model. *Transactions on Power Delivery, IEEE*, 23(3):1392–1401, Jul. 2008.
- [18] IEEE Std 1901-2010. IEEE Standard for Broadband over Power Line Networks: Medium Access Control and Physical Layer Specifications. <http://grouper.ieee.org/groups/1901/>, Dec. 2010.
- [19] Maxim integrated<sub>TM</sub>. <http://www.maximintegrated.com/glossary/definitions.mvp/term/Gaussian-frequency-shift-keying/gpk/519>.
- [20] Bluetooth special interest group. <https://www.bluetooth.org>.
- [21] Working Group for WLAN Standards. IEEE 802.11TM wireless local area networks. <http://www.ieee802.org/11/>.
- [22] T. Lunttila, S. Iraji, and H. Berg. Advanced coding schemes for a multiband OFDM ultrawideband system towards 1 Gbps. In *3rd IEEE Consumer Communications and Networking Conference (CCNC'2006)*, volume 1, pages 553–557, Jan. 2006.
- [23] FCC 02-48. Revision of part 15 on the commission’s rules regarding ultrawideband transmission systems. Apr. 2002.
- [24] R. Alemany, J. Perez, R. Llorente, V. Polo, and J. Marti. Coexistence of WiMAX 802.16d and MB-OFDM UWB in radio over multi-mode fiber indoor systems. In *International Topical Meeting on Microwave Photonics (MWP 2008) jointly held with the 2008 Asia-Pacific Microwave Photonics Conference (APMP)*, pages 74 –77, Oct. 2008.
- [25] J. D. Taylor. *Ultra Wideband Radar Technology*. New York: CRC Press, 2001.
- [26] B. Bosco, S. Franson, R. Emrick, S. Rockwell, and J. Holmes. A 60 GHz transceiver with multi-gigabit data rate capability. In *Radio and Wireless Conference, IEEE*, pages 135–138, Sep. 2004.
- [27] S. K. Reynolds, B. A. Floyd, U. R. Pfeiffer, T. Beukema, J. Grzyb, C. Haymes, B. Gaucher, and M. Soyuer. A Silicon 60-GHz Receiver and Transmitter Chipset for Broadband Communications. *Journal of Solid-State Circuits, IEEE*, 41(12):2820–2831, Dec. 2006.
-

- 
- [28] A. Tomkins, R. A. Aroca, T. Yamamoto, S. T. Nicolson, Y. Doi, and S. P. Voinigescu. A Zero-IF 60 GHz 65 nm CMOS Transceiver With Direct BPSK Modulation Demonstrating up to 6 Gb/s Data Rates Over a 2 m Wireless Link. *Journal of Solid-State Circuits, IEEE*, 44(8):2085–2099, Aug. 2009.
- [29] S. E. Gunnarsson, C. Karnfelt, H. Zirath, R. Kozhuharov, D. Kuylenskierna, A. Alping, and C. Fager. Highly integrated 60 GHz transmitter and receiver MMICs in a GaAs pHEMT technology. *Journal of Solid-State Circuits, IEEE*, 40(11):2174–2186, Nov. 2005.
- [30] Y. Le Guennec, M. Lourdiane, B. Cabon, G. Maury, and P. Lombard. Technologies for UWB-Over-Fiber. In *19th Annual Meeting of the IEEE Lasers & Electro-Optics Society (LEOS'2006)*, pages 518–519, Oct. 2006.
- [31] Y.-T. Hsueh, Z. Jia, H.-C. Chien, A. Chowdhury, J. Yu, and G.-K. Chang. Multiband 60-GHz Wireless Over Fiber Access System With High Dispersion Tolerance Using Frequency Tripling Technique. *Journal of Lightwave Technology*, 29(8):1105–1111, Apr. 2011.
- [32] M. Sauer, A. Kobayakov, and J. George. Radio Over Fiber for Picocellular Network Architectures. *Journal of Lightwave Technology*, 25(11):3301–3320, Nov. 2007.
- [33] Q. Liu, C. Qiao, G. Mitchell, and S. Stanton. Optical wireless communication networks for first- and last-mile broadband access [invited]. *Journal of Optical Networking*, 4(12):807–828, Dec. 2005.
- [34] V. Jungnickel, A. Forck, T. Haustein, U. Kruger, V. Pohl, and C. von Helmlolt. Electronic tracking for wireless infrared communications. *Transactions on Wireless Communications, IEEE*, 2(5):989–999, Sep. 2003.
- [35] D. C. O'Brien, G. E. Faulkner, E. B. Zyambo, K. Jim, D. J. Edwards, P. Stavrinou, G. Parry, J. Bellon, M. J. Sibley, V. A. Lalithambika, V. M. Joyner, R. J. Samsudin, D. M. Holburn, and R. J. Mears. Integrated transceivers for optical wireless communications. *Journal of Selected Topics in Quantum Electronics, IEEE*, 11(1):173–183, Jan.-Feb. 2005.
- [36] R. Villan, S. Voloshynovskiy, O. Koval, and T. Pun. Multilevel 2-D Bar Codes: Toward High-Capacity Storage Modules for Multimedia Security and Management. *Transactions on Information Forensics and Security, IEEE*, 1(4):405–420, Dec. 2006.
- [37] P. H. Siegel. Information-Theoretic Limits of Two-Dimensional Optical Recording Channels. In *Optical Data Storage Topical Meeting*, pages 165–167, 2006.
- [38] R. M. Shelby, J. A. Hoffnagle, G. W. Burr, C. M. Jefferson, M.-P. Bernal, H. Coufal, R. K. Grygier, H. Günther, R. M. Macfarlane, and G. T. Sincerbox. Pixel-matched holographic data storage with megabit pages. *Optics Letters*, 22(19):1509–1511, Oct. 1997.
-

- 
- [39] J. M. Kahn and J. R. Barry. Wireless infrared communications. *Proceedings of the IEEE*, 85(2):265–298, Feb. 1997.
  - [40] P. P. Smyth, P. L. Eardley, K. T. Dalton, D. R. Wisely, P. McKee, and D. Wood. Optical wireless: a prognosis. In *Wireless Data Transmission*, volume 2601, Dec. 1995.
  - [41] F. R. Gfeller and U. Bapst. Wireless in-house data communication via diffuse infrared radiation. *Proceedings of the IEEE*, 67(11):1474–1486, Nov. 1979.
  - [42] G. W. Marsh and J. M. Kahn. 50-Mb/s diffuse infrared free-space link using on-off keying with decision-feedback equalization. In *5th IEEE International Symposium on Personal, Indoor and Mobile Radio Communications, Wireless Networks - Catching the Mobile Future*, volume 4, pages 1086–1089 vol.4, Sep. 1994.
  - [43] <http://www.systemsupportolutions.com/terescope.html>.
  - [44] *Optical Communication Dictionary*. Lawrence Harte, 2012.
  - [45] CableFree Solutions Ltd. <http://www.cablefree.co.uk/>.
  - [46] Switzerland International Electrotechnical Commission, Geneva. IEC 60825-1: Safety of Laser Products. 1998.
  - [47] W. O. Popoola and Zabih Ghassemlooy. Bpsk subcarrier intensity modulated free-space optical communications in atmospheric turbulence. *J. Lightwave Technol.*, 27(8):967–973, Apr 2009.
  - [48] T. Komine and M. Nakagawa. Fundamental analysis for visible-light communication system using LED lights. *Transactions on Consumer Electronics, IEEE*, 50(1):100–107, Feb. 2004.
  - [49] Visible light communication consortium. <http://www.vlcc.net>.
  - [50] IEEE 802.15 WPAN-Visible Light Communication Interest Group (IGvlc). <http://ieee802.org/15/pub/IGvlc.html>.
  - [51] H. Elgala, R. Mesleh, H. Haas, and B. Pricope. OFDM Visible Light Wireless Communication Based on White LEDs. In *65th Vehicular Technology Conference, VTC'2007-Spring, IEEE*, pages 2185–2189, Apr. 2007.
  - [52] L Zeng, D. O'Brien, H. Minh, G. Faulkner, K. Lee, D. Jung, Y. Oh, and E. T. Won. High data rate multiple input multiple output (MIMO) optical wireless communications using white led lighting. *Journal on Selected Areas in Communications, IEEE*, 27(9):1654–1662, Dec. 2009.
  - [53] Infrared Data Association (IrDA). <http://www.irda.org>.
-

- [54] IrDA. Infrared Financial Messaging (IRFM<sup>TM</sup>) point and pay profile-version 1.0. In *Infrared Data Association*, Apr. 2002.
  - [55] JVC. Luciole link, 2003. [www.jvc.com](http://www.jvc.com).
  - [56] H. Le Minh, D. O'Brien, G. Faulkner, O. Bouchet, M. Wolf, L. Grobe, and J. Li. A 1.25-Gb/s Indoor Cellular Optical Wireless Communications Demonstrator. *Photonics Technology Letters, IEEE*, 22(21):1598–1600, Nov. 2010.
  - [57] OMEGA. Physical Layer Design and Specification - Demonstrator 2 - . [http://www.ict-omega.eu/fileadmin/documents/deliverables/Omega\\_D4.2b.pdf](http://www.ict-omega.eu/fileadmin/documents/deliverables/Omega_D4.2b.pdf).
-



---

## Figures and tables

### Figures

---

1.1	(a) Plastic optical fiber samples for home networks and (b) connector for plastic optical fiber (sc standard) . . . . .	27
1.2	Power line communications network deployment scheme [15] . . .	28
1.3	General components of a WiFi network (network view) . . . . .	31
1.4	Worldwide band allocation for 60 GHz technology . . . . .	32
1.5	60 GHz transmitter and receiver architectures [29] . . . . .	33
1.6	IM-DD Radio-over-Fiber scheme . . . . .	33
1.7	Radio-over-Fiber pico cellular architecture [32] . . . . .	34
1.8	NLOS topology . . . . .	36
1.9	WLOS topology . . . . .	37
1.10	Diffuse link topology . . . . .	38
1.11	FSO transmission systems [44] . . . . .	38
1.12	(a) Visible light wireless communication design, (b) Distribution and dimensions of LED matrices [48] . . . . .	40
1.13	Normalized IrDA links for multimedia communications . . . . .	41
1.14	Optical and RF wireless technologies . . . . .	42
1.15	Convergence between optical and radio frequency communications	44

---

### Tables

---

1.1	New and future services and the required bit rates . . . . .	26
1.2	Main characteristics of the Bluetooth technology [20] . . . . .	30
1.3	Summary of different RF technologies and their characteristics .	35

---



## Chapter 2

# Design of the wireless optical cells

### Contents

---

I	Proposed architecture . . . . .	<b>54</b>
I.1	Downlink description . . . . .	54
I.2	First downlink geometry approach . . . . .	55
I.3	Optical access point . . . . .	57
I.4	Different Uplink options . . . . .	58
I.4.1	Radio frequency uplink . . . . .	58
I.4.2	Optical uplink . . . . .	59
II	Optical sources . . . . .	<b>60</b>
III	Operational constraints . . . . .	<b>62</b>
III.1	Eye and skin safety constraints . . . . .	62
III.2	Ambient noise . . . . .	63
III.3	Reflected beams . . . . .	63
IV	Wavelength choice . . . . .	<b>64</b>
V	Power link budget: first approach . . . . .	<b>65</b>
VI	Optical control station . . . . .	<b>67</b>
VII	Green aspects of proposal system . . . . .	<b>68</b>
VIII	Conclusion . . . . .	<b>70</b>
	Bibliography . . . . .	<b>71</b>
	Figures and tables . . . . .	<b>72</b>

---

## Introduction

After a short description of existing indoor communications systems, a presentation of the advantages of optical communications in indoor environment and the definition of this work objectives, this chapter focuses on the proposed architecture, with a description of the system geometry and the components used at the physical layer, which will be deeply studied in the next chapters.

The study is limited to the downlink design, including the presentation of system components and the geometry of the free-space link, but the different uplink options are also mentioned. The optical source and other constraints such as eye safety and ambient noise are also presented in order to select the suitable system wavelength, leading to a first calculation of the power link budget to confirm the feasibility of the system. The low energy consumption and reduced environmental impact, referred to as the "Green" aspects of the system, are also mentioned. Such others system components as the receiver, the access point or the switch will also be introduced in this chapter to validate the system design and components choice. The second step, presented in chapter 4, will consist in the characterization of the modulated signal transmission, in order to estimate the bit error rate under varying transmission conditions.

## I Proposed architecture

In this section, the downlink architecture is described and the optical free-space cell is designed using a first approach of the system components.

### I.1 Downlink description

The overall principle takes back the basic architecture of RoF systems presented in chapter 1 [1] for indoor environment where, at the central station, the RF signal modulates an optical signal which is transmitted by an optical fiber to the base station and then, at the base station, the RF signal is recovered before broadcast in free-space, using an RF antenna. We propose here to remove the analog RF carrier to provide a transparent high bit rate all-optical digital transmission between the base station and the terminal receiver.

More precisely, system transports the optical wireless distribution from the access network to mobile terminals located in the rooms of a building or a home. It should also distribute the very high bit rate streams (HD video) generated by a central server throughout the in-building space. Unlike RoF systems which transport RF cells through optical fibers, the wireless cells transmitted here will be optical links with digital modulation schemes, hence reducing the system implementation complexity while providing the potential huge bit rates (several Gbps) of optical transmission links. The proposed system to implement an indoor wireless optical transmission is depicted schematically in figure 6.1.

Both the access traffic (FTTH) and locally generated home data streams are centralized using an optical control station (OCS), which can be viewed as an optical

---

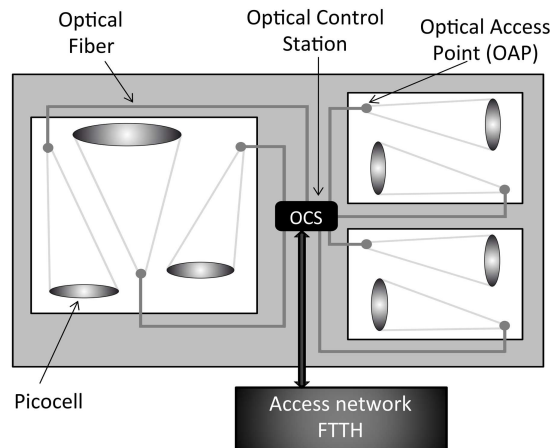


Figure 2.1: Hybrid indoor optical fiber distribution system

multi-port switch, with possible optical amplification at that stage. At the outputs of the OCS, the optical signals are distributed to optical access points (OAPs) on every room, using dedicated optical fibers. The role of the OCS will be precized in section VI. The downstream signals are then transferred from the OAP to the mobile terminals within a room using a wireless optical link signal. Compared to many standard optical wireless schemes using diffused links in a single room [2], the present fiber-distributed scheme offers NLOS links, which enables the power link budget to be consistent with Gbps communications [3].

## I.2 First downlink geometry approach

Figure 2.2 shows a three-dimensional view of the downlink, presenting the free-space optical cell distribution through an optical fiber in two different rooms, using two optical access points. This number is not fixed and can be changed depending on the room dimensions.

The first approach of the physical downlink with basic components and architecture details is depicted in figure 2.3. The OCS distributes the optical signal to the OAP through the optical fiber followed by a free-space transmission of the optical signal, possibly corrupted with ambient light noise before detection by the receiver. The different parts of the receiver (optical concentrator, filter and the photodiode) are also shown in this figure. Each of these components will be studied in the following sections or chapters to validate the downlink transmission scheme.

The free-space geometry is designed to meet the power budget requirement, which depends on both the maximum permissible optical power at the OAP output and the receiver area and sensitivity. Prior to this, the distribution of the OAPs in the rooms will be explained.

Figure 2.4 (a) illustrates the distribution of OAP in the ceiling of a  $4 \times 4$  m room. This room is divided in four equal  $2 \times 2$  m areas. An OAP is placed at the center

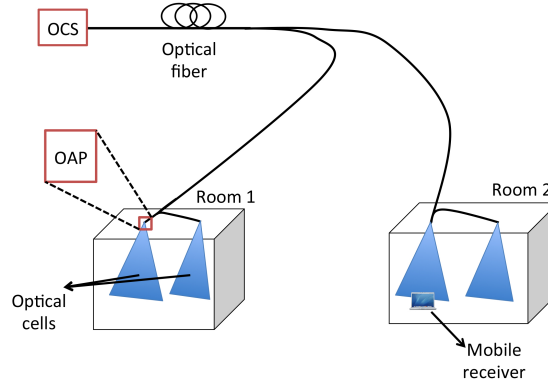


Figure 2.2: Optical downlink structure

of each of these parts. Different free-space configurations presented in this figure are managed by the OCS and will be detailed in the next section, dealing with the optical access point.

In reality, the end receivers are usually placed on a plane where we find tables or desks, generally at a height of 1 m from the ground. This plane is called "communication" plane or "active" plane. In the proposed architecture, the free-space link distance limit is that between the ceiling and the active plane. Considering the optical free-space cell presented in figure 2.4 (b), the connection with the fixed or mobile receiver will be ensured if it is placed on the  $C_1$  zone or above, contrarily to any terminal placed between the two planes  $C_1$  and  $C_2$ . In general, the rooms height is about 3 m, and then, the distance  $d_1$  between the OAP and the  $C_1$  zone is about 2 m. The study of this part of the system will continue in the chapter 4 through the description of the optical access point, defining the free-space covered zone.

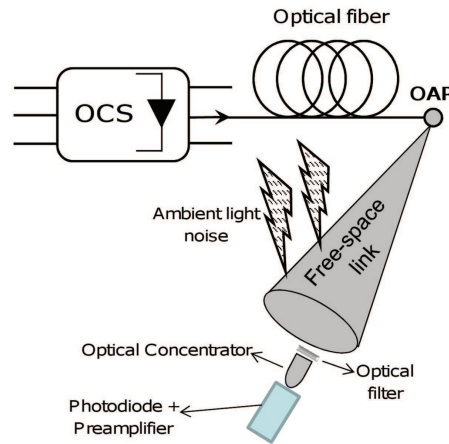


Figure 2.3: Optical downlink scheme

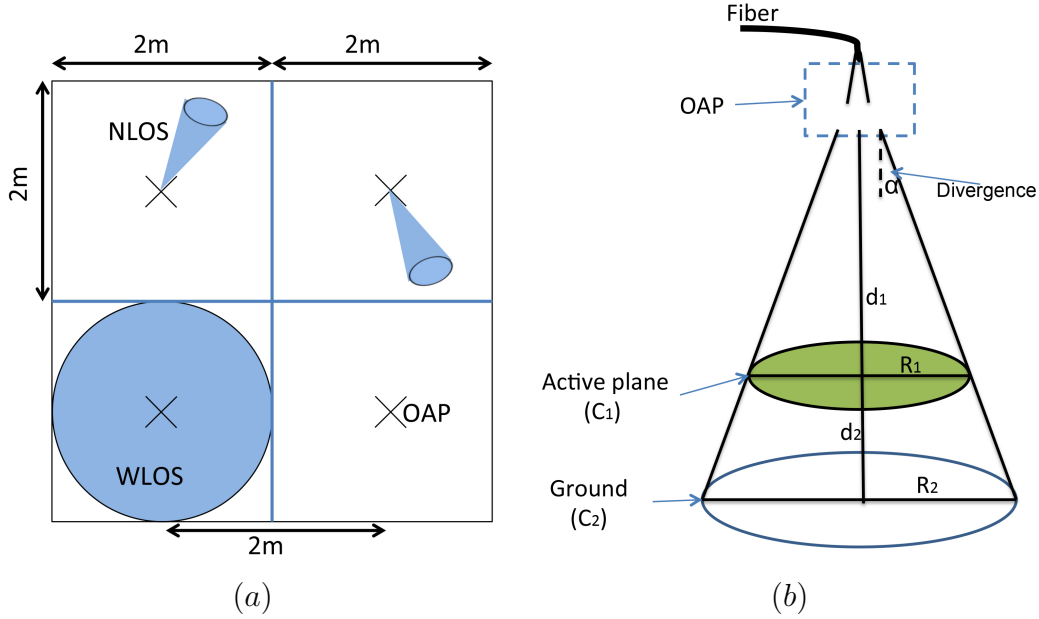


Figure 2.4: (a) OAP distribution within a  $4 \times 4$  m room with different free-space link mode and (b) Free-space active plane

### I.3 Optical access point

The optical access points are distributed in the desired rooms and should be placed at the ceiling with a number related to the room dimensions (figure 2.4 (a)). These OAPs ensure the transfer of the downstream signal to the mobile receiver through a free-space link. The OAP is an optical system whose role is to locate mobile receivers and to ensure the connection through the maximization of the signal-to-noise ratio (SNR) at photoreceiver output. It operates in two modes to ensure the downlink setting and the optical signal transfer to the receiver:

1. Medium LOS (MLOS) mode: a signal with medium divergence is transmitted in free-space ( $10 - 30^\circ$ ) to detect the presence of wireless terminals. In this mode, the signal power is diffused over a large area, making the received power at terminal stage lower than the receiver sensitivity but higher than the optical noise level. Thus, the receiver works as an optical sensor whose functionality is to detect a variation of the optical power at its detection area, then, inform the transmitter of the presence of the mobile terminal and its location in order to start the data transmission. The receiver-transmitter communication depends on the uplink channel mentioned in the next section.
2. Narrow LOS (NLOS) mode: as explained in section V, the large free-space attenuation limits the permitted divergence of the beam to a small angle in order to provide enough power at the receiver stage and then, the SNR required for an optical free-space transmission. To this aim, when a receiver detects the signal in WLOS mode, the free-space beam switches to the NLOS mode

with a reduced beam divergence ( $2 - 5^\circ$ ) around the receiver before starting the data transmission.

This two modes can be obtained by two different diffractive optical elements (DOEs) [4], placed at the output of the fiber and associated to a dynamic lens/mirror combination ensuring the switching between the free-space transmission modes. The DOE also has the function of free-space beam shaping. It will be studied and dimensioned in chapter 4, where its characteristics relatively to the fiber output optical signal and to the covered free-space cell will be shown. The position and number of optical beams can possibly be dynamically adjusted using the lens hologram configuration to provide reconfigurable all-optical hotspots. If necessary, the hotspot area can be easily outlined using a visible light mark.

In order to offer some mobility to the receiver<sup>1</sup>, the OAP may include a microelectromechanical system (MEMS) mirror [5] whose role is to track the mobile receivers by switching between DOEs that individually cover a defined zone. The OAP will also contain some elements used for the uplink, that will be discussed in the next section. The OAP should also ensure the switching between the two free-space mode (MLOS and LOS).

## I.4 Different Uplink options

In order to make the proposed system compatible with most network protocols which require a bidirectional link and to allow mobile users to upload some informations, the proposed architecture should implement an uplink. Due to technical constraints and a lack of time, the uplink is not deeply studied in this work, but we present some ideas to ensure the bidirectional link. The radio frequency uplink based on existing technologies and a new optical link are discussed in the next section.

### I.4.1 Radio frequency uplink

As a first step, and to present a system comparable with most telecommunications system which are bidirectional, the uplink on the proposed system can be based on radio frequency signals using WiFi or Bluetooth standards channels.

**Bluetooth uplink** This uplink approach is based on the use of the Bluetooth antennas included in the mobile terminals. Bluetooth antennas will also be placed at the OAPs or at the OCS, dependently to the corresponding covered distances. This solution is limited to a moderate bit rate not exceeding 24 Mbps.

**WiFi uplink** The WiFi uplink is a solution offering a higher bit rate which can exceed 300 Mbps. And, as explained in chapter 1, the covered area of WiFi using mono antenna system (MAS) is higher than the home networks area and a WiFi antenna on the OCS is enough for communication between the WiFi antenna on the mobile terminal and the OCS. In the case of using a distributed antenna system

---

<sup>1</sup>called "reduced mobility" differently to the full mobility of some RF systems (WiFi)



(DAS) for the uplink which can increase the bit rate compared to the MAS WiFi system, an antenna will be placed on each OAP to ensure the RF uplink.

The RF solutions presented here show a limited bit rate lower than the downlink optical bit rate. As a first step, we simplify the uplink by using an existing RF architecture but, after the validation of the downlink and to provide a transparent system where the downlink and the uplink will have the same order of magnitude in terms of bit rate, the uplink bit rate should be increased using the same downlink principle, which is the optical uplink presented shortly in next section.

### I.4.2 Optical uplink

Taking the LOS topology between OAP and receiver, which can be made manually or automatically, into account, the uplink can be also performed using an optical signal. In this case, the mobile receiver should contain an infrared transmitter and the OAP should contain an optical system to focus the maximum optical power coming from the terminal user into the fiber core.

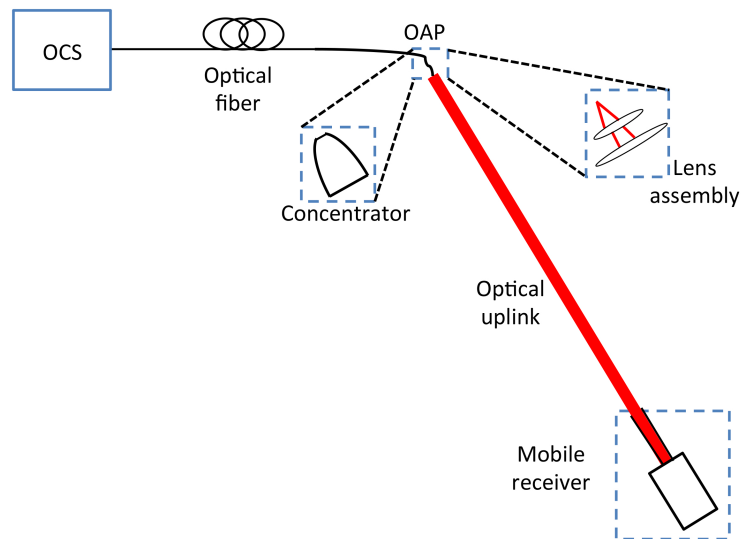


Figure 2.5: Optical uplink design using concentrator or lens to inject the optical signal into the fiber at OAP stage

The idea is feasible mainly with the use of large core ( $\approx 100 \mu\text{m}$ ) plastic optical fibers which will be studied in chapter 3 and an optical concentrator to increase the optical power injected into the fiber. The concentrator is also detailed in chapter 4. The uplink does not have the mobility problem of downlink because the OAP is fixed at the ceiling. The mobile user will only need to orientate the mobile receiver which is here the uplink transmitter in the direction of the downlink corresponding to the OAP. Corner-cube reflectors can be considered at that stage. Figure 2.5 shows this uplink approach. Optical amplification will be required at the OCS to ensure the uplink operation if the power received at the output of the fiber (uplink) is smaller than the necessary received power at the OCS stage. Alternatively, the

optical concentrator can be replaced with a lens system placed on the OAP, as also shown in figure 2.5, to reduce the uplink beam width and focus it into the fiber core. The different uplink possibilities described above are summarized in figure 2.6 showing the communication between transmitter and different receiver possibilities of uplink.

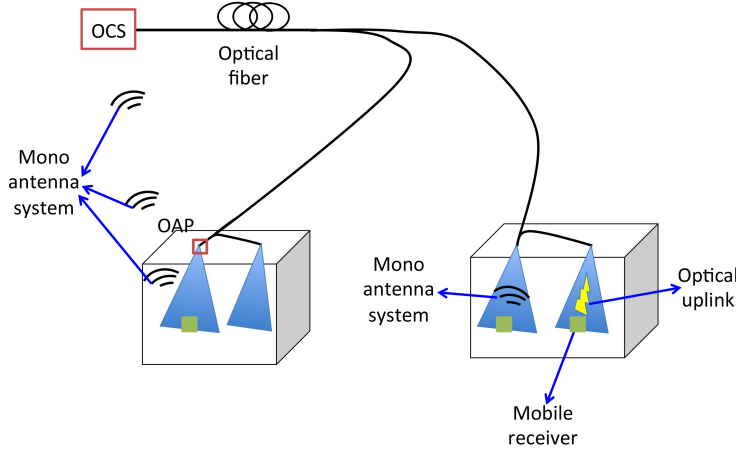


Figure 2.6: Different possibilities of uplink

After the description of the downlink and uplink of the proposed system, the optical sources will be explained in the next sections.

## II Optical sources

The light emitting diodes (LEDs) and the laser diodes (LDs) are the most common optical sources used in optical telecommunications. LEDs are generally considered as extended sources while LDs are assimilated to point sources. The LED is characterized by the incoherence between the majority of generated photons due to spontaneous emission contrarily to the LDs where the emission is stimulated and then the generated photons are coherent.

Table 2.1 summarizes the characteristics of LEDs and LDs as sources for high-speed indoor wireless links. It shows the necessity to use laser diodes for their large bandwidth and electro-optic (E/O) efficiency, with the possibility to consider LEDs with better characteristics expected in the future.

The most commonly used laser diodes in optical telecommunications systems are the Fabry-Perot (FP) laser, Distributed Feedback (DFB) laser and Vertical-cavity surface emitting laser (VCSEL). Until now, VCSELs are not widely used and fabricated in the 1550 nm window, and then, cannot be considered as an option for the proposed system due to the wavelength choice detailed in section IV. A DFB laser is a single frequency mode laser, while FP is a multimode laser with poorer performance at lower price. The FP laser can be considered as a better choice in a

Table 2.1: LED and LD characteristics for high-speed optical wireless links [6]

Characteristics	LED	LD
Spectral width	25 - 100 nm 10 - 50 THz	$10^{-5}$ - 5 nm 1 MHz to 2 THz
Modulation bandwidth	up to 100 MHz	up to tens of GHz
Electro-Optic efficiency	10 - 40%	30 - 70%
Safety	considered safety	needs diffusor especially for $\lambda < 1400\text{nm}$
Cost	low	moderate

multimode fiber low-cost deployment. As explained in chapter 3, a multimode polymer optical fiber is a good choice in terms of installation, maintenance in indoor environment having also a sufficient bandwidth to transmit the required bit rate. Another important parameter for the laser is the modulation bandwidth, which fixes the maximum frequency of the RF signal that modulates the laser. A DFB laser is characterised by a modulation bandwidth going up to 30 GHz while the FP bandwidth is lower than 10 GHz. This modulation bandwidth is sufficient to transmit some Gbps. Taking the different presented parameters into account, the FP laser is suitable for the studied system although the DFB laser presents some better physical characteristics.

Lasers are also classified in different types depending on the potential hazard on the accessible laser radiation and the type of protection respecting eye and skin safety.

Table 2.2: Laser safety classification [7]

Class 1	Safe during use including long term beam viewing directly by eye or while using optical viewing instruments (eye loupes or binoculars)
Class 1M	As for class 1 except possibility to be hazardous if user employs optics
Class 2	Low power; eye protection normally afforded by aversion responses
Class 2M	As for class 2 except possibility to be hazardous if user employs optics
Class 3R	Direct intrabeam viewing may be hazardous
Class 3B	Direct intrabeam viewing normally hazardous
Class 4	High power; diffuse reflection may be hazardous

Our system should be safe under any conditions and then, it will be class 1 laser whose maximum allowed emitted power is estimated in the next section.

### III Operational constraints

#### III.1 Eye and skin safety constraints

An optical signal transmitted in free-space can be harmful for humans within the covered zone. For this reason, any transmitted signal should respect the limits defined to ensure the human safety called generally "eye safety" or "eye and skin safety" because the eye is the most sensitive body part. Different zones of the eye can be damaged by an optical beam depending on the wavelength and the power level at this wavelength. Basically, an image crosses the cornea (front of the eye) and the crystalline lens that is behind the cornea and focuses onto the retina which detects the image. The cornea and crystalline lens are transparent for the visible and near infrared light (wavelength  $< 1400$  nm) and then, the signals in this wavelength range are detected by the retina and may damage it (figure 2.7 (a)). Beyond this wavelength ( $> 1400$  nm), light is blocked by the cornea, which can however be damaged for a power level exceeding safety standard (figure 2.7 (b)). These radiation effects on the eye are depicted in figures 2.7 (a) and (b).

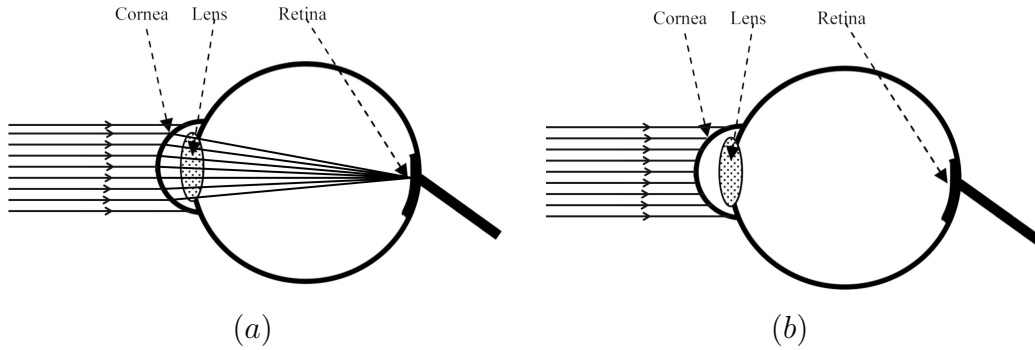


Figure 2.7: Effects on eye of an optical signal ranging from (a) Visible to  $\lambda = 1400$  nm and (b)  $\lambda > 1400$  nm

The variations of the eye power transmission and absorption as a function of the wavelength are depicted in figure 2.8. This figure shows that the optical signal in the visible range and near infrared (450-900 nm) is almost completely transmitted by the eye and partially absorbed by retina. These percentages decrease for higher wavelengths, to be negligible after 1400 nm.

For the 1550 nm wavelength, the cornea is the part of the eye which limits the level of emitted power in free-space. The radiometry factor used to define the maximum acceptable power at the studied wavelength is explained in appendix A. According to the European standard of eye safety [7], and for a maximal exposure time of  $10^4$  s which can be supposed a limit of time that a person directly looks at the OAP without any eye motion, the upper irradiance level that the cornea can support  $E_c$  is  $1000 \text{ W/m}^2$ . Also defined by the European standard of eye safety, the minimal distance  $d_c$  between the point of emission of the optical signal, which is here the

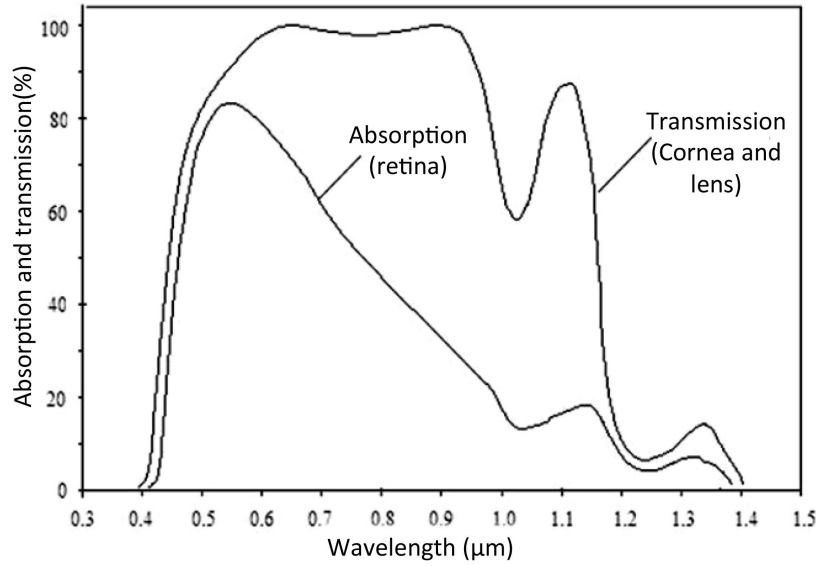


Figure 2.8: Retina transmission and absorption [8]

optical access point, and the cornea  $d_c = 100$  mm. The maximum allowed emitted power is then calculated by the formula:

$$P_0 = E_c \pi \alpha^2 d_c^2 \quad (2.1)$$

Where  $\alpha$  is the divergence semi-angle depending on the zone to be covered at 2.5 m. We shall consider here  $\alpha = 2$  degrees. Under these conditions ( $E_c = 1000$  W/m<sup>2</sup> and  $d_c = 100$  mm),  $P_0 = 38$  mW = 15.7 dBm.

### III.2 Ambient noise

In contrast to fiber communications, the optical free-space receiver is exposed to ambient light, introducing such additional noise sources as daylight, fluorescent, halogen or tungsten lamps. The optical power spectra of the three dominant sources of background illumination in indoor environment are given in figure 2.9 [9].

This figure shows that the fluorescent lamp and sun spectrum have a high power density at wavelength around 700 nm, while the tungsten lamp has a maximum power density at 1100 nm. This lamp type is the dominant source for ambient noise at 1550 nm, but, the noise effect at this wavelength is less harmful in comparison with its level at 850 nm or in the visible range.

To conclude, the ambient noise variation for different sources shows an advantage for the use of the 1550 nm wavelength taking the availability of lasers into account.

### III.3 Reflected beams

Reflection occurs when the signal meets a surface whose dimensions are large compared to the wavelength. Reflected signals depend principally on the surface mate-

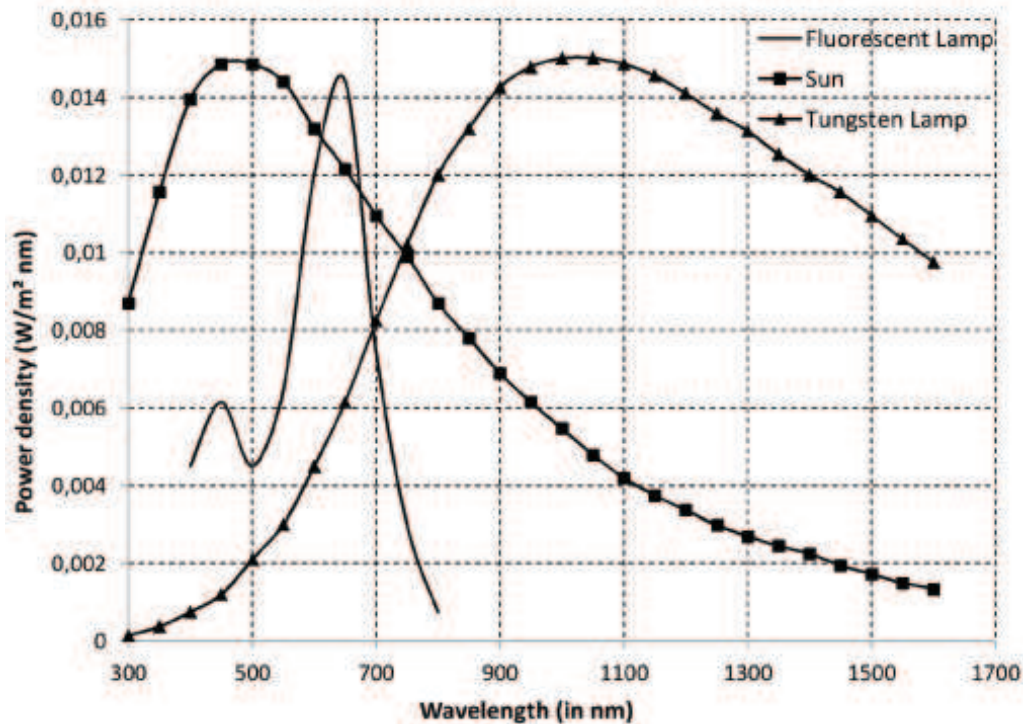


Figure 2.9: Spectral power densities of the three dominant sources of indoor background illumination [9]

rial, incident radiation wavelength and the angle of incidence. Different models were proposed to present the reflected signal such as the Lambert model and the Phong model. These models are described by an equation depending on several parameters like the material reflection coefficient, the incident optical power, the observation angle and the angle of incidence.

Although the optical free-space link is a LOS link requiring a direct view between the transmitter and the receiver, light reflection can occur due to indoor obstacles. This reflection does not mean that the connexion is switched off because other OAP will provide it, but the reflected beam may reach the photodetector area and interfere in a noisy manner at this stage. According to the Techim@ge project [10], the effect of reflection at the receiver stage can be considered as negligible.

## IV Wavelength choice

The choice of the suitable wavelength for the proposed architecture does not only depend on ambient noise and eye safety. We must also consider wavelengths where optical components exist and then, communications can be done. Respecting this criterion, the most suitable wavelengths are 850, 980, 1300 and 1550 nm. And the different characteristics are evaluated for these particular wavelengths.

Corresponding to the eye safety characteristics as shown in figure 2.8, the higher

wavelengths present lower effects on the retina and the wavelengths larger than 1500 nm are stopped by the cornea, showing more advantages for this wavelength range. In terms of availability, the components at 1550 nm are largely spread for telecommunications applications as compared to three others wavelengths. From this point of view, 850 nm components take the second place with the use of silicon based integration. Otherwise, an advantage can be seen for the 850 nm wavelength components in terms of cost due to large availability of the material used for fabrication. The 1550 nm wavelength shows an advantage relatively to the ambient light criteria compared to the three other wavelengths where for each of them, a type of ambient noise presents a high spectral density. Also, the 1550 nm wavelength is advantageous in terms of FTTx compatibility, where this wavelength is used. At the receiving stage which is detailed in chapter 4, the receiver area is smaller for higher wavelengths for a defined bandwidth. In this case, the smaller wavelength present the advantage to have a larger entrance area and, then, a higher optical detected power.

Table 2.3 summarizes the characteristics of the different studied wavelengths where the better choices show more '+'.

Table 2.3: Wavelengths comparison according to different characteristics

	850 nm	980 nm	1300 nm	1550 nm
Components cost	++++	+	+	++
Receiver area (for fixed bandwidth)	++++	+++	++	+
Eye safety	+	++	++	+++
Ambient noise	+	++	+++	++++
Components availability	++	+	+	++++
FTTx compatibility	+	+	+	++++
Total	13+	10+	10+	18+

Based on this study, the chosen system wavelength is the 1550 nm. We can see a disadvantage for this wavelength in terms of detection area. This problem will be partially solved by the use of an optical concentrator, a passive optical element used originally to concentrate the solar energy. It will be used here with small dimensions to concentrate the optical signal at its entrance area to its output small area [11]. This outgoing area will be adapted to the photodetector area. The characteristics of the concentrator are presented in chapter 4.

After the wavelength choice, the power budget of the free-space cell can be estimated in order to give a first idea of the system dimensions.

## V Power link budget: first approach

Now that the operational wavelength has been chosen and the different system constraints and first components approach have been presented, the link power budget can be calculated, allowing us to define the architecture geometry (figure 2.10).

The free-space loss is given (in dB) by the formula:

$$Att_{FS} = 10 \log_{10} \frac{A_d}{\pi(d \tan \alpha)^2} \quad (2.2)$$

where  $A_d$  is the detector area,  $d$  the distance between transmitter and receiver, and  $\alpha$  is the beam divergence semi-angle. In the case of narrow LOS transmission,  $\alpha$  is small (a few degrees), and,  $\tan \alpha \approx \alpha$ , so that the free-space loss value is given by:

$$Att_{FS} = 10 \log_{10} \frac{A_d}{\pi (\alpha^2 d^2)} \quad (2.3)$$

We have the relation between the three parameters that define the free-space optical cell. Respecting the eye safety standards, the maximum optical power diffused in

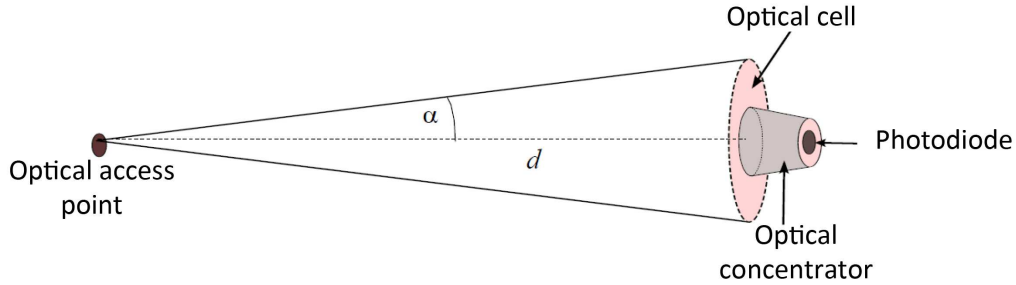


Figure 2.10: Free-space link geometry

free-space at 1550 nm is limited to 10 dBm. As will be shown in chapter 4, the receiver sensitivity is about  $-28$  dBm for a bit error rate of  $10^{-9}$ . The concentrator gain exceeds 16 dB and the optical filter attenuation does not exceed 1 dB. This free-space power budget is summarized in table 6.1. Additionally, the free-space

Table 2.4: Hybrid link power budget

Available power (before the HOE)	10 dBm	
Free space loss		50 dB
Optical filter		1 dB
Concentrator gain	16 dB	
System margin		3 dB
Receiver sensitivity	$-28$ dBm	
System attenuation + Margin		54 dB
Power budget	54 dB	

link distance will be about 2.5 m and the detector, whose sensitivity is considered in table 6.1, has a detection area  $A_d$  of  $0.2 \text{ mm}^2$ . Taking these two parameters and the 50 dB attenuation value into account and using equation 2.3, the system divergence angle will be limited to  $2^\circ$  and the free-space cell will have a limited diameter of 15



cm.

This dimensioning will be optimised in chapter 4 after the study and characterization of different system components. The next section will focus on the optical control station, its different functions and characteristics.

## VI Optical control station

The proposed system aims at transporting the access network traffic and locally generated data streams. As already stated in section I, the digital signals feeding the optical wireless cells are managed by the optical control station, whose role is to distribute the optical signals to the optical access points located in every room, using dedicated optical fiber links at 1550 nm. The OCS involves optical space-switching between the fibers and a possible optical amplification, depending on the hybrid (fiber + free-space) optical transmission link budget. The optical control station design is not considered here but only described based on the use of existing elements to show its feasibility and its different functionalities. The optical control station is shown in figure 2.11. It should ensure some specific functionalities such as:

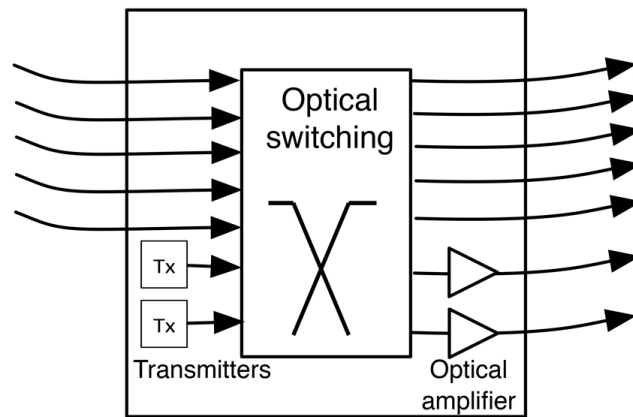


Figure 2.11: Optical control station structure

1. *Management of the communications with the mobile terminal inside the rooms:* The main function of the OCS is to provide the required data for a user and then, the principle role of the OCS is to send detecting signals and to start the data transfer when the user is detected.
2. *Routing the communications between rooms:* The communications between the rooms can also be done only at the OCS level without going up to access networks. This function is very important because users inside the same house or building can communicate and data locally generated can be transferred without adding any overload to the access network.

3. *To manage and ensure the integrity of links:* each room should contain some OAPs and then, the home will contain several links. These links will function in two modes which are (i) the standby mode used in the case where mobile receiver attempt to connect in order to transfer data, (ii) the transmission mode where the transfer data occurs. This functionality will be also managed at the OCS stage.
4. *Ensure the link between the indoor and access network:* the data transfer between the mobile terminal and the access networks and vice versa will be ensured by the OCS. The data should take, at the OCS, the required form to be transferred from the access network to mobile receivers in downlink and the required form of the access network in the uplink.

## VII Green aspects of proposal system

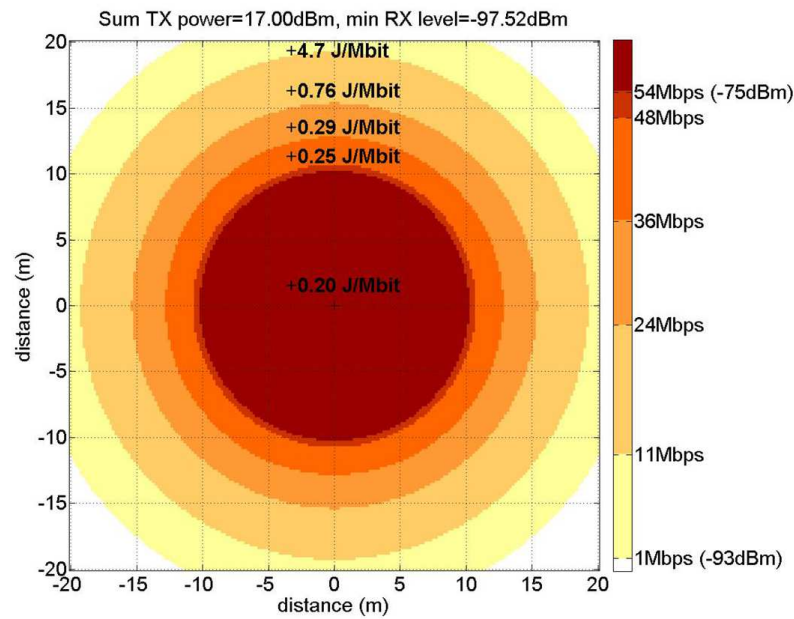
Today, a lot of researchers groups work to decrease the energy consumption of telecommunications networks and to product healthy systems. This point is included in the topics of green telecommunications, among which a large part deals with the access network.

A manner to express the green aspect of a communication system is to study its energy efficiency. This efficiency should be studied using a metric which permits us to compare it between different communications systems. This study is also a subject studied by our research group in the quest for network energy consumption reduction.

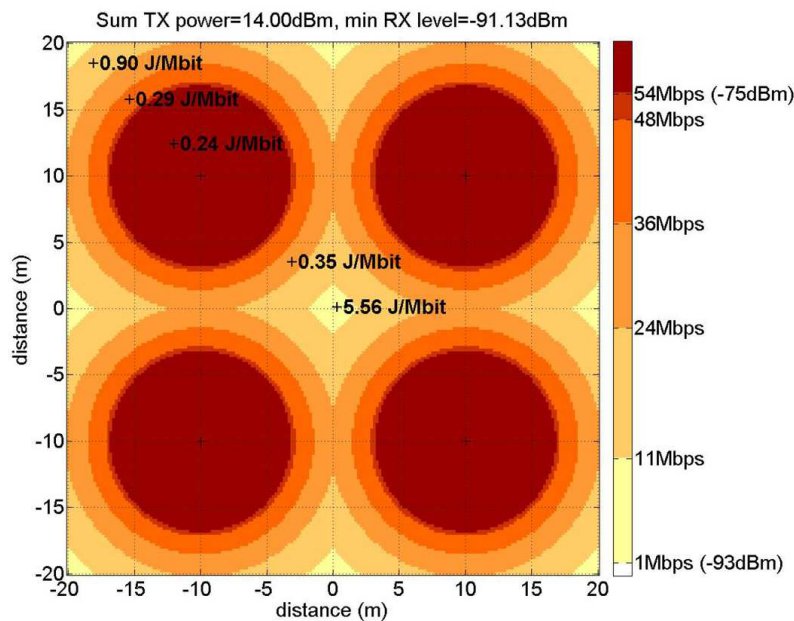
An evaluation of the energy efficiency of RF technologies was studied and the method used consists in taking the overall consumed electric power  $P_{tot}$  by all system components for a given technology and its effective bit rate  $D$  into account and then the energy required to transmit one bit  $E_b$  is calculated:  $E_b = P_{tot}/D$ . The energy efficiency is higher when the energy per bit is lower. A comparison of this energy efficiency between the standard WiFi and radio over fiber distributed indoor antenna WiFi is done in [12] and presented in figures 2.12.

Figure 2.12 (a) shows the map of the maximum reachable data rate with one access point and a radiated power of 17 dBm in an area with 20 m  $\times$  20 m dimensions. It shows that the circle of 10 m diameter around the access point ensures the maximum bit rate of 54 Mbps, then it decreases outside this zone to less than 1 Mbps in the corner. Figure 2.12 (b) shows the map of the maximum reachable data rate in the same area but using four access points distributed by RoF with a total radiated power of 14 dBm. We find a circle zone of 7 m around each access point at the maximum bit rate, which decreases to 11 Mbps in very small areas at the corners. The energy-per-bit  $E_b$  of this RoF system offering an increased average bit rate of 37.5 Mbps is 0.375 J/Mb for a bidirectional link. Considering that half of the consumed energy is for unidirectional link, we get  $E_b$  is 0.1875 J/Mb. This  $E_b$  value is estimated for the proposed architecture based on informations of components given in datasheets.

In our case, the laser at the OCS consumes an electrical power of 22 mW, the pho-



(a)



(b)

Figure 2.12: Map of the maximum 802.11 reachable data rate (a) with one access point, considering a radiated power of 17 dBm and (b) with four access points delivering a total power radiation of 14 dBm

toreceiver with the preamplifier has a power of 80 mw. The OAP contains a MEMS mirror or a electrical micro-motor to ensure the free-space beam steering having an electrical consumption less than 1 mW [5]. With theses values and for a bit rate

of 1 Gbps, the estimated  $E_b$  of the proposed system is 0.000103 J/Mb, giving an idea on our proposed system energy efficiency. This first estimation should be validated later by a real measurement of the total energy spend in the system and the comparison should take the covered zone parameter into account.

## VIII Conclusion

The all-optical indoor communications combining fiber and free-space optical transmission should give the possibility to provide a high bit rate, exceeding Gbps, indoor wireless communications system, that can be built based on commercialized low cost components.

The detailed study is limited to the downlink but, different possibilities of uplink are described, showing its feasibility. The optical power budget for the free-space optical cell is calculated, based on a first approach of the components properties. This validates the feasibility of the system and enables us to start the characterization of the different components to optimize the system performance. The feasibility of the optical control station which is not studied is also mentioned. The 1550 nm wavelength is chosen for the proposed system taking the system constraints and low cost components into account. The estimation of the system power consumption and its energy efficiency show a large advantage as compared to RF systems.

---

---

## Bibliography

- [1] A. M. J. Koonen and L. M. Garcia. Radio-Over-MMF Techniques - Part II: Microwave to Millimeter-Wave Systems. *Journal of Lightwave Technology*, 26(15):2396–2408, Aug. 2008.
  - [2] F. R. Gfeller and U. Bapst. Wireless in-house data communication via diffuse infrared radiation. *Proceedings of the IEEE*, 67(11):1474–1486, Nov. 1979.
  - [3] H. Le Minh, D. O’Brien, G. Faulkner, O. Bouchet, M. Wolf, L. Grobe, and J. Li. A 1.25-Gb/s Indoor Cellular Optical Wireless Communications Demonstrator. *Photonics Technology Letters, IEEE*, 22(21):1598–1600, Nov. 2010.
  - [4] D. H. Close. Holographic optical elements. *Optical Engineering*, (14):408–419, 1975.
  - [5] Inc Mirrorcle Technologies, 2012. <http://www.mirrorcletech.com/devices.html>.
  - [6] J. M. Kahn and J. R. Barry. Wireless infrared communications. *Proceedings of the IEEE*, 85(2):265–298, Feb. 1997.
  - [7] European Standard EN 60825-1: 2007 edition 2. Safety of laser Products - Part 1: Equipment classification and requirements. 2007.
  - [8] K. Semwal and S. C. Bhatt. Tuning of Wavelengths for Producing Eye Safe Laser Using Second Order Nonlinear Processes. *International Journal of Optics and Applications*, 2(3):20–28, Feb. 2012.
  - [9] A. Virtuani, E. Lotter, and M. Powalla. Influence of the light source on the low-irradiance performance of Cu(In,Ga)Se<sub>2</sub> solar cells. *Solar Energy Materials and Solar Cells*, 90(14):2141–2149, 2006.
  - [10] Techim@ges project. <http://www.images-et-reseaux.com/fr/les-projets/>.
  - [11] X. Ning, R. Winston, and J. O’Gallagher. Dielectric totally internally reflecting concentrators. *Applied Optics*, 26(2):300–305, Jan. 1987.
  - [12] Y. Josse, B. Fracasso, and P. Pajusco. Model for energy efficiency in radio over fiber distributed indoor antenna Wi-Fi network. In *14th International Symposium on Wireless Personal Multimedia Communications (WPMC’2011)*, pages 1–5, Oct. 2011.
-

## Figures and tables

### Figures

2.1	Hybrid indoor optical fiber distribution system . . . . .	55
2.2	Optical downlink structure . . . . .	56
2.3	Optical downlink scheme . . . . .	56
2.4	(a) OAP distribution within a $4 \times 4$ m room with different free-space link mode and (b) Free-space active plane . . . . .	57
2.5	Optical uplink design using concentrator or lens to inject the optical signal into the fiber at OAP stage . . . . .	59
2.6	Different possibilities of uplink . . . . .	60
2.7	Effects on eye of an optical signal ranging from (a) Visible to $\lambda = 1400$ nm and (b) $\lambda > 1400$ nm . . . . .	62
2.8	Retina transmission and absorption [8] . . . . .	63
2.9	Spectral power densities of the three dominant sources of indoor background illumination [9] . . . . .	64
2.10	Free-space link geometry . . . . .	66
2.11	Optical control station structure . . . . .	67
2.12	Map of the maximum 802.11 reachable data rate (a) with one access point, considering a radiated power of 17 dBm and (b) with four access points delivering a total power radiation of 14 dBm . . . . .	69

### Tables

2.1	LED and LD characteristics for high-speed optical wireless links [6] . . . . .	61
2.2	Laser safety classification [7] . . . . .	61
2.3	Wavelengths comparison according to different characteristics . . . . .	65
2.4	Hybrid link power budget . . . . .	66

## Chapter 3

# Fiber-distributed optical cells

### Contents

---

Introduction . . . . .	<b>74</b>
I Optical fiber for home networks . . . . .	<b>74</b>
II Perfluorinated graded index polymer optical fiber . . . . .	<b>75</b>
II.1 Fabrication and physical properties . . . . .	75
II.2 Theoretical transmission model of the PF-GI-POF . . . . .	78
II.3 PF-GI-POF characterization . . . . .	80
II.4 Temporal transmission characterization of the PF-GI-POF . . . . .	81
II.4.1 Modeling and simulation of the PF-GI-POF . . . . .	81
II.4.2 PF-GI-POF loss measurement . . . . .	85
II.4.3 Frequency response measurement . . . . .	90
II.5 Far-Field transmission characterization of the PF-GI-POF . . . . .	91
II.5.1 One-dimensional Far-Field profile . . . . .	92
II.5.2 Two-dimensional Far-Field measurement . . . . .	92
II.5.3 Far-field speckle modelling . . . . .	96
III Single-mode fiber for home networks . . . . .	<b>97</b>
III.1 Physical characteristics . . . . .	97
III.2 Spatial characterization of the G657 far-field profile . . . . .	97
IV Conclusion . . . . .	<b>99</b>
Bibliography . . . . .	<b>102</b>
Figures and tables . . . . .	<b>103</b>

---

## Introduction

Optical fibers can be classified in two categories: the single-mode fiber (SMF) and the multimode fiber (MMF). The word "single-mode" comes from the fact that there is only one mode propagating in the fiber. While single-mode fibers have a small core diameter (5 - 9  $\mu\text{m}$ ) at 1550 nm, multimode fibers exhibit larger cores (50, 62.5, 120  $\mu\text{m}$  in diameter and sometimes more than 1 mm). SMF is used in long haul high bit rate transmission systems due to its large bandwidth-length product. The corresponding value for MMF is much smaller (300 MHz.km [1]), which limits the MMF link distance. As a consequence of the low-cost and easiness of its connectorization process, MMF is ideal for short reach links up to a few hundreds of meters.

In this chapter, we determine the required characteristics of a fiber dedicated to home networks, with possible fiber choices suited to the requirements of our system. The characterization is performed by a simulation stage followed by experimental measurements.

## I Optical fiber for home networks

In homes, airports, hospitals, offices, many types of networks are used and optimized to transmit a particular service such as telephony, internet access, Video on Demand. The multiple networks coexist in time and in space due to the bandwidth limits of the used waveguide (coaxial cable, Ethernet cable, ...). After the deployment of the optical fiber from core networks to access networks, the fiber is introduced in in-home networks to offer a medium that can be used to transport different services and to respond to the evolution of the applications and the speed of data transmitted to the customers mainly driven by the broadcasting of high definition images and videos [2][3]. The optical fiber used in home networks to establish the interconnections between the rooms should have some specific characteristics. These characteristics can be divided in two groups. The first one contains the properties of the fiber to be installed in a home and to transmit properly the signal and the information contained. This "home" optical fiber should have a mechanical flexibility to be able to be bent around objects, and to be easily installed under baseboards or around door moldings. It should also be able to transmit a high bit rate stream (1-10 Gbps) along a few tens of meters between the OCS and the OAP. The second group of characteristics deals with the customers demand, the cost of material and the complexity of installation, which must be reasonable and acceptable by most people. The daily use, maintenance and any connection change must be performed by any user without any specific training and without any need for special tools.

Polymer optical fiber (POF) is gradually gaining ground as a serious candidate for the transmission at very high speed and short distance (<200m), both for local networks, professional use and in vehicles [4]. In addition to the decreasing price of the transmission support, the connectors for POF are unexpensive and do not require the precise alignment needed for single-mode fibers. These reasons motivated



us to consider the plastic fiber as a potential solution for our system. An alternative option for us is the glass single-mode fiber dedicated to home networks (G657) [5], which is less sensitive to small bending radii than the standard G652 SMF. G657 fiber will also be characterized to check its compatibility with the studied architecture, as another fiber link option.

## II Perfluorinated graded index polymer optical fiber

POFs have recently gained importance for short and medium transmission applications, especially after the idea of deploying a fiber with good mechanical flexibility as compared to the glass optical fiber (GOF) [6]. The first POF developed in 1987 was the step-index POF (SI-POF) with a bandwidth-length product limited to 5 MHz.km [7]; the fiber bandwidth is a figure of merit of the fiber. Therefore, the bit rate could not exceed 200 Mbps over 50 m. The graded-index POF (GI-POF) having the same advantages of SI-POF, in terms of mechanical flexibility and ease of connectorization, can provide a larger bandwidth offering the possibility to transmit a few Gbps over 100 m [8]. First POF transmissions were performed using the polymethyl-methacrylate (PMMA) fiber. The wavelengths used were in the visible range, and the fiber exhibited a strong attenuation in the infrared part of spectrum (1000 dB/km), where most telecommunication optical sources and receivers operate. The latest POF generation is the PF-GI-POF based on an amorphous perfluorinated polymer having a lower attenuation in the infrared range. In 2000, the Japanese company Asahi Glass proposed the first PF-GI-POF, with transmission performances similar to those of silica fibers [9]. In the first Telecom spectral window (1300 nm), these fibers have an attenuation lower than 15 dB/km [4] and allow maximum data rates of around 10 Gbit/s over 100 m, making it compatible with standard 10GEthernet. A rate of 40 Gbit/s over 200 m at the wavelength of 1550 nm has also been obtained with intensity modulated On-Off Keying (OOK) signals [10]. These reasons lead us to study more precisely the PF-GI-POF fiber as a candidate to be used in the system under consideration.

### II.1 Fabrication and physical properties

The first POF was fabricated using PMMA, also known under the Plexiglass brand. It is composed of several MMA monomers. Each one of these monomers includes 8 C-H bonds which are responsible for the high attenuation in the 600 - 750 nm wavelength range. The substitution of hydrogen in the C-H bonds by fluorine to form C-F bonds can eliminate most of the absorption bands and permit the fabrication of POF with enhanced a transmission in the infrared telecommunication bands (850 - 1550 nm). The POF obtained by this substitution is called PF-GI-POF. Figure 3.1 presents the theoretical and measured attenuation curves of the PF-GI-POF in comparison with the standard PMMA fiber, showing the lower attenuation of the PF-GI-POF. There are several fabrication methods using different polymerization processes causing some differences in the fiber characteristics. As a result, some

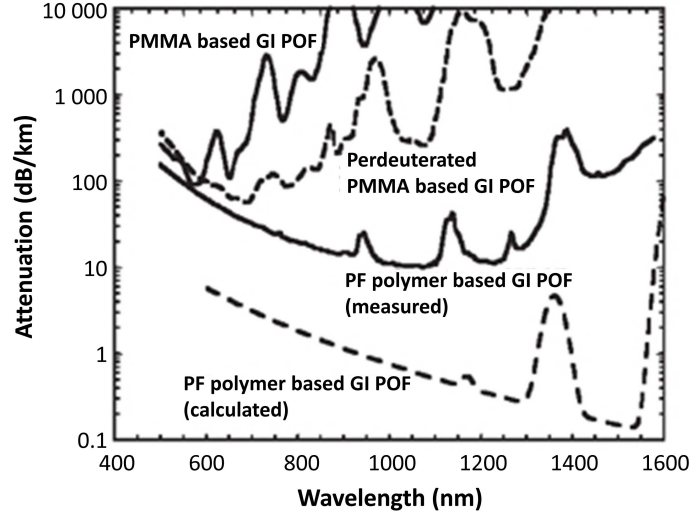


Figure 3.1: Attenuation spectra of PMMA and PF-GI-POFs [4]

impurities due to the gas, a different material crystallization, scattering centers and contamination change the performance of the obtained fiber. We report here three fabrication techniques:

1. *The interfacial gel polymerization*

This method was developed by Koike *et al.* from Keio University [8][11]. It is depicted in figure 3.2. This technique is based on the mixing of the MMA

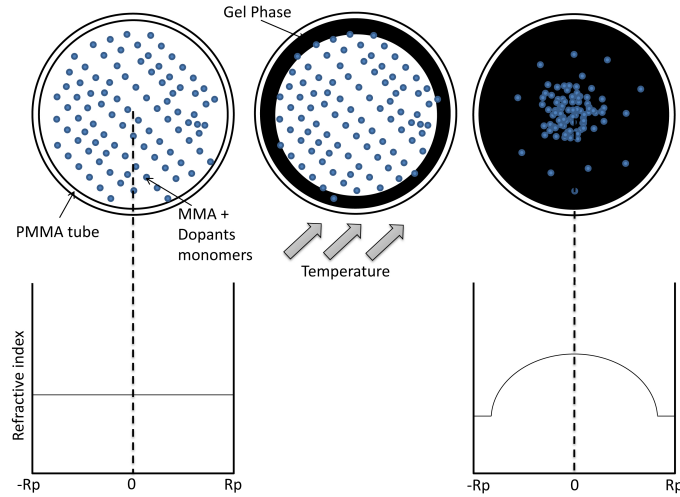


Figure 3.2: Interfacial gel polymerization method

monomers and dopants monomers in a PMMA tube with a diameter equal to the preform diameter and heated at 80°C. The polymerization starts with the MMA monomers having the smallest refractive index at the periphery of the

tube and forms a gel layer on the internal wall of the tube. The polymerization is continued with the higher refractive index monomers more and more towards the center of the tube forming the desired graded index profile. To date, this technique provides the PF-GI-POF type with the lowest fiber absorption. The Asahi Glass Company (AGC) fabricates the PF-GI-POF using this technique and the fiber is commercialized under the Lucina® trademark. But, AGC recently started the fabrication of a new PF-GI-POF called Fontex® with a better transmission characteristics (40 Gbps over 100 m [12]) and a higher mechanical flexibility than the Lucina®, which is now replaced by Fontex® after AGC announced the end of life of Lucina® [13].

## 2. *The centrifuging process and the combined copolymerization/rotation*

The centrifuging fabrication method of PF-GI-POF illustrated on figure 3.3 is based on the density difference between the two monomers [14]. The man-

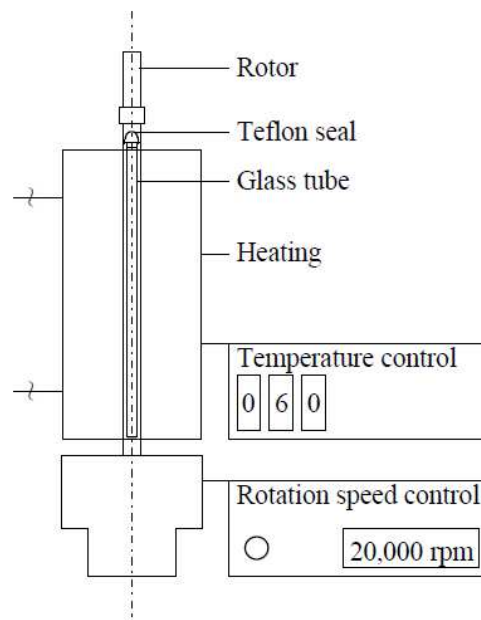


Figure 3.3: Copolymerization/rotating fabrication apparatus [14]

ufacturing process is done through a glass tube rotating at a speed of 20000 to 25000 rotations per minute (rpm) at a temperature of 60°C. The rotation speed fixes the position of different monomers according to the molecular weight forming the graded index profile.

## 3. *The combined extrusion of the core and the cladding materials*

This PF-GI-POF fabrication process is used by the Chromis fiberoptics company lead by W. White and commercialized under GigaPOF® trademark [15]. The co-extrusion method is illustrated in figure 3.4. The PF-GI-POF is fabricated using a CYTOP® [16] material which is used for the core and cladding. Two feeders, containing respectively a CYTOP® material used to perform the

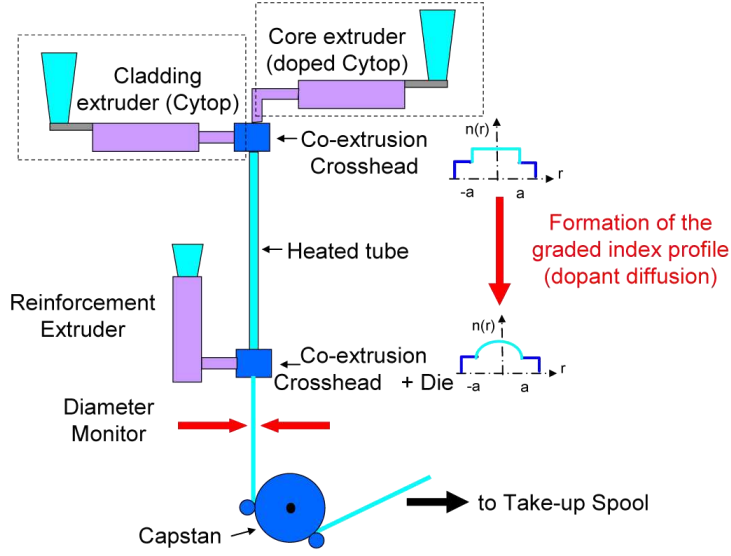


Figure 3.4: Co-extrusion fabrication method

cladding and a doped fluoropolymer CYTOP® used for the fiber core. The two materials are poured into a heated tube. Under the thermal effect, the polymerization is done with a diffusion of the dopant from the center to the tube wall forming the graded index profile. The fiber diameter is monitored at the output of the tube to fabricate the three different knowing core diameter of PF-GI-POF. This manufacturing process can present some impurities that yield some additional attenuation and some quality defects.

These different fabrication methods create PF-GI-POF with different performances, which impacts the fiber price and transmission limits.

A summary of the published data regarding the PF-GI-POF is presented in table 3.1, where the evaluation of the transmission records, bandwidth evolution, and reduction in attenuation along the years are listed. The wavelength of each transmission is also mentioned with a remark describing the experiment. This evolution started from 2.5 Gbps over 200 m and exceeds today a bit rate of 47 Gbps over 100 m. This progression shows that the PF-GI-POF is an interesting and favourable candidate for our proposed system. It is able to transmit the higher bit rate exceeding the 10 Gbps over the 20 m distance.

## II.2 Theoretical transmission model of the PF-GI-POF

The high bit rate expected by the PF-GI-POF fiber over the last years as shown in table 3.1 motivated us to study this fiber for the proposed architecture. For simulation purposes, the PF-GI-POF is modelled theoretically in the appropriate context of the system fiber link, in order to introduce it in the simulator.

In the literature, the multimode fiber was analyzed using different techniques from

Table 3.1: Published results concerning PF-GI-POF transmission trials

Year	Core diameter ( $\mu\text{m}$ )	Attenuation (dB/km)	$\lambda$ (nm)	Results	Ref
1997	125-300	56	1300	600 MHz.km	[17]
1997	120	56	1300	2.5 Gbps over 200m	[18]
1999	170	31	1310	2.5 Gbps over 550m	[19]
1999	130	33	1300	11 Gbps over 100m	[20]
2000	120	15	1300	509 MHz.km	[21]
2003	120	40	850	1500 MHz.100m	[22]
2007	120	40	800-1300	800 MHz.km	[23]
2007	120	40	1300	10 Gbps over 220 m	[24]
2007	50	115	1550	40 Gbps over 30 m	[10]
2010	50	X	1300	47.4 Gbps over 100 m	[25]

which we note the coupled power equations developed by Gloge [26], the propagation and time spreading of digital pulses through MMFs studied by Olshansky [27], the power flow equations used by Yabre [28][29] and the RF transfer function using an electric field propagation model proposed by Capmany [30][31]. The latter method is used to define the MMF transfer function in an optical analogue transmission system and the determined transfer function is an end-to-end linear RF transfer function defined by:

$$H(\Omega, z) = \sqrt{1 + \alpha_c^2} e^{-\frac{1}{2} \left( \frac{\beta_0'' z \Omega}{\sigma_c} \right)^2} \cos \left( \frac{\beta_0'' z \Omega^2}{2} + \arctan(\alpha_c) \right) x \sum_{\nu=1}^M 2\nu (C_{\nu\nu} + G_{\nu\nu}) e^{-2\alpha_\nu z} e^{j\Omega\tau_\nu} \quad (3.1)$$

where  $\alpha_c$  is the source chirp parameter,  $\beta_0''$  the first order chromatic dispersion parameter,  $\Omega$  the frequency of the RF modulating signal,  $z$  is the fiber length,  $\sigma_c$  is related directly to the source linewidth  $W$  ( $\sigma_c \approx 1/2W$ ),  $\nu$  the different mode group carried by the fiber,  $\alpha_\nu$  the modal attenuation,  $\tau_\nu$  time delayed of each sample,  $C_{\nu\nu}$  directly related to the coupling between the optical source and the group mode  $\nu$  and  $G_{\nu\nu}$  depends on the mode coupling along the MMF. This method is largely used to simulate the fiber part of a RoF transmission link. It is not perfectly adapted to an optical transmission where the optical characteristics of the signal at the fiber output are important.

In the latter case, another model defined by Yabre can be used. The Yabre method is based on the power flow equations to study the influence of most parameters of the transfer function of MMFs, which makes it adequate to describe the digital pulse propagations through MMFs corresponding to those which propagate in our system. In this method, the PF-GI-POF is modelled by the transfer function of a multimode fiber through the product of two separated functions, as follows [28]:

$$H_{\text{PF-GI-POF}}(z, \omega) = H_{\text{chromatic}}(z, \omega) \cdot H_{\text{modal}}(z, \omega) \quad (3.2)$$

where  $H_{\text{chromatic}}$  is the chromatic dispersion of PF-GI-POF and  $H_{\text{modal}}$  represents its modal dispersion that depends on the baseband angular frequency  $\omega$ . The chromatic transfer function is given by:

$$H_{\text{chromatic}}(z, \omega) = \frac{1}{(1 + i\omega/\omega_2)^{1/2}} \cdot \exp \left[ -\frac{(\omega/\omega_1)^2}{2(1 + i\omega/\omega_2)} \right] \quad (3.3)$$

where  $\omega_1$  and  $\omega_2$  are defined by:

$$\omega_1 = -\frac{1}{\sigma_\lambda D_0 z} \quad (3.4)$$

$$\omega_2 = -\frac{1}{\sigma_\lambda^2 (S_0 + 2D_0/\lambda) z} \quad (3.5)$$

with  $D_0$  the modal velocity dispersion averaged over all guided modes,  $S_0$  the averaged dispersion slope, and  $\sigma_\lambda$  the root mean square (rms) linewidth of the driving source.

The transfer function of the modal dispersion is calculated by:

$$H_{\text{modal}}(z, w) = \frac{\int_{x_0}^1 2x R(x, z, w) dx}{\int_{x_0}^1 2x R(x, z, 0) dx} \quad (3.6)$$

where  $x_0 = 1/M_t$ ,  $x = m/M_t$ ,  $m$  is the principal mode group number,  $M_t$  is the total number of mode groups that can be excited and  $R(x, z, \omega)$  is the modal power in the Fourier domain.

This model characterizes the fiber transmission in our case. It is used to verify the modelling and the simulation of the fiber. This simulation, and different PF-GI-POF characterizations will be explained in the next sections.

### II.3 PF-GI-POF characterization

In the multimode fiber, the optical signal is carried over different paths as it moves along the fiber. Each path defines an excited mode in the fiber core. The number of existing modes is variable, depending on the input launching conditions (ILC), that can be divided in two types:

- *The restricted mode launching (RML)* where a small number of modes are excited. The RML can be obtained when the signal is injected from a SMF. The fiber characterization under these launching conditions is interesting in our study. It is a way to use the injection from single-mode fiber (laser connected with single-mode fiber) and to assess the fiber output distribution if any misalignment occurs on the PF-GI-POF interconnections.
- *The overfilled launching (OFL)* where the maximum number of modes are excited. This ILC type can be obtained when the injection is performed using a fiber with a core diameter larger than the fiber core under test.

We need to characterize the PF-GI-POF fiber to check its compatibility with our system. More precisely the fiber behavior for different launching conditions must be carefully examined to assess its use in a home network, where it must be installed and maintained by the customer with an alignment error margin without losing the signal. This characterization includes the measurement of the transmission attenuation, the frequency response and the far-field output spatial profile showing the power distribution in the covered zone for different ILC under RML conditions.

## II.4 Temporal transmission characterization of the PF-GI-POF

In this first characterization, we study by simulation the impulse response, the frequency response, the eye diagram at the output of the fiber for different ILCs for the PF-GI-POF. We compare the PF-GI-POF fiber with the results obtained to other multimode fibers. Then, we physically measure the fiber transmission loss and the frequency response also for different launching conditions. The PF-GI-POF considered here is the GigaPOF® model manufactured by Chromis Fiberoptics, whose cladding diameter is 490  $\mu\text{m}$  and with three different core diameters 50, 62.5 and 120 microns. The fiber numerical aperture (NA) is 0.19.

### II.4.1 Modeling and simulation of the PF-GI-POF

A first simulation is carried out to assess the PF-GI-POF in terms of bandwidth and eye diagram quality, which are the parameters that quantify and limit the transmission bit rate. For that purpose, we model the fiber using the optical simulation software VPI<sup>TM</sup> Transmission Maker [32] to simulate the fiber transmission for different ILCs, fiber lengths and types, such as silica and PMMA graded-index (GI) multimode fibers.

**VPI<sup>TM</sup> modeling** The VPI<sup>TM</sup> Transmission Maker software allows the design and characterization of an optical system ranging from long haul, metro, access and short range links. Its huge library of components and demos files offers the possibility to develop and simulate a large variety of optical transmission systems. This simulator is completed by a cosimulation tool using standard programming languages in order to build a model for any element that does not exist in the VPI<sup>TM</sup> library, like the PF-GI-POF model. The generic multimode fiber module is described by the virtual component "MultimodeFiber.vtms", whose default parameters correspond to the silica multimode fiber. This module introduces a radial profile of truncated parabolic index  $n(r)$ , a Sellmeier development  $n(\lambda)$  and a relative refractive index  $\Delta$  defined by:

$$n^2(r) = \begin{cases} n_1^2 [1 - 2\Delta(r/a)^\alpha], & \text{if } 0 \leq r \leq a \\ n_1^2 (1 - 2\Delta), & \text{if } r > a \end{cases} \quad (3.7)$$

$$n^2(\lambda) = 1 + \sum_{i=1}^3 \frac{A_i \lambda^2}{\lambda^2 - l_i^2} \quad (3.8)$$

and

$$\Delta = \frac{n_1^2 - n_2^2}{2n_1^2} \quad (3.9)$$

where  $a$  and  $\alpha$  are respectively the fiber core radius and profile coefficient, the parameters  $l_i$ ,  $A_i$  are the wavelengths and coefficients of the resonant material and  $n_1$  and  $n_2$  are respectively the refractive index at the axis of the fiber and the core/cladding interface. The variation of the refractive index as a function of wavelength for a classic PMMA and PF-GI-POF is shown in figure 3.5 (a) and the radial variation of the refractive index of PF-GI-POF is shown in figure 3.5 (b). The simulation tool

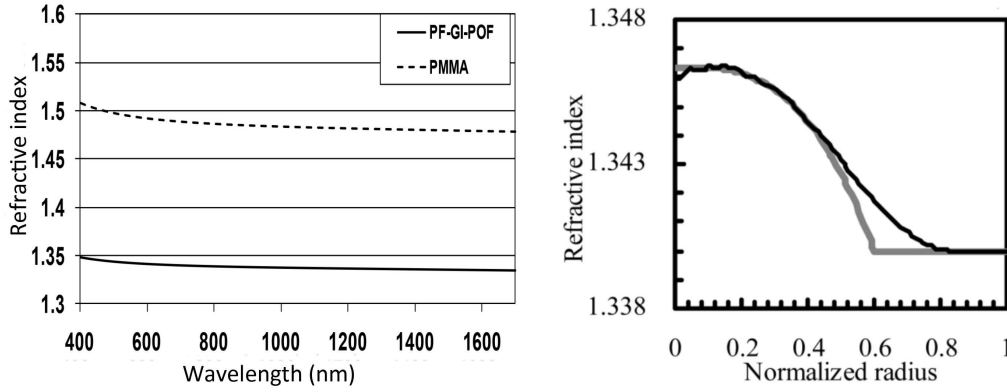


Figure 3.5: (a) Variation of the refractive index as a function of wavelength for PMMA and PF-GI-POF and (b) radial variation of the refractive index of PF-GI-POF

provides such characterizations of the optical link based on such physical parameters changes as the POF index profile, length, ILCs, source linewidth and type of modulation used. The parameters of the three simulated MMF are listed in table 3.2:

Even though these parameters are known for the most common polymer fibers (PMMA), obtaining them and especially the Sellmeier coefficient for the PF-GI-POF has required repeated contacts with the laboratory fabricating the polymer who finally accepted to provide us these values, allowing us to use them for research purposes only but not to diffuse them.

**Impulse response** The impulse response simulation is performed in the purpose of studying the degradation of the optical signal after transmission for different launching conditions, to be consistent with a high speed modulated signal at a bit rate exceeding the Gbps. The input signal is a Gaussian pulse with a full width at half maximum (FWHM) of 20 ps modulating a DFB laser diode at 1550 nm, with a spectral width of 12 GHz. The spatial laser mode has a diameter of 10 microns. This simulation is performed for the three studied fibers and the PF-GI-POF is simulated for the three core diameters (50, 62.5 and 120  $\mu\text{m}$ ) of the GigaPOF® and for different lengths. We vary the launching conditions from an on-axis injection



Table 3.2: Parameters of simulated MMF (X=confidential)

			GI Silica MMF [32]	GI PMMA [33]	PF-GI-POF
Sellmeier coefficients	Resonant material	$A_1$	0.0696	0.4855	X
		$A_2$	0.4079	0.0461	X
		$A_3$	0.6897	0.3484	X
	Wavelength coefficients	$l_1$	68.40	104.3	X
		$l_2$	116.2	87.85	X
		$l_3$	989.6	92.71	X
Relative refractive index $\Delta$			0.01	0.005	0.005
Core maximum index			1.44	1.392	1.347

(fiber) to an offset exceeding  $15\ \mu\text{m}$ . Figure 3.6 (a) shows the simulated impulse

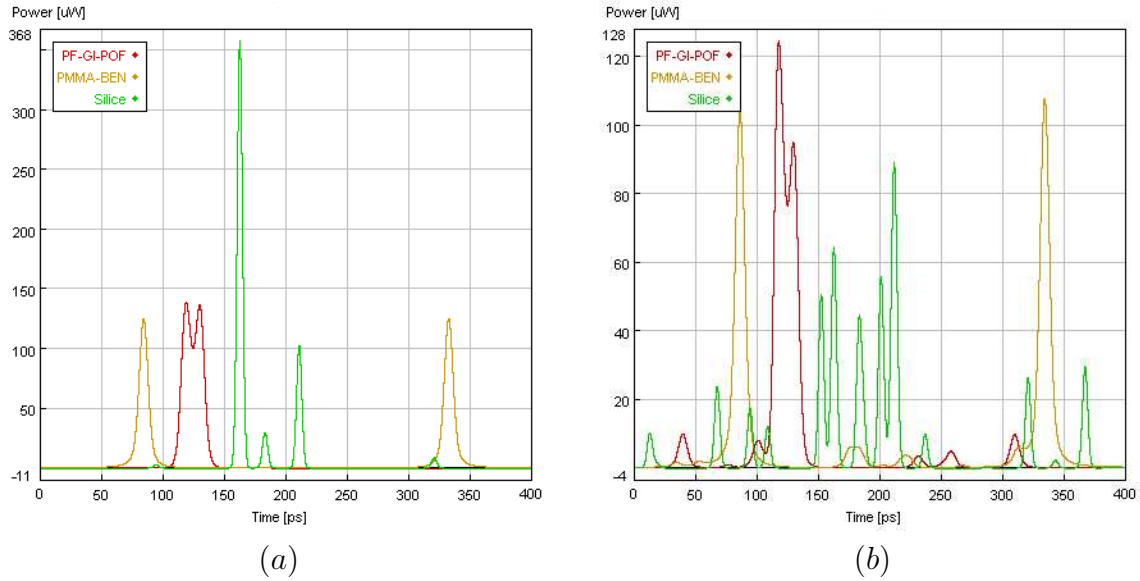


Figure 3.6: Simulated impulse response at any output of 50 m of silica multimode fiber, PMMA and PF-GI-POF (a) without offset and (b) with a  $15\ \mu\text{m}$  offset

response without offset for the silica MMF, the PMMA and the PF-GI-POF all of which having a core diameter of  $50\ \mu\text{m}$ . Figure 3.6 (b) shows the impulse response for the same fibers with  $15\ \mu\text{m}$  offset. In figure 3.6 (a), most of the energy is transmitted through one mode group for the PF-GI-POF and silica MMF, while it is divided between two mode groups for the PMMA. In figure 3.6 (b), only the PF-GI-POF transmits the energy through one mode group, unlike the two other fibers which show several mode groups with different propagation delays. The results for other PF-GI-POF core diameters and for different fiber lengths are similar and do

not contradict the conclusion.

**Frequency response** The characterization of the frequency response is performed with the same physical conditions than the impulse response simulation (input signal, laser, wavelength, spectral width, spatial mode diameter,...) for the three studied MMF. This simulation is done for different fiber lengths, different core diameters and for different offset launching conditions from an injection without any offset to an offset of  $15\ \mu\text{m}$ . The frequency response simulation results are depicted in figure

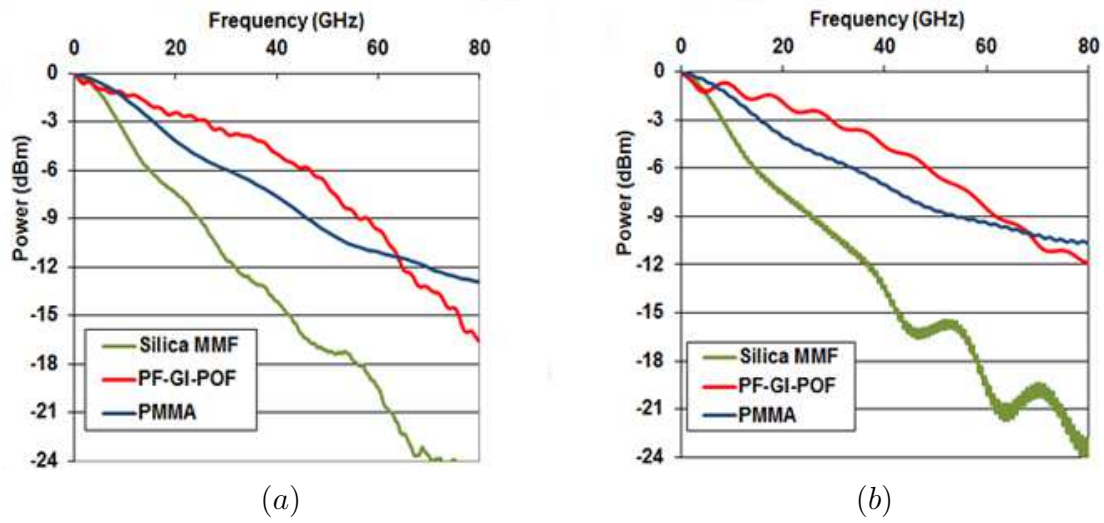


Figure 3.7: Simulated frequency response at the output of 50 m of silica multimode fiber, PMMA and PF-GI-POF (a) without any offset and (b) with an offset of  $15\ \mu\text{m}$

3.7. It shows an advantage for the PF-GI-POF in terms of  $-3\ \text{dB}$  bandwidth in comparison with the two other MMFs for different launching conditions.

**Eye diagram** The optical eye diagrams are observed under the simulation of a 10 Gbps bit rate for the three types of fiber. The modulation used is OOK-NRZ. The simulation is performed with 2048 bits using a sample rate of 1280 GHz.

Figure 3.8 (a) presents the simulated eye diagrams at the output of 100 m of the studied MMFs with an input signal launched along the axis of the fiber and figure 3.8 (b) shows the eye diagrams corresponding to an offset of  $15\ \mu\text{m}$ . The eye diagrams obtained without any offset are almost similar and open for the three fibers. Nevertheless, the eye remains clearly open for the PF-GI-POF in the presence of an offset, unlike the GI-PMMA and silica MMF for which the eye diagram tends to close. This shows the relative robustness of the PF-GI-POF with respect to the introduction of an input spatial offset, and hence to possible connectors misalignments.

These simulation results show the advantage of the PF-GI-POF as compared to the other simulated MMF, through an offset margin exceeding  $10\ \mu\text{m}$  and stable characteristics in terms of impulse response and bandwidth.

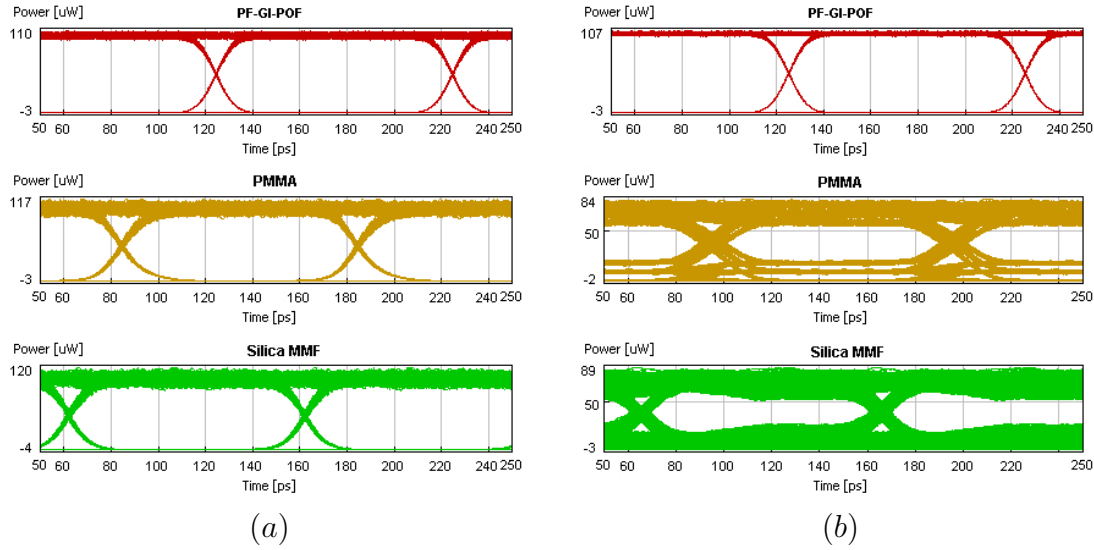


Figure 3.8: Simulated 10 Gbps eye diagram (OOK-NRZ) at the output of 100 m of silica multimode fiber, PMMA and PF-GI-POF (a) without any offset and (b) with a 15  $\mu\text{m}$  offset

#### II.4.2 PF-GI-POF loss measurement

The stability of the transmission attenuation value at the PF-GI-POF output for varying injection offsets can be evaluated through the experimental measurement of the fiber loss under different launching conditions in RML mode, where an offset from the fiber axis is supposed to simulate a connection error i.e. misalignment. This experiment consists in injecting an optical signal at a point of the fiber core, sweeping it to scan the fiber core and measuring the output power for different offset launching conditions. The optical signal is injected into the PF-GI-POF by means of a SMF fiber to ensure a RML condition. These experiments have been carried out during a 3-month collaboration research work at the Electronics Technology department of the University Carlos III of Madrid (UC3M) within the Displays and Photonics Applications Group (GDAF), under the supervision of Prof. Carmen Vasquez. The measurements were performed at the two 1303 nm and 1550 nm wavelengths. The 1303 nm laser is a Fabry-Perot source while the 1550 nm laser is a DFB structure. Lengths of 50 m and 100 m are examined to assess the range of performance suitable for the proposed architecture. In all cases, the PF-GI-POF samples have been manufactured by Chromis Fiberoptics, Inc.

**Experimental conditions** The experimental setup for the PF-GI-POF excess loss measurement using an offset launch via SMF is depicted in figure 3.9. The output of the used optical source is connected to a single-mode fiber, to generate an optical signal which is transmitted through a SMF coupler (95:5). The output with 5% of the power is used to monitor the optical power stability, and the second output signal is injected in the PF-GI-POF through a 4  $f$  imaging setup. At re-

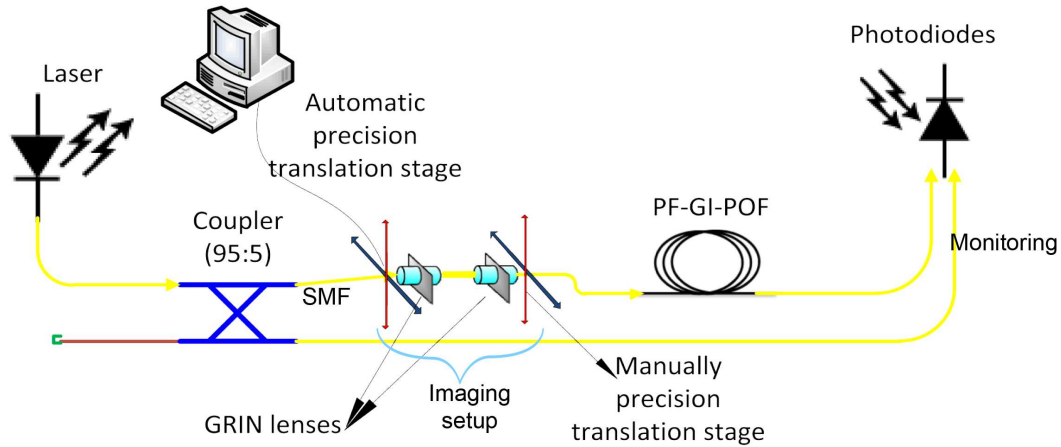


Figure 3.9: Experimental setup for PF-GI-POF excess loss measurements using offset launch via SMF

ception, the optical output power from the PF-GI-POF is measured by an InGaAs photodetector, supporting the large core size of the multimode optical fibers.

The PF-GI-POF excess loss versus SMF offset launch is measured. The input SMF is initially positioned perpendicular to the PF-GI-POF input endface and at the center of the fiber core. It is supposed that the maximum received power occurs at this latter position, and we estimate a negligible error of  $3\text{ }\mu\text{m}$  for this assumption, identical to the repeatability step provided by the precision translation stage manufacturer.

**One-dimensional measurement results** Two transversal radial offsets ( $X, Y$  axes) are scanned across the entire endface of the PF-GI-POF under test, with  $5\text{ }\mu\text{m}$  increments. The relative measured power versus the offset for SMF launch after both 50 m and 100 m PF-GI-POF links is observed. These distances are suitable for most of the estimated and already deployed indoor optical cabling solutions. Different core diameters and operating wavelength conditions have also been evaluated. Some measurement results are shown in the set of figures 3.10. They are presented as a relative power where the reference is the maximum value measured on the axis of the fiber. This reference is shifted from the vertical axis for some curves of the figures due to the small offset errors occurring in finding the fiber axis. Figure 3.10 (a) and (b) show the comparison of transmission loss according to two orthogonal axis and for the two wavelengths, through 50 m of PF-GI-POF with a core diameter of 50 and  $62.5\text{ }\mu\text{m}$  respectively. Figure 3.10 (c) shows the transmission loss comparison along 100 m of PF-GI-POF at 1550 nm and for two different core diameters (50 and  $62.5\text{ }\mu\text{m}$ ). Figure 3.10 (d) compares the relative fiber insertion loss according to the two wavelengths through 100 m and a core diameter of  $120\text{ }\mu\text{m}$ . These curves indicate an offset margin exceeding  $\pm 10\text{ }\mu\text{m}$  with less than 1 dB of attenuation variation. The fiber with  $120\text{ }\mu\text{m}$  core diameter has a larger offset margin exceeding  $20\text{ }\mu\text{m}$  but also shows some attenuation fluctuations at some points

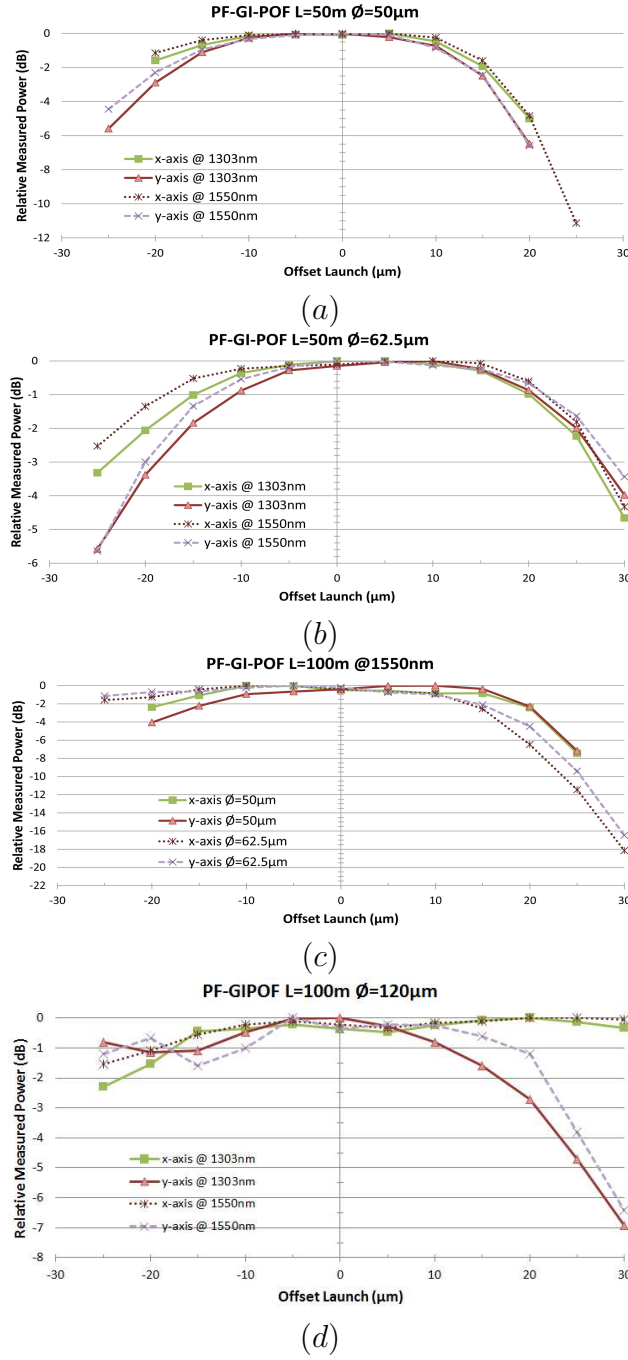


Figure 3.10: Relative measured power at the PF-GI-POF output for different offset launch conditions, (a) comparison between two wavelengths for a 50 m length and 50  $\mu\text{m}$  core diameter, (b) comparison between two wavelengths for a 50 m length and 62.5  $\mu\text{m}$  core diameter, (c) comparison between two core diameters for a 100 m length and 1550 nm of wavelength and (d) comparison between two wavelengths for a 100 m length and 120  $\mu\text{m}$  core diameter

where the loss value exceeds the 1 dB defined margin.

We also simulate the fiber attenuation with different core diameters using the VPI<sup>TM</sup> Transmission Maker software for different offset launch conditions, but the results are not in agreement with the measurements. The simulated loss curve is quite far from the obtained experimental results and the attenuation is almost constant. This discrepancy is probably due to the loss modelling within the multimode optical fiber module by the VPI<sup>TM</sup> software, which considers the part of signal injected through the fiber core depending on the fiber numerical aperture, the offset launching conditions and the attenuation defined as parameter.

Table 3.3 summarizes the metrics that have been measured for the PF-GI-POF samples under test. It should be mentioned that we have set the criteria of 1 dB excess loss (compared to center launch) for the allowable offset launch tolerance (AOLT). We consider this value as strongly limiting but suitable for the our proposed application. A ratio between the AOLT and the fiber core diameter, namely (AOLT/a),

Table 3.3: Summary of measured metrics during the evaluation of the offset launch characterization

Operating wavelength	1300nm		1550nm	
Fiber length	50m	100m	50m	100m
Fiber core diameter	50 $\mu$ m/62.5 $\mu$ m	50 $\mu$ m/62.5 $\mu$ m	50 $\mu$ m/62.5 $\mu$ m	50 $\mu$ m/62.5 $\mu$ m
Attenuation at fiber center (dB)	1.92/2.44	3.76/5.62	14.12/14.73	27.91/28.01
AOLT (1dB) X axis ( $\mu$ m)	$\pm 15/\pm 17.5$	$\pm 12.5/\pm 13$	$\pm 17.5/\pm 20$	$\pm 14.5/\pm 18.5$
AOLT (1dB) Y axis ( $\mu$ m)	$\pm 13/\pm 16$	$\pm 12/\pm 15.5$	$\pm 13.5/\pm 18$	$\pm 14/\pm 17.5$
Slope at 3dB fall (dB/ $\mu$ m)	-1.216/-0.396	-1/-0.874	-0.828/-0.504	-0.974/-0.788

has been also defined, given in percentage, thus quantifying an efficiency parameter of how light can be injected into the fiber under test with regards to its diameter. In the last row of this table, we present the slope as the variation of the excess loss with the offset launch, in dB/ $\mu$ m units, from 3 dB of excess loss (compared to center launch). The uni-dimensional measurement of the PF-GI-POF loss for different launching conditions validates the PF-GI-POF use in terms of offset on RML conditions. But, this uni-axial measurement does not totally validate the overall area of the fiber output and a complementary full output scan will be done to validate the fiber use.

**Two-dimensional measurement results** The previous result should be complemented by a more detailed attenuation measurement, for input launching conditions

at any point of the fiber core input. For this purpose, a 2D-grid containing the locations of the input launching points is chosen, covering an offset range of  $\pm 25 \mu\text{m}$  with  $5 \mu\text{m}$ -steps in both dimensions. Figures 6.2 shows the 2D loss measurement

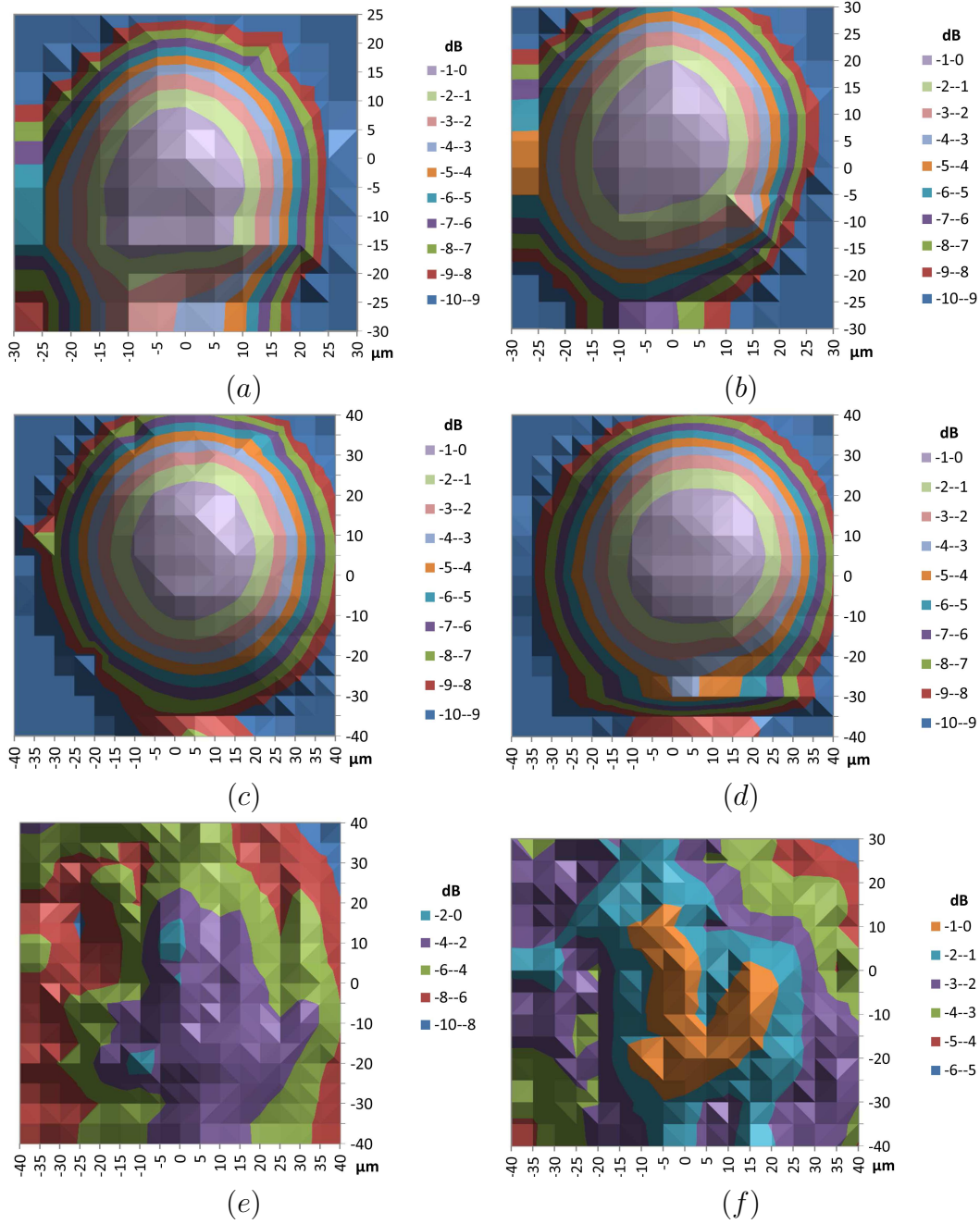


Figure 3.11: Relative measured power excess loss at 50 m of PF-GI-POF for different offset launch conditions with a  $5 \mu\text{m}$  step at 1303 nm for (a) 50 m, (c) 62.5  $\mu\text{m}$ , (e) 120  $\mu\text{m}$  core diameters and at 1550 nm for (b) 50  $\mu\text{m}$ , (d) 62.5  $\mu\text{m}$ , (f) 120  $\mu\text{m}$  core diameters

for the three core diameters and for the two wavelengths. A full 2D scan of the fiber



core is performed with a step of  $5\ \mu\text{m}$  and a step of  $2\ \mu\text{m}$  for the zone of radius  $10\ \mu\text{m}$  around fiber axis. For the  $50$  and  $62.5\ \mu\text{m}$  core diameters, the  $1\ \text{dB}$  excess loss limits a quasi-circular zone with a radius exceeding  $10\ \mu\text{m}$  around the fiber axis. This conclusion is not valid for the PF-GI-POF of  $120\ \mu\text{m}$ , where the fluctuations of the excess loss do not allow this fiber core diameter to be retained as a good choice for our architecture, contrarily to the two other PF-GI-POF core diameters.

### II.4.3 Frequency response measurement

We now wish to characterise the frequency response dependence of the PF-GI-POF as a function of the launching conditions, using the same system as for the PF-GI-POF loss measurement. The measurements are again performed at the two  $1303\ \text{nm}$  and  $1550\ \text{nm}$  wavelengths, in the GDAF group of University Carlos III of Madrid.

**Experimental setup** Figure 3.12 shows the experimental setup used to measure the frequency response of the PF-GI-POF for different launching conditions. The frequency response is measured using a lightwave component analyzer (LCA) from Agilent [Agilent 8703B, 50MHz-20GHz]. For both wavelengths, the lasers are externally AM modulated using an electro-optic (E/O) Mach-Zehnder modulator (JDSU AM-130 at  $1300\ \text{nm}$  and JDSU AM-155 at  $1550\ \text{nm}$ ) with a bandwidth of up to  $20\ \text{GHz}$ . At the receiver stage, a high speed PIN photodiode from Discovery Semiconductors [Model DSC30S] is used to detect the optical signal. This photodiode is specifically designed for multimode fibers and has a  $-3\ \text{dB}$  bandwidth of  $24\ \text{GHz}$ . The experimental link is calibrated with regards to both the E/O intensity modulator, the photodetector electrical responses, before introducing the PF-GI-POF.

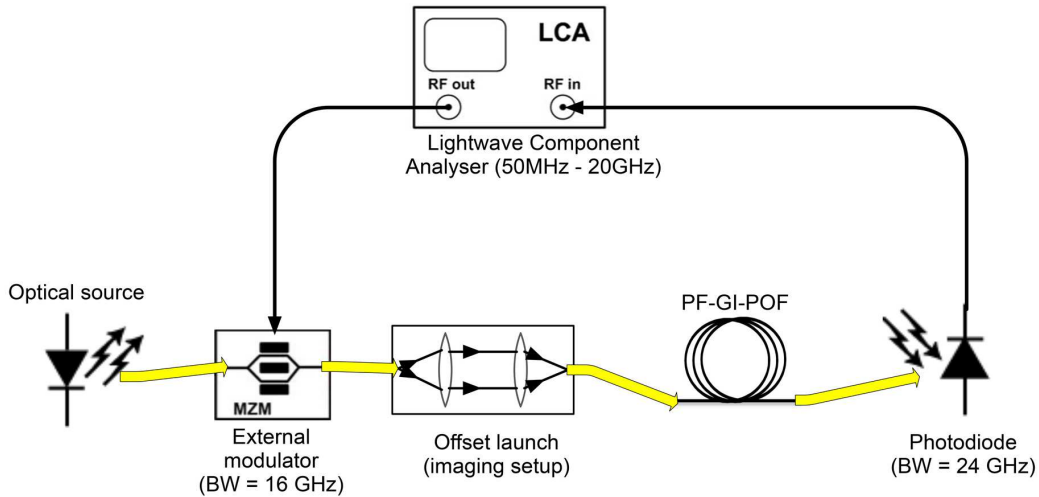


Figure 3.12: Experimental setup used to measure the frequency response of the PF-GI-POF, using an offset launch via a SMF



**Measurement results** Using the experimental test bench previously described, we measure the frequency response of the PF-GI-POF for different core diameters. The frequency response is evaluated at the center of the fiber and for  $\pm 25 \mu\text{m}$  offset, following two orthogonal axes from the center of the fiber with a  $5 \mu\text{m}$  step. The frequency response is measured at 1300 nm and 1550 nm. The 1300 nm source is a Fabry-Perot laser while the 1550 nm source is a DFB laser. The frequency response

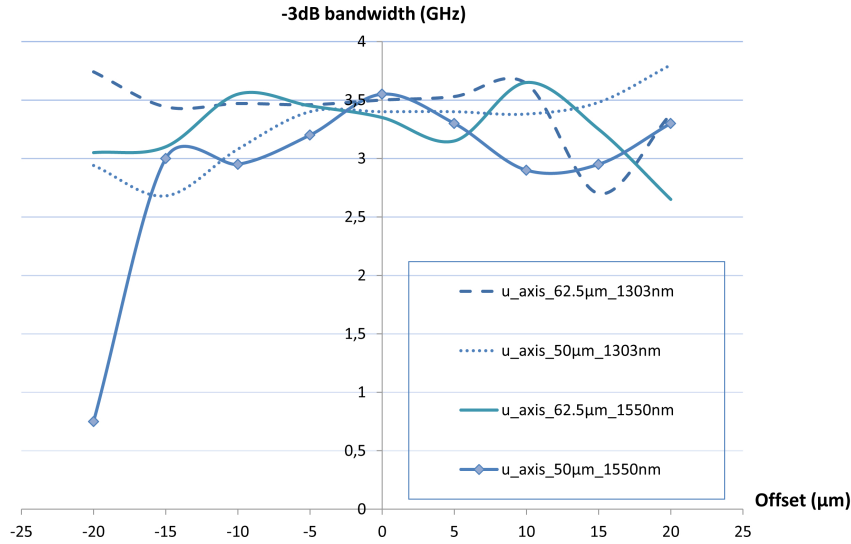


Figure 3.13: Variation of the  $-3$  dB bandwidth over 50 m of PF-GI-POF depending on the offset for two different core diameters (50 and 62.5 microns) and two wavelengths (1303 and 1550 nm)

is studied relatively to the  $-3$  dB bandwidth, which is an important parameter to precise the upper limits of the fiber transmission. The results of the  $-3$  dB bandwidth at the output of 50 m of PF-GI-POF of 50 and 62.5 microns of core diameter and for two wavelengths 1300 and 1550 nm are illustrated in figure 6.3. The experimental curves show a  $-3$  dB bandwidth exceeding 3 GHz for an offset margin of  $\pm 15 \mu\text{m}$ .

The results of the frequency measurement validate also the ability to use PF-GI-POF on the proposed system. The next step will be observe the spatial profile at the PF-GI-POF output, in order to estimate the power profile uniformity of the free-space optical cell.

## II.5 Far-Field transmission characterization of the PF-GI-POF

In the proposed architecture, the optical signal emerging from the fiber is used to cover an area (picocell), via an optical collimation and deflection. The connection geometry is supposed to be in straight line with the receiver to avoid any multipath distortion. The average distance of the free-space optical link is  $d = 2$  m and the

spatial distribution of the light power within the pico-cell is strongly related to the Fraunhofer diffraction pattern of the beam emerging from the fiber. To measure the uniformity of the power distribution in the covered cell, we shall capture the optical power at a few centimeters away from the fiber output. From this far-field measure, it is possible to estimate the beam profile at a distance  $d$  (with a scaling factor).

### II.5.1 One-dimensional Far-Field profile

**Experimental conditions** The system used here to inject the optical signal from a SMF to PF-GI-POF is based on a 4f reflective imaging system. The experiment is performed at the Optics Department. At the receiver side, a single-mode fiber probe is equipped by an angular micro-controller. This fiber probe permits a unidimensional scan relative to the fiber output under test at a fixed acquisition therefrom distance  $z$  and an angular movement defined by an angle  $\theta$  ranging from  $-30^\circ$  to  $+30^\circ$ . The micro-controller is controlled by computer. The value of the measured power for each value of  $\theta$  is saved on the computer. This first characterization is performed at 1535 nm using a non-jacketing PF-GI-POF of 20 m in length.

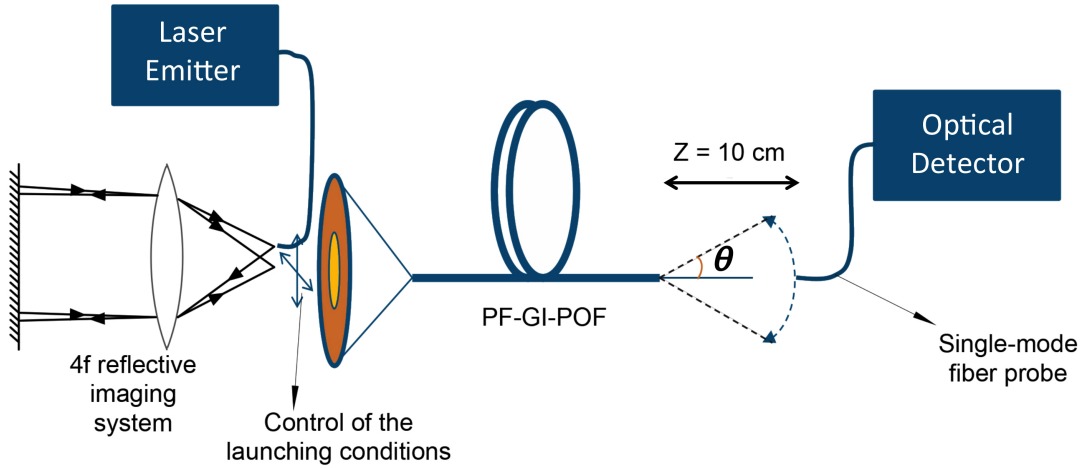


Figure 3.14: Bench set-up for one-dimensional far-field profile measurement

**One-dimensional spatial profile results** We measure experimentally the far-field profile emitted by the POF for two different core diameters 50 and 120  $\mu\text{m}$  and different launching conditions and the results are shown in figure 3.15. The acquisition distance  $z$  is here 10 cm. The measurement results show a more uniform profile for a core diameter of 50 microns, with a variation of the launching conditions.

### II.5.2 Two-dimensional Far-Field measurement

**Experimental conditions** The far-field intensity pattern can also be obtained from a single two-dimensional image acquisition using a 2D sensor. The method

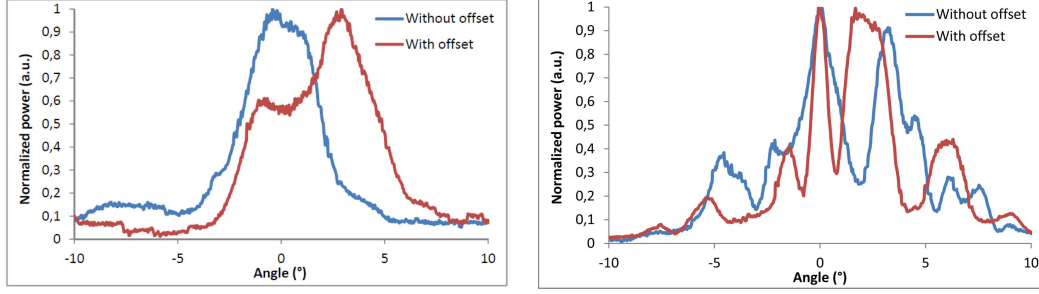


Figure 3.15: 1D far-field profile at the output of 20 m of PF-GI-POF with a core diameter of 50  $\mu\text{m}$  (right) and 120  $\mu\text{m}$  (left) measured at 1550 nm, for two different injection conditions

is faster than the scanning method and it avoids the vertical pre-aligning of the detecting system with the fiber axis to find the far-field pattern (FFP) diameter. The acquisition setup geometry is shown in figure 3.16 with observation distance  $d$ ,

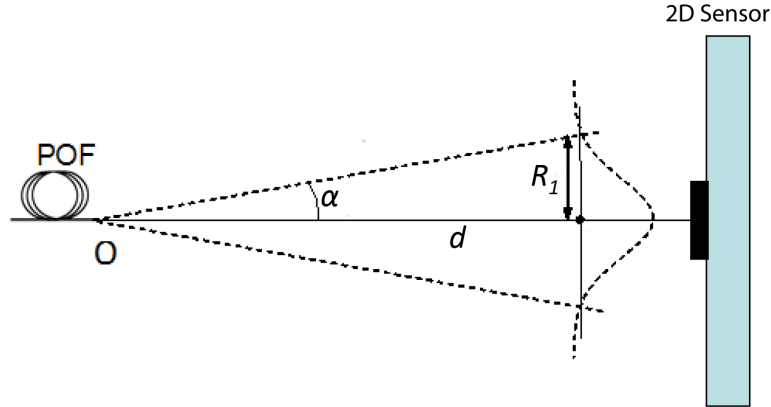


Figure 3.16: Far-field pattern acquisition geometry

half-width of the diffracted pattern  $R_1$  and divergence angle  $\alpha$ . The far-field pattern is obtained from observation distances greater than  $d > (2\alpha^2)/\lambda$ , yielding  $10^{-4}$  m for the present multimode fibers. The range of appropriate observation distances depends on the sensor diameter, which should be greater than  $2R_1$ . The relationship between the beam width and the observation distance is given by:

$$d = R_1 \sqrt{\frac{1}{NA^2} - 1} \approx \frac{R_1}{NA} \quad (3.10)$$

where  $NA$  is the numerical aperture of the fiber. With  $NA = 0.19$  for the present fiber, we obtain a maximum observation distance of  $d = 3 \text{ mm}/0.19 \approx 16 \text{ mm}$  from the fiber endface. The offset launching conditions is controlled here with the same 4f transmission system used in section II.4.2. A positioning mini-bench, fabricated

according to a custom design, is used to hold the 2D sensor, a "z-axis" translation stage, the fiber holder (FC connector) attached to an "x-y" translation stage and a foundation plate to support the different elements.

**Spatial profile measurement** The first spatial far-field are measured using a charge coupled device (CCD) camera from DataRay Inc. (WincamD-UCD12-IR) [34]. The camera sensor is a  $1360 \times 1024$  pixel ( $4.6 \mu\text{m}$  pitch) CCD array coated with a phosphor-on-silicon layer to obtain the required light sensitivity at 1550 nm. However, the power profile measurement presented large distortions much larger than the expected results. The first idea to explain this difference was the phosphor-on-silicon layer of the CCD camera and its non-linearity. The measurement is then repeated using an InGaAs camera [C10633-13, from Hamamatsu] with a high sensitivity in the infrared region (from 900 nm to 1700 nm). The sensor is made up with an array of  $320 \times 256$  pixels ( $30 \mu\text{m}$  pitch), which can be connected to the computer by a standard USB 2.0 port for 14-bit image acquisition with exposure control. The overall implementation of the acquisition setup is shown in figure 3.17. This far-field profile measurement are performed for a PF-GI-POF of 50 and 120  $\mu\text{m}$

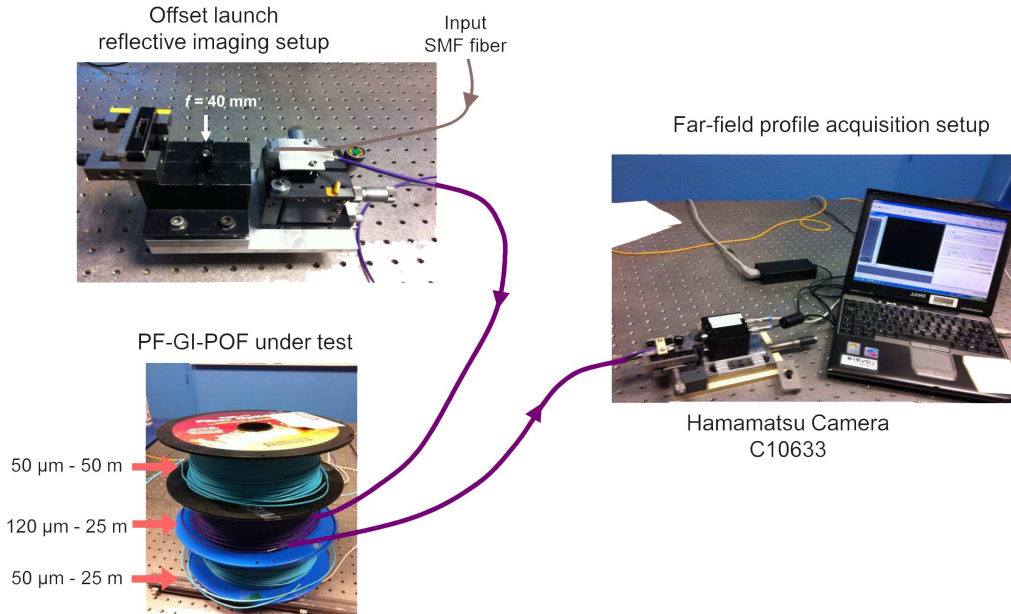


Figure 3.17: Setup of far-field acquisition using an InGaAs camera

and the injection system is the same as that used in the one-dimensional far-field measurement ( $4f$  reflection system). Three different lasers are used with 1300, 1535 and 1550 nm wavelengths respectively using offset launch variations ranging from the fiber axis to 10  $\mu\text{m}$ . The spectra of 1535, 1550 nm wavelengths are shown in figures 3.18 (a) and (b). Figure 3.18 (a) shows that the 1535 nm wavelength laser has a -3 dB spectral width of 2 pm while the 1550 nm wavelength laser a -3 dB spectral width of 1 pm presented on figure 3.18 (b).

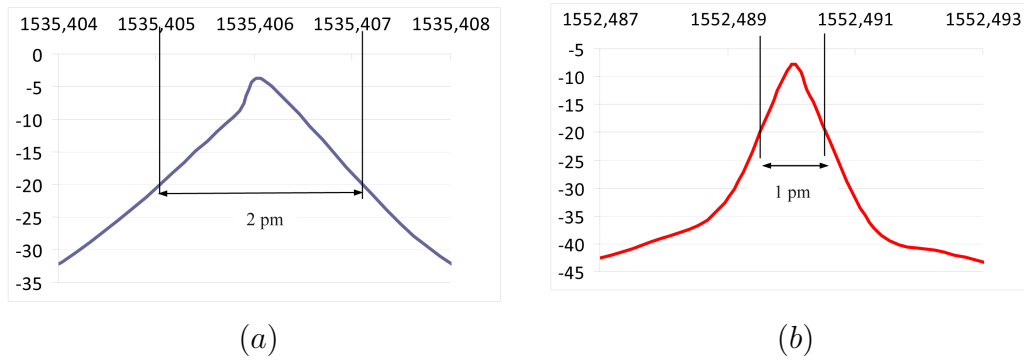


Figure 3.18: Measured spectrum of the laser source (a) at 1535 nm and (b) at 1550 nm

The far-field profiles measured by the InGaAs camera are summarized in figure 6.4 (50  $\mu\text{m}$  core diameter) and figure 3.20 (120  $\mu\text{m}$  core diameter). The spatial distribu-

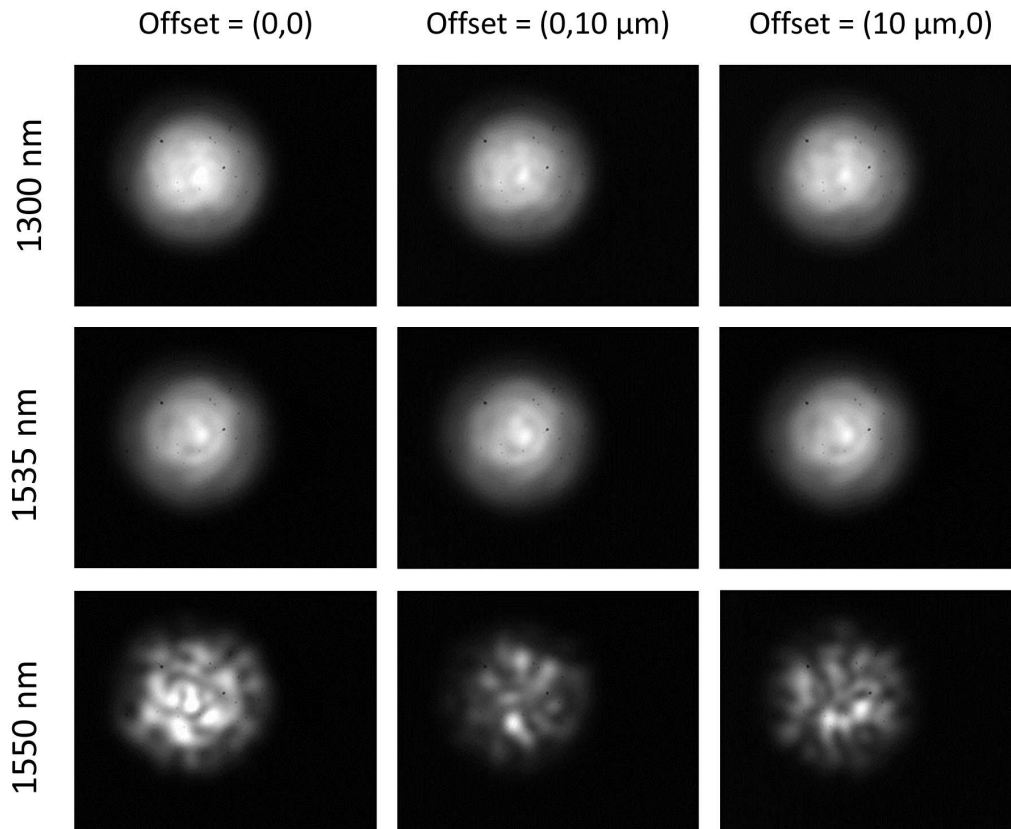


Figure 3.19: Spatial profile at the output of 25 m PF-GI-POF with a 50  $\mu\text{m}$  core diameter using an InGaAs camera. Two orthogonal 10  $\mu\text{m}$  offsets are performed (2<sup>nd</sup> and 3<sup>rd</sup> columns)

tions show a weak dependence on the offset launching conditions, in both directions.

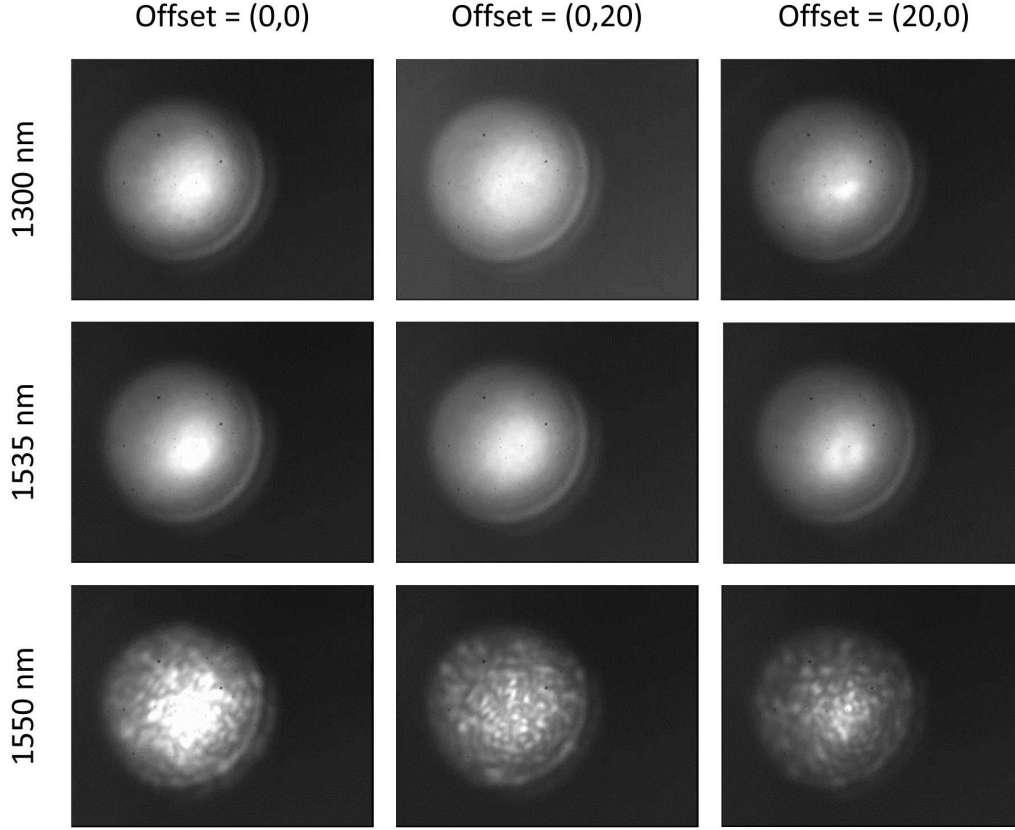


Figure 3.20: Spatial profile at the output of 25 m PF-GI-POF with a core diameter of  $120\ \mu\text{m}$  using InGaAs camera

The most crucial parameter seems to be spectral width of the input source. This can be seen with the 1550 nm laser, whose higher coherence time generates the speckle patterns noticed in figure 6.4. This point tends to be confirmed by the far-field results obtained with the  $120\ \mu\text{m}$  PF-GI-POF (figure 3.20).

### II.5.3 Far-field speckle modelling

For several decades, it has been known that the far-field distribution at the output end of a multimode fiber using a coherent laser beam at the input is subject to a speckle pattern [35][36]. The phenomenon results from random interferences among many guided modes propagating along slightly different paths and group velocities. In addition, the evolution of the speckle contrast along the fiber length is strongly related to the mode coupling between the propagation modes, which is strong with PF-GI-POF structures. In general, the number of speckles cells is proportional to the number of modes guided by an optical fiber. At the fiber output, the highest-order mode undergoes a critical angle  $\theta$ , such that  $\sin \theta = \text{NA}$ , where  $\text{NA} = (n_1^2 - n_2^2)^{1/2}$  is the numerical aperture. Therefore, using the basic law of coherent interferometry, the smallest speckle size  $\delta s$  may be approximately given by half the fringe spacing,

i.e.

$$\delta s = \frac{\lambda}{2 \cdot \text{NA}} \quad (3.11)$$

If all modes at intermediate (two-dimensional) angles interfere, beams with the corresponding lower spatial frequencies interfere, but the finest structure of the fringe pattern is still determined by the size of  $\delta s$ . In addition to this structural description (static), it was shown that the fluctuations of speckle in time (or modal noise) strongly depend on the input launching conditions [36], which are imposed by the characteristics of both the laser source (spectral and spatial) and imperfect fiber connectors.

All these elements make a rigorous analysis of the spatial distributions obtained in figures 3.19 and 3.20 rather complex, and out of the scope of this work. In the present case, we shall adopt a coherent beam shaping solution to circumvent the problem of optical beam uniformity at the receiver cell, as presented in the first section of the next chapter.

### III Single-mode fiber for home networks

The G657 fiber is a new full spectrum SMF fiber characterized by small bend radii. It is optimized for home fiber applications and LAN/WAN networks. Its small bend radius enables this fiber to be more easily installed in the walls than the G652, and to be a serious candidate for our architecture. This solution is studied as an alternative solution for the system with respect to the PF-GI-POF solution provided that its cost and simplicity of use can be precisely evaluated.

#### III.1 Physical characteristics

The G.657 standard, introduced in December 2006, approves the model of SMF with a small bending radius and presents two categories of SMF for use in the access network under the acronyms G657A and G657B. The A category operates in the 1260 to 1625 nm wavelength range with the same transmission and interconnection properties as the G652D fibers. The B category is suitable for transmission at 1310, 1550, 1565 nm for restricted distances corresponding to in-house installations. The comparison between the SMF standard (G652) and the G657 is presented in table 3.4.

#### III.2 Spatial characterization of the G657 far-field profile

The far-field profile was measured at the output of a 100 m of G657 SMF. No offset problem was encountered with this fiber, whose connectors ensure a perfect fiber alignment. The measurement was repeated in the same acquisition conditions than for the PF-GI-POF far-field measurement, using an InGaAs camera. The tests were performed with the three lasers sources (1300, 1535 and 1550 nm) and for different

Table 3.4: Comparison between the original SMF (G652) and the G657 standards

	Standard SMF (G652)	G657
Startup year of fabrication	1983	2005
Attenuation at 1550 nm (dB/km)	< 0.25	< 0.21
Max. attenuation for 7.5 mm bending radius (1 loop)	3.5 dB	0.19 dB
Max. attenuation for 7.5 mm bending radius (10 loops)	35 dB	1.45 dB
Max. attenuation for 10 mm bending radius (1 loop)	0.44 dB	0.02 dB
Max. attenuation for 10 mm bending radius (10 loops)	4.7 dB	0.25 dB

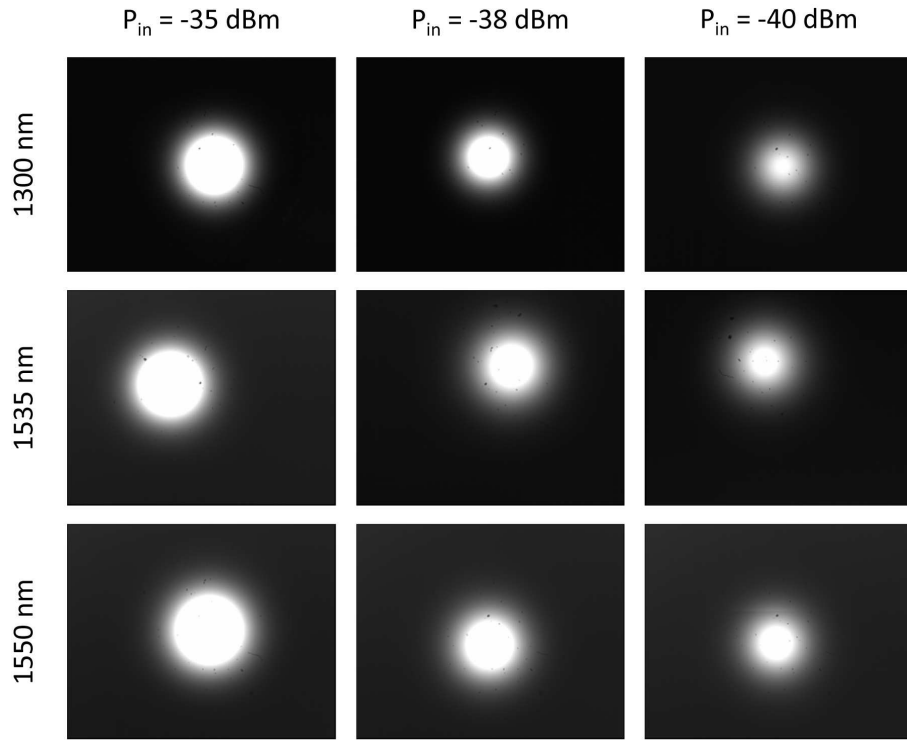


Figure 3.21: Spatial profile (far-field) measured at the output of a 100 m G657 SMF. The power at the output of the fiber has to be adapted to the high-sensitivity of the sensor array

optical power values. The results are shown in figure 3.21. The uniform gaussian profile appears at the G657 output for different laser sources showing no "speckle-like" areas. This confirms that the G657 is perfectly transparent to the transmitted optical signal. This fiber type can also be used in the studied architecture.



## IV Conclusion

The fibered part of the system plays a key role in the proposed system. The idea of distributing the "optical cell" by optical fiber interconnections makes the system realistic to be installed in different building and home in contrast with optical free-space where a laser distributes the optical signal. Besides, the optical signal diffused at the fiber output should meet the required bandwidth, impulse response and output profile to ensure that the optical free-space cell can deliver high bit rate to end users.

Two types of fiber to be used in home networks were studied. The first type is the PF-GI-POF which is the most attractive due to its ease of use and its low-cost connectorization, while the second type is a silica single-mode fiber dedicated to home networks. Each of them is characterized to be used for the proposed architecture.

The second part of the link is the free-space optical cell, which will be characterized in the next chapter. Beam shaping will be considered at the optical access point to improve the optical cell power uniformity at the receiver plane.

---

## Bibliography

- [1] [http://www.thorlabs.com/newgrouppage9.cfm?objectgroup\\_id=2928](http://www.thorlabs.com/newgrouppage9.cfm?objectgroup_id=2928).
  - [2] A. M. J. Koonen, H. P. A. Van den Boom, F. Willems, J. W. M. Bergmans, and G. D. Khoe. Broadband multi-service in-house networks using mode group diversity multiplexing. In *International Conference on Plastic Optical Fiber (POF'2002)*, pages 87–90, 2002.
  - [3] A. M. J. Koonen. Novel signal multiplexing methods for integration of services in in-building broadband multimode fiber networks. In *ISSLS*, 2004.
  - [4] Y. Koike and T. Ishigure. High-Bandwidth Plastic Optical Fiber for Fiber to the Display. *Journal of Lightwave Technology*, 24(12):4541–4553, Dec. 2006.
  - [5] [http://www.pacific-technology.fr/cbx/s4\\_breve641.htm](http://www.pacific-technology.fr/cbx/s4_breve641.htm).
  - [6] T. Ishigure, Y. Aruga, and Y. Koike. High-Bandwidth PVDF-Clad GI POE with ultra-low bending loss. *Journal of Lightwave Technology*, 25(1):335–345, Jan. 2007.
  - [7] J. Meier, W. Lieber, W. Heinlein, W. Groh, P. Herbrechtsmeier, and J. Theis. Time-domain bandwidth measurements of step-index plastic optical fibres. *Electronics Letters*, 23(22):1208–1209, 22 1987.
  - [8] T. Ishigure, A. Horibe, E. Nihei, and Y. Koike. High-Bandwidth, High-numerical aperture graded index polymer optical fiber. *Journal of Lightwave Technology*, 13(8):1686–1691, Aug. 1995.
  - [9] T. Ishigure, Y. Koike, and J. W. Fleming. Optimum index profile of the perfluorinated polymer-based GI polymer optical fiber and its dispersion properties. *Journal of Lightwave Technology*, 18(2):178–184, 2000.
  - [10] A. Polley, R. J. Gandhi, and S. E. Ralph. 40Gbps links using plastic optical fiber. In *Conference on Optical Fiber Communication and the National Fiber Optic Engineers (OFC/NFOEC'2007)*, pages 1–3, Mar. 2007.
  - [11] T. Ishigure, M. Sato, A. Kondo, and Y. Koike. High-Bandwidth graded index polymer optical fiber with high temperature stability. *Journal of Lightwave Technology*, 20(8):1443–1448, Aug. 2002.
  - [12] [http://www.lucina.jp/eg\\_fontex/pdf/tehnical.pdf](http://www.lucina.jp/eg_fontex/pdf/tehnical.pdf).
  - [13] [http://www.lucina.jp/eg\\_fontex/](http://www.lucina.jp/eg_fontex/).
  - [14] F. G. H. Van Duijnhoven. *Gradient refractive index polymers produced in a centrifugal field: preparation, characterization and properties*. PhD thesis, Proefschrift Technische Universiteit Eindhoven, Eindhoven, Netherlands, 1999.
  - [15] <http://www.chromisfiber.com/datacenter.htm>.
-

- 
- [16] W. White. New perspectives on the advantages of GI-POF. In *POF World West*, 2006.
  - [17] N. Yoshiyuki. Performance of Perfluorinated POF. In *International Conference on Plastic Optical Fiber (POF'1997)*, pages 27–28, 1997.
  - [18] H. Imai. Applications of Perfluorinated Polymer Optical Fiber to Optical Transmission. In *International Conference on Plastic Optical Fiber (POF'1997)*, pages 29–30, 1997.
  - [19] W. Li, G. D. Khoe, H. P. A. Van den Boom, G. Yabre, H. de Waardt, Y. Koike, M. Naritomi, and N. Yoshihara. Record 2.5 Gbit/s 550 m GI POF transmission experiments at 840 and 1310 nm wavelength. In *International Conference on Plastic Optical Fiber (POF'1999)*, pages 60–63, 1999.
  - [20] G. Giaretta, W. White, M. Wegmuller, and T. Onishi. High-speed (11 Gbit/s) data transmission using perfluorinated graded-index polymer optical fibers for short interconnects (<100 m). *Photonics Technology Letters, IEEE*, 12(3):347–349, Mar. 2000.
  - [21] K. Kogenazawa and T. Onishi. Progress in Perfluorinated GI-POF LUCINA (TM). In *International Conference on Plastic Optical Fiber (POF'1999)*, pages 60–63, 1999.
  - [22] J. Goudeau, G. Widawski, M. Rossbach, B. Bareel, R. Helvenstein, and L. Huff. GI POF For Gb Ethernet Links. In *International Conference on Plastic Optical Fiber (POF'2004)*, pages 76–81, 2004.
  - [23] D. DuToit. Perfluorinated Graded-Index POF. In *Optical Fiber Communication Conference (OFC'2007)*, 2007.
  - [24] S. C. Lee, F. Breyer, S. Randel, B. Spinnler, I. L. L. Polo, D. Van den Borne, J. Zeng, E. de Man, H. P. A. Van den Boom, and A. M. J. Koonen. 10.7 Gbit/s Transmission over 220 m Polymer Optical Fiber using Maximum Likelihood Sequence Estimation. In *Conference on Optical Fiber Communication and the National Fiber Optic Engineers Conference (OFC/NFOEC'2007)*, pages 1–3, Mar. 2007.
  - [25] H. Yang, S. C. J. Lee, E. Tangdionga, C. Okonkwo, H. Van den Boom, F. Breyer, S. Randel, and A. Koonen. 47.4 Gb/s Transmission Over 100 m Graded-Index Plastic Optical Fiber Based on Rate-Adaptive Discrete Multi-tone Modulation. *Journal of Lightwave Technology*, 28(4):352–359, Feb. 2010.
  - [26] D. Gloge. Optical power flow in multimode fibers. *Bell System Technical Journal*, 51(8):1767–1783, Oct. 1972.
  - [27] R. Olshansky. Mode Coupling Effects in Graded-index Optical Fibers. *Applied Optics*, 14(4):935–945, Apr. 1975.
-

- [28] G. Yabre. Comprehensive theory of dispersion in graded-index optical fibers. *Journal of Lightwave Technology*, 18(2):166–177, Feb. 2000.
  - [29] G. Yabre. Theoretical investigation on the dispersion of graded-index polymer optical fibers. *Journal of Lightwave Technology*, 18(6):869–877, Jun. 2000.
  - [30] J. Capmany, A. Martínez, B. Ortega, and D. Pastor. Transfer function of analog fiber-optic systems driven by Fabry-Perot lasers. 22(10):2099–2106, Oct. 2005.
  - [31] I. Gasulla and J. Capmany. RF transfer function of analogue multimode fiber links using an electric field propagation model: Application to Broadband Radio over fiber systems. In *International Topical Meeting on Microwave Photonics (MWP '06)*, pages 1–4, Oct. 2006.
  - [32] <http://www.vpiphotonics.com/>.
  - [33] T. Ishigure, E. Nihei, and Y. Koike. Optimum refractive-index profile of the graded-index polymer optical fiber, toward gigabit data links. *Applied Optics*, 35(12):2048–2053, Apr. 1996.
  - [34] <http://www.dataray.com/>.
  - [35] L. I. Goldfischer. Autocorrelation function and power spectral density of laser-produced speckle patterns. *J. Opt. Soc. Am.*, 55(3):247–252, Mar 1965.
  - [36] M. Imai. Statistical properties of optical fiber speckles. *Bulletin of the Faculty of Engineering, Hokkaido University*, (130), 1986.
-

## Figures and tables

### Figures

3.1	Attenuation spectra of PMMA and PF-GI-POFs [4] . . . . .	76
3.2	Interfacial gel polymerization method . . . . .	76
3.3	Copolymerization/rotating fabrication apparatus [14] . . . . .	77
3.4	Co-extrusion fabrication method . . . . .	78
3.5	(a) Variation of the refractive index as a function of wavelength for PMMA and PF-GI-POF and (b) radial variation of the refractive index of PF-GI-POF . . . . .	82
3.6	Simulated impulse response at any output of 50 m of silica multimode fiber, PMMA and PF-GI-POF (a) without offset and (b) with a 15 $\mu\text{m}$ offset . . . . .	83
3.7	Simulated frequency response at the output of 50 m of silica multimode fiber, PMMA and PF-GI-POF (a) without any offset and (b) with an offset of 15 $\mu\text{m}$ . . . . .	84
3.8	Simulated 10 Gbps eye diagram (OOK-NRZ) at the output of 100 m of silica multimode fiber, PMMA and PF-GI-POF (a) without any offset and (b) with a 15 $\mu\text{m}$ offset . . . . .	85
3.9	Experimental setup for PF-GI-POF excess loss measurements using offset launch via SMF . . . . .	86
3.10	Relative measured power at the PF-GI-POF output for different offset launch conditions, (a) comparison between two wavelengths for a 50 m length and 50 $\mu\text{m}$ core diameter, (b) comparison between two wavelengths for a 50 m length and 62.5 $\mu\text{m}$ core diameter, (c) comparison between two core diameters for a 100 m length and 1550 nm of wavelength and (d) comparison between two wavelengths for a 100 m length and 120 $\mu\text{m}$ core diameter . . . . .	87
3.11	Relative measured power excess loss at 50 m of PF-GI-POF for different offset launch conditions with a 5 $\mu\text{m}$ step at 1303 nm for (a) 50 m, (c) 62.5 $\mu\text{m}$ , (e) 120 $\mu\text{m}$ core diameters and at 1550 nm for (b) 50 $\mu\text{m}$ , (d) 62.5 $\mu\text{m}$ , (f) 120 $\mu\text{m}$ core diameters . . . . .	89
3.12	Experimental setup used to measure the frequency response of the PF-GI-POF, using an offset launch via a SMF . . . . .	90
3.13	Variation of the $-3$ dB bandwidth over 50 m of PF-GI-POF depending on the offset for two different core diameters (50 and 62.5 microns) and two wavelengths (1303 and 1550 nm) . . . . .	91
3.14	Bench set-up for one-dimensional far-field profile measurement . . . . .	92
3.15	1D far-field profile at the output of 20 m of PF-GI-POF with a core diameter of 50 $\mu\text{m}$ (right) and 120 $\mu\text{m}$ (left) measured at 1550 nm, for two different injection conditions . . . . .	93
3.16	Far-field pattern acquisition geometry . . . . .	93

---

3.17	Setup of far-field acquisition using an InGaAs camera . . . . .	94
3.18	Measured spectrum of the laser source (a) at 1535 nm and (b) at 1550 nm . . . . .	95
3.19	Spatial profile at the output of 25 m PF-GI-POF with a 50 $\mu\text{m}$ core diameter using an InGaAs camera. Two orthogonal 10 $\mu\text{m}$ offsets are performed ( $2^{\text{nd}}$ and $3^{\text{rd}}$ columns) . . . . .	95
3.20	Spatial profile at the output of 25 m PF-GI-POF with a core diameter of 120 $\mu\text{m}$ using InGaAs camera . . . . .	96
3.21	Spatial profile (far-field) measured at the output of a 100 m G657 SMF. The power at the output of the fiber has to be adapted to the high-sensitivity of the sensor array . . . . .	98

---

## Tables

---

3.1	Published results concerning PF-GI-POF transmission trials . . .	79
3.2	Parameters of simulated MMF (X=confidential) . . . . .	83
3.3	Summary of measured metrics during the evaluation of the offset launch characterization . . . . .	88
3.4	Comparison between the original SMF (G652) and the G657 standards . . . . .	98

---

## Chapter 4

# Optical free-space cell dimensioning

### Contents

---

Introduction . . . . .	<b>107</b>
I Optical access point . . . . .	<b>107</b>
I.1 Diffractive optical element . . . . .	107
I.2 Optical beam free-space profile . . . . .	110
II Wireless receiver . . . . .	<b>112</b>
II.1 Optical filter . . . . .	112
II.2 Optical concentrator . . . . .	113
II.2.1 CPC design, fabrication and gain simulation . . . . .	116
II.2.2 CPC gain measurement . . . . .	116
II.3 Pre-amplified photodiode . . . . .	118
II.3.1 Photodiode characteristics . . . . .	118
II.3.2 Preamplifier characteristics . . . . .	120
II.4 Receiver noises . . . . .	121
II.4.1 Different receiver noise types . . . . .	122
II.4.2 Ambient noise . . . . .	123
II.4.3 Conclusion . . . . .	124
III NLOS free-space link performance . . . . .	<b>124</b>
III.1 Modulation scheme . . . . .	124
III.1.1 Transmission techniques . . . . .	125
III.1.2 On-Off Keying modulation . . . . .	127
III.2 Signal-to-noise ratio and receiver sensitivity . . . . .	130
III.3 Dimensioning of the NLOS link . . . . .	133
IV Software modelling and simulation of the free-space link . . . . .	<b>137</b>
V Conclusion . . . . .	<b>139</b>

---

Bibliography . . . . .	<b>141</b>
Figures and tables . . . . .	<b>142</b>

---



## Introduction

Unlike most indoor optical wireless systems characterized by either LOS links or diffused beam transmission, the idea in this work is to uniformly cover a limited area around the receiver through a narrow line-of-sight link that can be moved to track the receiver. The reception area will be referred to as an optical-cell, and sometimes "femto-cell" in the home networks taxonomy.

In this chapter, we will first define the modules of the optical access point that will be used to build the free-space link. Then, the wireless receiver and its different components will be studied. In a third step, the different noise sources and their dominant factor will be considered to estimate the available signal-to-noise ratio (hence, the BER) at the user's terminal, using a standard OOK-NRZ modulation scheme. This study will enable us to determine the dimensions of the optical free-space cell and to estimate the bit rate limits on the proposed prototype. The digital transmission through the free-space link will finally be simulated using the VPI<sup>TM</sup> and Matlab softwares, in order to confirm the validity of the optical cell dimensioning.

## I Optical access point

As explained in chapter II, the optical access point is the part of the system defining the free-space link geometry and hotspot positioning, and consequently, the covered area and the signal power distribution within this area. The basic element of the OAP used in the downlink is a diffractive optical element that will perform the spatial shaping functions defined above. In the next sections, this element will be characterized and its effect on the distributed optical hotspot will be explained.

### I.1 Diffractive optical element

A diffractive optical element (DOE) is a thin phase hologram that modifies light rays by diffraction to produce an arbitrary light distribution at a given plane [1]. In other words, the optical beam crossing the DOE is diffracted to create a new

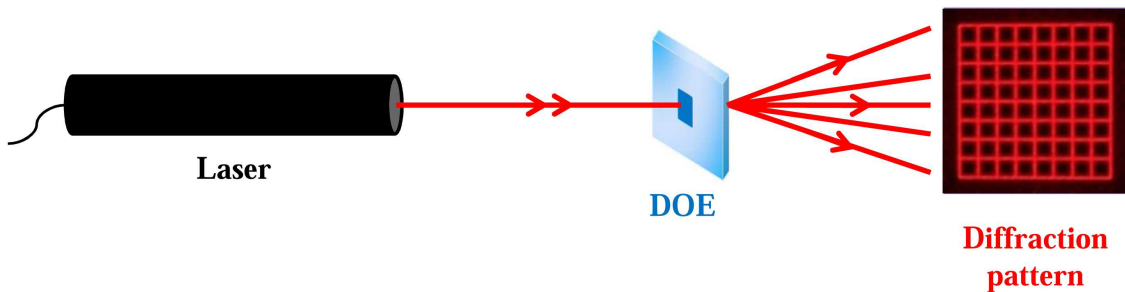


Figure 4.1: Simplified representation of the DOE operation [2]

optical beam distribution called diffraction pattern [3]. The diffraction phenomenon

depends on the wavelength, which can be the same order of magnitude than the DOE resolution. Figure 4.1 presents a simplified scheme of the DOE operation. The spatial resolution of its structure is about a few microns and the etching depth ranges from 10 nm to a few microns. The DOE used on the OAP will have two main functions which are:

1. *Beam shaping*, or spatial conversion of the gaussian profile of the optical signal emerging from the fiber into a "flat-top" spatial profile at the receiver cell (see figure 4.2). This operation is necessary to make the optical power at the optical cell uniform. The illuminating laser beam shape must be adapted to the DOE size. The diffraction pattern can be observed (and used) either in the Fresnel or Fraunhofer regimes.

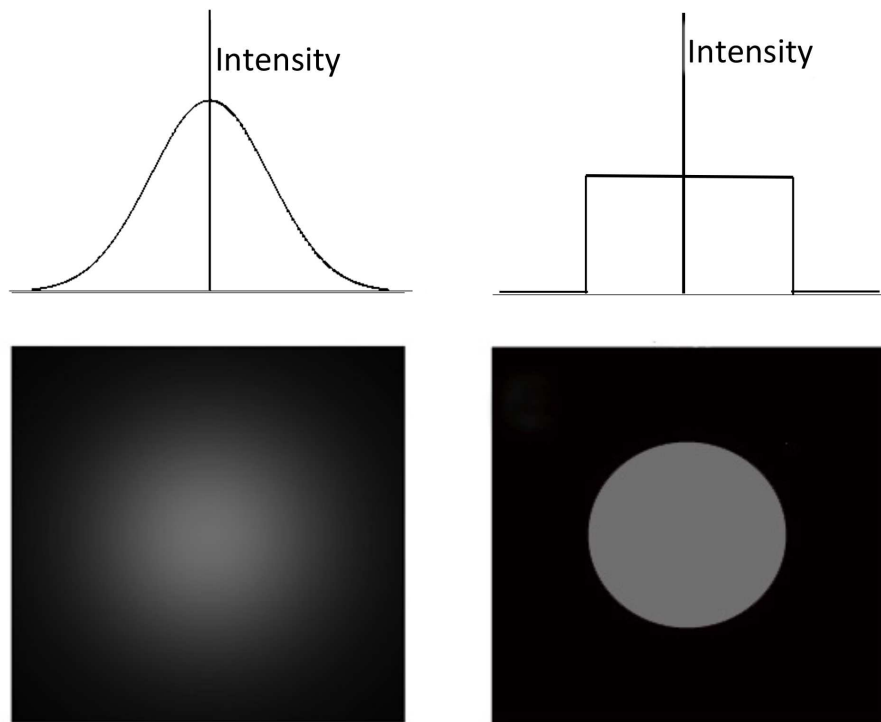


Figure 4.2: Gaussian to flat-top profile conversion

2. *Beam replication*, to circumvent the fiber speckle non-uniformities which can degrade the optical cell at the receiver, especially, if a multimode fiber is used before the OAP. This phenomenon was observed and explained in chapter 3. As schematically depicted in figure 4.3, the solution consists here in using a special type of DOE, called "array illuminator", that spatially replicates the far field of the fiber in two-dimensions along a spatial uniform grid [4].

These two functions of beam shaping and beam replication can be obtained by the same 2D array illuminator, that will replicate the input fiber far-field along a

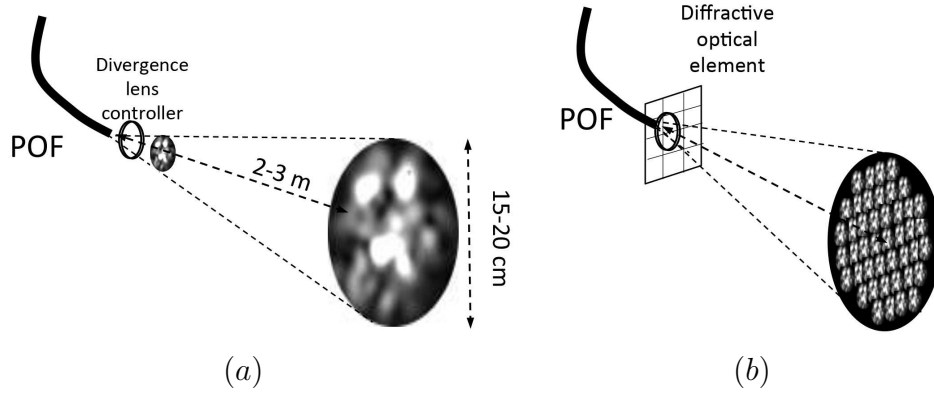


Figure 4.3: Optical cell at the output of the PF-GI-POF (a) without DOE and (b) using a DOE that replicates the fiber far-field along 2D circular grid

circular spatial grid corresponding to the optical cell area. In other words, the DOE design must ensure the uniform distribution of the optical power in the optical free-space cell that was defined in chapter II. Hence, the DOE parameters should be chosen dependently from the free-space distance, the detection area dimensions and the divergence angle. The conceived DOE will be fabricated to replicate the image at its entrance  $n$  times in the covered area at the required distance with a replication distance (in 2D) smaller than the mobile receiver area. This condition will ensure the presence of the optical signal at the receiver entrance. The calculation of the DOE parameters is explained in appendix B. Once defined, the DOE structure was numerically calculated and physically fabricated in our department by Prof. Kevin Heggarty. The pattern profile of the two phase levels DOE is obtained via an iterative inverse Fourier transform algorithm [5]. The computed phase-pattern is then etched in a transparent material using the lab-facilities of our DOE group to obtain the required circular AIL. Figure 4.4 summarizes the different steps of the digital DOE conception and fabrication. Two types of DOE are designed and fabricated: one

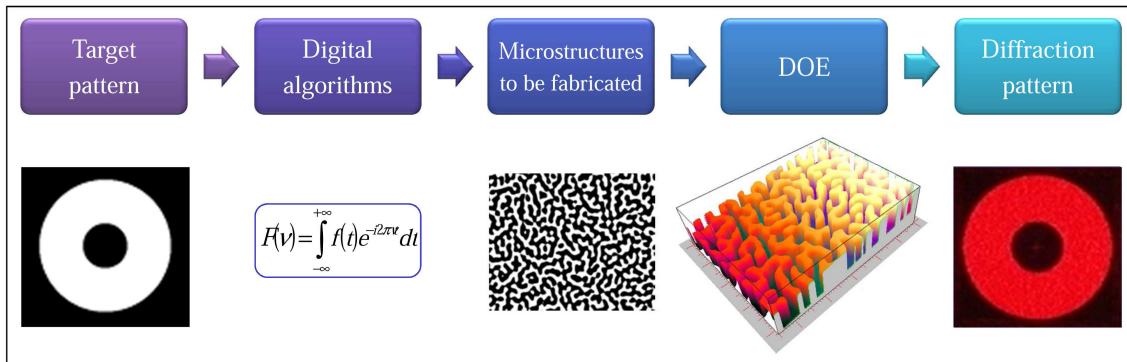


Figure 4.4: Computer design and fabrication of a DOE (Fourier type) [2]

optimized at  $\lambda_1 = 633$  nm for the first visual test, and the second at  $\lambda_2 = 1550$  nm,

to be used in the free-space link.

## I.2 Optical beam free-space profile

Once fabricated, the DOE is tested and characterized to assess its performance. Figure 4.5 represents a part of its diffraction pattern at 1550 nm, as detected by the Hamamatsu InGaAs camera used to measure the farfield profile at the fiber output (see appendix B). Different pattern distributions are obtained by defocusing the positive lens used to collimate the fiber output. The overall diffraction pattern contains about 300 diffraction orders arranged in a circular manner as shown in figure 4.6. Figure 4.5 (a) shows a zoom on 9 diffraction orders of the diffraction

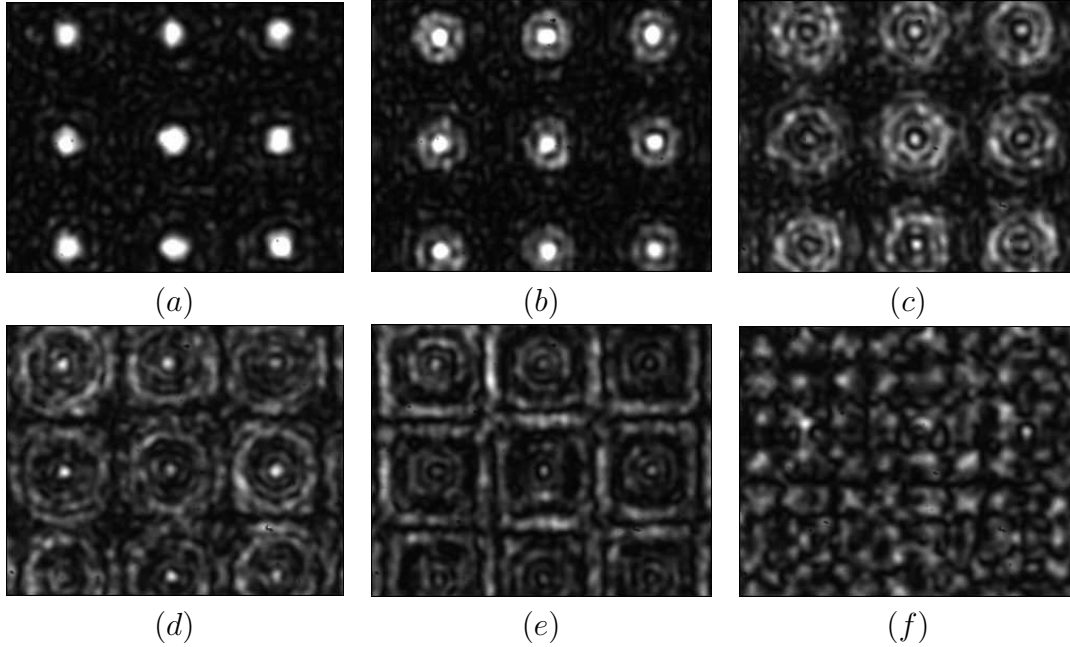
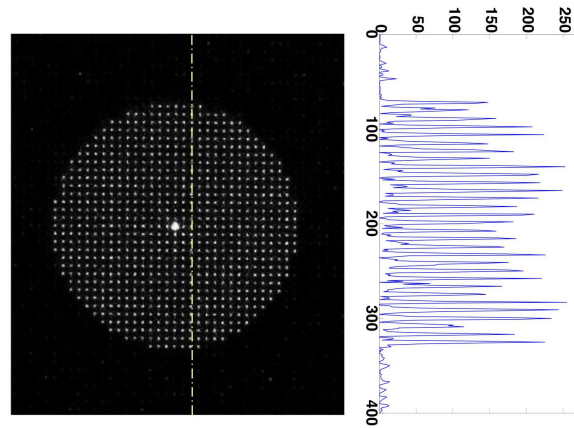
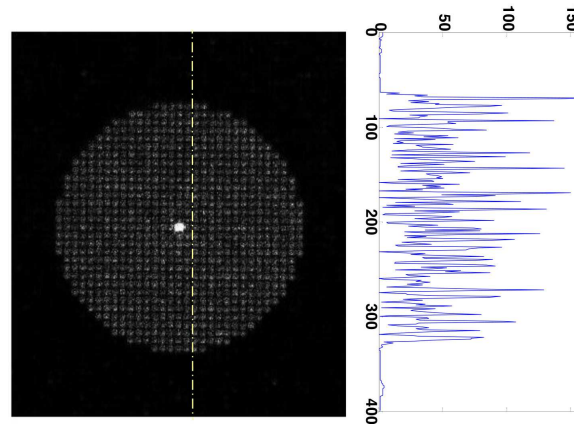


Figure 4.5: Enlarged portion of the diffraction pattern showing 9 points at the focused distance, and successively defocused

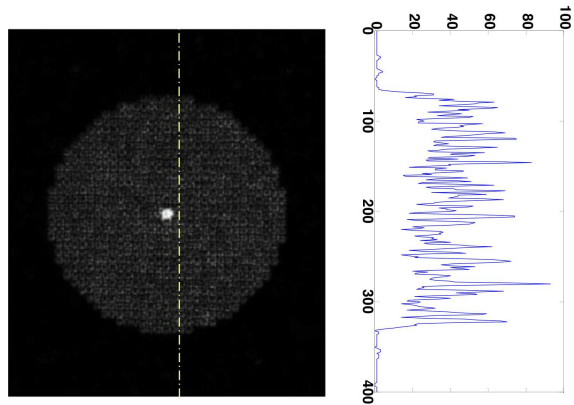
pattern figure in a focused configuration. Using increasing small defocusing (approx  $20\ \mu\text{m}$  steps), the diffraction orders progressively blur in other figures 4.5 (b-f) and the last image shows a relatively uniform power distribution, within the optical cell. Figure 4.6 (a) presents an overall view of the diffractive cell [6] in the plane at the focused distance and 4.6 (b), (c) the diffractive cell with two defocusing. We can also see the corresponding gray level profiles proportional to image intensity as a function of the pixel index. This curves shows that the optical intensity variation on the defocused cell is smaller compared to focused one. In this latter case, the distribution of optical power is more uniform.



(a)



(b)



(c)

Figure 4.6: DOE cells distributions and their corresponding gray level profiles proportional to the image intensity captured by the camera (arbitrary units) as a function of the pixel index. The varying parameter between (a), (b) and (c) is the defocusing between the lens and the DOE

## II Wireless receiver

The wireless receiver is the mobile device to be connected to the laptop or any other mobile terminal to detect the optical signal. It is composed of an optical filter to reduce the noise coming from the ambient light, an optical concentrator to give some power gain, a photodiode to ensure the opto-electrical conversion, a preamplifier and an electrical signal processing circuit. The different components of this mobile receiver are depicted in figure 4.7. Their functionalities and influence on the system design are studied in the next subsections with the aim to present a realistic receiver design that can be implemented in home networks with broadband transmission.

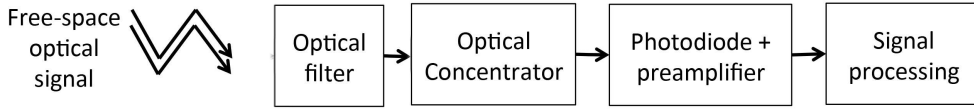


Figure 4.7: Mobile optical receiver scheme

### II.1 Optical filter

To attenuate the noisy ambient light, optical receivers employ longpass or bandpass optical filters. A longpass filter only transmits the optical light at wavelengths beyond the cutoff wavelength. It is fabricated with colored plastic or glass and operates independently from the angle of incidence. Bandpass filters are usually fabricated from multi-layer of thin dielectric films, as depicted in figure 4.8 (a) showing different layers and their refractive index. Such bandwidths as narrow as 1 nm at -3 dB can be obtained by this type of filter lead to eliminate a large amount of the ambient noise, which make this filter type more interesting for our applications [7].

The transmission characteristics in the case of bandpass can be approximated to an  $m$ th-order Butterworth response of the form:

$$T_f(\lambda_0, \theta_i) \approx \frac{T_{f0}}{1 + \left( \frac{\lambda_0 - \lambda_{pk}(\theta_i)}{\Delta\lambda/2} \right)^{2m_f}} \quad (4.1)$$

where  $\theta_i$  is the angle of incidence,  $\lambda_0$  is the center wavelength at normal incidence,  $T_{f0}$  is the peak transmission, and  $\Delta\lambda$  is the optical bandwidth of the filter,  $m_f$  is the Butterworth order, and

$$\lambda_{pk}(\theta) = \lambda_{normal} \left[ 1 - \left( \frac{n_1}{N^*} \right)^2 \sin^2 \theta \right]^{1/2} \quad (4.2)$$

is the wavelength of peak transmission for light incident at angle  $\theta$ .  $\lambda_{normal}$  is the wavelength of peak transmission for normal incidence,  $N^*$  is the effective refractive

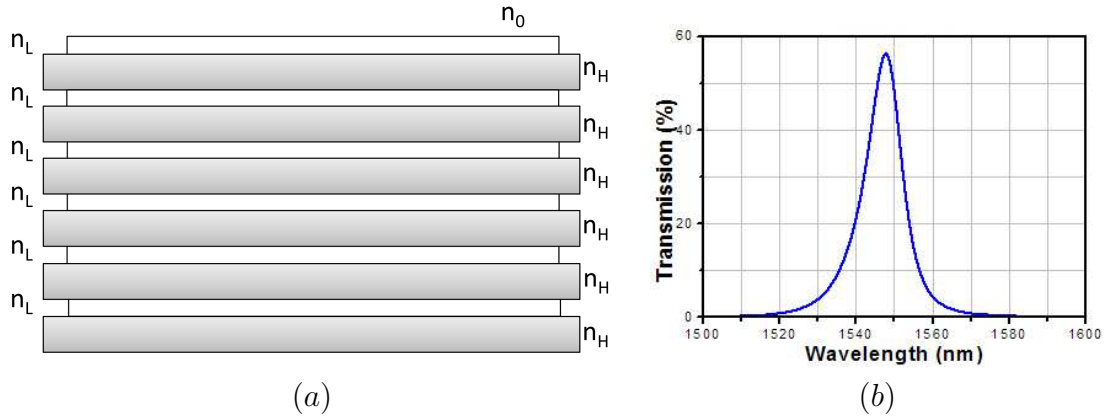


Figure 4.8: (a) Thin-film filter [8] and (b) optical filter transmission

index of the filter. Figure 4.8 (b) presents the variation of the optical filter transmission for a commercialized optical filter centered at 1550 nm and a bandwidth of  $12 \pm 2.4$  nm [9].

## II.2 Optical concentrator

The detected optical power by the photodiode is proportional to its effective area. Increasing this area in the goal of increasing the detected optical power decreases the bandwidth and increases the noise level (see section II.3). The concentrator is an optical passive element which increases the effective area of the detector without affecting the other parameters of the photodiode. The concentrator compensates for a part of the high attenuation in free-space by transforming light rays, incident over a large area on its entrance aperture, into a set of light rays that emerge at the output from a smaller area (see figure 4.9). Its operation is based on Lagrange invariant or Etendue which refers to the product of the angular extent and the diameter of a beam of an optical signal. The maximum theoretical gain of an optical concentrator

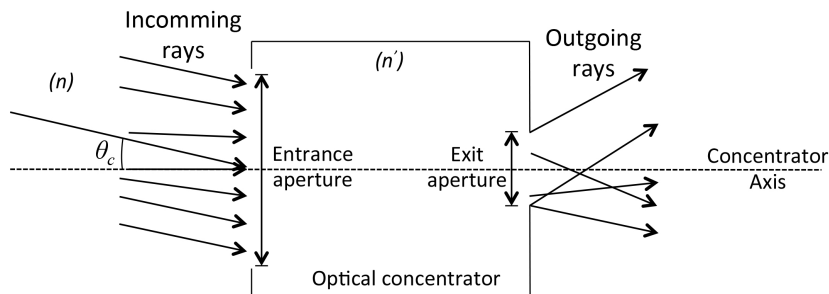


Figure 4.9: Schematic representation of an optical concentrator [8]

is given by the following relation [10]:

$$G = \left( \frac{n' \sin \theta'}{n \sin \theta_c} \right)^2 \quad (4.3)$$

where  $n'$  and  $n$  are the refractive indices of the concentrator, and the environment that surrounds the concentrator, respectively, and  $\theta_c$  and  $\theta'$  are the maximum angle of rays impinging onto the concentrator and outgoing from the concentrator, respectively. As explained by Kahn et al. [11], the photodetector effective detection area for an angle of incidence  $\theta_i$  is given by:

$$A_{\text{eff}} = A \cos \theta_i \quad (4.4)$$

where  $A$  is the photodetector detection area. Taking this relation into account, and according to the study presented in Street et al. [12],  $\sin \theta_c$  is approximately about 0.82 and the actual gain is expressed by  $G = 0.82 \cdot n'^2 / \sin^2 \theta_c$ , with  $n$  is equal to 1 corresponding to the air refractive index, and  $n'$  is the index of the concentrator. Optical concentrators can be classified in two categories: imaging and non-imaging. Imaging concentrators are generally used in fixed systems because the photodiode should be positioned at the focal point. Non-imaging concentrators are preferred to provide mobility of the receiver. In our system, we considered non-imaging concentrators which are adequate for the proposed mobile receiver. Three types of non-imaging concentrators have been listed in the literature and presented by Welford and Winston on their book "High Collection Nonimaging Optics" [7].

**Hemispherical concentrator** [11] The hemispherical concentrator or hemispherical lens is the most commonly used concentrator due to its easy manufacturing and simplicity of use. This type of concentrator is characterised by a wide FOV which

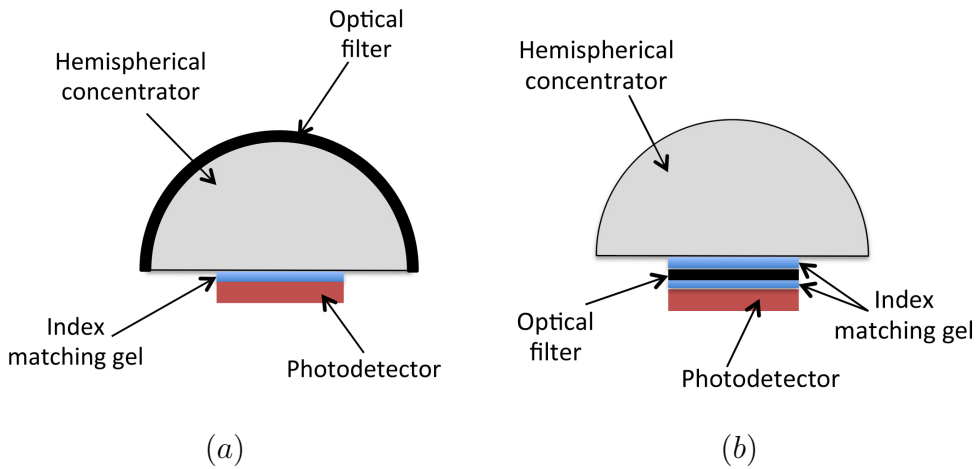


Figure 4.10: Photoreceiver structure based on a hemispherical concentrator



approaches  $90^\circ$  and an omnidirectional gain  $G \approx n^2$  over its entire FOV. These characteristics make this concentrator suitable for diffuse non-directed links. The large FOV of this concentrator makes also the level of received ambient noise very high with the difficulty to place the optical filter before the concentrator as shown in figure 4.10 (a) in contrast of figure 4.10 (b) where the optical filter is placed after the concentrator [13].

**Compound parabolic concentrator** [14] The compound parabolic concentrator (CPC) is a non-imaging concentrator with a higher gain compared to the hemispherical concentrator but with a narrow FOV. The flatness of the entrance and the output aperture give the possibility to position the optical filter at the input or output surface with the advantage to place it before the concentrator which can eliminate the ambient noise before the concentration. Figure 4.11 (a) shows a CPC with an optical filter at its entrance area and a photodiode with an index matching gel between concentrator and photodiode. This concentrator seems to be the sim-

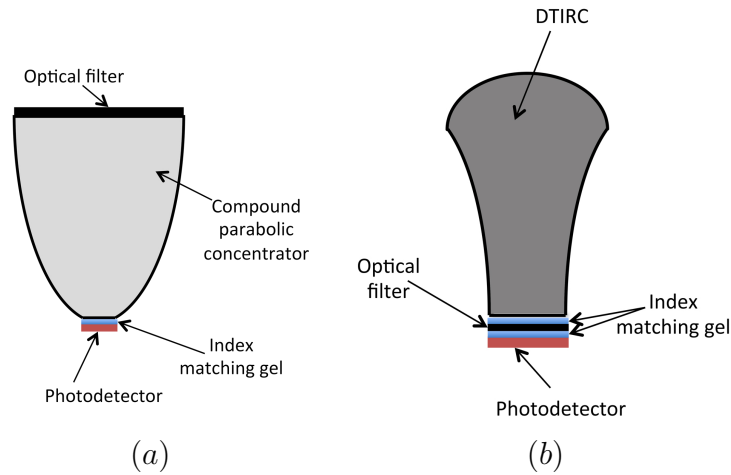


Figure 4.11: (a) Compound parabolic concentrator, (b) Dielectric totally internally reflecting concentrator

plest non-imaging concentrator with a higher gain for our system. To this aim, this concentrator was precisely studied, simulated and some prototypes were designed in our lab for the present application.

**Dielectric totally internally reflecting concentrator** [10] The dielectric totally internally reflecting concentrator (DTIRC) is a type of non-imaging concentrator combining the refractive and reflective properties of a dielectric material to offer a higher gain in comparison to the CPC, with a more compact size. The faces of the DTIRC are curved similarly to the CPC but with a curved entrance area as shown in figure 4.11 (b). This characteristic yields the option to place the optical filter before concentration difficult and expensive. This concentrator is not chosen on our characterization due to the complexity in the fabrication.

### II.2.1 CPC design, fabrication and gain simulation

A compound parabolic concentrator meeting the size requirements of the optical receiver (i.e. detection area  $\simeq 0.2 \text{ mm}^2$ ) was designed via a Matlab program corresponding to the geometrical characterization of the CPC presented in [7]. In this program, the output area of the concentrator corresponding to the photodetector area, the maximum acceptance angle at the concentrator entrance and the refractive index of the material are used as input parameters and the Matlab program calculates the concentrator dimensions (entrance diameter, concentrator length). A computed profile is illustrated in figure 4.12. The second part of the Matlab is de-

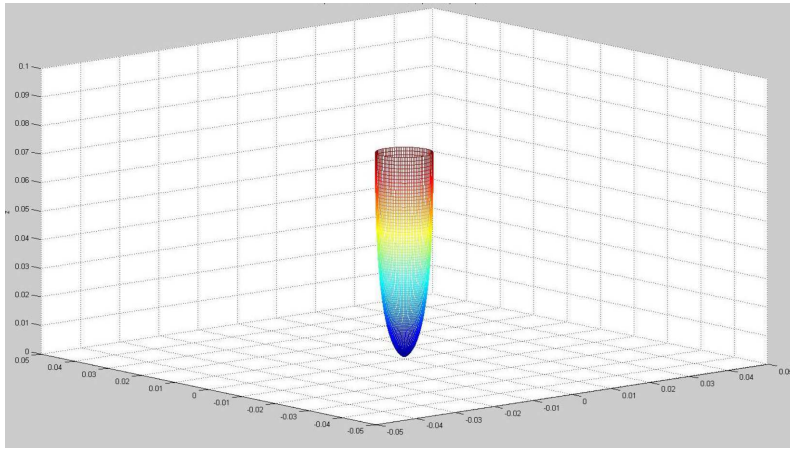


Figure 4.12: Profile of a custom CPC concentrator generated by a Matlab code. The device is 5 mm long, its input area diameter is 7 mm and the theoretical gain is 16 dB (see figure 4.15)

voted to the numerical concentrator gain calculation using the ray tracing method. This is an original method to calculate the concentrator gain with the possibility to modify different geometrical parameters. Figure 4.13 shows the average simulated gain result and its standard deviation for a incident rays number ranging from 400 to 2000 repeated 10 times (10 experiences). The Matlab code is not yet optimized but first simulation results show a good efficiency of the program.

### II.2.2 CPC gain measurement

After designing the CPC profile, several concentrator prototypes were fabricated using the facilities of our microwave department. The used material is a plexiglas type called "Altuglas". The transmission curves of Altuglas for different wavelengths is shown in figure 4.14 [15]. This material was available as a tube of 7 mm of diameter limiting the entrance diameter of the CPC to this length. Two concentrator prototypes respecting this entrance diameter and output diameter of 500 microns were designed and fabricated with a corresponding entrance angle of approximately  $6^\circ$ , which is suited to the free-space link configuration (figure 4.15). Figure 4.16

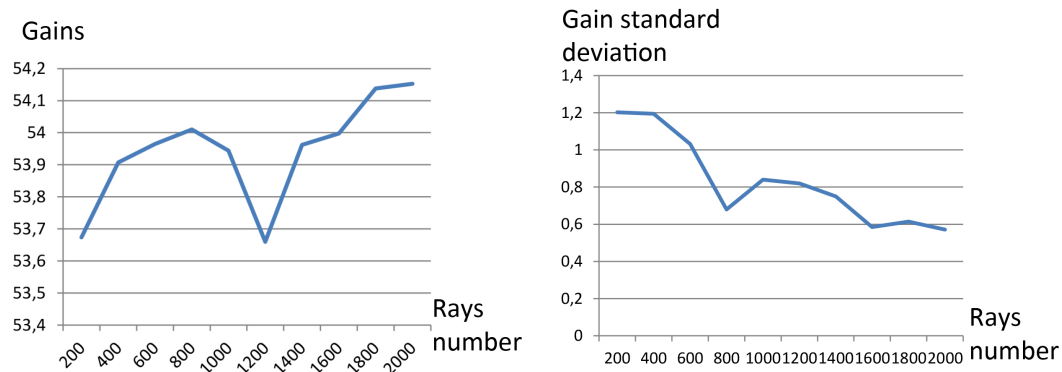


Figure 4.13: Average simulated gain (left) and gain standard deviation (right) as function of rays number for 10 experiences

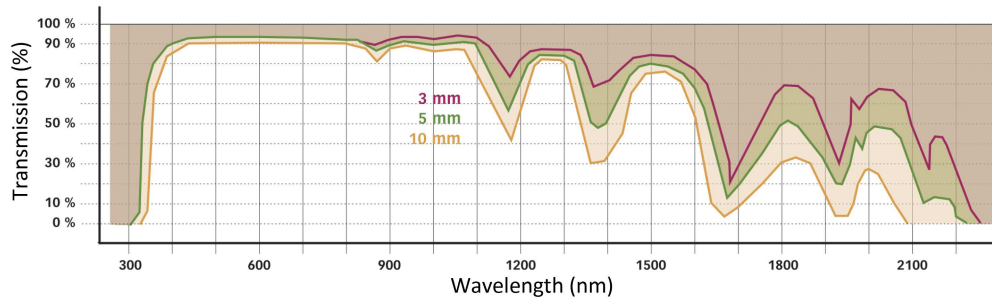


Figure 4.14: Transmission of Altuglas material in function of wavelength



Figure 4.15: Fabricated concentrator prototypes (CPC types)

presents the bench setup used to measure the concentrators gain and the measurement results using a red light laser (633 nm) and infrared laser (1550 nm) are presented in table 4.1. The concentrator gain is measured in an aligned configu-

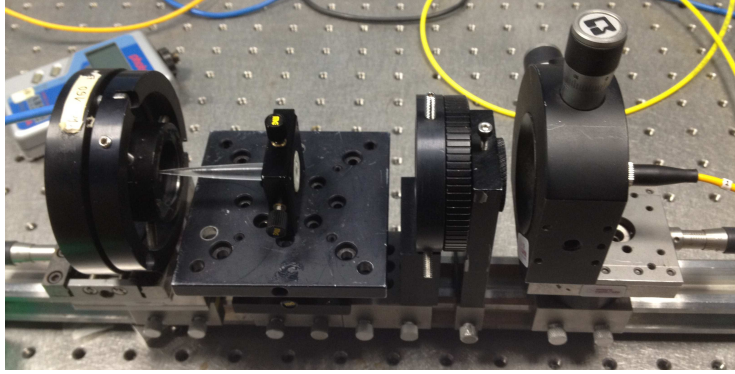


Figure 4.16: Concentrator gain measurement bench setup

Table 4.1: Measured concentrator gain

Prototype	Concentrator position	Visible light (633 nm)	Infrared (1550 nm)
1	Aligned	13.7 dB	11.95 dB
	With deflection ( $\approx 5^\circ$ )	13.5 dB	11.58 dB
2	Aligned	15.5 dB	7.36 dB
	With deflection ( $\approx 5^\circ$ )	14.55 dB	6.74 dB

ration where the entrance concentrator area is perpendicular to the parallel beam. It is also performed with a deflection of the concentrator relatively to the parallel beam at an angle of  $5^\circ$ . The results show a gain lower than that expected (16 dB) and a large gain variation between the two prototypes. This can be explained by the 3D etching fabrication process, where some mechanical vibrations may have caused slight deviations in the CPC profile. The Altuglas material can be replaced by another material with a higher refractive index and/or better transmission coefficient. Finally, the measurement method shown in figure 4.16 can be optimized in terms of positioning between the concentrator and the photodiode. The measurement of the concentrator gain is also performed in the presence of the DOE at the OAP stage. This measurement is crucial in showing the concentrator behavior with the different DOE orders. The concentrator is moved inside the free-space cell generated by the DOE wherein the optical power is measured at each point illustrating the stability of the gain and the received optical power except at the zeroth diffractive order.

## II.3 Pre-amplified photodiode

### II.3.1 Photodiode characteristics

The photodiode is the main element of the mobile receiver. It converts the optical signal at its input into an electrical signal at its output. The photodiode covers a large band of wavelength ranging from 400 to 1600 nm, using different material. Each of these materials shows a higher responsivity at a defined wavelength and

can operate on a defined wavelength range. Table 4.2 summarizes the photodiode materials, the corresponding operating wavelength and the maximum responsivity at its corresponding wavelength.

Table 4.2: Photodiode material and operating wavelength

Material	Operating wavelength (nm)	Responsivity (A/W)
Si	500-900	$\approx 0.6$ @ 850 nm
Ge	900-1300	$\approx 0.5$ @ 1300 nm
GaAs	750-850	$\approx 0.6$ @ 850 nm
InGaAs	1000-1600	$\approx 0.98$ @ 1550 nm

Most high-speed photodiodes have been developed so far for single-mode fiber optics applications, meaning that the collecting aperture is rather small (from 20 to 50  $\mu\text{m}$ ) with specific characteristics as high sensitivity, fast response and low noise. In the present application, the photodiode should exhibit some specific features in order to detect a sufficient signal power, minimum noise and to operate at high speed of several Gbps. These features are:

- High sensitivity at the system wavelength for a given bit error rate ( $10^{-7}$  –  $10^{-9}$ ) to recover the transmitted information at the receiver,
- Large area of detection which, increases the collected power signal and effective detection FOV,
- High electrical response of the photodetector or "responsivity" expressed in A/W,
- Short response time, which is absolutely necessary for high-speed transmission (1 Gbps),
- The receiver should have, other building modules, a low cost (some tens of euros) permitting to a large number of customers to benefit from the system.

The most popular types of photodiodes are the PIN and avalanche photodiode (APD). The PIN photodiode is formed by a PN junction based on two doped region P and N between which a intrinsic region I is introduced. The APD has an additional layer called multiplication layer responsible of the generation of second pairs of electrons when the electrons cross this layer. Whereas the responsivity of a PIN photodiode is lower than 1, the APD responsivity is increased through the current gain by a factor  $M$ , called the avalanche multiplication factor, and the electrical signal is increased by  $M^2$ .

The capacitance of the photodiode (PIN or APD) can be estimated by the equation:

$$C_D = \frac{\epsilon_0 \epsilon_r}{d_r} A_D \quad (4.5)$$

where  $\epsilon_0 = 8.85 \cdot 10^{-12} \text{ Fm}^{-1}$  is the permittivity of free-space,  $\epsilon_r$  the relative permittivity of the semiconductor material,  $d_r$  the thickness of the i-region and  $A_D$  the photodiode area. An increment of the thickness  $d_r$  is desirable to reduce the capacitance but the transit time increases with  $d_r$ , however the rise time increases also but should be limited to ensure the high bit rate transmission.

To be consistent with Gbps transmission using an On-Off Keying modulation, a silicon photodiode will have a  $d_r$  of  $20 \mu\text{m}$ , and the corresponding capacitance per area  $C_D$  is about  $5 \text{ pF/mm}^2$ . For InGaAs photodiodes, an i-region thickness of  $5 \mu\text{m}$  corresponds to a capacitance of  $23.5 \text{ pF/mm}^2$  [16]. Otherwise, as shown in [17], the average InGaAs capacitance is of about  $60 \text{ pF/mm}^2$ , twelve times the value of Si devices. The Germanium on Silicon presents the similar conclusion relatively to Si devices. In the present context, where the  $1550 \text{ nm}$  wavelength is selected to be the system wavelength, InGaAs receiver will suffer from a small detection area (few hundreds of microns diameter) to allow Gbps transmissions. This area will be increased using the optical concentrator described above.

The responsivity photodiode parameter  $r_\lambda$  is given by:

$$r_\lambda = \eta \frac{\lambda}{1.24 \mu\text{m}} A/W \quad (4.6)$$

Where  $\eta$  is the quantum efficiency. The typical responsivity of a silicon PIN photodiode is about  $r_{0.85 \mu\text{m}} \approx 0.5 \text{ A/W}$  while the corresponding value for an InGaAs photodiode is  $r_{1.3 \mu\text{m}} \approx r_{1.55 \mu\text{m}} \approx 1 \text{ A/W}$ , which is twice larger [18]. For APD photodiodes, the responsivity is multiplied by the  $M$  coefficient offering a gain for the system that can be about 10, based on the voltage used on the mobile terminal.

### II.3.2 Preamplifier characteristics

The current generated by the photodiode must be electrically amplified. There are three types of preamplifiers which are the low impedance (generally  $50 \Omega$ ), high impedance, and transimpedance (TIA). Each type presents advantages and disadvantages depending on the aimed application.

Low-impedance is the simplest front-end amplifier. This type of preamplifier introduces a high thermal noise making it not useful for high bit rate optical wireless system. High impedance consists in a high input impedance device with a large detector bias resistor to reduce thermal noise. The simplified scheme of a photodetector with low- and high-impedance amplifier is shown in figure 4.17 (a). The high-impedance amplifier introduces some degradation of the frequency response and then, the resulting bandwidth will be small for high-speed transmission (Gbps). This amplifier type requires an equaliser after the amplifier, but this solution is not attractive due to the introduced noise at higher frequencies. Figure 4.17 (b) shows the simplified scheme of a transimpedance preamplifier. TIA is widely used for current-to-voltage conversion where both a high bandwidth and high sensitivity are required. This front-end structure presents a low noise which reduces the effect of decreasing of bandwidth. With this characteristics, transimpedance amplifier seems

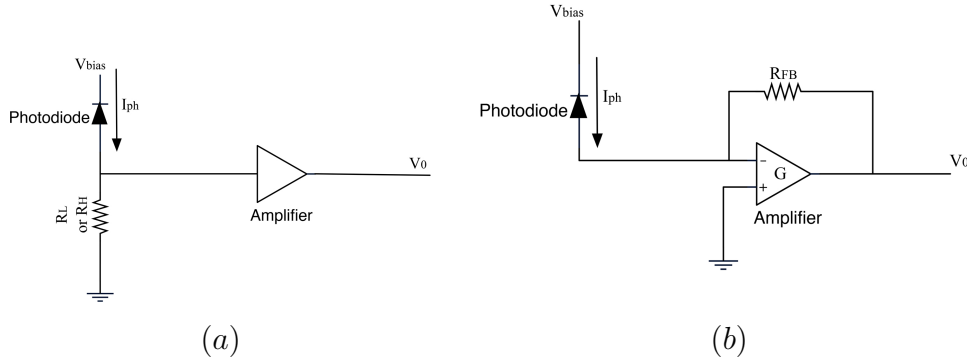


Figure 4.17: Simplified scheme of a photodetector with (a) low-or high-impedance and (b) transimpedance front-end amplifiers

to be the most adapted for the proposed high bit rate optical link. Different noises featuring the preamplifier effects are presented in the next sections.

## II.4 Receiver noises

In this section, we consider the noise created by the receiver and all unwanted disturbances to determine the quality of the transmitted signal. At the optical receiver, this noise can be classified in two fundamental mechanisms, which are the shot noise and the thermal noise. The different sources of noise current as dark noise, ambient light, and thermal noise are presented in the electronic equivalent scheme of figure 4.18. In the next paragraphs, different current noise sources at photoreceiver

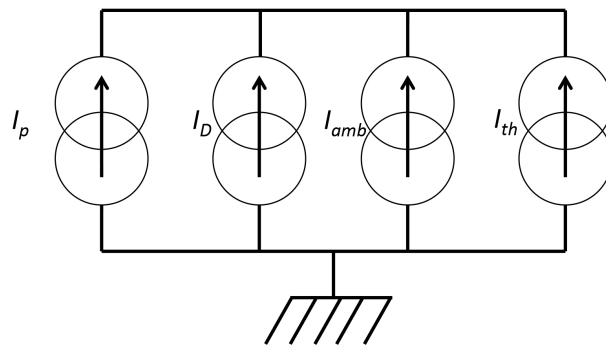


Figure 4.18: Different noise current at photodiode stage

stage are described and numerical values are presented for a commercially PIN-based InGaAs device dedicated to high-speed free-space detection [19]. The device FEMTO HSA-X-S-2G-IN [20] has a bandwidth of 2 GHz and a transimpedance gain of 5000 V/A.

### II.4.1 Different receiver noise types

**Shot noise** Shot noise is a consequence of the generation of the electrons of the photocurrent at random times. Dark current, quantum noise and ambient light noise are shot noise components within the photocurrent.

The dark current noise results from the current that continues to pass through the photodiode in the absence of incident light, independent by from the optical signal. The dark noise current power spectral density is defined by:

$$N_D = 2qI_D \quad (4.7)$$

where  $q = 1.602 \cdot 10^{-19}$  C is the charge of electron,  $I_D$  is the dark current. Using parameters values given before and an  $I_D = 10^{-9}$  A for the Femto photoreceiver, the dark noise spectral density has a value of  $3.2 \cdot 10^{-27}$  A<sup>2</sup>/Hz.

The quantum noise is due to the discrete nature of the photo-detection process and depends on the incident optical power. This noise current power spectral density can be evaluated by:

$$N_q = 2qI_p = 2qr_\lambda P_s \quad (4.8)$$

where  $I_p$  is the photocurrent produced by the diode due to an averaged optical incident power and, then,  $P_s$  is the average detected optical power by the photodiode, which will be equal to the photodiode sensitivity. Based on the Femto responsivity and sensitivity values (see table 4.5), the quantum noise value is about  $1.2 \cdot 10^{-25}$  A<sup>2</sup>/Hz.

In the case of a PIN photodiode, the shot noise has a power spectral density current given by:

$$N_{sn} = 2q(I_D + I_p + I_{amb}) \quad (4.9)$$

where  $I_{amb}$  is the average photocurrent created by the ambient light. This current density of this noise type is calculated in the next section.

The shot noise depending from the photocurrent is not similar for PIN and APD devices. For the latter type, the generated current is amplified, yielding the shot noise equation:

$$N_{sn} = 2q(I_D + I_p + I_{amb})M^2F(M) \quad (4.10)$$

where  $F(M)$  is a function depending on the photoreceiver material, modelling the noise due to the multiplication process.

**Thermal noise** or Johnson noise is a spontaneous fluctuations due to the the thermal interactions between the free electrons and the vibrating ions in a conducting medium. The thermal noise can be calculated by:

$$N_{tn} = 4KT/R_{sh} \quad (4.11)$$

where  $K = 1.38 \cdot 10^{-23}$  J/K is the Boltzman constant,  $T = 300$ K, the ambient temperature and  $R_{sh} = 5 \cdot 10^8$  is the shunt resistance of the receiver. The numerical value of the thermal noise in the presented case is about  $3.3 \cdot 10^{-29}$  A<sup>2</sup>/Hz.



**Preamplifier noise** As shown in section II.3.2, the photocurrent is generally amplified using a preamplifier. This device introduces additional noise at the receiver stage. The power spectral density current corresponding to this noise is given by:

$$N_{preamp} = \frac{P_{preamp}^{in}}{R_L} \quad (4.12)$$

where  $R_L$  is the load resistance and  $P_{preamp}^{in}$  is the equivalent input spectral power density of the preamplifier defined by the relation  $P_{preamp}^{in} = FKT$  (W/Hz) with  $F$  the preamplifier noise figure. For Femto photoreceiver where  $F = 5.1$  and  $R_L = 50 \Omega$ ,  $N_{preamp} = 2.67 \cdot 10^{-22} \text{ A}^2/\text{Hz}$ .

**Preamplifier  $f^2$  noise** Unlike RF detectors, optical detectors suffer from an  $f^2$  noise component. This noise is not visible at low bit rate, but its power density increases with  $f^2$  to present an important contribution at the receiver stage. This noise component can be calculated by [12]:

$$N_{preamp f^2} = \frac{2qI_c(2\pi C_{tot})^2}{S^2} + 4KT(R_{bb} + R_s)(2\pi C_D)^2 \quad (4.13)$$

Where  $I_c$  is the collector current,  $C_{tot} = C_D + C_{EB} + C_{CB}$  is the total receiver capacitance with  $C_{EB} = 1.1 \text{ pF}$  and  $C_{CB} = 0.25 \text{ pF}$  the BJT emitter-base and collector base capacitance,  $R_s + R_{bb} = 10\Omega$  are the series resistances,  $T = 330\text{K}$  is the absolute temperature,  $I_c$  (optimized between 0.5-5 mA) is the collector current and  $S = 1/g_m$  with  $g_m = 35.15$  the conductance. Based on these values calculated for the Femto photoreceiver, the density current of the preamplifier  $f^2$  noise is about  $4 \cdot 10^{-40} \text{ A}^2/\text{Hz}$  [17].

All these noise depends of the bit rate and the noise variance  $\sigma^2$  is given by:

$$\sigma^2 = (N_{sn} + N_{th})I_2R_b + N_{preamp f^2}I_3R_b^3 \quad (4.14)$$

Where  $I_2 = 0.502$  and  $I_3 = 0.0843$  the Personick integrals and  $R_b$  the bit rate in Mbps. For an  $R_b$  of 1000 Mbps, the first part of the noise variance (shot and thermal noise) is about  $6 \cdot 10^{-23} \text{ A}^2$  while the second part (preamplifier  $f^2$  noise) presents a noise variance of  $3.4 \cdot 10^{-32} \text{ A}^2$ . To conclude, at this bit rate, the preamplifier  $f^2$  noise is considered negligible.

## II.4.2 Ambient noise

The natural and artificial sources of ambient light in indoor environment produce a shot noise at the photodiode which is defined by [21]:

$$N_{amb} = 2qI_{amb} = 2qr_\lambda P_{amb} \quad (4.15)$$

Contrarily to the noise created at the receiver stage, the part of the ambient noise which is not eliminated by the optical filter (considering the optical filter at the entrance area of concentrator) passes through the optical concentrator where it

is amplified. Assuming the optical concentrator as non-imaging and ideal with a constant gain within this field-of-view, the received optical background power is given by:

$$P_{amb} = E_{bk} A_d G_{bk} T_0 \Delta\lambda \quad (4.16)$$

where  $E_{bk}$  is irradiance of the background ambient light,  $A_d$  is the photodetector area,  $G_{bk} = n^2$  is the optical gain of the concentrator for the ambient radiation [14],  $T_0$  is the transmittance of the optical band-pass filter  $\lambda_0$ ,  $\Delta\lambda$  is the optical filter bandwidth.

Under all this considerations and irradiance background light at 1550 nm wavelength ( $E_{bk}=0.12$  W/m<sup>2</sup>/nm,  $\Delta\lambda = 10$  nm and  $A_d = 0.2$  mm<sup>2</sup>), the ambient noise is equal to  $N_{amb} = 2.18 \cdot 10^{-29}$  A<sup>2</sup>/Hz.

### II.4.3 Conclusion

The different noise contributions are summarized in table 4.3.

Table 4.3: Different receiver noise and its spectral density

Noise current	Power spectral density (A <sup>2</sup> /Hz)
Ambient light	$2.2 \cdot 10^{-29}$
Dark current	$3.2 \cdot 10^{-27}$
Thermal noise	$3.3 \cdot 10^{-29}$
Quantum noise	$1.2 \cdot 10^{-25}$
Preamplifier noise	$2.6 \cdot 10^{-22}$
Total	$2.6 \cdot 10^{-22}$

This estimation shows that the dominant noise will be generated by the preamplifier and other noises are negligible by several magnitude order differences.

Based on this result, the signal-to-noise ratio will be estimated to quantify the performance of the NLOS link.

## III NLOS free-space link performance

The performance of the free-space link is evaluated in terms of the received signal-to-noise ratio for the modulated transmitted signal, which will define the limits of the free-space transmission in terms of the maximum bit rate, link distance, and covered area.

### III.1 Modulation scheme

The choice of the modulation scheme has a direct impact on the design of the proposed optical wireless system. It affects such important parameters as bandwidth and power efficiency.

### III.1.1 Transmission techniques

**Modulation** Such analog modulations as amplitude modulation (AM) and frequency modulation (FM) were used in the past for optical wireless communications. FM is theoretically better due to the additive noise brought by amplitude modulation [22].

In digital transmission, an analog carrier is modulated by a discrete signal. The fundamental digital modulations are based on keying with a finite number of states. All these states define the alphabet of the modulation. If the alphabet consists of  $M_m=2^n$  alternative symbols, each symbol represents a message consisting of  $n$  bit per second (bps). If the symbol rate is  $f_s = 1/T$  symbol per second (sps), the bit rate is  $nf_s$  bps.

The most fundamental linear digital modulation techniques are the amplitude shift keying ( $M_m$ -ASK), the phase shift keying ( $M_m$ -PSK) and the quadrature modulation ( $M_m$ -QAM), for which the information is respectively provided by the amplitude, phase, and both amplitude and phase. Light intensity is actually a positive value and then, when  $M_m=2$ , 2-ASK modulation is equivalent to a switch and is referred to as On-Off keying (OOK). The frequency shift keying modulation ( $M_m$ -FSK) is not a linear modulation and therefore more difficult to use.

Coded modulation by the position, the amplitude or the duration of the pulse with  $M_m$  states are respectively denoted as pulse position modulation ( $M_m$ -PPM), pulse amplitude modulation ( $M_m$ -PAM) and pulse duration modulation ( $M_m$ -PDM). They have been used in many applications. In this technique, each set of  $n$  bits is associated with the position, amplitude or duration of the pulse.

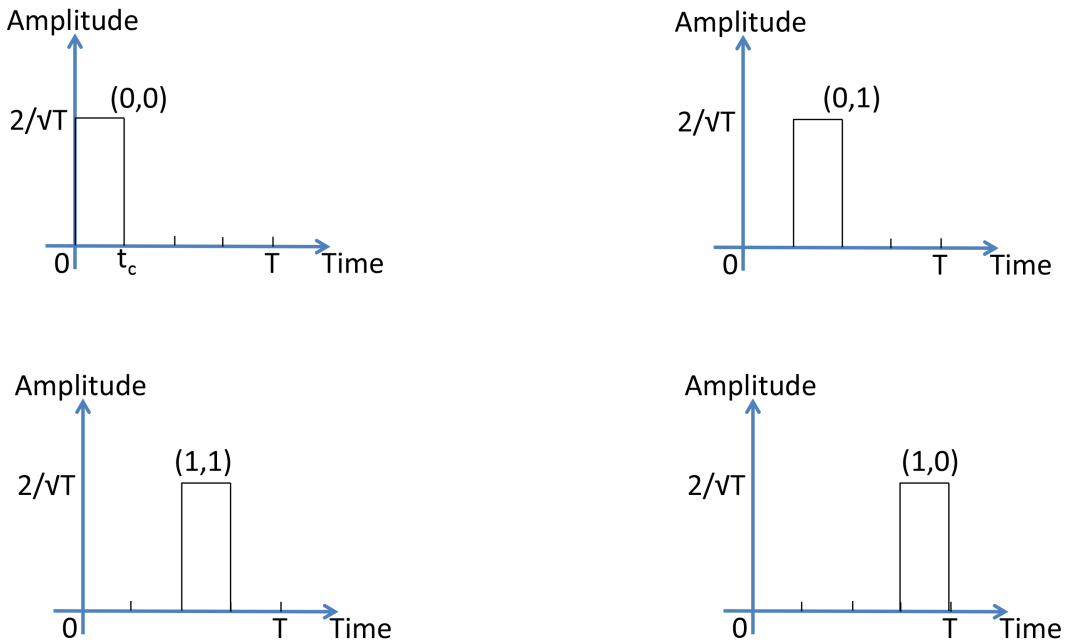


Figure 4.19: 4-PPM modulation

Figure 4.19 shows an example of 4-PPM modulation alphabet which is adopted in the IrDA standard for communications at short distance and a bit rate of 4 Mbps. The symbol duration is decided in 4 segments or chips ( $M_m=4$ ). The light intensity is present only during the corresponding chip to a define couple of bits.

**IM/DD transmission model scheme** To date, circuits that use phase processing are still difficult to conceive and are considered as expensive for applications covered by this study. Therefore, we do not consider the case of the coherent detection at the receiver stage, but we remain in the conventional transmission scheme where the optical intensity carries information on the transmitter and a photodiode converts the optical power collected at its detection area into electrical intensity. This transmission model is called IM/DD and presented in figure 4.20.

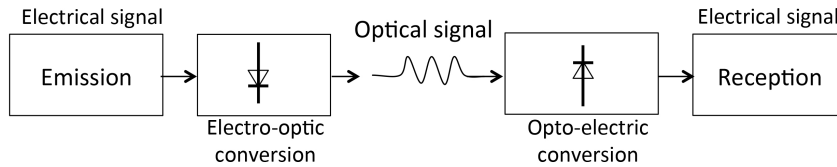


Figure 4.20: IM/DD transmission scheme

**Waveform** The single carrier (SC) transmission where symbols are transmitted in series is the preferred optical transmission technology to date. However, the bit rates become higher than the bandwidth of wireless optical channel and available opto-electronic circuits. Therefore, it becomes interesting to consider the multi carrier (MC) waveforms adopted in wireless radio standards. In MC transmission,

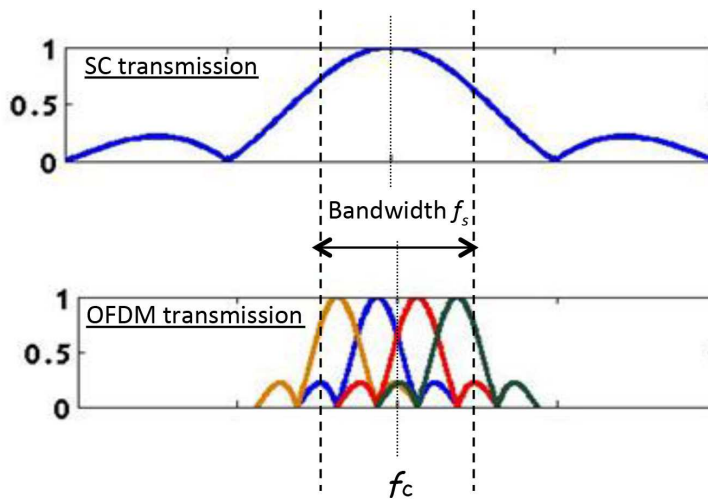


Figure 4.21: Comparison of spectra of SC and OFDM waveforms

information symbols are spread in the frequency domain on multiple subcarriers. The frequency of the subcarriers are the closest possible, thereby minimizing the useful frequency band, and the subcarriers are taken orthogonally to each other. The transmission is called OFDM for orthogonal frequency division multiplexing. Each of the subcarriers is modulated by one of the modulation schemes described previously. The symbol rate per subcarrier is  $f_s^{OFDM} = f_s/L$  where  $L$  is the number of subcarriers [23]. A comparison between the spectrum of each technique (SC and OFDM) is shown in figure 4.21 for  $L = 4$ . Assuming a suitable choice of the sampling frequency of the digital-analog converter in figure 4.22, the modulation is implemented through a baseband inverse fast Fourier transform ( $FFT^{-1}$ ).

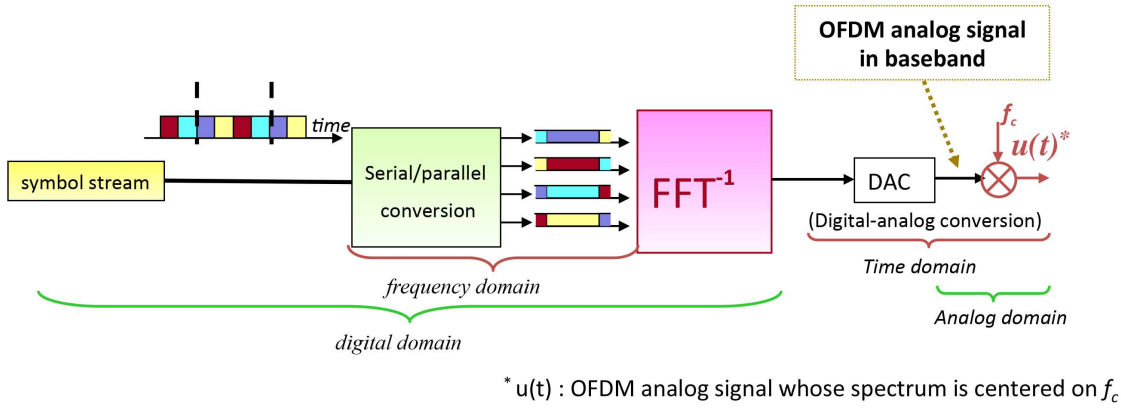


Figure 4.22: OFDM transmitter scheme

**Conclusion** SC transmission appears to be the easiest transmission scheme in the context of the present optical wireless links, with possible design of a demonstrator showing the feasibility of the proposed topology. Moreover, as we work with LOS/NLOS links, the bandwidth aimed is compatible with the target bit rate for a classical SC transmission.  $M_m$ -PPM and OOK modulations are suitable for IM/DD transmissions. However, the normalized bandwidth requirement is 1 for OOK-NRZ modulation and  $M_m/\log_2 M_m$  for  $M_m$ -PPM modulation [8]. We choose the OOK-NRZ modulation that has a better spectral efficiency. This modulation type is modelled in the next paragraph.

### III.1.2 On-Off Keying modulation

On-Off Keying is the preferred and most common modulation scheme in optical wireless communications due to its robustness and simplicity of implementation. The bit rate and the symbol rate are the same ( $n = 1$ ). A modulated data using this modulation can be represented by return-to-zero (RZ) or non-return-to-zero (NRZ) pulses as shown in figure 4.23. The OOK-RZ bandwidth normalized to the OOK-NRZ scheme is  $1/\gamma$  where  $\gamma$  the duty cycle as shown in figure 4.23 (a). It is

then better to use OOK-NRZ over the useful frequency band.

The OOK-NRZ symbols  $a_k$  take a value between two binary levels  $\{0, A\}$ . The pulse is transmitted when a  $A$  is sent while no pulse is transmitted for a 0 [24]. We assume that the symbols are independent, identically distributed i.e.:

$$\Pr\{a_n = 0\} = \Pr\{a_n = A\} = 1/2 \quad (4.17)$$

Figure 4.24 shows the model of a baseband transmission channel with an optimal

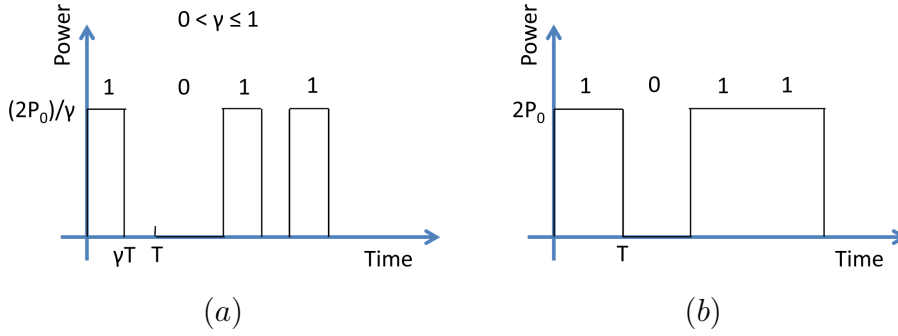


Figure 4.23: (a) OOK-RZ modulation and (b) OOK-NRZ modulation codes

receiver with respect to the minimization of the error probability. The transmitted

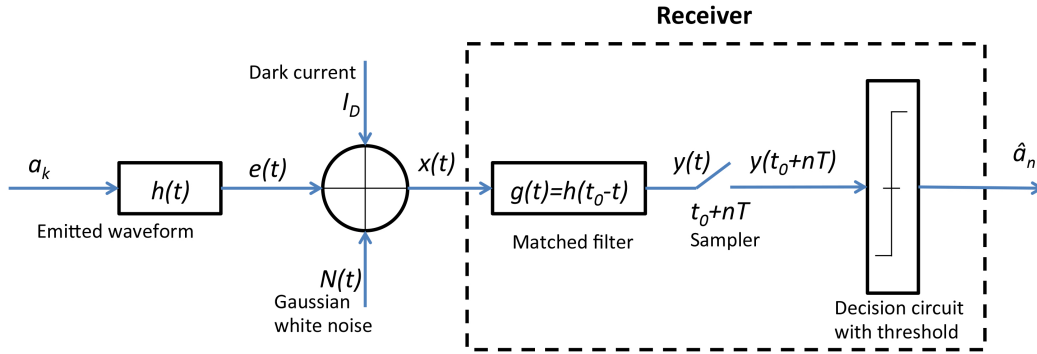


Figure 4.24: Model of baseband transmission

signal  $e(t)$  with a symbol rate of  $f_s = 1/T$  can be written as:

$$e(t) = \sum_{k=-\infty}^{+\infty} a_k h(t - KT) \quad (4.18)$$

where  $h(t)$  is a gate function of amplitude  $1/\sqrt{T}$  and period  $T$ . In this model, the channel effect is reduced to the addition of a gaussian white noise  $N(t)$  and dark current  $I_D$ . The receiver is formed by a filter  $g(t)$  matched to the received signal waveform  $h(t)$  at the initial sampling time  $t_0$ , a sampler at symbol time and

a decision circuit with threshold  $S$ .

The signal  $y(t)$  at the output of the matched filter is given by the equation:

$$y(t) = \sum_{k=-\infty}^{+\infty} a_k r(t - KT) + w(t) \quad (4.19)$$

where  $r(t) = (h \otimes g)(t)$  and  $w(t) = (n \otimes g)(t)$  ( $\otimes$  is the convolution operation)

At the sampler output, we have:

$$y(t_0 + nT) = \sum_k a_{n-k} r(t_0 + kT) + w(t_0 + nT) \quad (4.20)$$

Assuming perfect time synchronization and considering the absence of inter-symbol interference (ISI) which gives  $r(t_0 + kT) = 0 \forall k \neq 0$ , its yields:

$$y(t_0 + nT) = a_n + I_D \sqrt{T} + w(t_0 + nT) \quad (4.21)$$

We suppose that the noise samples  $w(t_0 + nT)$  are Gaussian, centred, with a variance  $\sigma_0^2$  ( $\sigma_A^2$ ) respectively for a received symbol 0 ( $A$ ), as shown in figure 4.25.

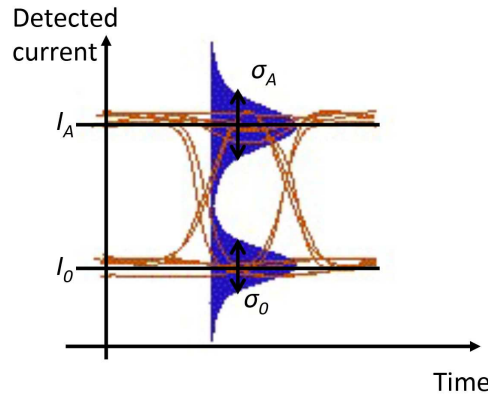


Figure 4.25: Eye diagram with conditional probability density associated with the "0" and "A" current distributions,  $I_0$  and  $I_A$  are the average values,  $\sigma_0^2$  and  $\sigma_A^2$  are the variances

At the thresholding circuit, the decision of the symbol value will be taken in the following manner:

$$\begin{aligned} \hat{a} &= A \quad \text{if} \quad y(t_0 + nT) \geq S \\ \hat{a} &= 0 \quad \text{if} \quad y(t_0 + nT) < S \end{aligned}$$

In this case, the symbol error probability is defined by:

$$P_e = \frac{1}{2} \Pr\{w(t_0 + nT) < S - I_A\} + \frac{1}{2} \Pr\{w(t_0 + nT) > S - I_0\} \quad (4.22)$$

where  $I_A = A + I_D$  and  $I_0 = I_D$

Then, using the conditional probability density functions of the noise levels:

$$P_e = \frac{1}{2\sqrt{2\pi}\sigma} \int_{(S-I_0)/\sigma_0\sqrt{2}}^{+\infty} \exp\{-z^2\} dz + \frac{1}{2\sqrt{2\pi}\sigma} \int_{-\infty}^{(S-I_A)/\sigma_A\sqrt{2}} \exp\{-z^2\} dz \quad (4.23)$$

Using the "erfc" function defined by  $\text{erfc}(x) = 2\sqrt{\pi} \int_x^{+\infty} \exp(-u^2) du$ , we obtain

$$P_e = \frac{1}{4} \text{erfc} \left( \frac{S - I_0}{\sqrt{2}\sigma_0} \right) + \frac{1}{4} \text{erfc} \left( \frac{I_A - S}{\sqrt{2}\sigma_0} \right) \quad (4.24)$$

The optimal threshold expression is reached when the two terms of the right hand side of 4.24 are equal, yielding  $S = \frac{I_1\sigma_0 + I_0\sigma_A}{\sigma_0 + \sigma_A}$  and in this case, the error probability becomes :

$$P_e = \frac{1}{2} \text{erfc} \left( \frac{I_1 - I_0}{\sqrt{2}(\sigma_0 + \sigma_A)} \right) \quad (4.25)$$

We note that the error probability can also be defined according to the quality factor  $Q$ , whose expression is given by:

$$Q = \frac{I_A - I_0}{\sqrt{2}(\sigma_0 + \sigma_A)} \quad (4.26)$$

Considering the assumptions  $\sigma_0^2 = \sigma_A^2 = \sigma^2$  and an ideal additive white gaussian noise (AWGN)  $I_D = 0$ , the expression of the error probability can finally be written by:

$$P_e = \frac{1}{2} \text{erfc} \left( \frac{A}{2\sqrt{2}\sigma} \right) \quad (4.27)$$

### III.2 Signal-to-noise ratio and receiver sensitivity

The signal-to-noise ratio SNR at the input of receiver can be defined as a function of the maximum value or the mean value and the mean power of the noise current considered at the input of the receiver. At the photodiode stage and with the assumption of two symbols with the same probability, we have  $I_{pp} = rP_{pp} = 2rP_s$  where  $r$  is the photodiode responsivity and  $P_{pp}$  and  $P_s$  are respectively the peak-to-peak and averaged optical power detected by the photodiode. We also have  $I_{pp} = A$  and  $I_{av} = A/2$ .

The SNR can be defined in two different ways:

$$\text{SNR}_{pp} = \frac{I_{pp}^2}{i_{tot}^2} = \frac{A^2}{i_{tot}^2} = \frac{A^2}{\sigma^2} \quad (4.28)$$

where  $i_{tot}$  is the total input-referred noise current. Otherwise, in the case of average value, the SNR is expressed by:

$$\text{SNR}_{av} = \frac{I_{av}^2}{i_{tot}^2} = \frac{A^2}{2i_{tot}^2} = \frac{A^2}{2\sigma^2} \quad (4.29)$$



With the SNR definitions of equations 4.28, 4.29 and the expression given by relation 4.27, the symbol error probability can be defined as a function of the SNR in a twofold manner:

$$P_e = \frac{1}{2} \operatorname{erfc} \left( \sqrt{\frac{\operatorname{SNR}_{\text{pp}}}{8}} \right) \quad (4.30)$$

$$P_e = \frac{1}{2} \operatorname{erfc} \left( \sqrt{\frac{\operatorname{SNR}_{\text{av}}}{2}} \right) \quad (4.31)$$

These two relations are presented graphically in figure 4.26 as reference curves. The symbol error rate can be considered as an approximation of the error probability when the observation time tends to the infinity. Subsequently, the  $P_e$  will be treated as bit error rate BER, term rather used with OOK-NRZ modulation in the optical domain ( $P_e \simeq \text{BER} = \text{SER}$ ).

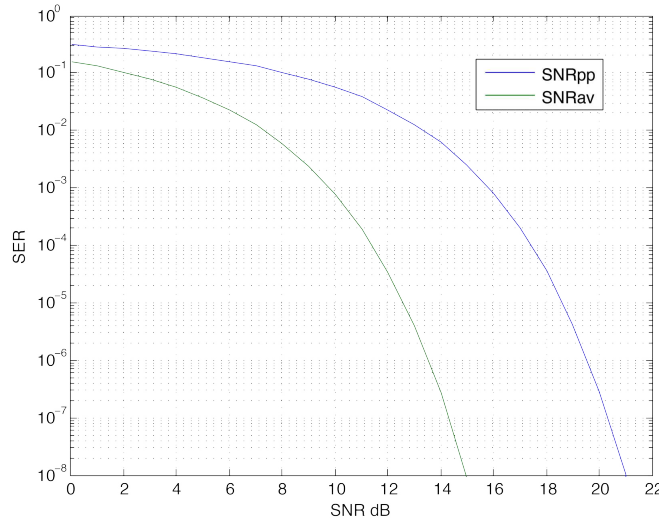


Figure 4.26: SER (i.e. BER) performances of OOK-NRZ modulation over the AWGN channel

Using the free-space link scheme depicted in figure 4.26, the average optical power collected by the detector can be expressed by:

$$P_s = E_s G \bar{T} A_d \quad (4.32)$$

where  $E_s$  is the irradiance ( $\text{W}/\text{m}^2$ ) of the optical signal impinging at the concentrator input,  $G = \eta_c n^2 / \sin^2 \theta_c$  is the concentrator gain for this particular signal,  $\bar{T}$  is the average optical filter transmission of the signal and  $A_d$  is the photodetector area. For the present NLOS link,  $\bar{T} \simeq 1$ . If  $P_0$  is the optical power emitted at the optical emitter (OAP) and  $d$  is the distance between the OAP and the photoreceiver (figure 4.27), then the average received irradiance is  $E_s = P_0 / A_c$ , yielding, using the small angle approximation ( $\tan \alpha \simeq \alpha$ ), the expression for the received optical power:

$$P_s = \frac{\eta_c P_0 n^2 A_d}{\pi (\alpha d \sin \theta_c)^2} \quad (4.33)$$

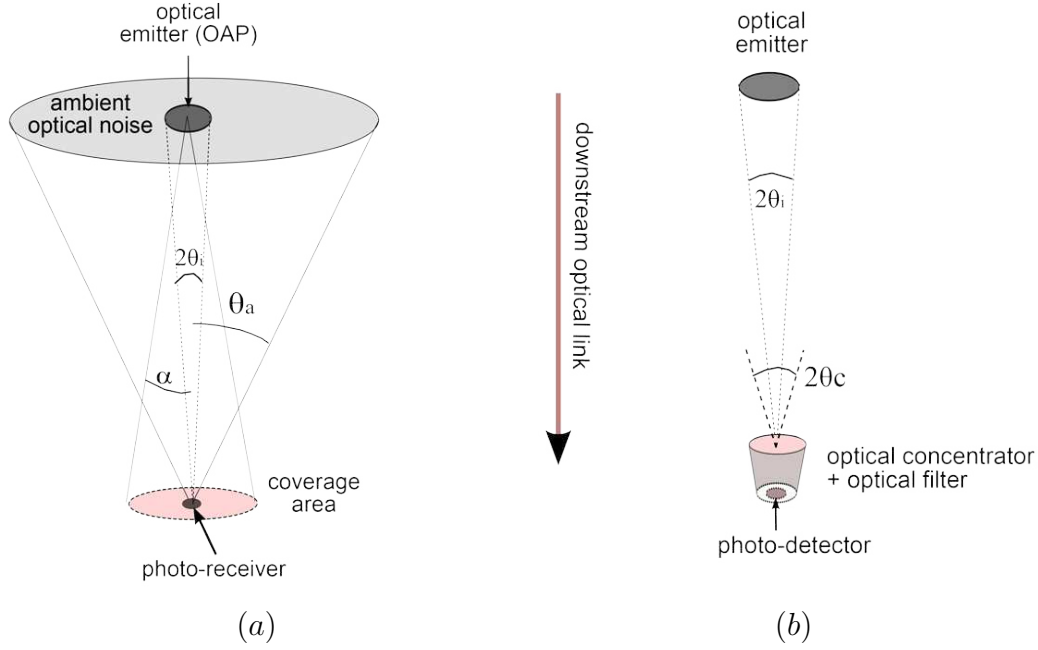


Figure 4.27: Free-space link geometry. Both the coverage area and the detector surface area supposed to be circular, with areas  $A_c$  and  $A_d$ , respectively

The  $\text{SNR}_{pp}$  of the electrical signal provided by the photodiode in the direct modulation scheme can then be estimated by:

$$\text{SNR}_{pp} = \frac{I_{pp}^2}{i_{tot}^2} = \frac{(2r_\lambda P_s)^2}{i_{tot}^2} \quad (4.34)$$

Considering the preamplifier noise is the main noise (section II.4.3), the  $i_{tot}$  value

Table 4.4: Receiver sensitivities in dBm

$B_e$ $NEP$ $\sigma^2$	HSA-X-S-2G-IN Femto 2 GHz $13.4 \text{ pW}/\sqrt{Hz}$ $3.6 \cdot 10^{-13} A^2$	HCA-400 Femto 400 MHz $19.2 \text{ pW}/\sqrt{Hz}$ $1.5 \cdot 10^{-13} A^2$	PDA 10 CF-EC Thorlabs 150 MHz $12 \text{ pW}/\sqrt{Hz}$ $1.9 \cdot 10^{-14} A^2$	"dream" sensor 1 GHz $6 \text{ pW}/\sqrt{Hz}$ $3.6 \cdot 10^{-14} A^2$
$SER = 10^{-3}$ ( $\text{SNR}_{pp}=16\text{dB}$ )	-26	-28.9	-33.4	-32
$SER = 10^{-6}$ ( $\text{SNR}_{pp}=19.4\text{dB}$ )	-25.3	-27.3	-31.7.	-30.4
$SER = 10^{-9}$ ( $\text{SNR}_{pp}=21.5\text{dB}$ )	-24.3	-26.2	-30.6.	-29.3

can be calculated by the relation  $i_{tot} = r_\lambda \cdot NEP \sqrt{B_e}$ , where  $NEP$  is defined as the

noise equivalent power spectral density, and  $B_e$  the receiver bandwidth. The  $NEP$  corresponds to the optical power which is equal to input equivalent noise power of the photoreceiver over one hertz output bandwidth. This parameter is usually given by manufacturers as a value that can permit to calculate the noise current generated by the photodetector. The  $NEP$  value of the considered photodetector (Femto HSA-X-S-2G-IN model [20]) is  $13 \text{ pW}/\sqrt{\text{Hz}}$ , yielding  $i_{tot} = 5.2 \cdot 10^{-7} \text{ A}$  with  $r_\lambda = 0.9 \text{ A/W}$  and  $B_e = 2 \text{ GHz}$ . Using equations 4.33 and 4.34, the corresponding output  $SNR_{pp}$  is 16 dB.

The photoreceiver sensitivity  $P_{sens}$  is the minimum input optical power yielding a given SNR (or SER). Its value can be estimated in the present case by  $P_{sens} = i_{tot} \sqrt{SNR_{pp}} / 2r_\lambda$ , leading to  $P_{sens} = -26 \text{ dBm}$  for  $SNR_{pp}$  of 16 dB (or SER  $\approx 10^{-3}$ ). The sensitivities for different commercial photoreceivers and an matched photoreceiver called "dream" sensor are shown in table 4.4. Table 4.5 summarizes the system parameters in the present NLOS downlink using the Femto [20] 2 GHz photoreceiver.

Table 4.5: Free-space link parameters

Parameter	Symbol	Value
Photodiode responsivity (PIN)	$r_\lambda$	0.9 A/W
Emitted power (at the Tx)	$P_0$	10 mW
Concentrator refractive index	$n'$	1.48
Detector surface	$A_d$	$\pi(0.25 \text{ mm})^2$
Ambient background spectral irradiance (1550 nm)	$E_{bk}$	$0.012 \text{ W/m}^2/\text{nm}$
Emitter-receiver distance	$d$	2.5 m
Divergence angle	$\alpha$	$2^\circ$
Concentrator field of view	$\theta_c$	$10^\circ$
Optical band-pass filter bandwidth	$\Delta\lambda$	10 nm
Photodiode electrical bandwidth	$B_e$	2 GHz
Optical filter transmission	$T$	1

### III.3 Dimensioning of the NLOS link

Using equations 4.30, 4.33 and 4.34, The dimensioning of NLOS free-space link is performed by fixing some parameters on these equations and evaluating the evolution of system or component parameters as a function of other system or component parameters in order to optimise this link. In this study, the concentrator gain is fixed at 16 dB and other useful values for the calculations are given in tables 4.4 and 4.5.

A suitable formatting of equation 4.30, 4.33 and 4.34 will allow to highlight the parameters studied for the NLOS free-space link.

**Distance** The distance can be expressed by:

$$d = \sqrt{\frac{r_\lambda A_d G}{\sqrt{2}\pi\alpha^2}} \sqrt{\frac{P_0}{\sigma \operatorname{erfc}^{-1}(2\operatorname{BER})}} \quad (4.35)$$

The variation of the acceptable link distance as a function of the emitted power  $P_0$  for different noise variances at the preamplifier input is presented in figure 6.5. The present noise variance values are the values of commercialized photodetectors

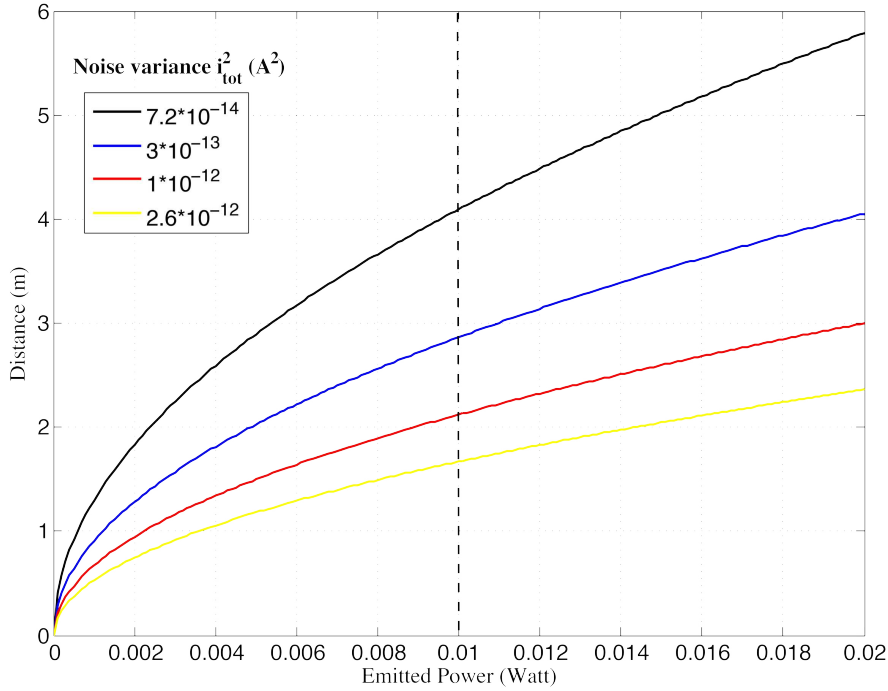


Figure 4.28: Distance in function of emitted power for different noise variance

suitable to our system having different characteristics such as detection area, bandwidth or packaging. The BER is fixed at  $10^{-7}$  and the emitted power varies from 0 to 20 mW. In this figure, we can see a free-space cell transmission exceeding 2 m based on a commercialized photodetectors with an optical power limited to 10 mW (10 dBm).

This free-space distance can be also expressed in function of the photoreceiver bandwidth  $\Delta f$  by:

$$d = \sqrt{\frac{A_d G}{\sqrt{2}\pi\alpha^2}} \sqrt{\frac{P_0}{NEP \sqrt{\Delta f} \operatorname{erfc}^{-1}(2\operatorname{BER})}} \quad (4.36)$$

The variation of the free-space link as a function of the emitted power for photodetector bandwidths ranging from 1 GHz to 3 GHz is shown in figure 6.6. We conclude from this figure that for a BER of  $10^{-7}$ , a 1 Gbps free-space cell can be successfully transmitted at a distance exceeding 2.5 m.

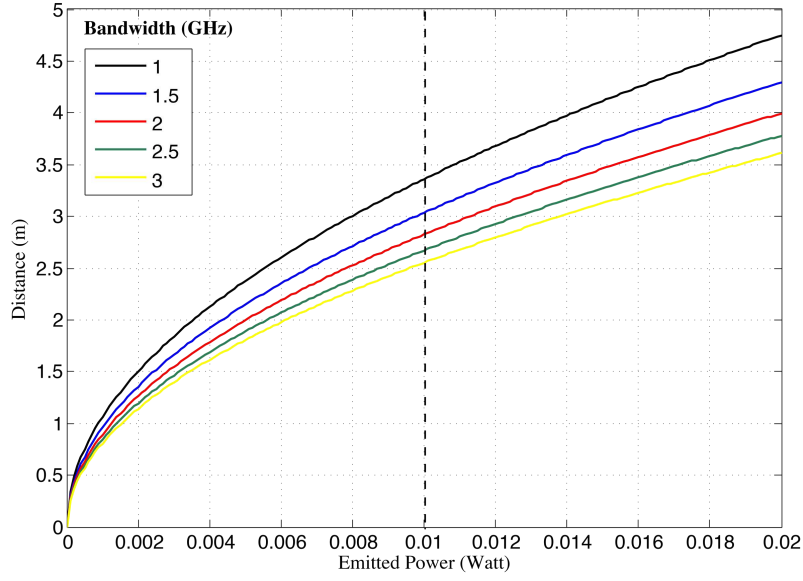


Figure 4.29: Distance as a function of the emitted power for different photodetector bandwidth

**Beam divergence** The free-space link distance can be fixed at 2 m and the divergence angle  $\alpha$  can be expressed as a function of the emitted power and other system parameters, as shown in equation 4.37.

$$\alpha = \sqrt{\frac{r_\lambda A_d G}{\sqrt{2\pi} d^2}} \sqrt{\frac{P_0}{\sigma \text{erfc}^{-1}(2\text{BER})}} \quad (4.37)$$

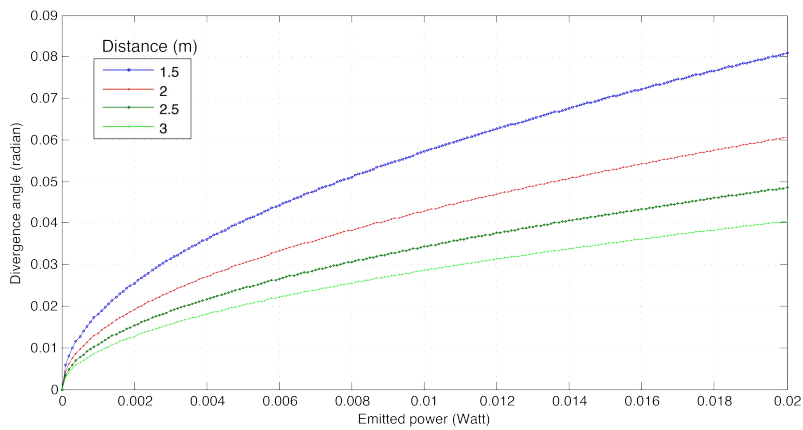


Figure 4.30: Divergence angle as a function of the emitted power

This relation permits us to study the divergence angle limit and therefore the covered area. Based on this equation, the divergence angle is evaluated as a function of the

emitted power for different link distances and the corresponding curves are presented in figure 4.30.

**Photodiode area** The photodiode area can be expressed by:

$$A_d = \frac{\alpha^2 \sqrt{2\pi} d^2 \sigma}{r_\lambda G P_0} \operatorname{erfc}^{-1}(2\operatorname{BER}) \quad (4.38)$$

The detector area is evaluated as a function of the emitted power for a free-space link distance ranging from 1.5 to 3 m, with a noise variance of  $3.6 \cdot 10^{-13} A^2$ . This variation is presented in the figure 4.31 for a BER of  $10^{-7}$ .

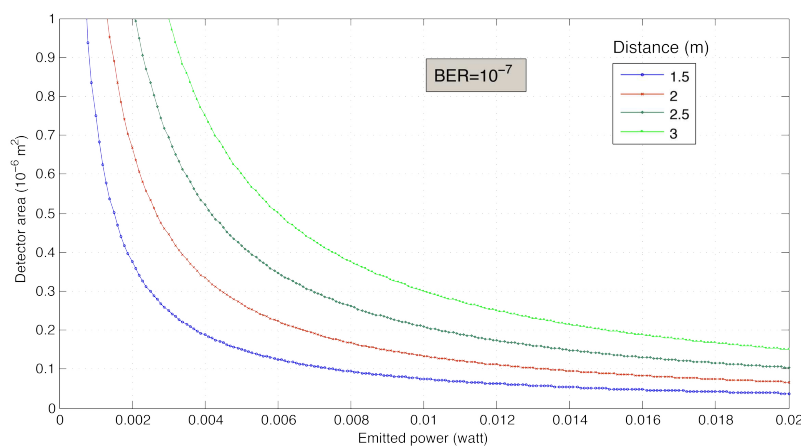


Figure 4.31: Detector area as a function of the emitted power for different free-space link distance

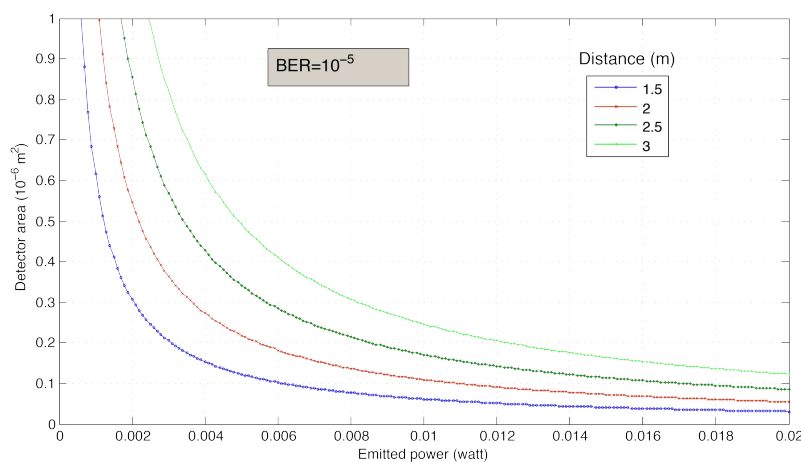


Figure 4.32: Detector area as a function of emitted power for different free-space distance link

Figure 4.32 presents the BER as a function of the emitted power in the same conditions than figure 4.31 but for a BER of  $10^{-5}$ . We can see clearly that the transmission can be performed using a receiver with smaller detection area. This increasing of error number means that the received signal contains more error, while some signal processing can be used to extract the transmitted information at this BER (error-correcting code (ECC)).

**Conclusion** This dimensioning validates the feasibility of the free-space link with the previous proposed parameters (distance 2.5 m, divergence  $2^\circ$  (0.035 rd), photodetector area  $0.2 \cdot 10^{-6} \text{m}^2$ , 2 GHz bandwidth). This dimensioning gives also the possibility to dimension the free-space cell in any other situation where some characteristics or parameters are fixed.

## IV Software modelling and simulation of the free-space link

The NLOS free-space link is modelled using the VPI<sup>TM</sup> [25] software which provides the optical transmitter and receiver and Matlab co-simulation routines, which are generated to represent both free-space propagation and the optical concentration stages. Free-space propagation is modelled as an attenuation depending on the di-

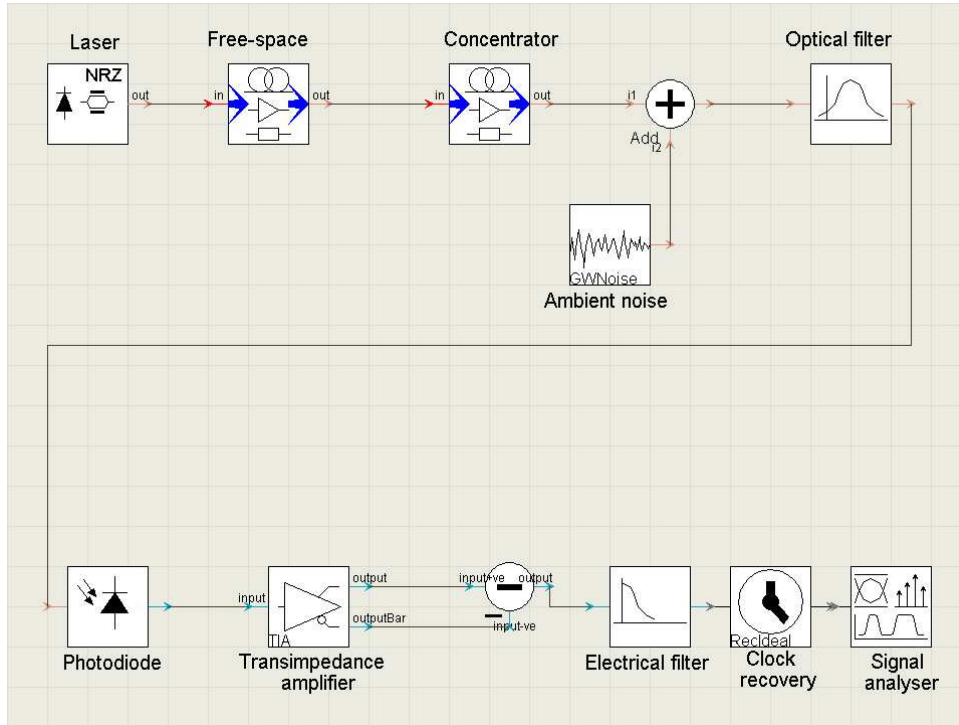


Figure 4.33: Scheme of the VPI simulation of the NLOS free-space link

vergence angle at the output of the fiber, the free-space distance which define the

covered zone and the photodetector area. The ambient light noises is also included in the free-space module using the noise source of VPI<sup>TM</sup> library for which we attribute the calculated noise density of ambient light. The optical concentrator is also modelled from the same manner and it is introduced, such as optical gain calculated on Matlab depending on the concentrator type and its parameters such as the outgoing aperture, the maximum entrance angle and the refractive index of the concentrator material. All values are introduced as parameters and can be modified easily through the VPI<sup>TM</sup> file.

The laser used here is an externally modulated laser, which consists of a pseudo random binary sequence (PRBS) generator, a Mach-Zender modulator, a NRZ encoder and a rise time adjustment from the VPI<sup>TM</sup> library. This different modules give the possibility to change different optical signal parameters. The directly modulation using an FP laser is not considered here.

The photoreceiver used is composed of a PIN photodiode, a transimpedance amplifier (TIA) with a 5000 V/A transimpedance, an input equivalent noise of  $5.8 \cdot 10^{-7}$  A and a 4<sup>th</sup>-order Bessel bandpass electrical filter in the [10KHz - 2GHz] range. A clock recovery is used after the filter to ensure the synchronisation of the system. Figure 4.33 shows the block diagram of the simulated free-space NLOS link.

The system is simulated at 2.5 Gbps using an OOK-NRZ modulation at the trans-

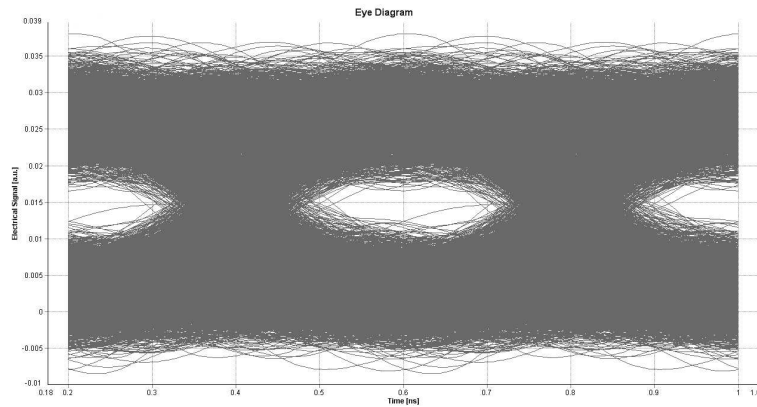


Figure 4.34: Simulated eye-diagram at the receiver stage of the optical free-space link transmission using a PIN-based photoreceiver (2.5 Gbps OOK-NRZ modulation)

mitting stage generated by a DFB laser with an averaged optical power of 10 mW. The simulation is performed on 8192 bits with a sample rate of 160 GHz. The detected output eye diagrams are shown in figure 4.34 (4.35) after the transmission in free-space cell using a PIN (APD) photodiode. In the first case, the estimated BER is about  $10^{-6}$  which can be sufficient to validate the free-space transmission, while, the use of an APD ensures an error-free transmission.

The assumption of the standard deviation value ( $\sigma$ ) was checked for the PIN but not for APD. It should also be calculated for the APD taking the avalanche coefficient into account.



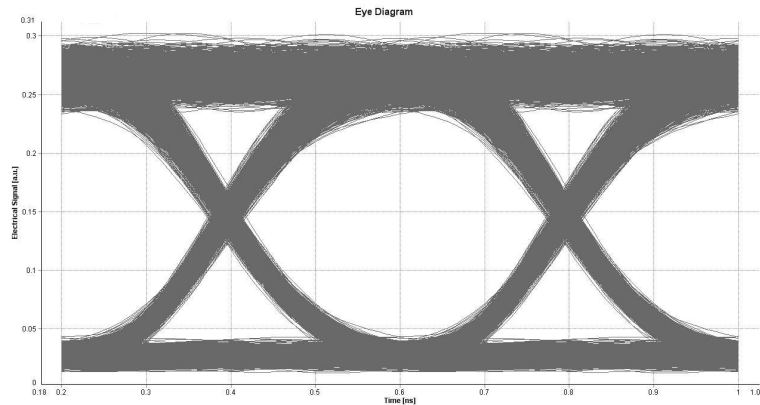


Figure 4.35: Simulated eye-diagram at the receiver stage of the free-space link using a APD-based photoreceiver (2.5 Gbps OOK-NRZ modulation)

## V Conclusion

The free-space link is the most complicated part of the high bit rate optical wireless indoor system. Its study is not limited to the signal free-space propagation, but it spreads inevitably to the optical access point and the receiver characterization. These two systems parts were described and investigated in this chapter and the required components of each of them are presented. The characterization enables us to define an innovative free-space cell based on commercialized components with an acceptable dimensions to be used by mobile indoor end-users. In a second part of this chapter, the transmitted modulated signal is characterized in the presence of different noises that can affect the link. This study was used to calculate the received system signal-to-noise ratio and thus define the system dimensioning limits. This free-space cell is also simulated and the eye diagram and bit error rates are calculated in order to present a first validation and to give the opportunity to simulate the entire link. The global simulation and the experimentally characterization of the entire link will be the subject of the last chapter.

## Bibliography

- [1] H. P. Herzig. *Holography: holographic optical elements, computer-generated holography and diffractive optics*. Handbook of Laser Technology and Applications, Institute of Physics Publishing, Bristol, 2004.
  - [2] A. Chan Yong. *Fabrication d'éléments optiques diffractifs par microstructuration de matériaux polymères*. PhD thesis, Télécom Bretagne, 2013.
  - [3] S. Martellucci and A. N. Chester. *Diffractive Optics and Optical Microsystems*. Plenum Press, 1997.
  - [4] N. Streibl. Beam shaping with optical array generators. *Journal of Modern Optics*, 36(12):1559–1573, 1989.
  - [5] O. Ripoll, V. Kettunen, and H. P. Herzig. Review of iterative Fourier-transform algorithms for beam shaping applications. *Optical Engineering*, 43(11):2549–2556, 2004.
  - [6] <http://www.dataray.com/>.
  - [7] W. T. Welford and R. Wintson. *High Collection Nonimaging optics*. Academic Press, 1989.
  - [8] R. Ramirez-Iniguez, S. Idrus, and Z. Sun. *Optical Wireless Communications—IR for Wireless Connectivity*. Taylor & Francis Group, Boca Raton.
  - [9] Thorlabs optical filter, 2012. [http://www.thorlabs.com/NewGroupPage9.cfm?ObjectGroup\\_ID=1000](http://www.thorlabs.com/NewGroupPage9.cfm?ObjectGroup_ID=1000).
  - [10] X. Ning, R. Winston, and J. O’Gallagher. Dielectric totally internally reflecting concentrators. *Applied Optics*, 26(2):300–305, Jan. 1987.
  - [11] J. M. Kahn and J. R. Barry. Wireless infrared communications. *Proceedings of the IEEE*, 85(2):265–298, Feb. 1997.
  - [12] A.M. Street, P.N. Stavrinou, D.C. O’Brien, and D.J. Edwards. Indoor optical wireless systems—a review. *Optical and Quantum Electronics*, 29:349–378, 1997.
  - [13] J. P. Savicki and S. P. Morgan. Hemispherical concentrators and spectral filters for planar sensors in diffuse radiation fields. *Applied Optics*, 33(34):8057–8061, Dec. 1994.
  - [14] K. P. Ho and J. M. Kahn. Compound parabolic concentrators for narrowband wireless infrared receivers. *Optical Engineering*, 34(5):1385–1395, 1995.
  - [15] Altuglas International ARKENA Group, 2012. <http://www.altuglas.com>.
  - [16] D. C. O’Brien, G. E. Faulkner, and al. Integrated Transceivers for Optical Wireless Communications. *IEEE Journal of Selected Topics in Quantum Electronics*, pages 173–183, 2005.
-

- [17] M. Wolf, J. Li, L. Grobe, D. O'Brien, H. Minh, and O. Bouchet. Challenges in Gbps Wireless Optical Transmission. In *Mobile Lightweight Wireless Systems*, volume 45, pages 484–495. Springer Berlin Heidelberg, 2010.
  - [18] G. Agrawal. *Lightwave Technology: Components and Devices*. John Wiley & Sons, 2005.
  - [19] Z. Toffano. *Optoélectronique - Composants photoniques et fibres optiques*. Collection Technosup éditions Ellipses, 2001.
  - [20] Femto, 2012. [http://www.femto.de/datasheet/DE-HSA-X-S-2G-IN\\_R8.pdf](http://www.femto.de/datasheet/DE-HSA-X-S-2G-IN_R8.pdf).
  - [21] F. R. Gfeller and U. Bapst. Wireless in-house data communication via diffuse infrared radiation. *Proceedings of the IEEE*, 67(11):1474–1486, Nov. 1979.
  - [22] K. Pahlavan. Wireless communications for office information networks. *Communications Magazine, IEEE*, 23(6):19–27, Jun. 1985.
  - [23] A. Goldsmith. *Wireless communications*. Cambridge university press, 2005.
  - [24] F. G. Stremler. *Introduction to Communication Systems*. Addison-wesley, 1982.
  - [25] <http://www.vpiphotonics.com/>.
-

## Figures and tables

### Figures

4.1	Simplified representation of the DOE operation [2] . . . . .	107
4.2	Gaussian to flat-top profile conversion . . . . .	108
4.3	Optical cell at the output of the PF-GI-POF (a) without DOE and (b) using a DOE that replicates the fiber far-field along 2D circular grid . . . . .	109
4.4	Computer design and fabrication of a DOE (Fourier type) [2] . .	109
4.5	Enlarged portion of the diffraction pattern showing 9 points at the focused distance, and successively defocused . . . . .	110
4.6	DOE cells distributions and their corresponding gray level profiles proportional to the image intensity captured by the camera (arbitrary units) as a function of the pixel index. The varying parameter between (a), (b) and (c) is the defocusing between the lens and the DOE . . . . .	111
4.7	Mobile optical receiver scheme . . . . .	112
4.8	(a) Thin-film filter [8] and (b) optical filter transmission . . . . .	113
4.9	Schematic representation of an optical concentrator [8] . . . . .	113
4.10	Photoreceiver structure based on a hemispherical concentrator .	114
4.11	(a) Compound parabolic concentrator, (b) Dielectric totally internally reflecting concentrator . . . . .	115
4.12	Profile of a custom CPC concentrator generated by a Matlab code. The device is 5 mm long, its input area diameter is 7 mm and the theoretical gain is 16 dB (see figure 4.15) . . . . .	116
4.13	Average simulated gain (left) and gain standard deviation (right) as function of rays number for 10 experiences . . . . .	117
4.14	Transmission of Altuglas material in function of wavelength . . .	117
4.15	Fabricated concentrator prototypes (CPC types) . . . . .	117
4.16	Concentrator gain measurement bench setup . . . . .	118
4.17	Simplified scheme of a photodetector with (a) low-or high-impedance and (b) transimpedance front-end amplifiers . . . . .	121
4.18	Different noise current at photodiode stage . . . . .	121
4.19	4-PPM modulation . . . . .	125
4.20	IM/DD transmission scheme . . . . .	126
4.21	Comparison of spectra of SC and OFDM waveforms . . . . .	126
4.22	OFDM transmitter scheme . . . . .	127
4.23	(a) OOK-RZ modulation and (b) OOK-NRZ modulation codes .	128
4.24	Model of baseband transmission . . . . .	128

---

4.25	Eye diagram with conditional probability density associated with the "0" and "A" current distributions, $I_0$ and $I_A$ are the average values, $\sigma_0^2$ and $\sigma_A^2$ are the variances . . . . .	129
4.26	SER (i.e. BER) performances of OOK-NRZ modulation over the AWGN channel . . . . .	131
4.27	Free-space link geometry. Both the coverage area and the detector surface area supposed to be circular, with areas $A_c$ and $A_d$ , respectively . . . . .	132
4.28	Distance in function of emitted power for different noise variance	134
4.29	Distance as a function of the emitted power for different photodetector bandwidth . . . . .	135
4.30	Divergence angle as a function of the emitted power . . . . .	135
4.31	Detector area as a function of the emitted power for different free-space link distance . . . . .	136
4.32	Detector area as a function of emitted power for different free-space distance link . . . . .	136
4.33	Scheme of the VPI simulation of the NLOS free-space link . . . .	137
4.34	Simulated eye-diagram at the receiver stage of the optical free-space link transmission using a PIN-based photoreceiver (2.5 Gbps OOK-NRZ modulation) . . . . .	138
4.35	Simulated eye-diagram at the receiver stage of the free-space link using a APD-based photoreceiver (2.5 Gbps OOK-NRZ modulation)	139

---

## Tables

---

4.1	Measured concentrator gain . . . . .	118
4.2	Photodiode material and operating wavelength . . . . .	119
4.3	Different receiver noise and its spectral density . . . . .	124
4.4	Receiver sensitivities in dBm . . . . .	132
4.5	Free-space link parameters . . . . .	133

---



## Chapter 5

# Optical downlink performance: simulation and experimental results

### Contents

---

Introduction . . . . .	<b>146</b>
I    Downlink transmission software simulation . . . . .	<b>146</b>
II   Experimental test of the downlink . . . . .	<b>148</b>
III  Conclusion . . . . .	<b>156</b>
Bibliography . . . . .	<b>157</b>
Figures and tables . . . . .	<b>158</b>

---

## Introduction

In this chapter, the overall system including all the link elements is first simulated using the VPI<sup>TM</sup> optical transmission software. A Matlab co-simulation is used to model the components that are not included in the VPI<sup>TM</sup> module library [1]. The second part of the chapter will be dedicated to the presentation and characterisation of the system experimental prototype transmission test.

## I Downlink transmission software simulation

The all-optical proposed downlink is simulated to evaluate the system performance in terms of electrical eye diagram and bit error rate at the receiver stage. VPI<sup>TM</sup> Transmission Maker is a powerful software that allows the variation of any parameters using the "parameters sweeping" option. This freedom degree can be used to optimize the model and parameters of each components and the dimensioning of the whole system called "virtual prototyping". This complex method was not adopted here because the downlink parameters and their influence on the signal quality have already been considered in chapters 3 and 4. In this framework, optical simulation is used as first step to check the proposed design and estimate the BER at the receiving stage.

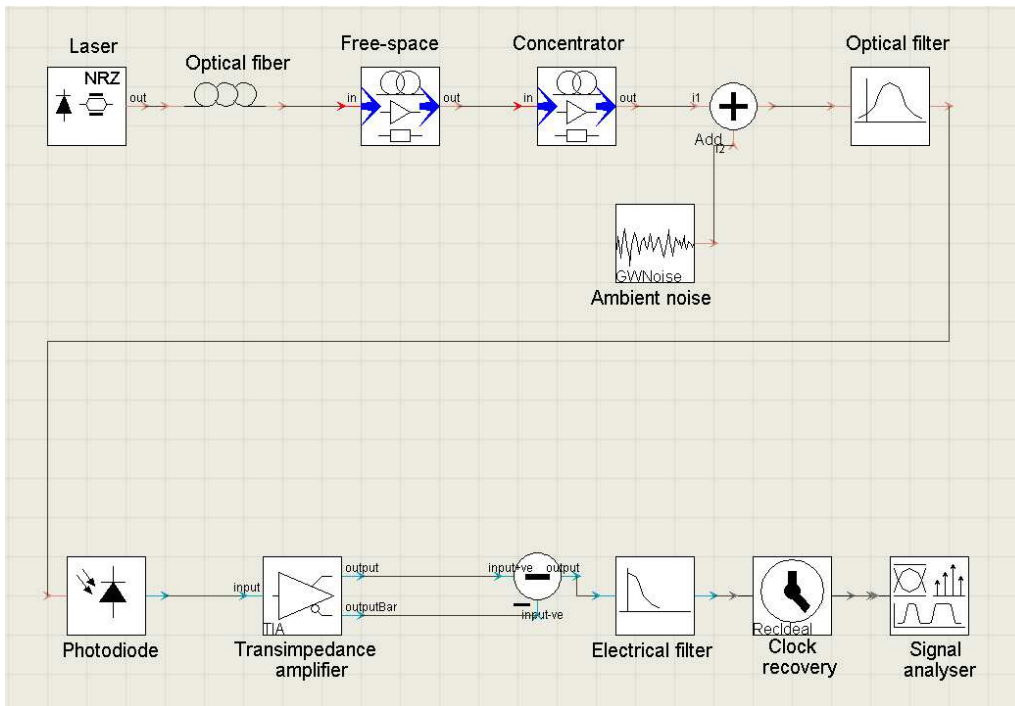


Figure 5.1: Scheme of the global simulation (VPI<sup>TM</sup> universe) including all components and all physical effects (noises and free-space attenuation) of the hybrid optical transmission



This global transmission is performed from the simulation model discussed in chapter 3 for the fiber and chapter 4 for the free-space link, where the Matlab software is used to describe the modules that are not listed in VPI<sup>TM</sup> library. The simulation is performed for the two studied fiber types (PF-GI-POF [2] and G657 [3]). Figure 6.7 presents the schematic block of the global simulation.

The optical wireless cell geometry, the receiver parameters and the different noise values are the same than those defined in chapter 4. The fiber span length is 20 m, which represents the average link length in an indoor architecture and the laser power is set to have a power of 10 dBm at the input of the free-space module. The first simulated link uses SMF G657 and the electrical eye diagram at the receiver stage at 2.5 Gbps OOK-NRZ modulation is represented in figure 5.2 (a) for the PIN photodiode and in figure 5.2 (b) for an APD photodiode with an  $M$  factor of 10. The simulation is performed on 2048 bits and the estimated BER using a Gaus-

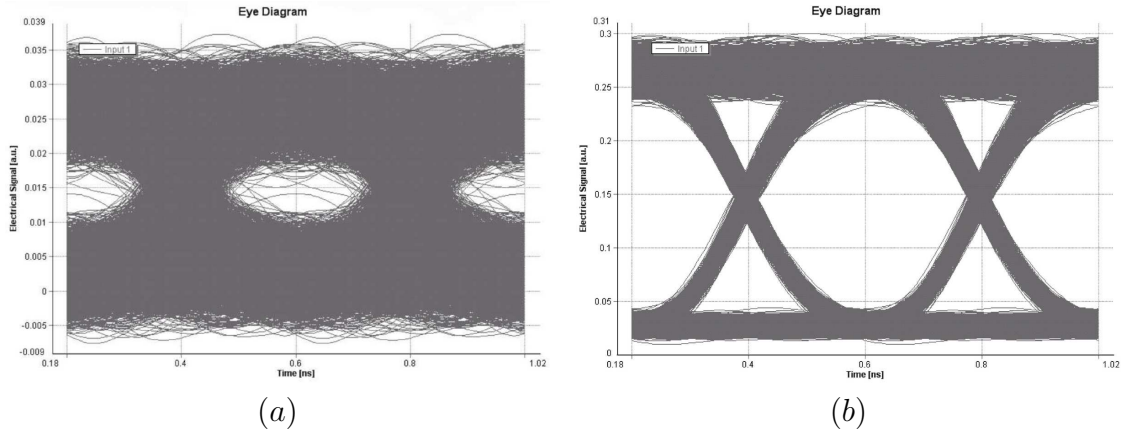


Figure 5.2: Simulated eye-diagrams at the receiver stage of the optical downlink transmission with 20 m of SMF G657 fiber using (a) PIN-based and (b) APD-based photoreceiver (2.5 Gbps OOK-NRZ external modulation)

sian estimation method is  $1.5 \cdot 10^{-5}$ . The use of an APD photodiode shows a large improvement in the eye diagram and an error-free transmission (estimated BER =  $8.9 \cdot 10^{-70}$ ).

The simulation is also carried out using 20 m of PF-GI-POF with 50  $\mu\text{m}$  core diameter, in the same conditions than for the first simulation and the simulated eye diagrams are shown in figure 6.8, using (a) a PIN and (b) an APD photodiode. Both simulations show the feasibility of the system at 2.5 Gbps with OOK-NRZ modulation. It also validates the possibility to use both the SMF (G657) and PF-GI-POF fiber. In the limits of validity of the physical models used to represent the modules in the software, especially the free-space transmission link and the PF-GI-POF modules, these simulation results show an almost error-free transmission at the receiving stage in case of an APD-based photoreceiver.

In order to confirm this first result, an experimental downlink is built in the purpose to measure physically the eye diagram and BER. This study is described in the next section.

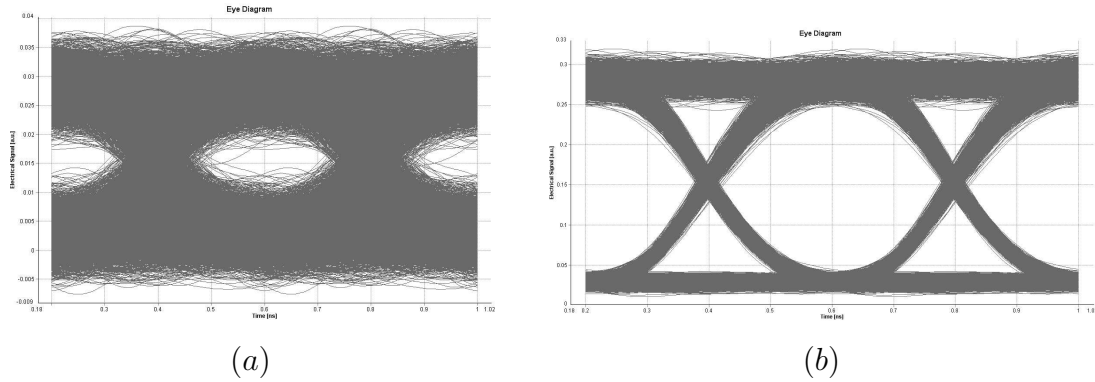


Figure 5.3: Simulated eye-diagrams at the receiver stage of the optical downlink transmission with 20 m of PF-GI-POF fiber using (a) PIN-based and (b) APD-based photoreceiver (2.5 Gbps OOK-NRZ external modulation)

## II Experimental test of the downlink

The last and crucial validation of the system is the experimental part. An experimental test bench is built including all the system components (see figure 6.9). The test of the downlink is done by the visualization of the eye diagram and the measurement of bit error rate. The measurement is performed at different bit rates ranging from 125 Mbps to 1 Gbps. The first step consists in calibrating the interfaces by a back-to-back measurement between the transmitter and the receiver. The different components are then introduced successively in the link. This method permits a progressive assessment of the different modules in order to evaluate finally the whole link.

At the receiving stage, the eye diagram is displayed using a numerical sampling oscilloscope<sup>1</sup> "picoScope 9231 A" with a -3 dB bandwidth of 12 GHz. This device is a digital signal analyser designed for the complex tasks involving high-speed electrical signals, including signal analysis, timing analysis, testing of high-speed digital communications systems with 5 TS/s<sup>2</sup> equivalent sample rate [4]. This picoscope also contains an optical input to directly test the incoming optical signal. The signal used to modulate the laser is an RF signal delivered by an arbitrary wave generator (AWG) from Tektronix [AWG 7102, 2 channels 10 GS/s (20 GS/s)] [5].

### • STEP 1: BACK-TO-BACK LINK

As shown in figure 5.5, we first calibrate the back-to-back electrical eye diagram at the output of the picoscope by connecting the AWG to the picoscope. The picoscope is connected to the second output of the AWG used to trigger the bit sequence. The resulting eye diagram for the signal generated by the AWG at 250 Mbps is shown in 5.6 (a) and at 1 Gbps in figure 5.6 (b). The resulting eye diagrams are perfectly open and clearly show the absence of any noise generation at the picoscope. These

<sup>1</sup>From Pico technologies

<sup>2</sup>TeraSamples/seconde

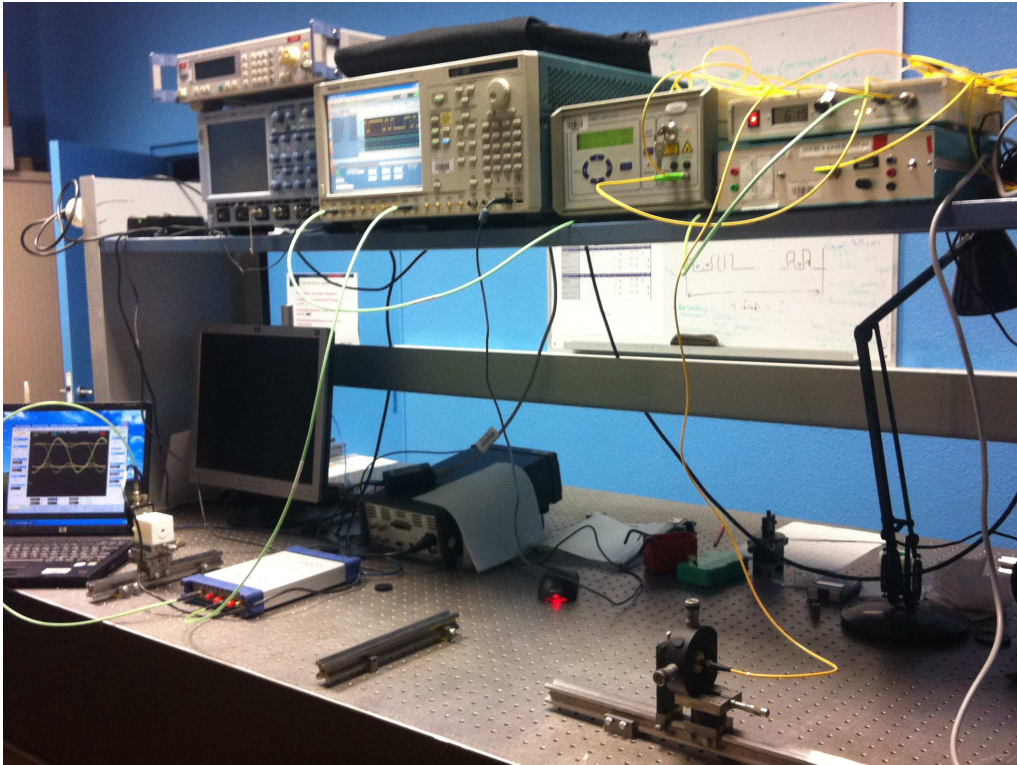


Figure 5.4: Scheme of the global simulation including all components and all effects (noises and attenuations)

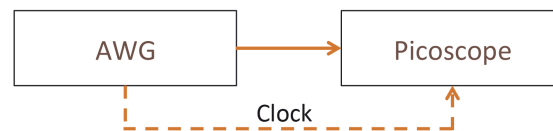


Figure 5.5: Schematic block corresponding to the electrical connection between the AWG and the picoscope (calibration procedure)

electrical eye diagrams validate the use of this picoscope on our characterizations as reference to compare other eye diagrams obtained after the introduction of different system components.

#### • STEP 2: LASER TEST

The next step was to introduce the optical laser on the channel to evaluate the effects of direct modulation. Figure 5.7 shows a schematic block of the test components. In this measurement, the 1550 nm DFB laser whose spectrum is shown in figure 3.18 on chapter 3 is connected to the optical input of the picoscope, and figure 5.8 (a) and (b) represent the eye diagrams resulting from the introduction of the laser, respectively at a bit rate of 500 Mbps and 1 Gbps, using an OOK-NRZ modulation. The resulting electrical eye diagram is clearly open at a bit rate of 1 Gbps showing

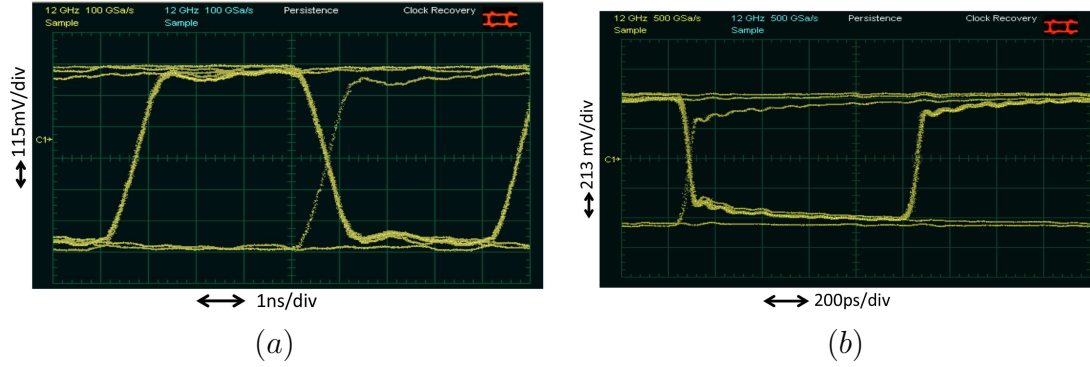


Figure 5.6: Measured back-to-back eye diagram for OOK-NRZ at (a) 250 Mbps and (b) 1 Gbps, generated by the AWG

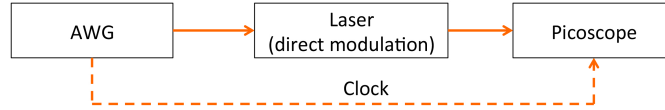


Figure 5.7: Schematic Block of signal at the output of the laser

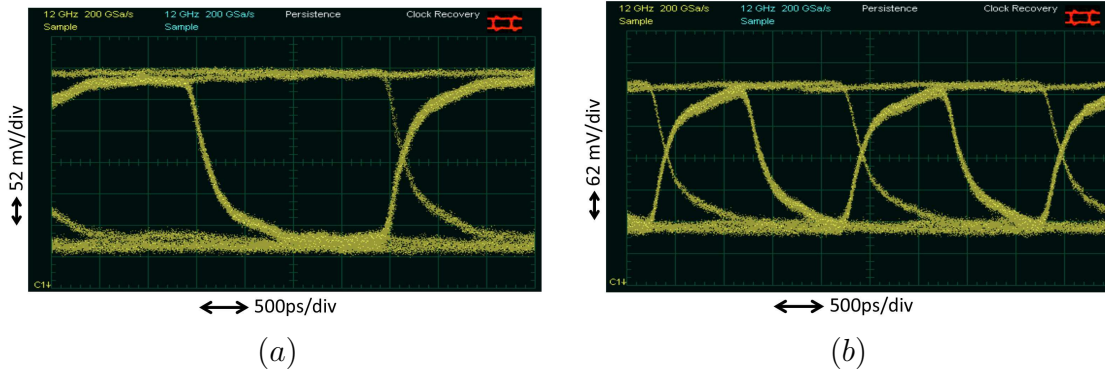


Figure 5.8: Measured eye diagram (OOK-NRZ) at the output of the directly modulated laser at (a) 500 Mbps and (b) 1 Gbps, generated by the AWG

the transparency of laser modulation in this elementary link.

#### • STEP 3: FREE-SPACE LINK USING THORLABS PHOTORECEIVER

The introduction of the free-space span should be accompanied by the use of a the wireless receiver. As shown in chapter 4, the receiver should contain the photoreceiver, the concentrator, and the optical filter. These components will be introduced successively in the link. The photoreceiver can be tested by the definition of a free-space cell smaller than that defined in the network scenario, but corresponding to the same power density at the photodetector area in the presence of the concentra-

tor. The first free-space transmission was performed using a Thorlabs photoreceiver [PDA 10 CF-EC] with a -3 dB bandwidth of 150 MHz and a 0.5 mm diameter of detection area [6]. The schematic block of this test is shown in figure 5.9 (a). The

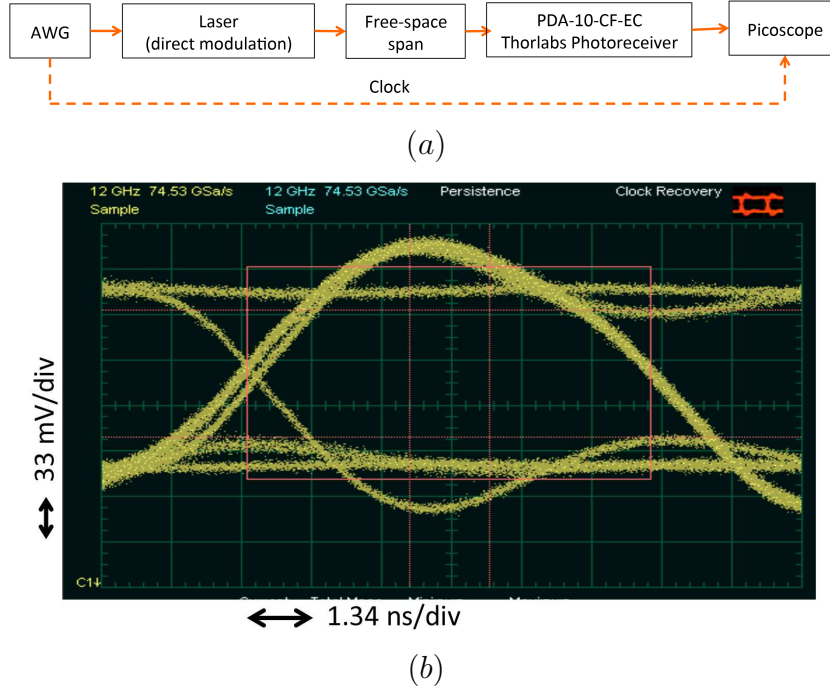


Figure 5.9: (a) Schematic block for the setup of AWG, OOK-NRZ directly modulated laser, free-space and the Thorlabs photodiode and (b) the measured eye diagram for a free-space transmission of 75 cm at 125 Mbps

free-space distance is about 75 cm, the emitted optical power is about 1 dBm and the optical cell has a diameter of about 1 cm. The bit rate is limited to 125 Mbps, due to the limitation of the Thorlabs photoreceiver bandwidth. The eye diagram is measured at the center of the cell and shown in figure 5.9 (b). This eye diagram is degraded compared to that shown before but it stills clearly open with an estimated SNR of 16 dB. The signal level decreases and the noise appears on the eye diagram.

#### • STEP 4: COMBINED SMF FREE-SPACE LINK USING THORLABS PHOTORECEIVER

As shown in chapter 3, the fibered part of the system can be established using single-mode silica fiber or PF-GI-POF. Although the fiber link has a distance that does not exceed 30m, 25 km of silica SMF are introduced in the test shown in figure 5.10 (a). The conditions are the same than for the previous measurement and the resulted eye diagram is shown in figure 5.10 (b). The measured SNR is around 10 dB which is smaller than the previous measurement without fiber. This difference can be explained by to the signal attenuation through the fiber which can be compensated by increasing the emitted power signal respecting the maximum permissible optical



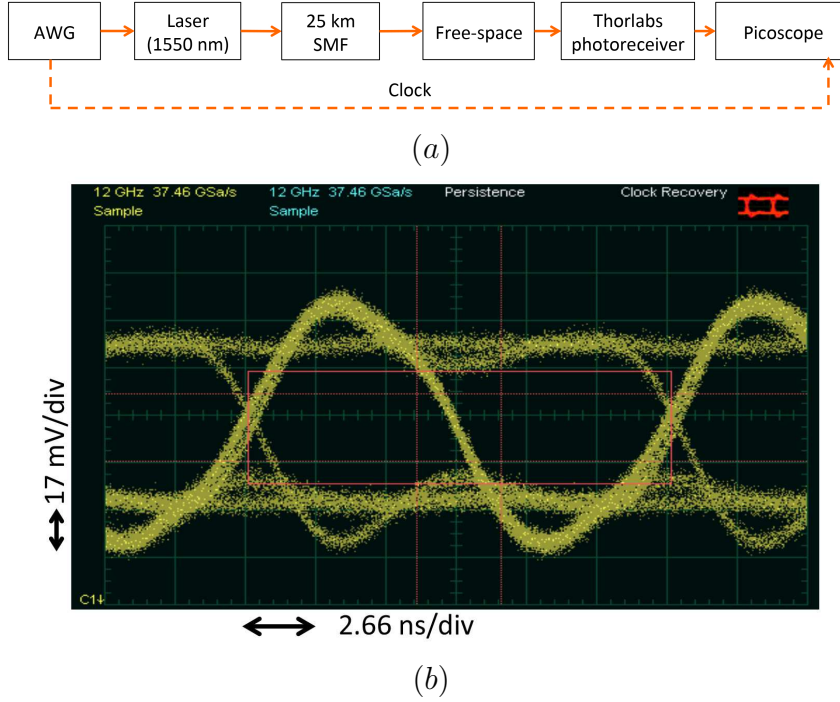


Figure 5.10: (a) Schematic block for the link combining SMF and free-space using Thorlabs photodiode and (b) the measured eye diagram for a free-space transmission of 75 cm at 125 Mbps

power at the fiber output (using an EDFA).

- STEP 5: FREE-SPACE LINK USING FEMTO PHOTORECEIVER

This first validation of the free-space link at a bit rate of 125 Mbps is considered, far from the expected bit rate. The photoreceiver is replaced by the 2 GHz bandwidth device fabricated by Femto [7] with the reference HSA-X-S-2G-IN (see chapter 4). The parameters used for the global link simulation shown in section I of this chapter correspond to this photoreceiver. Figure 5.11 shows the schematic block for the free-space transmission using the Femto photoreceiver. No optical fiber is used at this step. Figures 5.12 (a) and (b) show respectively the eye diagrams at 500 Mbps

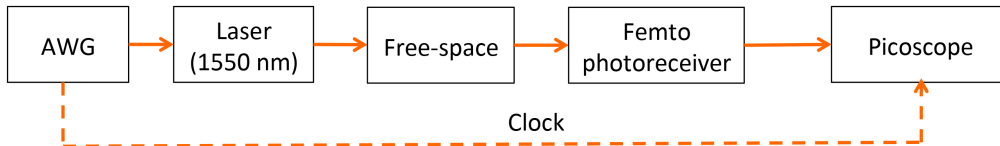


Figure 5.11: Schematic block of the link combining SMF and free-space using femto photoreceiver

and 1 Gbps at the center of free-space cell of around 1 cm at a distance of 75 cm

and an optical power emitted in free-space of 3 dBm. The eye diagrams shows more

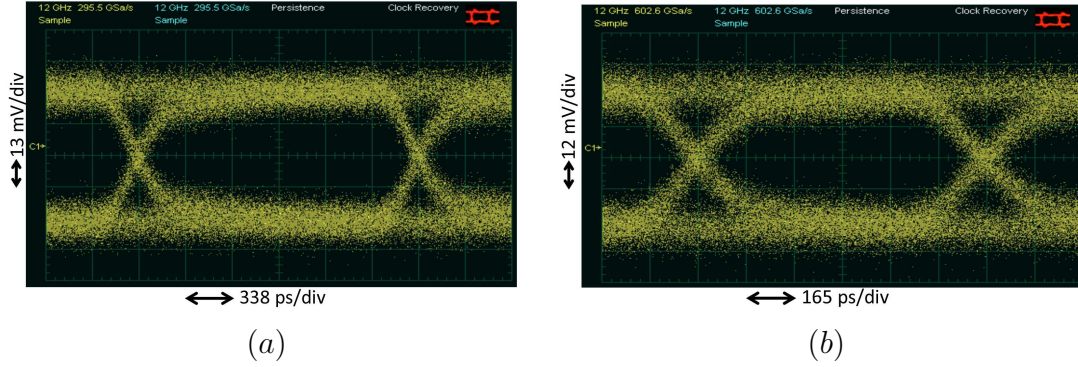


Figure 5.12: Measured eye diagram after free-space propagation using the 2 GHz Femto photoreceiver (a) 500 Mbps, (b) 1 Gbps

degradation as compared to previous measurement due to the lower sensitivity and lower optical detected power (smaller detection area) of the Femto photoreceiver as compared to the Thorlabs device. The SNR and the eye diagram can be improved by the increase of optical emitted power to 10 dBm as presented in the next steps.

• STEP 6: COMBINED PF-GI-POF FREE-SPACE LINK USING FEMTO PHOTORECEIVER

We now introduce the PF-GI-POF in the link. The schematic block is illustrated in figure 5.13. In this test, the optical power at the fiber output is about 5 dBm and

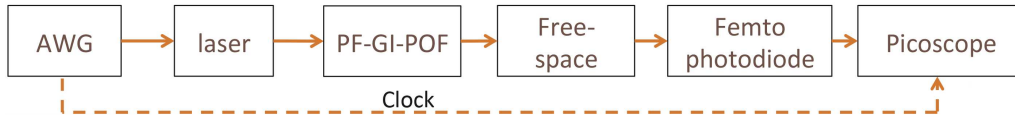


Figure 5.13: Schematic block combining PF-GI-POF and free-space using Femto photoreceiver

the measurement is performed at 1 Gbps at a distance of 95 cm. The PF-GI-POF has a length of 20 m which, corresponds to an attenuation of about 5 dB.

Figure 5.14 (a) shows the eye diagram at the receiver stage in the case of a focused beam at the receiver input. This measurement is performed in this configuration to show the PF-GI-POF effect. The optical signal at the OAP is then defocused to obtain again a 1 cm diameter cell and the corresponding eye diagram is shown in figure 5.14 (b), with the presence of some noise but with an open eye diagram corresponding to a sufficient SNR.

•STEP 7: FREE-SPACE LINK WITH CONCENTRATOR USING THORLABS PHOTORECEIVER

The optical concentrator is now introduced in the link presented on figure 5.9 (a).

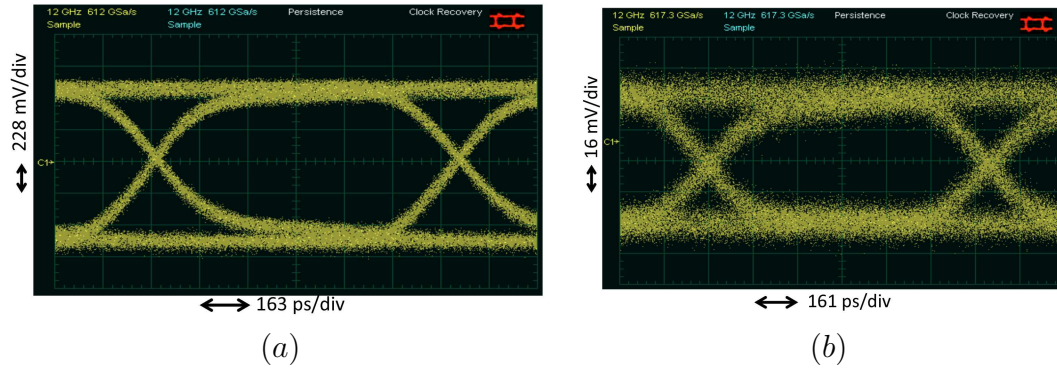


Figure 5.14: Measured eye diagram at the femto photodetector stage for a signal propagates in PF-GI-POF and free-space with (a) signal focused at the detector area and (b) at the center of a cell of 1 cm of diameter

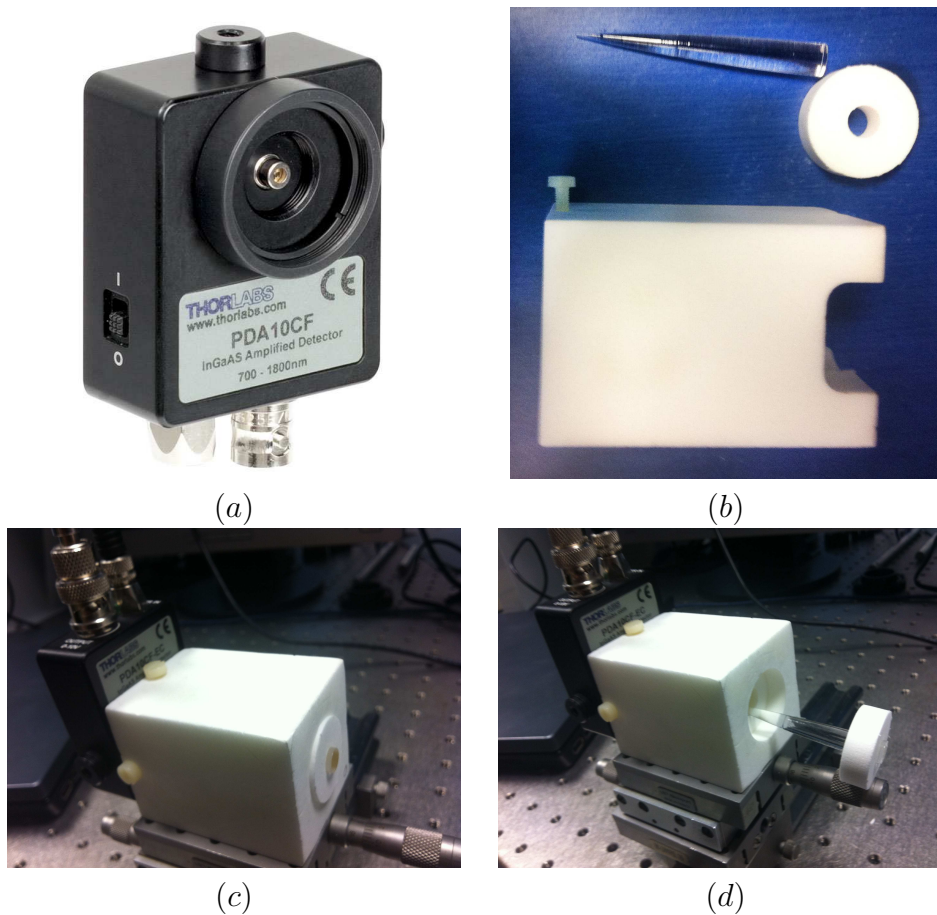


Figure 5.15: Mechanical setup to position the concentrator at the entrance pupil of the Thorlabs photoreceiver

Figure 5.15 (a) and (b) shows the setup of the concentrator at the entrance of the



photodiode receiver. An intermediate cubic piece fabricated using a polymer material called ROHACELL HF 71 [8] is employed to align the output face of the concentrator ( $500\text{ }\mu\text{m}$  of diameter) on the input window of the Thorlabs photodiode ( $500\text{ }\mu\text{m}$  of diameter).

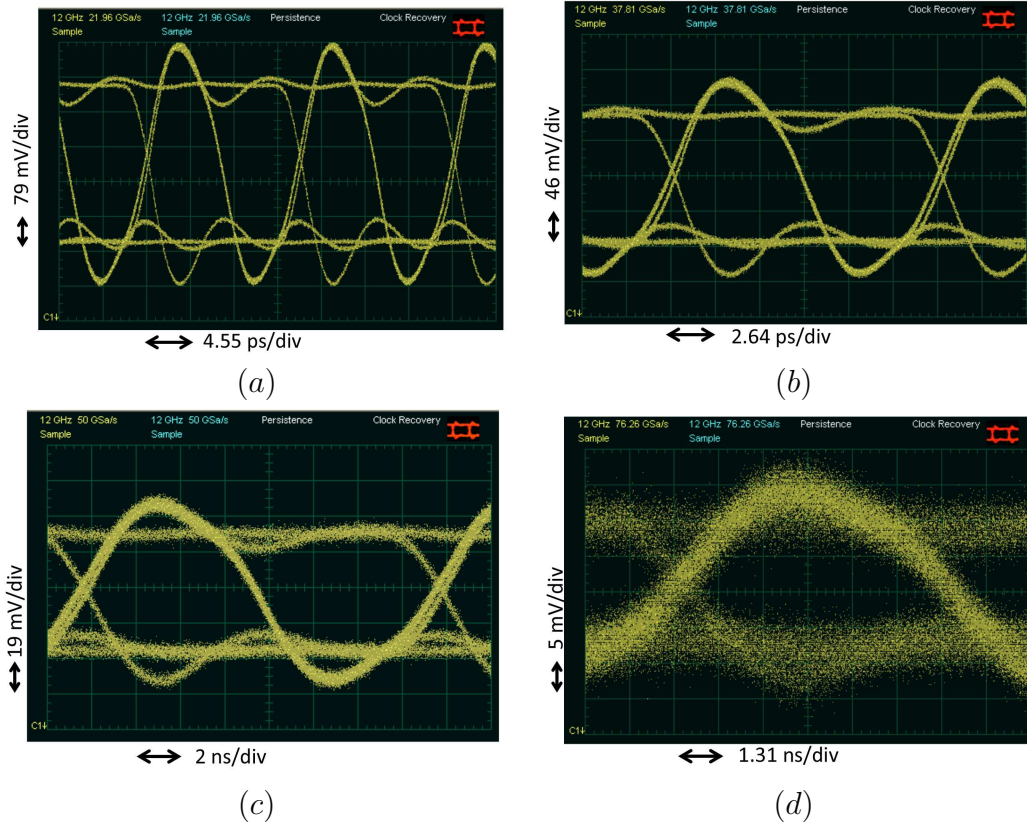


Figure 5.16: Measured eye diagram after free-space propagation in the presence of concentrator at the center of a cell of 1 cm (a), 2 cm (b), 4 cm of diameter (c) and at 2 cm from the center of a cell of 4 cm of diameter (d) at 125 Mbps OOK-NRZ using Thorlabs photoreceiver.

This experimental test is performed at a bit rate of 125 Mbps (OOK-NRZ) and a free-space distance of 110 cm using the same directly modulated DFB laser used previously. The optical power at the fiber output is 10 dBm.

Figure 6.10 shows respectively the eye diagrams at the center of a cell of 1 cm (a), 2 cm (b) and 4 cm (c) of diameter. We can see clearly the gain of the concentrator with more opened eye diagrams. Figure 6.10 (d) shows the eye diagram at 2 cm from the center of the cell of 4 cm. the eye diagram is degraded, but still open. These measurements are performed also without the concentrator, showing a concentrator gain of 5 dB for the different configurations presented above. This value is smaller than the measured concentrator gain in the chapter 4. It is due to the protection glass window of the Thorlabs photodetector, which prevents the direct contact of the concentrator with the detection area.

We then repeat this operation with the Femto photoreceiver, but unsuccessfully.

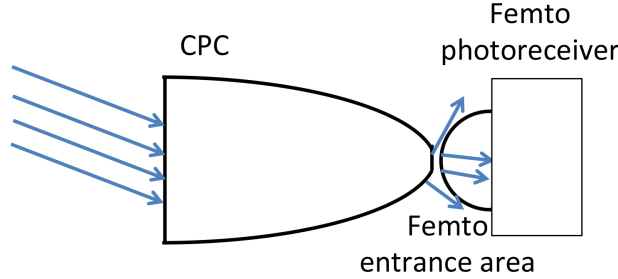


Figure 5.17: Connection impairment between the concentrator and the Femto photoreceiver input

The main reason was the bad power coupling between the concentrator output and the receiver input, due to the presence of a hemispherical lens (concentrator) at that stage, as shown in figure 5.17. The absence of possibility to obtain the expected concentrator gain makes the test of free-space transmission impossible with the DOE designed to give the 10 cm uniform optical cell at 2.5 m. This point is currently being studied and a solution will be determined in a near future.

### III Conclusion

The simulation of the overall all-optical downlink confirms the transmission at a bit rate of 2.5 Gbps using OOK-NRZ modulation. The experimental test approves respectively the choice of different system component and the feasibility of the entire downlink. The experimental test was performed at some reduced distance (free-space and cell dimensions) due to the absence of concentrator in some of the measurements, and the low gain of concentrator at its presence. We note that the difficulty of having similar test conditions (power, distance, ...) due to different characteristics of the components. The limit in the concentrator gain is due to the difficulty to connect the concentrator to the input of the commercial high bandwidth photodetector.

The fabricated DOE was not introduced in this link due to its incompatibility with the reduced system dimensions. It will be tested by changing the DOE characteristics to be adapted with the experimental bench or the expected concentrator gain should be compensated by increasing the emitted power only to validate the DOE effect.

## Bibliography

- [1] <http://www.vpiphotonics.com/>.
  - [2] [http://www.thorlabs.de/newgrouppage9.cfm?objectgroup\\_id=2928](http://www.thorlabs.de/newgrouppage9.cfm?objectgroup_id=2928).
  - [3] [http://www.pacific-technology.fr/cbx/s4\\_breve641.htm](http://www.pacific-technology.fr/cbx/s4_breve641.htm).
  - [4] Pico Technology. PC Sampling Oscilloscope, 2012. <http://www.picotech.com/picoscope9200.html>.
  - [5] <http://www.electrorent.com/products/search/pdf/tek-awg7102.pdf>.
  - [6] <http://www.thorlabs.com/thorproduct.cfm?partnumber=pda10cf>.
  - [7] Femto, 2012. [http://www.femto.de/datasheet/DE-HSA-X-S-2G-IN\\_R8.pdf](http://www.femto.de/datasheet/DE-HSA-X-S-2G-IN_R8.pdf).
  - [8] <http://www.rohacell.com/sites/dc/downloadcenter/evonik/product/rohacell/product-information/rohacell%20hf%20product%20information.pdf>.
-

## Figures and tables

### Figures

---

5.1	Scheme of the global simulation (VPI <sup>TM</sup> universe) including all components and all physical effects (noises and free-space attenuation) of the hybrid optical transmission . . . . .	146
5.2	Simulated eye-diagrams at the receiver stage of the optical downlink transmission with 20 m of SMF G657 fiber using (a) PIN-based and (b) APD-based photoreceiver (2.5 Gbps OOK-NRZ external modulation) . . . . .	147
5.3	Simulated eye-diagrams at the receiver stage of the optical downlink transmission with 20 m of PF-GI-POF fiber using (a) PIN-based and (b) APD-based photoreceiver (2.5 Gbps OOK-NRZ external modulation) . . . . .	148
5.4	Scheme of the global simulation including all components and all effects (noises and attenuations) . . . . .	149
5.5	Schematic block corresponding to the electrical connection between the AWG and the oscilloscope (calibration procedure) . . . .	149
5.6	Measured back-to-back eye diagram for OOK-NRZ at (a) 250 Mbps and (b) 1 Gbps, generated by the AWG . . . . .	150
5.7	Schematic Block of signal at the output of the laser . . . . .	150
5.8	Measured eye diagram (OOK-NRZ) at the output of the directly modulated laser at (a) 500 Mbps and (b) 1 Gbps, generated by the AWG . . . . .	150
5.9	(a) Schematic block for the setup of AWG, OOK-NRZ directly modulated laser, free-space and the Thorlabs photodiode and (b) the measured eye diagram for a free-space transmission of 75 cm at 125 Mbps . . . . .	151
5.10	(a) Schematic block for the link combining SMF and free-space using Thorlabs photodiode and (b) the measured eye diagram for a free-space transmission of 75 cm at 125 Mbps . . . . .	152
5.11	Schematic block of the link combining SMF and free-space using femto photoreceiver . . . . .	152
5.12	Measured eye diagram after free-space propagation using the 2 GHz Femto photoreceiver (a) 500 Mbps, (b) 1 Gbps . . . . .	153
5.13	Schematic block combining PF-GI-POF and free-space using Femto photoreceiver . . . . .	153
5.14	Measured eye diagram at the femto photodetector stage for a signal propagates in PF-GI-POF and free-space with (a) signal focused at the detector area and (b) at the center of a cell of 1 cm of diameter . . . . .	154
5.15	Mechanical setup to position the concentrator at the entrance pupil of the Thorlabs photoreceiver . . . . .	154

---

5.16	Measured eye diagram after free-space propagation in the presence of concentrator at the center of a cell of 1 cm (a), 2 cm (b), 4 cm of diameter (c) and at 2 cm from the center of a cell of 4 cm of diameter (d) at 125 Mbps OOK-NRZ using Thorlabs photoreceiver. . . . .	155
5.17	Connection impairment between the concentrator and the Femto photoreceiver input . . . . .	156

---



# Conclusions

## Summary

This thesis provides the evaluation of an *all-optical* indoor high bit rate wireless system. At the start of the investigations, a novel architecture based on the fiber distribution of free-space optical pico-cells is proposed. Unlike Radio-over-Fiber systems using RF cells, the digital optical signal is here directly transmitted in free-space to provide a transparent high bit rate optical wireless cell. The optical cell traffic originates from both the access network and locally generated indoor data streams, which are multiplexed at the physical layer using an Optical Control Station (OCS). The latter also switches the information towards the appropriate optical access points in the rooms of the building. A deep study of the OCS structure and implementation was out of the scope of this work, but such transparent optical fiber switching technologies as MEMS or liquid crystal modulators are mature enough to provide efficient solutions. The downstream optical signals are then transferred from the optical access point (OAP) to the mobile terminals in the rooms using NLOS wireless optical links, whose power link budget is consistent with Gbps communications. The reduced mobility imposed by the NLOS geometry was the price to pay for such a very high link bandwidth.

The resulting physical design is dedicated to the wireless distribution of new bandwidth-hungry applications, like multimedia services in the Gbps bit rate range. A key-idea at that step was to combine custom designed and commercially available modules to limit the overall cost and hence facilitate the system large-scale deployment. However, the major difficulty faced from the beginning of the work was the large technical stretch of the addressed topic, covering both architectural, component and device, as well as transmission system considerations.

In the purpose of assessing the practicability of the investigated approach, many simulations and physical tests were performed on both the components and system parts, which led us to handle many questions, among which :

- *What type of optical fiber is best adapted to the transparent distribution of indoor optical cells ?*
  - *What is the optimal carrier wavelength to implement the hybrid all-optical channel ?*
-

- *What is the adequate optical free-space link topology and the best trade-off between the bit rate limit value and mobility range?*
- *What technologies and optical modules to implement moderate-cost optical access points and optical wireless receivers ?*

All these crucial points have been addressed throughout the manuscript. In particular, the operating wavelength chosen lies in the "Telecom" 1550 wavelength nm band for different criteria, among which eye safety plays an important role, but also the wide circulation of efficient sources at a -relatively- moderate cost (especially with the expected improvement 1.5  $\mu\text{m}$  VCSELS), FTTx compatibility and the reduced effect of ambient noise compared to other optical wavelengths.

Regardless of the chapter division of the manuscript, this work was organised into almost parallel three sub-tasks :

- (i) *dimensioning* of the system and selection of suitable opto-electronics technologies (chapter 1, 2, 3)
- (ii) *simulation* of the hybrid optical channel (mixed fiber optics and free-space) using the VPI<sup>TM</sup> transmission maker and Matlab softwares after the characterization and dimensioning of the fibered part (chapter 3), the free-space cell (chapter 4) and the overall system (chapter 5)
- (iii) *experimental tests and measurements* to validate the performance of the system (chapter 5).

A significant issue was the physical assessment of different stages of the proposed system, a necessary prerequisite before testing the overall optical transmission chain.

**Optical fibers.** The PF-GI-POF and G657 single mode fibers were investigated relatively to the required characteristics for indoor environment such as small bending radius, ease of installation, bandwidth and cost. The attenuation, impulse response, frequency response and far-field profiles for different launching conditions were experimentally investigated for the three different core diameters (50, 62.5 or 120  $\mu\text{m}$ ) of PF-GI-POF. The single-mode G657 was supposed to meet the bandwidth requirements, thus only the far-field profiles were characterized. The PF-GI-POF tests show an acceptable attenuation for short distance (3 dB in our case) with a bandwidth that permits the transmission of several Gbps over 100 m, offering a low-cost and easy connection with a margin exceeding  $\pm 15 \mu\text{m}$  lateral misalignment relatively to the fiber axis. The POF fiber performance was also assessed by software simulation but a discrepancy was noticed with respect to the experimental measured values, probably due to some approximations in the relevant physical parameters implemented in the multimode fiber model of VPI<sup>TM</sup>.

**Free-Space cell dimensioning.** A large part of this work was focused on the free-space cell modelling and design, which both includes the optical access point,



the free-space span and the mobile receiver. The latter is composed of an optical filter to reduce the ambient light noise. An optical compound parabolic concentrator was also used at this level to partly compensate for the large free-space attenuation, even using NLOS links. Custom mini-optical concentrator prototypes were designed and fabricated in our lab, to be adapted to commercial high-speed photoreceiver devices. The concentrator prototypes were then characterized both in the visible and IR ranges, and their gain was measured experimentally to average values lower than about 5 dB with respect to the theoretical value. This can be partly explained by material absorption, fabrication errors and detector misalignment.

Also deeply studied was the optical cell shape and power uniformity, which were investigated using a particular beam-shaping diffractive technique. Dedicated diffractive optical elements (DOEs) were designed, fabricated and tested both in the visible and infrared ranges, using the technical facilities of the Optics Department's laboratory. Optical cells with the expected size and uniformity were obtained and measured at both wavelengths. The next step will be the integration of compact DOEs within the OAP structure.

Based on a commercialized free-space photoreceiver with a bandwidth of 2 GHz, the different noise values were calculated to permit the estimation of the system signal-to-noise ratio using a OOK-NRZ modulation. This enabled the theoretical dimensioning of the present optical free-space cell for various system parameters such as the free-space link distance, beam divergence, detector area, receiver bandwidth and noise variance. Of course, the NLOS link model developed can be easily adapted to varying configurations.

The dimensioning of the free-space link was not only intended to optimize the OAP and mobile receiver designs, but aimed to provide a set of realistic receiver parameters useful for further investigations.

**Simulated and experimental validation.** A significant part of this study is dedicated to the assessment of the proposed optical downlink. While software simulation results validate the system feasibility, the experimental link demonstrator was tested with reduced free-space distance and cell area, due to concentrator gain lower than expected. Through acceptable BER and eye diagrams at a bit rate of 125 Mbps using OOK-NRZ modulation, the tests show the possibility of the system transmission in its complete version. The high-speed test combining the 2GHz photoreceiver and concentrator was corrupted by the mechanical mismatch between the detector and the concentrator geometries. This point still remains under study.

Finally, the system energy consumption was estimated, and, the system energy efficiency was compared relatively to that of other wireless indoor systems, showing a large advantage for the present system.

As a conclusion and despite the previous reservations on the experimental part, we believe that this work proposes a first realistic approach of an OWC network using non-expensive elements with a high bit rate ( $>1$  Gbps) and a very low consumption, as compared to existing radio-frequency solutions.

## Perspectives

The major perspectives of this work are the overall system integration, including the optical control station to distribute the signals to the rooms and the study of the up-link.

**Mobile receiver.** In continuation of this work, the concentrator fabrication method should be optimized in order to achieve the expected gain (15 dB). The material used for fabrication can be replaced by another material presenting both a higher refractive index and a higher transmission coefficient at 1550 nm.

A more efficient receiver including the concentrator, the photodiode and the preamplifier circuit could be obtained jointly through the collaboration with a photoreceiver designer. This step might lead to a joint optimization of both the detection area and the electrical front-end, depending on the aimed bandwidth. The result of this improvement will be the optical power budget which will enlarge the covered area or the link distance.

**Beam tracking.** Since the design makes use of NLOS links, it is desirable to consider beam tracking to improve the system mobility. At the physical level, beam tracking involves 2D beam deflection using a compact technology. Likewise to the optical space-switch implementation at the OCS level, beam steering can be considered here in the form of MEMS mirrors or liquid-crystal spatial-light modulators, where both technologies provide energy-efficient, fast and accurate beam-steering components. An interesting option provided by liquid crystal devices operating by diffraction is the ability to track multiple mobile terminals in parallel. An exactly similar configuration (but with a scale factor) was successfully used to implement optical tweezers to move cells in biological samples. In our case and depending on the overall area to be tracked by the optical beam, the key-parameter is here the maximum deflection angle, which will require to use space diversity techniques at both the OAP and the receiver.

**High-speed duplex link.** In this work, only the downlink was presented. An investigation of the optical uplink design as presented in chapter 2 (signal injected into the fiber core at the optical access point, transmitter at the mobile receiver, fixed optical access point,...) may lead to the implementation of a full duplex optical link. However this point will deserve deep investigation especially at the experimental level.

In order to exploit the optical bandwidth more efficiently and make multi-user applications easier, OFDM waveform should also be investigated. This powerful optical modulation format will increase the channel capacity and compensate for the degradation of high-speed transmission signal.

**Energy consumption.** A physical measurement of the system energy consumption will be essential to confirm the estimated advantage of the proposed system relatively to the existing radio frequency technologies.

---

**New applications.** The principle of using NLOS distributed Gbps signals also meets the requirements of railway transport, to connect high-speed trains to the broadband access network. In this case, SMF should be used along the railway to distribute dynamic NLOS infrared cells on a "train-tracking" manner. This point is currently being investigated in a collaboration project.

---



# Chapter 6

## Résumé détaillé

### Contents

---

I	Sujet, problématique et état de l'art . . . . .	<b>168</b>
II	Méthodologie . . . . .	<b>169</b>
III	Architecture proposée . . . . .	<b>169</b>
IV	Validation du budget optique . . . . .	<b>170</b>
V	Caractérisation de la fibre pour la distribution des cellules optiques en espace libre . . . . .	<b>171</b>
VI	Caractérisation de la cellule optique en espace libre . . . . .	<b>174</b>
	VI.1 Point d'accès optique . . . . .	174
	VI.2 Dimensionnement de la cellule optique en espace libre . .	174
VII	Simulation et test expérimental du système global . . . . .	<b>175</b>
	VII.1 Simulation du lien descendant . . . . .	175
	VII.2 Test experimental du lien descendant . . . . .	177
VIII	Conclusion . . . . .	<b>178</b>

---

## I Sujet, problématique et état de l'art

La multiplication anarchique d'équipements informatiques et multimédia au sein des habitations privées, des bâtiments industriels et des lieux publics conduit à une augmentation significative de la consommation d'énergie. Les préoccupations environnementales se heurtent à une demande sans cesse croissante de la part des opérateurs et des industriels, de promouvoir le haut débit dans le Réseau Local Domestique (RLD) avec une offre de services de plus en plus diversifiée. Le haut débit domestique ne fera que renforcer ces nouveaux enjeux en matière de consommation énergétique et de santé publique.

Pour les 28 millions de foyers français potentiellement équipés, la fourniture de l'énergie cumulée correspondante équivaut à la production de trois centrales thermiques de moyenne puissance. Une extrapolation à l'Europe prévoit qu'en 2012, la consommation des réseaux domestiques de l'Union atteindra les 100 TWh annuels. Bien entendu, ce chiffre n'inclut pas la consommation énergétique du réseau d'accès et du réseau cœur. La demande en très haut débit domestique est forte, sous la pression conjuguée de l'introduction du réseau d'accès optique chez l'abonné (100 Mbit/s et au-delà) et de la prolifération de sources et de récepteurs multimédia en Haute-Définition (HD). Dans ce dernier cas, une contrainte de mobilité des liaisons apparaît rapidement pour éviter des coûts d'interfaçage et de câblage prohibitifs. Pour preuve de l'activité dans ce domaine, on peut citer des initiatives récentes visant à redéfinir le RLD dans un contexte à très haut débit : d'une part, les projets européens Alpha et Omega, visant à développer un RLD fournissant des services sans-fil à 1 Gbit/s, et d'autre part, le projet Techim@ges du Pôle Image et Réseau. Dans tous les cas, l'optique sans fil en ligne directe est considérée comme le recours ultime, dès lors que les débits visés dépassent plusieurs Gbit/s.

Par rapport à l'offre existante en transmission sans fil Radio-Fréquence (RF), notre étude vise à caractériser et évaluer une technologie de RLD "tout-optique", fournissant des cellules optiques en ligne directe à très haut débit (plusieurs Gbit/s), via un réseau d'inter-connexions en fibre optique. Ce dernier point est une approche originale par rapport à l'état de l'art actuel. Le dimensionnement de ce RLD passe par la caractérisation physique du canal de transmission optique fibre/espace libre et le choix d'une forme d'onde adaptée. En outre, la validation de la solution retenue doit intégrer des critères environnementaux, tels que la minimisation de la consommation énergétique et le respect des normes sanitaires, le tout visant des coûts d'implantation et d'entretien les plus bas possibles.

Ce chapitre présente un résumé du travail effectué pendant cette thèse. Après avoir défini la méthodologie du travail, l'architecture proposée est décrite avec une première approche des composants du système et une validation du budget de puissance optique. Après cela, la caractérisation théorique, par simulations et tests expérimentaux de la communication fibrée et de la transmission sans fil sont présentées avant de finir par la simulation et les mesures expérimentales du système global ainsi qu'une conclusion.

---

---

## II Méthodologie

L'ingénierie du réseau innovant défini selon les critères précédents (dit "GROWTH", pour GRreen Optical Wireless inTo Home network) est une étude résolument amont. Le travail est découpé en quatre parties :

- Dimensionnement de l'architecture GROWTH et sélection des technologies opto-électroniques associées. On établit les spécifications de l'architecture et des composants permettant de valider les bilans de liaisons compatibles avec un rapport signal-sur-bruit (SNR) minimal en réception, un coût d'implantation et une consommation énergétique faibles, et enfin le respect des normes sanitaires.
- Simulation du canal optique mixte "Fibre optique + Espace libre" : cette tâche s'effectue à partir de la plate-forme du logiciel "VPI Transmission Maker", standard mondial en matière de simulation de transmission optique. On caractérise ainsi différents types de fibres (monomode et multimode silice, multimode polymère) en termes de Réponse Impulsionnelle (RI) et/ou de dispersion inter-modales, en fonction des conditions d'injection dans la fibre, des caractéristiques géométriques et de la longueur de cette dernière. Le canal espace libre est assimilé à un simple filtre temporel dans un premier temps. Les caractéristiques des optiques de formation de faisceau définies pour les bornes optiques doivent être prises en compte pour affiner le modèle logiciel. Par la suite, on incorpore des phénomènes physiques et des modèles de composants plus affinés, tels que le multitrajet (espace libre) et le dispositif de concentration optique.
- Choix de la forme d'onde : la génération d'un nombre limité de réponses impulsionnelles (2 ou 3), représentatives du canal optique hybride et découlant de l'étude du point (2) est exploitée par simulation logicielle (Matlab) pour choisir une forme d'onde (mono- ou multiporteuse) utilisée en association avec le couple égaliseur/codeur de canal. Si ces formes d'onde ont déjà été longuement étudiées en RF, elles ne l'ont été que très succinctement en transmission optique mais jamais de manière rigoureuse au niveau du réseau.
- Mesures expérimentales : au niveau physique, un banc d'expérimentation est progressivement monté pour mesurer le Taux d'Erreur Binaire (TEB) de liaisons mixtes "fibre + espace libre" en fonction des caractéristiques physiques des canaux et du schéma émetteur/récepteur retenu.

## III Architecture proposée

Le cadre de la présente étude est le dimensionnement et la caractérisation d'un réseau de fibre optique pour distribuer à très haut débit des cellules optiques sans fil avec un faible impact environnemental et sanitaire (Figure 1). Ce système est basé sur une solution proposée pour les réseaux Radio-sur-Fibre (RoF), sauf que la sous-porteuse

---

RF analogique est remplacée ici par les données optiques numériques. Contrairement aux systèmes RoF qui transportent les cellules RF par fibres optiques, les cellules ici sont transmises sans fil via un lien optique avec des schémas de modulation numériques, réduisant ainsi la complexité de transmission. La longueur d'onde adaptée à cette transmission est de 1550 nm choisie pour des raisons de sécurité oculaire. Le réseau (FTTH) fournit un signal optique à la Station de Contrôle Optique (SCO) dans la maison, qui peut être considérée comme un commutateur optique multiport avec amplification optique possible à ce stade. Au niveau des sorties de la SCO, les signaux optiques sont distribués à des Points d'Accès Optiques (PAO) dans chaque pièce, en utilisant des fibres optiques dédiées. Ces signaux sont transférés du PAO à des terminaux mobiles au sein d'une pièce en utilisant une liaison optique sans fil à très faible divergence (Narrow Line-of-Sight (NLOS)), qui permet d'envisager une communication allant au-delà du Gbit/s. Ce signal optique diffusé

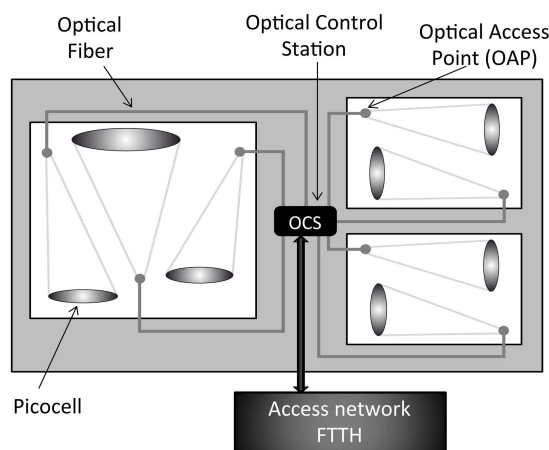


Figure 6.1: Réseau domestique de distribution des cellules optiques par fibre optique

en espace libre doit être capté par un récepteur mobile formé par l'assemblage de plusieurs éléments. L'élément principal de ce récepteur est une photodiode possédant une bande passante suffisamment large pour atteindre un débit dépassant le Gbit/s. Une photodiode ayant cette bande passante a une faible surface de détection, ce qui implique l'augmentation des pertes en espace libre. Une partie de cette perte est compensée par un concentrateur optique qui est un élément optique passif capable de faire converger les rayons optiques entrant par sa large surface d'entrée sur sa petite surface de sortie. Plusieurs prototypes du concentrateur adapté à la photodiode utilisée ont été usinés via une collaboration des moyens technologiques des départements optique et micro-ondes de Télécom Bretagne.

## IV Validation du budget optique

Après définition de l'architecture du système, on s'est intéressé aux choix des différents composants du système. Cela nous a permis de calculer le budget de la



puissance entre l'émetteur et le récepteur et de valider la faisabilité de notre système tout en définissant la géométrie en espace libre. Dans ce système conçu pour être installé chez le grand public, toutes les normes de sécurité et précisément celles de sécurité oculaire sont respectées. Dans cette estimation, une puissance optique de 10 dBm est distribuée à la sortie du PAO, l'atténuation est de 50 dB en espace libre dans une configuration offrant une couverture d'une zone de 10 cm de diamètre à une distance de 2,5 m du plafond. Le filtrage optique pour réduire l'effet de la lumière ambiante ajoute 1 dB de perte pour le système. Le concentrateur optique offre un gain de 16 dB au système et le photodétecteur utilisé a une sensibilité de -28 dBm. Cette validation énergétique est résumée dans ce tableau où on voit que le budget permis de puissance optique est égal à toutes les atténuations avec une certaine marge. Après ce premier pas dans cette étude, des simulations et des

Table 6.1: Budget de puissance du lien optique en espace libre

Puissance permise (à la sortie du HOE)	10 dBm	
Pertes en espace libre		50 dB
Filtre optique		1 dB
Gain du concentrateur	16 dB	
Marge du système		3 dB
Sensibilité du récepteur	- 28 dBm	
Atténuation du système + Marge		54 dB
Budget de puissance	54 dB	

caractérisations avancées pour le système et ses différentes parties ont été lancées.

## V Caractérisation de la fibre pour la distribution des cellules optiques en espace libre

La fibre PF-GI-POF était le premier choix pour la fibre utilisée dans le système pour connecter les différentes pièces de la maison. Ce choix a été bien étudié pour ses différents avantages en termes de flexibilité mécanique, de simplicité d'installation, de maintenance par les clients eux-mêmes sans le besoin d'un kit spécial ou d'un spécialiste, de non-précision parfaite des connexions grâce à son large cœur et aussi pour une question de prix. Dans cette caractérisation, on a commencé par des simulations de propagation à travers la fibre PF-GI-POF, tout en la comparant avec d'autres types de fibres multimodes. Cela a été suivi par des mesures du profil spatial à la sortie de la fibre selon un axe déterminé qui ont été faites à l'ENSSAT de Lannion. Ce travail a abouti à de bons résultats mais on a bien vu le besoin d'approfondir cette étude. Cela a été fait par une collaboration (bourse de l'UEB) lors d'un séjour de trois mois à l'Université Carlos III de Madrid en été 2011. Les mesures effectuées sont les suivantes :

- Les pertes de transmission à travers la fibre pour différentes conditions d'injection

(décalage par rapport à l'axe de la fibre) (figure 6.2). Cette mesure montre une très faible sensibilité de la puissance à la sortie de la fibre par rapport à la variation des conditions d'injection avec une marge supérieure à  $\pm 10 \mu\text{m}$  avec moins de 1 dB de variation.

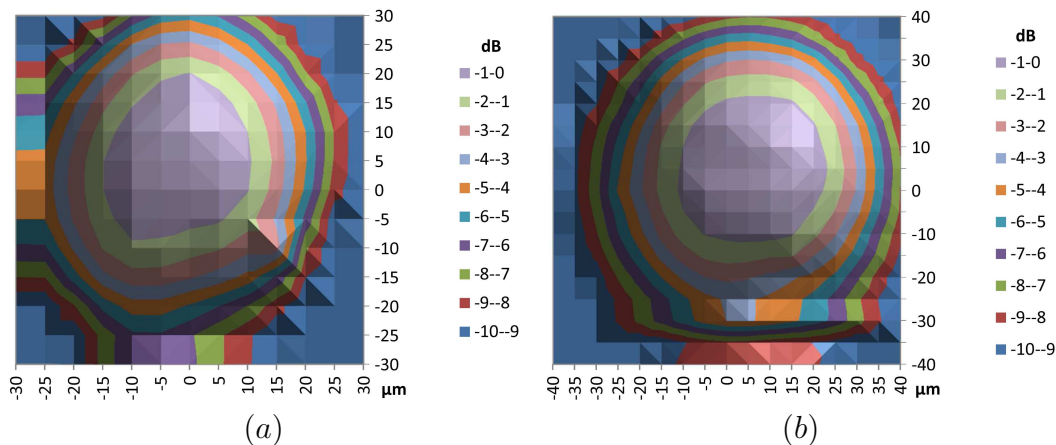


Figure 6.2: Pertes de transmission mesurées à la sortie de 50 m de PF-GI-POF pour différentes conditions d'injection avec un pas de  $5 \mu\text{m}$  à la longueur d'onde 1550 nm pour une fibre de (a)  $50 \mu\text{m}$  et (b)  $62,5 \mu\text{m}$  de diamètre de cœur

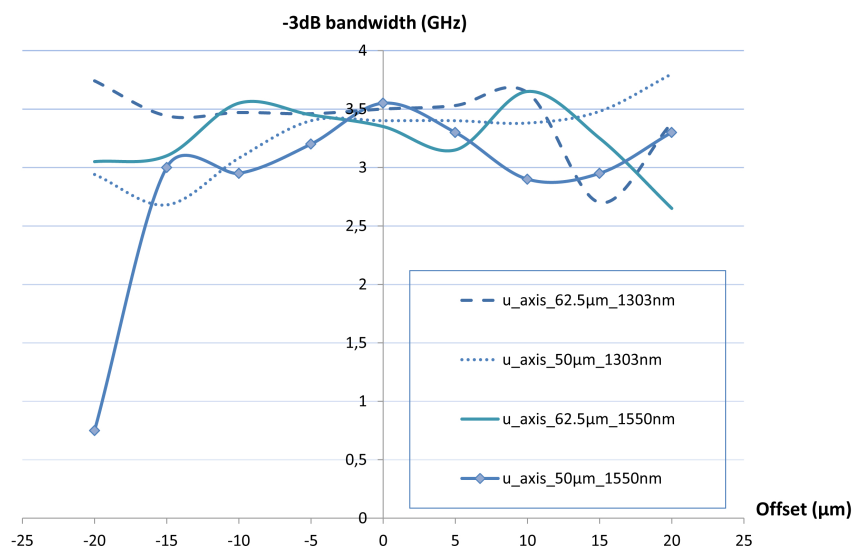


Figure 6.3: Variation de la bande passante à  $-3 \text{ dB}$  à travers 50 m de PF-GI-POF en fonction de l'offset pour deux diamètres de cœur ( $50$  et  $62,5 \mu\text{m}$ ) et deux longueurs d'ondes ( $1303$  et  $1550 \text{ nm}$ )

- La réponse en fréquence de la liaison fibrée, en utilisant un analyseur de spectre RF couplé à un photo-détecteur rapide de  $20 \text{ GHz}$  de bande-passante pour

des conditions d'injection variables. Le paramètre objectif mesuré ici sera la bande-passante à -3 dB. Les courbes de la figure 6.3 résument les mesures de la réponse fréquentielle à travers 50 m de la fibre PF-GI-POF pour deux longueurs d'onde (1300 et 1550 nm) et pour deux diamètres de cœur. Ces courbes montrent qu'on a une bande passante à -3 dB supérieure à 3 GHz pour une marge supérieure à  $\pm 15 \mu\text{m}$ .

- La distribution optique spatiale des modes émergeant de l'extrémité de la fibre, en mettant en place un système de mesure en champ lointain (figure 6.4). Le

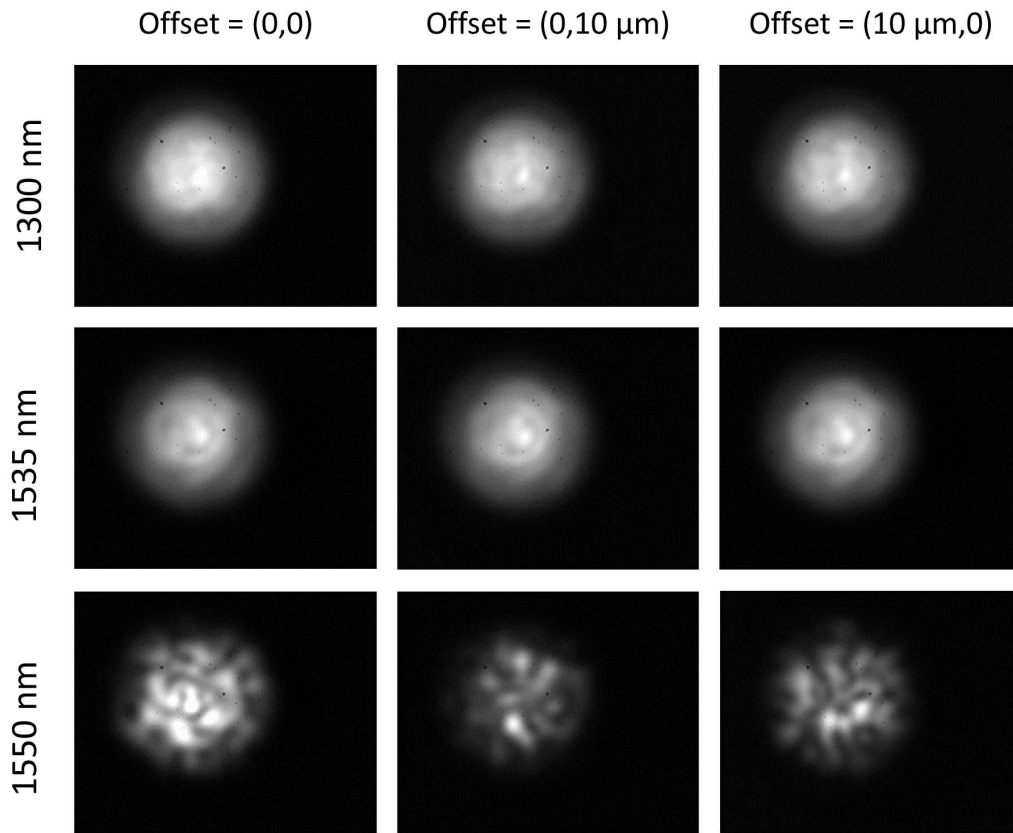


Figure 6.4: Profil spatial à la sortie de 25 m de PF-GI-POF ayant un diamètre de cœur de  $50 \mu\text{m}$  avec une caméra InGaAs. Deux offsets orthogonaux de  $10 \mu\text{m}$  ont été réalisés (colonnes 2 et 3)

profil spatial du signal optique à la sortie de la PF-GI-POF représente des variations de la puissance optique du signal gaussien dû au speckle. Cette variation cause des différences du niveau de puissance au niveau de la zone couverte située à 2,5 m du plafond.

Ces caractérisations ont été également réalisées pour la fibre monomode en silice G657 dédiée pour les réseaux domestiques et qui a présentée de très bonnes performances. La fibre PF-GI-POF reste cependant le premier choix grâce à son faible coût de connexion et à sa simplicité d'installation et de maintenance. Dans la

prochaine section, l'uniformité et le dimensionnement de la cellule optique en espace libre seront présentés.

## VI Caractérisation de la cellule optique en espace libre

Le caractérisation de la cellule optique en espace libre comprend la caractérisation du point d'accès optique qui va définir le profil du signal transmis en espace libre, la caractérisation du récepteur ainsi que le dimensionnement de la cellule optique.

### VI.1 Point d'accès optique

Le point d'accès optique est la partie du système responsable de la définition de la géométrie du lien en espace libre et de la position de la cellule optique, et par suite la zone couverte et la distribution de la puissance optique à l'intérieur de cette zone. Le composant principal du point d'accès optique est l'élément optique diffractif qui est un hologramme capable de modifier le trajet des rayons lumineux par diffraction. Avec cet élément, on fait une réplique pour uniformiser la cellule.

### VI.2 Dimensionnement de la cellule optique en espace libre

Le dimensionnement de la cellule optique en espace libre est fait en fixant quelques paramètres des équations permettant de calculer le rapport SNR du système en fonction des composants choisis et des différents paramètres du système. Les équations ci-dessous montrent la variation de la distance du lien en espace libre en fonction de la variance de la puissance de bruit et de la bande passante du photorécepteur respectivement.

$$d = \sqrt{\frac{r_\lambda A_d G}{\sqrt{2}\pi\alpha^2}} \sqrt{\frac{P_0}{\sigma \operatorname{erfc}^{-1}(2\operatorname{BER})}} \quad (6.1)$$

$$d = \sqrt{\frac{A_d G}{\sqrt{2}\pi\alpha^2}} \sqrt{\frac{P_0}{NEP\sqrt{\Delta f} \operatorname{erfc}^{-1}(2\operatorname{BER})}} \quad (6.2)$$

Où  $r_\lambda$  la responsivité de la photodiode,  $A_d$  l'aire de la surface de détection de la photodiode,  $G$  est le gain du concentrateur,  $\alpha$  le semi-angle de divergence à l'émission,  $P_0$  la puissance optique à la sortie du point d'accès optique,  $\sigma$  la variance de la puissance de bruit. Les figures 6.5 et 6.6 représentent la variation de la distance en fonction de la puissance émise respectivement pour différentes variances de bruit des photorécepteurs du commerce et différentes bandes passantes du récepteur allant de 1 GHz à 3 GHz. Ces figures nous permettent de conclure qu'une cellule optique peut être transmise à une distance dépassant 2,5 m à un débit de 1 Gbit/s avec un taux d'erreur binaire de  $10^{-7}$  et ce avec une modulation NRZ-OOK.

---

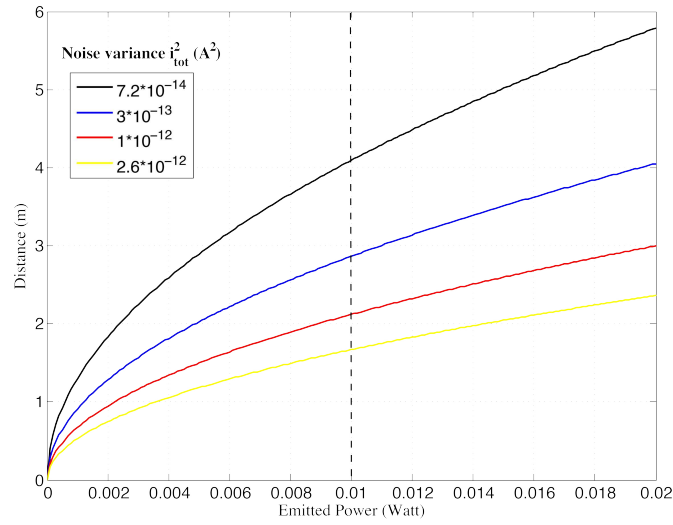


Figure 6.5: Distance en fonction de la puissance émise pour différentes variances de bruit

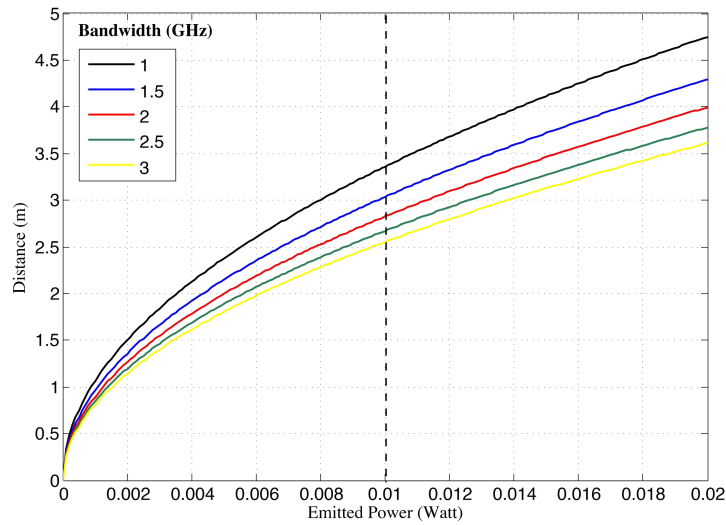


Figure 6.6: Distance en fonction de la puissance émise pour différentes bandes passantes du photodétecteur

## VII Simulation et test expérimental du système global

### VII.1 Simulation du lien descendant

Le lien descendant du système "tout-optique" proposé est simulé dans le but de l'évaluer en termes de diagramme de l'œil électrique et de taux d'erreur binaire au niveau du récepteur. Cette simulation est faite en utilisant le logiciel "VPI Transmission Maker" un puissant outil de simulation des systèmes optiques permettant

les variations des différents paramètres. La figure 6.7 représente la simulation globale du lien descendant. Les diagrammes de l'œil ci-dessous sont celles mesurés à

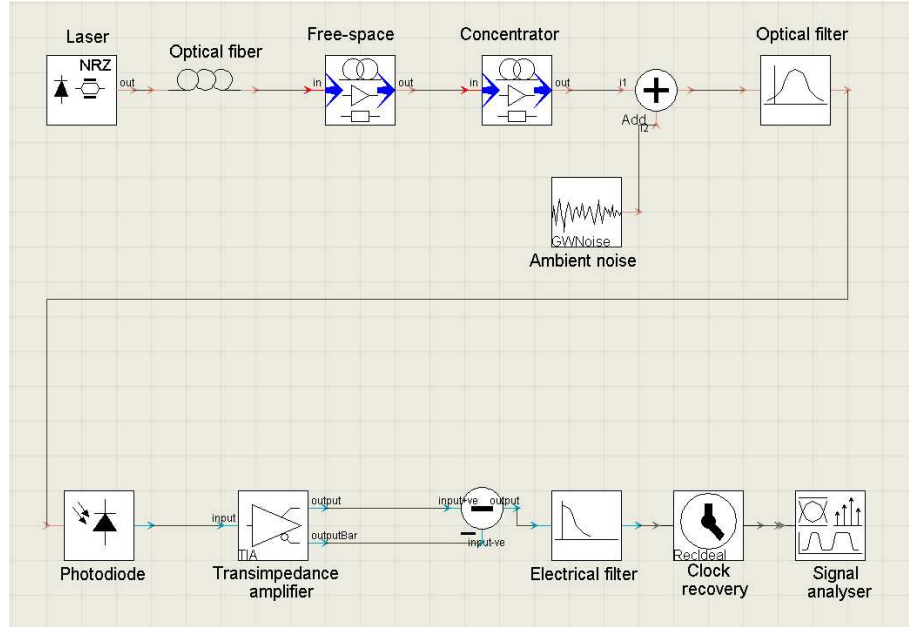


Figure 6.7: Schéma de la simulation globale incluant tous les composants et les effets physiques (bruit et atténuation) du transmission optique hybride

la sortie du récepteur avec une modulation NRZ-OOK à 2.5 Gbit/s dans le cas d'utilisation d'une photodiode PIN (figure 6.8 (a)) et une APD (figure 6.8 (b)) avec une propagation en espace libre pour 2 m avec une divergence de 2° et une puissance à la sortie du PAO de 10 dBm. La simulation a été faite sur 2048 bits et le taux

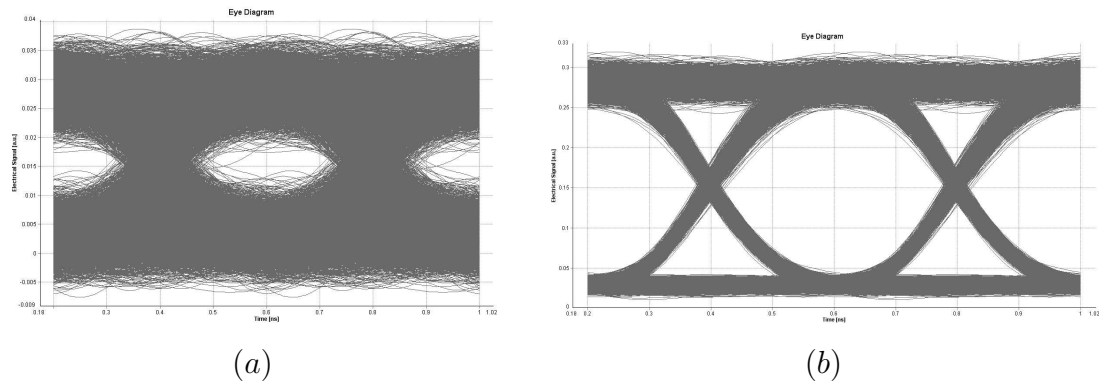


Figure 6.8: Diagramme de l'œil simulé au niveau du récepteur du lien descendant avec 20 m de PF-GI-POF en utilisant un photorécepteur (a) PIN et (b) APD (modulation externe OOK-NRZ à 2,5 Gbit/s)

d'erreur binaire estimé dans le cas de la photodiode PIN est  $1,5 \cdot 10^{-5}$  et  $8,9 \cdot 10^{-70}$

avec l'APD. Une étude théorique portant sur l'efficacité énergétique de ce système en comparant avec les systèmes RF a montré un grand avantage pour cette solution.

## VII.2 Test expérimental du lien descendant

Après la validation du système par simulation, la dernière étape est la validation expérimentale du système. La figure 6.9 représente le banc expérimental incluant les différents composants du système. Les tests du système sont faits en visualisant le diagramme de l'œil et en mesurant le taux d'erreur binaire à des débits allant de 125 Mbit/s à 1 Gbit/s.

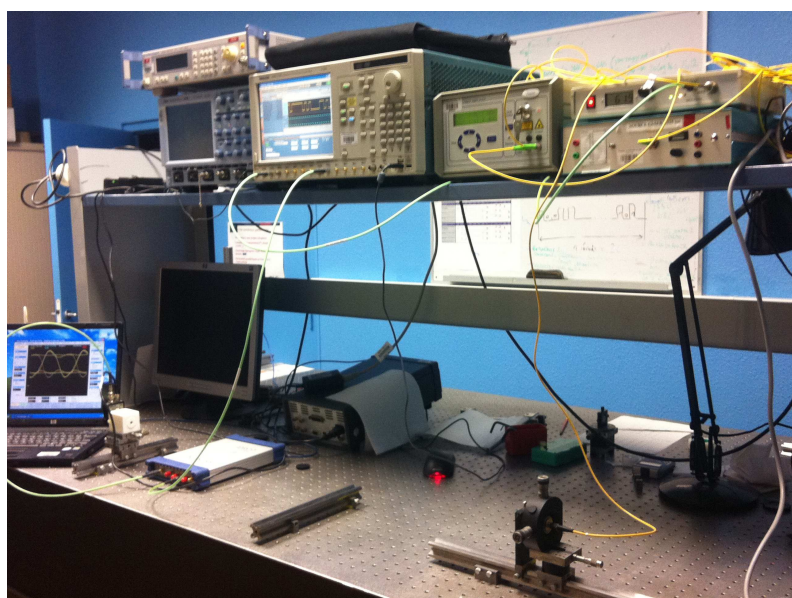


Figure 6.9: Schéma du banc expérimental du lien descendant

Les tests expérimentaux sont débutés par un diagramme d'œil électrique de référence entre le générateur de signaux et le picoscope (oscilloscope numérique) et les différents composants sont ajoutés successivement en regardant les effets introduits par chaque composant en termes de bruit et de perturbation. Les diagrammes de l'œil présentés dans les figures 6.10 correspondent aux diagrammes de l'œil électrique au niveau du récepteur à la présence des différents composants du système à l'exception de l'élément holographique respectivement au centre d'une cellule de 1 cm (a), 2 cm (b), 4 cm (c) de diamètre et à 2 cm de centre de la cellule de 4 cm (d) et cela à un débit de 125 Mbit/s. La distance entre le point d'accès optique et le récepteur est environ 1 m et la cellule a un diamètre de 4 cm à cause d'une réduction du budget optique. Cette réduction est causée par le concentrateur ayant un gain inférieur au gain attendu, les pertes de connexion entre le concentrateur et la photodiode et l'absence de l'élément holographique et par suite du profil uniforme.



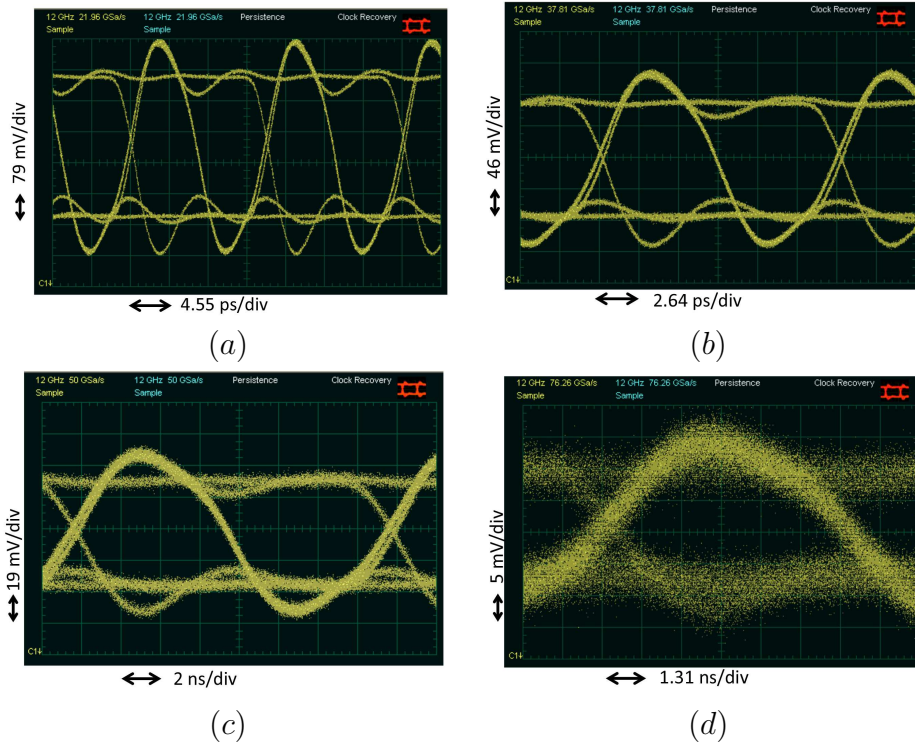


Figure 6.10: Diagramme de l'œil mesuré après une propagation en espace libre en présence du concentrateur au centre d'une cellule de 1 cm (a), 2 cm (b), 4 cm de diamètre (c) et à 2 cm du centre d'une cellule de 4 cm de diamètre (d) à un débit de 125 Mbit/s avec la modulation OOK-NRZ en utilisant le photorécepteur Thorlabs [PDA 10 CF-EC]

## VIII Conclusion

Dans cette thèse, une nouvelle architecture de réseau optique sans-fil pour les réseaux domestiques à très haut-débit ( $> 1$  Gbit/s) est proposée et étudiée. Ce système est basé sur la distribution des femto-cellules optiques dans chaque pièce d'une maison par l'intermédiaire d'un réseau d'interconnexions en fibre optique. L'architecture optique et sa mise en œuvre ont d'abord été réalisées en la validant en termes de bilan de liaison optique. Une fibre polymère perfluorée à gradient d'indice (PF-GI-POF) est sélectionnée en raison de son bon compromis entre la bande passante, la souplesse et l'endurance mécanique dans un environnement intérieur. Cette fibre a été expérimentalement étudiée et caractérisée en pertes de transmission, de réponse en fréquence et de profil de champ lointain, en fonction des conditions d'injection par rapport à l'axe de la fibre. Cette étape est cruciale pour valider la facilité d'installation et de maintenance de la connexion, dans le but d'être effectué par les utilisateurs eux-mêmes. Un prototype virtuel du système a ensuite été conçu en utilisant le logiciel VPI et Matlab en co-simulation, montrant la validité de la liaison descendante à un débit de 2 Gbit/s. L'efficacité énergétique (en J/Mbit) du système proposé est également estimée, montrant un grand avantage par rapport



aux systèmes sans-fil RF existants.

La femto-cellule optique en espace libre a été dimensionnée théoriquement en portée et en surface en fonction des caractéristiques optiques du récepteur, la puissance maximale admissible dans l'espace libre (sécurité oculaire) et l'influence des différentes sources de bruit. Cela nous a permis de montrer qu'en utilisant des dispositifs optoélectroniques standard, le plan de communication situé à une distance de 2 à 3 m du plafond peut être recouvert de femto-cellules de 20 cm de diamètre. Finalement, un prototype physique de la liaison optique descendante est présenté, en combinant la portée de fibre et la transmission en espace libre à 1550 nm, à des débits allant jusqu'à 2 Gbit/s. La qualité de ce lien est évaluée en observant les diagrammes de l'œil reçus et en mesurant le taux d'erreur binaire.

---



## List of publications

1. Hani Al Hajjar, Bruno Fracasso and Dominique Leroux, "*Indoor distributed optical wireless Gbps link dimensioning*", Optical Fiber Communications (OFC) conference, Anaheim, CA, USA, Mars 2013
  2. Hani Al Hajjar, Bruno Fracasso and Dominique Leroux, "*Fiber-distributed Indoor High Bitrate Optical Wireless System*", Wireless Personal Communications Journal, Springer-Verlag
  3. Hani Al Hajjar, Bruno Fracasso and Dominique Leroux, "*Fiber-distributed Indoor High Bitrate Optical Wireless System*", the 14th International Symposium on Wireless Personal Multimedia Communications (WPMC), Brest, France, October 2011
  4. Hani Al Hajjar, David Sanchez Montero, Pedro Contreras Lallana, Bruno Fracasso and Carmen Vasquez, "*Offset-launch characterization of transmission loss in PF-GI-POF for wireless home networks*", 20th International Conference on Polymer Optical Fibers (POF), Bilbao, Spain, September 2011
  5. Hani Al Hajjar, Bruno Fracasso and Dominique Leroux, "*Transmission characterization of PF-GI-POF for high bitrate indoor wireless network*", 20th International Conference on Polymer Optical Fibers (POF)", Bilbao, Espagne, September 2011
  6. Hani Al Hajjar, Bruno Fracasso and Dominique Leroux, "*Fiber-fed multipoint indoor optical wireless system*", International Symposium on Green Radio over Fiber and All Optical technologies for Wireless Access Networks (GROWAN), Brest, France, June 2011
  7. Hani Al Hajjar, Bruno Fracasso et Dominique Leroux, "*Caractérisations temporelle et spatiale de la fibre PF-GI-POF pour les réseaux domestiques optiques à très haut débit*", 29ème Journée Nationale d'Optique Guidée (JNOG), Besançon, France, Octobre 2010
-



## Appendices

---



## Appendix A

### Definitions of some radiometry elements

Radiometry is the measure of the flux intensity of electromagnetic radiation on different wavelength range. This flux and other radiometry factor such as radiance, irradiance and intensity are defined here and the parameters of this radiation are presented in figure A.1.

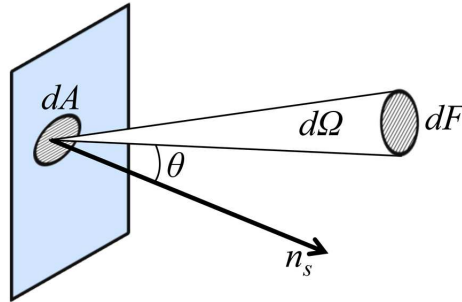


Figure A.1: Elementary source element and its radiometry parameters

- *Flux*: The optical radiation transports some energy. This energy which is transported at the speed of light in a propagation medium, and a given rate per time unit is called "Flux" represented by  $F$  in watt ( $W$ ).
- *Radiance*: is the infinitesimally amount of radiant flux contained in an virtual ray of light arriving at or leaving a point on a surface in a given direction. The radiance is represented by  $L$  and measured on  $(W.m^{-2}.sr^{-1})$  in a direction  $\theta$ .

$$L = \frac{d^2 F}{dA d\Omega \cos \theta} \quad (A.1)$$

Where  $\theta$  is the angle between the normal for the surface and the specified direction and  $\Omega$  is the solid angle subtended by the observation.

When calculated the source radiance,  $A$  represents the source area, and  $\Omega$  is the solid angle into which the light is emitted, while  $A$  refers to detector area and  $\Omega$  the solid angle subtended by the source as viewed from the detector.

- *Irradiance*: It is the radiant flux which arriving at the surface per unit area at a point on a surface, where the surface can be real or imaginary. This flux can arrive from any direction above the surface, as indicated by the rays. Irradiance is presented by  $E$  measured on  $\text{W.m}^{-2}$  and given by the equation:

$$E = \frac{dF}{dA \cos \theta} \quad (\text{A.2})$$

- *Source intensity*: The intensity source  $I$ , in a specified direction, is the elementary emitted flux  $dF$  in the elementary solid angle  $d\Omega$  in the considered direction.

$$I = \frac{dF}{d\Omega} \quad (\text{A.3})$$

Radiance and irradiance can be also presented depending on the signal wavelength and they are called in this case spectral radiance and spectral irradiance, respectively. The SI unit of spectral radiance  $L_\lambda$  is  $\text{W.m}^{-2}\text{sr}^{-1}\text{Hz}^{-1}$  or  $\text{W.m}^{-2}\text{sr}^{-1}\text{nm}^{-1}$ , while spectral irradiance  $E_\lambda$  is measured by  $\text{W.m}^{-2}\text{Hz}^{-1}$  or  $\text{W.m}^{-2}\text{nm}^{-1}$ .

---



## Appendix B

# Beam shaping at the Optical Access Point

### I. DOE dimensioning

The diffractive optical element used in the optical access point is a periodic phase element whose role is to generate a set of uniform diffraction orders arranged in a disk configuration. It belongs to the category of DOEs called "array illuminators" (AIL). More information on the design and fabrication of these optical elements can be found in the literature [1], [2]. Figure B.1 shows a schematic view of the AIL operation, including both the DOE (OAP plane) and the diffraction pattern characteristics at the optical cell plane, which is supposed to be generated in the Fraunhofer (Fourier) regime.

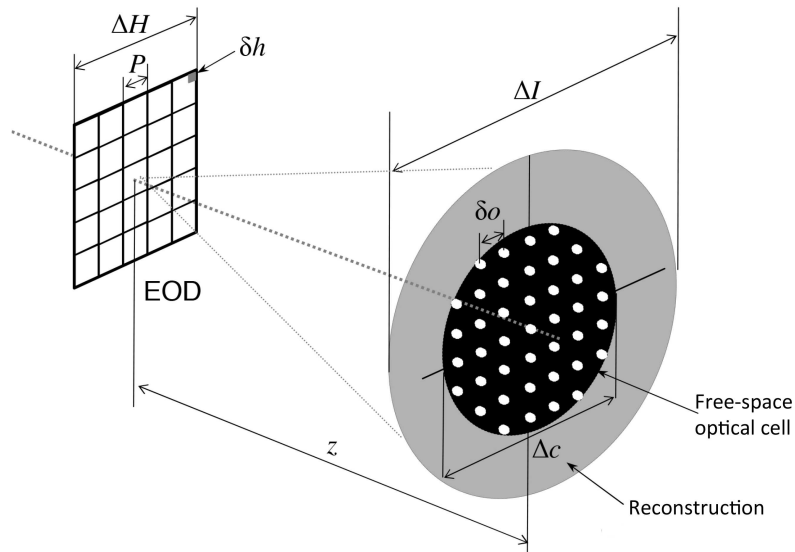


Figure B.1: Basic reconstruction scheme of the AIL DOE. The component is here supposed to be illuminated by a plane monochromatic wave.

The illumination wave is supposed to be a collimated beam at wavelength  $\lambda$ .

All relevant parameters are listed in Table B.1. Only three of them (wavelength, operating distance and cell diameter) are imposed *a priori* by the free-space link overall design. The remaining parameters have to be determined from the DOE technological fabrication constraints.

Physical parameter	Variable	Value
Operating wavelength	$\lambda$	1.55 $\mu\text{m}$
Distance between the DOE and the reconstruction plane	$z$	2.5 m
Reconstructed cell dimensions	$\Delta C$	15 cm
DOE resolution	$\delta h$	$\times$
Number of sampling points in the DOE per dimension	$N_{pts}$	$\times$
Spatial period of the DOE	$P$	$\times$
Number of pixels per period in the DOE	$N_{ppp}$	$\times$
Size of the reconstructed image (per dimension)	$\Delta I$	$\times$
Spatial resolution of the reconstructed image	$\delta I$	$\times$
DOE size	$\Delta H$	$\times$
Spacing between two adjacent diffraction orders	$\delta o$	$\times$
Number of orders in the reconstructed cell (per dimension)	$N_{ord}$	$\times$

Table B.1: *List of the parameters used in the AIL-DOE reconstruction process. A "×" symbol indicate that the parameter is to be determined by the dimensioning process.*

Considering the elementary laws of diffraction and using a paraxial diffraction model in the Fraunhofer region, we can write :

$$\delta o = \frac{\lambda z}{P}, \quad \Delta I = \frac{\lambda z}{\delta h} \quad \text{and} \quad \delta I = \frac{\lambda z}{\Delta H}. \quad (\text{B.1})$$

This yields the "well-known" relationship concerning the beam reconstruction parameters in digital holography [3], namely:

$$\delta I \cdot \delta h = \frac{\lambda z}{\Delta H} \cdot \frac{\Delta H}{N_{pts}} = \frac{\lambda z}{N_{pts}}, \quad \text{and} \quad \Delta I \cdot \Delta H = \frac{\lambda z}{\delta h} \cdot \Delta H = \lambda z \cdot N_{pts}. \quad (\text{B.2})$$

Additionally, we can write the basic relations concerning the DOE and cell geometrical structures :

$$\Delta C = N_{ord} \delta o, \quad P = N_{ppp} \delta h = \frac{\Delta H}{N_{per}}. \quad (\text{B.3})$$

Combining these relations yields the "cell-image" ratio and the "hologram complexity" laws, respectively defined by :

$$\frac{\Delta I}{\Delta C} = \frac{\lambda z}{\delta h} \cdot \frac{N_{ppp} \delta h}{N_{ord} \lambda z} = \frac{N_{ppp}}{N_{ord}} \quad \text{and} \quad \frac{N_{ord}}{N_{per}} = \frac{\Delta C}{\delta o} \cdot \frac{P}{\Delta H} = \frac{\lambda z}{\delta o^2} \frac{\Delta C}{\Delta H} \quad (\text{B.4})$$

The DOE fabrication process (photoresist + photoplotter) imposes an upper limit to the DOE resolution at  $\delta h = 1\mu\text{m}$ . In addition, the DOE size is limited by the diameter of the Fourier lens used at the OAP (1/2"), as justified in the next section of this appendix. From these constraints and the above dimensioning relations, a set of consistent DOE parameters can be determined, as those provided in table B.2.

Physical parameter	Variable	Value
Distance between the DOE and the reconstruction plane	$z$	2.5 m
Reconstructed cell dimensions	$\Delta C$	15 cm
DOE resolution	$\delta h$	1 $\mu\text{m}$
Number of sampling points in the DOE per dimension	$N_{pts}$	12700
Spatial period of the DOE	$P$	1.94
Number of pixels per period in the DOE	$N_{ppp}$	1938
Size of the reconstructed image (per dimension)	$\Delta I$	3.88 m
Spatial resolution of the reconstructed image	$\delta I$	305 $\mu\text{m}$
DOE size	$\Delta H$	12.7 mm
Spacing between two adjacent diffraction orders	$\delta o$	2 mm
Number of orders in the reconstructed cell (per dimension)	$N_{ord}$	75

Table B.2: *DOE parameters : numerical values.*

Figure B.2 (a) shows the binary phase pattern, corresponding to one spatial period of the DOE, whose diffraction pattern intensity is shown in figure B.4 (31 spots in cell diameter). The DOE computer design and fabrication has been performed by prof. Kevin Heggarty, from Telecom Bretagne, in the lab facilities of the Optical Department. The DOE pattern in B.2 (b) is an improved version, which diffracts 601 spots along the diameter of the optical cell (250  $\mu\text{m}$  between two diffraction orders)

## II Collimating lens parameters

The OAP structure dedicated to beam forming is schematically depicted in figure B.3. The reference configuration corresponds to the fiber output located at the object (rear) focal point of the positive lens, hence producing a collimated beam at the output of the lens. The lens choice can be made so as to limit aberrations and vignetting. This depends on both the lens diameter  $D$  and focal length  $f$ , and the numerical aperture NA of the fiber. A thumb law can be used here by considering that the beam half-width  $w$  at the lens plane should not exceed the half-diameter of the lens as shown in figure B.3 (a), which can be expressed by  $w < D/4$ , or, in other words  $f_{\#} < 1/(4 \cdot NA)$ , where  $f_{\#} = f/D$  is the lens  $f$ -number. With NA = 0.1 and 0.2 for the SMF and POF fibers, respectively, we obtain  $f_{\#}^{\text{SMF}} < 2.5$  and  $f_{\#}^{\text{POF}} < 1.25$ . To ensure a compact OAP design, a 1/2" lens diameter is considered, yielding  $f = 20$  mm as a suitable value.

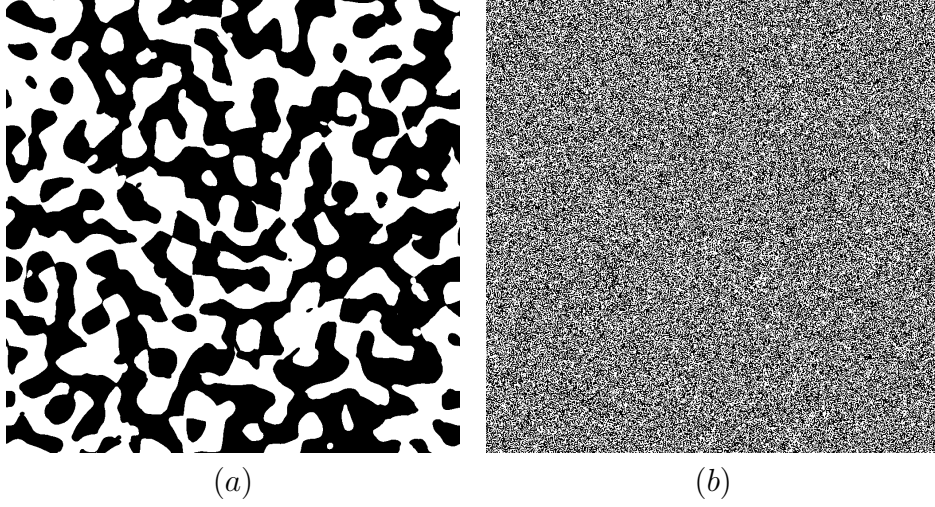


Figure B.2: Binary DOE phase patterns (one spatial period) with black and white areas correspond to 0 and  $\pi$  phase shifts at the design wavelength (1550nm)

### III. Optical cell control

As shown in figure B.3 (b), the optical cell is focused at the working distance ( $\approx 2\text{-}3$  m) by positioning the fiber at a distance  $f + d$  from the lens plane. The situation is depicted in figure B.3 (c) where F and F' denote the lens rear and front foci respectively. In this situation, we have  $\overline{OF} = -f$  and  $\overline{OF'} = f$  and  $\overline{OA} = -f + d$ . If  $OA' = z$  is the distance at which the image is focussed in the image plane, then, using the imaging lens conjugation law  $\frac{1}{OA'} - \frac{1}{OA} = \frac{1}{f}$ . With  $d \ll f$ , we obtain the approximation  $d \simeq f^2/z$ . Numerically, using  $f = 20$  mm and  $z = 2.5$  m, we obtain a reference working distance of  $d = 160$   $\mu\text{m}$ . This means that the DOE placed after the lens will produce a cell filled with bright spots, corresponding to the diffraction orders of the DOE. (see figure B.4 (a)).

The spatial uniformity of the cell can then be controlled by a lens defocussing, using

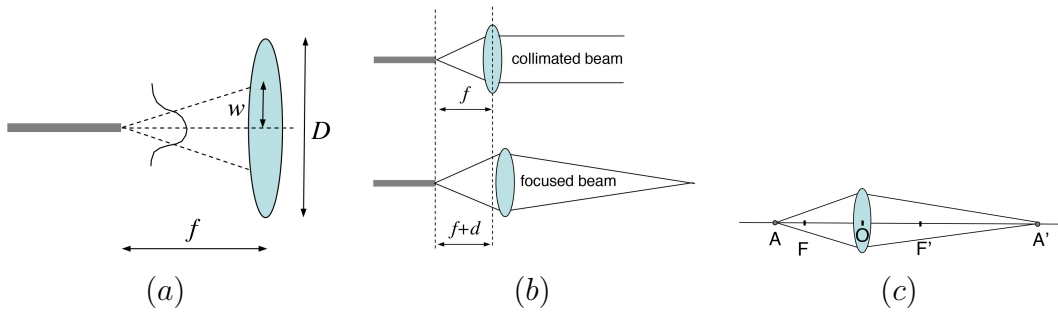


Figure B.3: (a) limits of beam half width relative to lens diameter, (b) source position relative to the lens and the corresponding emerged beam (collimated or focused) and (c) the image A' at the lens output corresponding to an object A

an additional shift in the  $d$  value to produce a spatial optical cell that tends to be uniform in power. This operation is illustrated in figure B.4 (b) and (c).

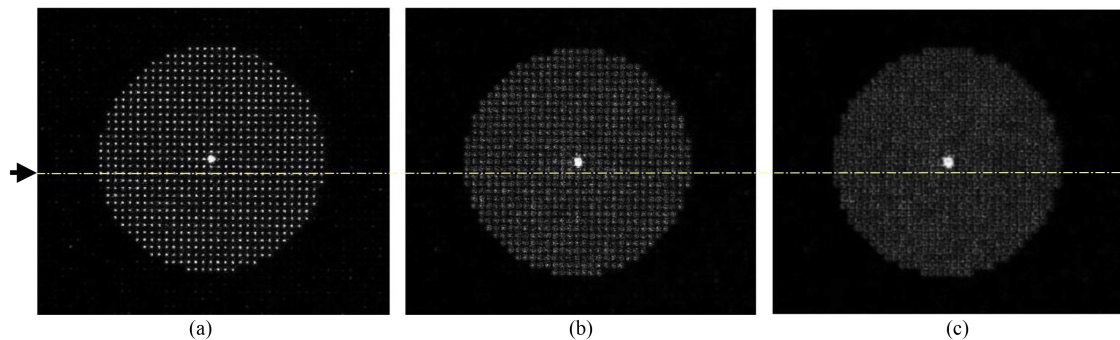


Figure B.4: Optical cell uniformity control, using a defocusing of the lens at the OAP. The corresponding line profiles are shown in figure 4.6 (Chapter 4)

Figure B.5 (a) shows the OAP prototype with the FC-PC fiber connector on the left side. Figure B.5 (b) is a split view of the device with (from left to right) fiber holder, housing, lens holder rings 1, lens, lens holder rings 2 and protection cap. The DOE is glued onto the flat side of the lens.

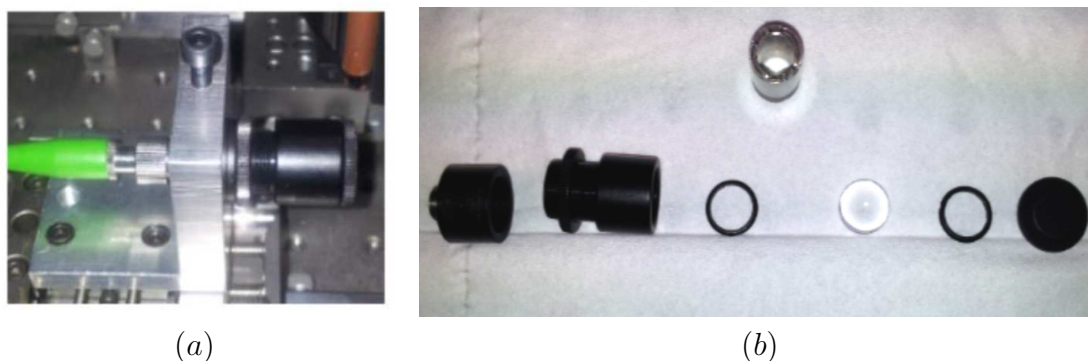


Figure B.5: OAP assembly using commercially available optomechanical components (1/2" Thorlabs units).

## Bibliography

- [1] J. Jahns, M. M. Downs, M. E. Prise, N. Streibl, and S. J. Walker. Dammann gratings for laser beam shaping. *Journal of Optical Engineering*, 28(12), Dec. 1989.
- [2] H. Lüpken, T. Peter, F. Wyrowski, and O. Bryngdahl. Phase synthesis for array illuminator. *Optics Communications*, 91(3–4):163 – 167, 1992.
- [3] A. W. Lohmann and D. P. Paris. Binary fraunhofer holograms, generated by computer. *Appl. Opt.*, 6(10):1739–1748, Oct 1967.